A Model Development for Reconstruction of Three-Dimensional Defects based on MFL Signals

Dissertation
zur Erlangung des Grades
des Doktors der Ingenieurwissenschaften
der Naturwissenschaftlich-Technischen Fakultät
der Universität des Saarlandes

von
Isabel Cristina Pérez Blanco

Saarbrücken
2020

Tag des Kolloquiums:	22.10.2020
Dekan:	Prof. Dr. rer. nat. Guido Kickelbick
Berichterstatter:	Prof. Dr.-Ing. Christian Boller
	Prof. Dr.-Ing. Gerhard Mook
Vorsitz:	Prof. Dr. Andreas Schütze
Akad. Mitarbeiter:	Dr. Ing. Frank Aubertin

In te, Dómine, sperávi: non confúndar in ætérnum.

(From Te Deum)

Abstract

Corrosion has been statistically placed as the primary cause for pipeline failures well beyond other factors. The inability to accurately size corrosion defects located in pipelines can result in erroneous integrity strategies with fatal consequences, even when appropriate inspection processes have been conducted. Underestimation or overestimation of the defect size causes on one hand pipeline failures and on the other unnecessary assessments. Several strategies for defect sizing based on MFL signals have been developed in recent years. However, the industry still urges for reliability improvements.

The current thesis develops a model based on calibration curves for the reconstruction of defects, based on MFL signals. A thorough study of different parameters involved allows for the understanding of the relationships between defect dimensions and MFL signal features. The methodology of this research includes theoretical, numerical and experimental assessments resulting in the development of a reliable three-dimensional model. Calibration curves are reported for inner as well as for outer defect configuration. Such curves permit the accurate establishment of the defect length and depth by means of the signal duration and amplitude. The results of this study for a single defect can be further implemented in order to investigate the superposition of MFL signals coming from adjacent defects. The MFL signal superposition is demonstrated through simulations and experiments.

Zusammenfassung

Nach der Statistik ist Korrosion, neben anderen Faktoren, die primäre Ursache für Rohrleitungsversagen. Die Unfähigkeit, Korrosionsfehler in Rohrleitungen genau zu dimensionieren, kann zu fehlerhaften Integritätsstrategien mit fatalen Folgen führen, selbst wenn geeignete Prüfprozesse angewendet werden. Eine Unterschätzung oder Überschätzung der Fehlergröße führt einerseits zu Pipelineversagen und andererseits zu unnötigen Untersuchungen. In den letzten Jahren wurden verschiedene Strategien zur Fehlergrößenbestimmung basierend auf Signalen des magnetischen Streuflusses entwickelt. Die Industrie drängt jedoch weiterhin auf eine Verbesserung der Zuverlässigkeit durch diese Technik.

In der vorliegenden Arbeit werden Kalibrierkurven für die Rekonstruktion von Fehlstellen basierend auf Signalen des magnetischen Streuflusses beschrieben. Eine gründliche Untersuchung der verschiedenen Einflussparameter ermöglicht die Beziehungen zwischen den Dimensionen der Fehlstellen und Signalmerkmalen des magnetischen Streuflusses zu verstehen. Die Methodik dieser Forschung umfasst theoretische, numerische und experimentelle Bewertungen, die zur Entwicklung eines zuverlässigen dreidimensionalen Modells führen. Kalibrierkurven werden sowohl für Innen- als auch für Außenfehler angegeben. Solche Kurven ermöglichen die genaue Ermittlung der Fehlstellenlänge und -tiefe anhand der Signallänge und -amplitude. Die Ergebnisse, die in dieser Studie für Einzelfehler gewonnen wurden können verwendet werden, um Untersuchungen an benachbarten Fehlstellen durchzuführen, bei denen sich die Signale des magnetischen Streuflusses überlagern.

Acknowledgements

This work would not have been possible without the financial support of DAAD, COLCIENCIAS, ICETEX, the Ministry of National Education of Colombia and primarily the Corporation for the Investigation of Corrosion (CIC). In particular I thank Dr. rer. nat. Jorge Hernando Panqueva Alvarez for his personal witness and for entrusting me with this work. Likewise I offer deep gratitude to Prof. Dr.-Ing. Christian Boller for providing me with the possibility to complete the doctorate accompanied by opportune advice, and for joining the Fraunhofer Institute for Non-destructive Testing (IZFP) and the Chair of Non-destructive Testing & Quality Assurance (LZfPQ).

I am deeply indebted to Prof. e.h. Dr. rer. nat. Dr.-Ing. e.h. Gerd Dobmann for his persistent charity in nurturing this work through his extraordinary knowledge and his permanent willingness. I am truly fortunate to have had the opportunity to work with him and learn from his virtues and strengths.

Finally, I would be remiss if I did not acknowledge the guidance and innumerable sacrifices made by my parents Gonzalo and Edilia, and the invaluable company and encouragement from my son Nicolas through the difficult circumstances experienced while I pursued this doctorate. I would also like to recognize the professional, moral and financial support of our friends, who are evidence that who finds a faithful friend finds a treasure.

Contents

List of Figures

List of Tables

Terminology

2D	Two-dimensional
3D	Three-dimensional
ADC	Analog to digital converter
AER	Alberta Energy Regulator
ANN	Artificial Neural Networks
ANSI	American National Standards Institute
API	American Petroleum Institute
ASME	American Society of Mechanical Engineers
ASNT	American Society of Nondestructive Testing
BP	British Petroleum Company
BTU	British Thermal Unit
CGS	Centimetre-Gram-Second system of units
CIC	Corporation for the Investigation of Corrosion
DA	Direct Assessment
DIN	German Institute for Standarization
DMC	Dipolar Magnetic Charge
DOF	Degrees of freedom
EMAT	Electromagnetic Acoustic Transducer
EN	European Standard
ET	Eddy Current Testing
FEA	Finite Element Analysis
FEM	Finite Element Method
FFS	Fitness-For-Service
hit/miss	NDE system response (detection/no–detection) when a flaw is present.
HRMFL	High Resolution Magnetic Flux Leakage
HVP	High Vapour Preassure
H_x	Axial Component of the Magnetic Field
H_{x1}	Axial Component of the Magnetic Field at 1 mm lift-off
H_y	Circumferential Component of the Magnetic Field
H_z	Radial Component of the Magnetic Field
ILI	In-line Inspection
INGAA	Interstate Natural Gas Association of America
INS	Inertial Navigation System
ITION	In–line Inspection Tool for Hydrocarbons Pipelines
IZFP	Fraunhofer Institute for Nondestructive Testing
LPI	Liquid penetrant inspection

MAOP	Maximum Allowable Operating Preassure
MFL	Magnetic Flux Leakage
MMS	Modular Measurement system
MT	Magnetic Particle Testing
NACE	National Association of Corrosion Engineers
NDE	Non-destructive Evaluation
NDT	Non-destructive Testing
NEB	National Energy Board
OPR	Onshore Pipeline Regulations
PDAM	Pipeline Defect Assessment Manual
PDE	Partial Differential Equation
PIG	Pipeline Inspection Gauge
POD	Probability of Detection
POF	Pipeline Operators Forum
POI	Probability of Identification
PT	Dye Penetrant Inspection
PTPD	Peak-to-peak-distance
PWHM	Peak-width at half-maximum
RT	Radiographic Testing
SI	International System of Units
SNR	Signal-to-Noise Ratio
UT	Ultrasonic Testing
Vpp	Volts peak to peak

1

Introduction

Despite all efforts from industry and scientists to establish new energy sources that satisfy the energy demand worldwide, there is still an evident need to continue taking advantage of fossil fuels as primary energy sources. Section 1.1 presents an overview of the global pipeline background. It addresses energy consumption and tendencies across the world to introduce the fundamental role of pipelines in today's society. Although pipelines are considered the safest means of transport for oil and natural gas, there are still challenges to be solved concerning pipeline integrity management, as will be discussed later. Section 1.2 outlines the motivation of the author and the sponsors of this work, along with the current problematic and industrial requirement.

1.1 Pipelines in International Context

An analysis of the energy market per year around the world is published usually in June by the British Petroleum Company (BP). BP reports in [2], the consumption of every fuel type in the world using the statistical review for the year 2014 (see Figure 1.1). Oil and natural gas provided more than half of the total energy demand in the world. Despite the deceleration of global primary energy consumption in 2014 of 0.9% compared with 2.3% in 2013 and, in relation with the average of the previous ten years (2004-2014) of 2.1%, an increase of the consumption is revealed, in particular of oil (0.8%) and natural gas (0.4%) [2].

By far, the most suitable mode of transportation for large quantities of oil and natural gas along extensive distances are pipelines. In fact, transportation companies currently rely only on a few alternatives. Table 1.1 shows a comparison of the efficiency of freight transport in terms of energy requirements of operation for different methods of transportation [3]. In the table, BTU describes the British Thermal Unit and BTU/ton-mile is the unit used to express energy intensity, namely the energy consumption per freight transport for ton. In addition to the favourable cost-efficiency relation, well-maintained pipelines are: potentially safe, environmentally friendly and reliable, as they

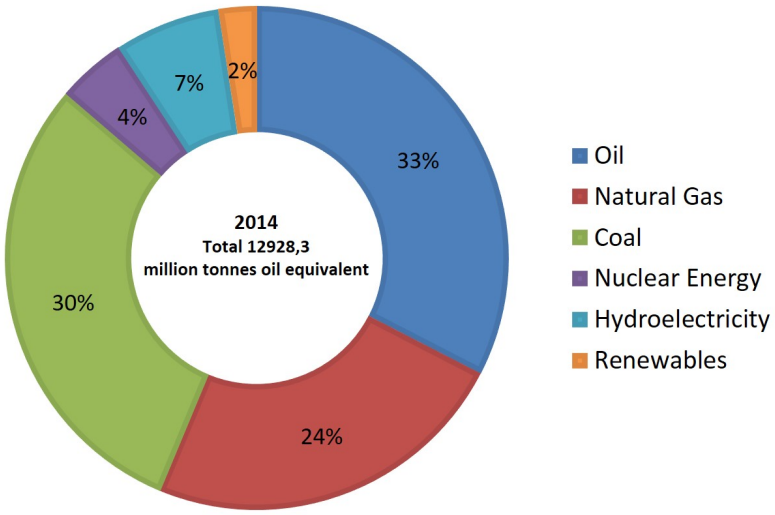

Figure 1.1: *World energy consumption - 2014 [2].*

suffer minimum disruptions and climate conditioning.

Mode of Transportation	**Energy Consumption** [BTU/ton-mile]
Pipeline	450
Waterway (Barge)	540
Railroad	680
Truck	2,300
Airplane	37,000

Table 1.1: *Energy requirements to operate different modes of transportation [3].*

All these advantages from pipelines explain their extensive use in the world. The Pipeline & Gas Journal (P&GJ) reported in its issue of March 2014 an onshore and offshore pipeline operation of 183,190 miles of active crude oil, 155,290 miles of petroleum products and 677,560 of natural gas around the world [4]. Also in January of the same year, P&GJ published the results of a global survey revealing that 109,066 miles of pipelines were in planning or construction stages [5]. Different issues worldwide have triggered investments on pipeline construction over recent years, including the rising consumption of oil and gas in Asia-Pacific due to the growth in their economies, the shale gas development in USA, the decision of nuclear phase-out from different governments, the profitable development of offshore technologies and the increasing consumption of natural gas in South and Central America [4, 5]. The global behaviour for the year 2016 does not differ with results of the BP survey in January 2016 disclosing an amount of 94,799 miles of pipelines being planned and under construction [6].

This is, in general, an attractive scenario for the pipeline market and also a de-

Date	Country	Consequences
January 25	Canada	Natural gas shortage
February 10	USA	No damages of third-party properties
February 13	USA	People injured, damages of houses and vehicles
March 14	USA	Evacuation of people
May 26	USA	Natural gas shortage
June 10	Malaysia	Evacuation of people, damages of houses and vehicles
June 12	India	People killed and injured
June 30	India	People killed and injured, homes destruction
July 1	China	Evacuation of people
July 31	Taiwan	People killed and injured, high public and privat damages

Table 1.2: *Natural gas pipeline accidents January - July 2014.*

manding task for transportation companies and regulatory institutions to guarantee the integrity of pipeline systems. Accidents of diverse magnitude occur often causing environmental, economic and sometimes also human losses. Table 1.2 presents a sketch of large-diameter pipeline accidents that happened in the first seven months of 2014, as an example of reported cases by news in different countries [7].

A look at reported data from the National Energy Board (NEB) in Canada clearly outlines that it is still necessary to improve the inspection and the integration of management techniques to avoid pipeline failures. NEB reports 102 incidents on average per year, in the period between 2008 and 2012, which includes severe injuries and fatalities. These data are based on reported pipeline failures, whose operation is regulated by NEB [8]. NEB classified the incidents according to their definitions in the Onshore Pipeline Regulations (OPR). Different environmental releases are considered for statistics; they include natural gas, high vapour pressure (HVP), low vapour pressure liquid, fire and operation beyond design.

The comparison between statistics of incidents occurred in different regions or countries reports sometimes inconsistencies given that every regulatory jurisdiction can have different criteria for reporting and classification of events. Furthermore, every jurisdiction has its specific pipeline infrastructure with different characteristics. In particular, the case of Alberta in Canada will be discussed here to analyse the causes of incidents statistically. Alberta Energy Regulator (AER) is the corresponding regulatory body for energy-related pipelines in Alberta. AER possesses demanding legislation, whereby every event should be reported independently on volume release of the transported product, as well as every harm in the pipeline or its external protection.

The AER published in August 2013 detailed information about pipeline statistics and incidents in Alberta. The report known as 2013-B: Pipeline Performance in Alberta, 1990-2012 [9] collected data between January 1990 and December 2012. The results

reveal a total of 17,605 incidents, from them: 15,609 are leaks, 1,116 hits with no release and 880 ruptures. Definitions of the terms included in AER data are listed in Appendix A for correct interpretation. AER categorises anomalies in 13 different groups according to their cause. Figure 1.2 illustrates the distribution of reported failures according to the reason. The frequency of every cause is calculated as a percentage of the total releases based on the collected information. A total of 16,489 releases, including leaks and ruptures, occurred in this period of 22 years. For a precise description of every category, see table A.2 in Appendix A. In general, failures are primarily caused by corrosion as demonstrated using percentages in Figure 1.2. Internal or external corrosion provokes almost 70% of the anomalies. Specifically, internal corrosion remains the leading factor with 54.8%.

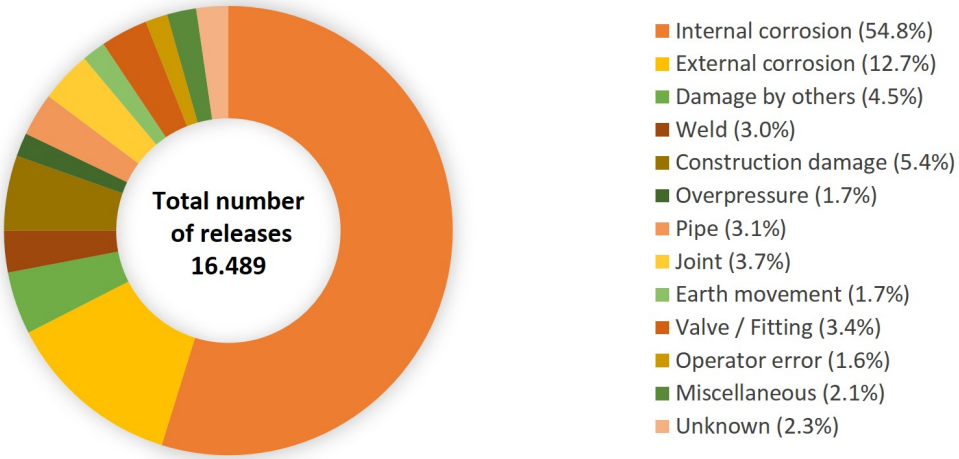

Figure 1.2: *Total number of failure by cause per year [9].*

1.2 Motivation

As a member of the technology group in the **C**orporation for the **I**nvestigation of **C**orrosion (CIC) in Colombia, I deal with the related challenges concerning inspection of pipelines. Main CIC customers are companies that transport oil and natural gas across Colombia and foreseeably also in other South American countries. Just as in the rest of the world, the pipeline network in Colombia is extending. According to the international construction report published by the Pipeline and Gas Journal 2014 [10], the Bicentenario pipeline is nowadays under construction. It will carry 450,000-bpd (barrel-per-day) of heavy crude. In addition, this project includes the construction of two tanks with a capacity of 600,000-bbl (barrels of crude oil). Concurrently with the new pipeline extension, the existing hydrocarbon infrastructure in Colombia is older than 25 years. Throughout this in-service time, several factors as corrosion, mechanical effort, landslides, mishandling, and third-part damages have affected pipeline integrity. Therefore, national enterprises have been forced in the last years to contract even more frequently intelligent inspection services to determine pipelines condition.

Rightly, international pipeline integrity regulations have also increased the require-

ments concerning management, assessment, and mitigation of risks in hydrocarbon transportation. Therefore, in the last decades, improved in-line inspection (ILI) tools have been developed based on available non-destructive testing (NDT) techniques. Currently, in Colombia, these specialised inspection services are performed by foreign companies under global technological standards. However, the regularity of inspections is constrained by high service costs with lacking options of negotiations, limited interaction with the customer to analyse the results and restricted customer support for decision making regarding the safe operation, rehabilitation and repair. Furthermore, the number of cases where these foreign ILI tools do not meet national requirements and conditions are prevalent [11].

The CIC has developed the ITION-I tool in response to the active interest to offer solutions against corrosion. It is an ILI tool that provides inertial and operational information of the inspected pipeline. More than 1,100 kilometres are successfully examined using this technology by 20 runs along pipelines carrying different hydrocarbons which are transported by several companies in Colombia. Attending further requirements from national companies, the CIC is nowadays implementing the so-called ITION-MFL project. ITION-MFL is an improved version of the ITION-I technology which includes a module for defect detection and measurement of pipeline wall thickness. It takes advantage of the magnetic flux leakage (MFL) technique. MFL is a well-known method for inspection of in-place pipelines, its cost is low compared with other technologies, and it can adequately detect reductions in the pipeline wall.

Despite the use of the MFL technique for pipeline inspection since the sixties, the accuracy of MFL signal interpretation is a growing international concern of research [12–17]. There are several parameters, some of them uncontrollable ones, which affect MFL signals and make their interpretation difficult. The lack of a conclusive model for defect characterisation due to the complexity of the three-dimensional magnetic analysis from a theoretical point of view is also an influential factor. Defect sizing is, in any case, a piece of pivotal information considering that the integrity of pipeline systems can be only guaranteed based on proper decisions from real pipeline conditions.

1.3 Outline

The current work responds to the necessity for a reliable sizing of flaws present in ferromagnetic materials. The influential parameters are assessed trough an extensive study using analytical, numerical and experimental approaches. A three–dimensional numerical model is developed and processed using COMSOL Multiphysics as a simulation tool. The model is validated, employing a set of experiments. A model for defect reconstruction is established utilising simulated and experimental results which can determine the dimensions of a flaw, improving current models lacking accuracy.

To achieve the proposed goals, the current thesis begins with an overall introduction emphasising the importance of pipelines in an international context and their related release risk, which places corrosion as the leading cause. Likewise, in the national context,

related Colombian industry urges pipeline inspection companies to improve the precision of the results. Chapter 2 presents the current state, including the type of defects, non-destructive testing methods, reliability of inspection results, the main components of the magnetic flux leakage technique; while Chapter 3 deals with different approaches to perform MFL signal modelling as well as a discussion about magnetic saturation concept. In particular, the statement and approach involving a general view of the current thesis are summarised in Chapter 4, taking advantage of conceptual charts. Chapter 5 provides the methodology used throughout this research, paying attention to qualitative and quantitative features. Chapter 6 presents a summarised report of total results organised from general aspects of magnetism to specific characteristics of MFL signals. In particular, all these results are discussed in Chapter 7, including an evaluation of the conducted methodology. Finally, in conclusion, Chapter 8 provides specific answers to the proposed aims and recommendations for future work.

2

State of the Art

Oil and gas companies, together with regulatory offices worldwide, have worked hard in the last decades to develop mechanisms that effectively ensure the integrity of pipelines and pipeline systems. As a result of this effort, the industry counts nowadays on different norms and standards to provide accurate guidance on processes and methods. These regulations consider all possible variables which can affect the characteristics of the inspected object and its functionality. In the case of pipelines, reductions of diameter or wall thickness are critical parameters for an assessment of real pipeline conditions. Estimation of the wall thickness along the pipeline allows inspectors not only to locate defects but also supplies information to calculate vital integrity factors such as remaining life, acceptability of a dent, crack or gauge, determination of the future corrosion allowance and residual stresses, among others. All of these factors help inspectors to make a right decision upon the pipeline treatment to be applied.

2.1 Type of Defects

Anomalies in the pipeline wall can appear during manufacture, installation and operation processes. These defects can be classified, for instance, depending on the cause, geometry, risk quantification, maintenance purpose or their impact on the system security. Appendix B lists standard definitions from the Pipeline Operators Forum (POF) regarding pipeline irregularities. The POF generates different documents concerning good integrity practices to avoid failures. Unfortunately, most of the accidents involve human and environmental victims. The current work reports a general classification of the feasible anomalies according to the most used criteria in the industry. Specifically, the anomalies in pipelines can be divided but not restricted to the following four categories:

- Metal loss (e.g. corrosion, pitting and gouges)
- Cracks

- Deformation (e.g. dents and grooves)
- Metallurgical (e.g. hard spots, weld anomaly)

This study focuses on defects classified under the metal loss class. In order to avoid misunderstanding, it will be first considered the definition of the entailed terms needed for defect description. Flaw location regards position and orientation. While flaw dimensions will be expressed in terms of length (L), width (W), depth (d) and wall thickness (t) as defined by POF in Figure 2.1 [18]. The pigging direction in the figure is described from left to right and accordingly, the defect features. In addition to these variables, the

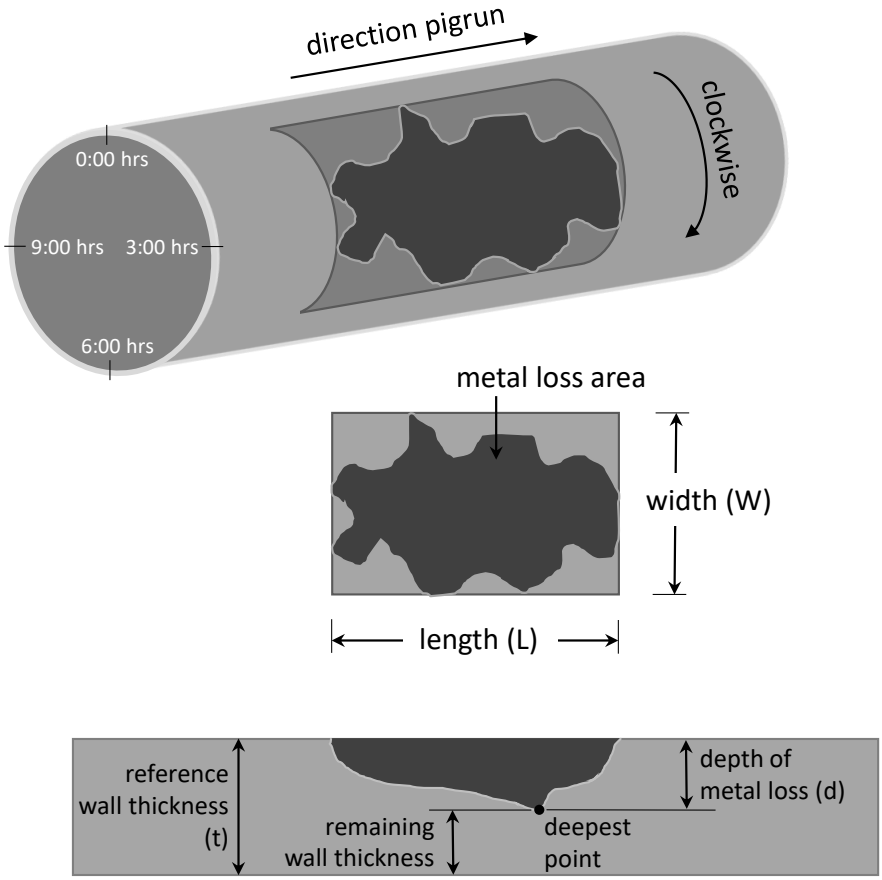

Figure 2.1: *Location and dimensions of metal loss anomaly [18].*

POF defines an auxiliary parameter named A, which is used for geometrical classification of defects detected by NDT techniques [18]. The parameter A expresses the wall thickness in the following terms:

$$\begin{aligned} A &= 10mm \quad if \quad t < 10mm \\ A &= t \quad\quad\;\; if \quad t \geq 10mm \end{aligned}$$

A metal loss anomaly is geometrically classified according to its dimensions. Figure 2.2 [19] presents a possible sorting in terms of A. This classification permits a quantitative characterisation of the PIG performance revealing its measurement capabilities. Efficiency specifications of a particular ILI tool are defined based on an established probability of detection (POD).

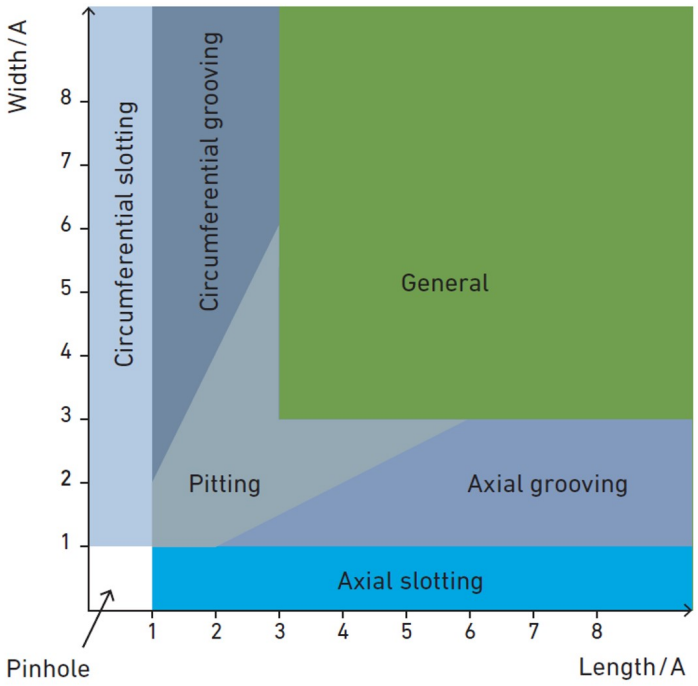

Figure 2.2: *Graphical representation of metal loss anomalies per dimension class [19].*

In the last decades, POD determination has been widely used in general industrial applications and specifically to defined reliability of NDT methods [20–25]. POD curves in NDT are produced as a function of several physical and operational parameters including flaw size, flaw type, geometry, material, NDT method applied, test conditions and, theoretical and practical qualifications of the inspection personnel. The procedure to obtain a POD curve demands first the establishment of criteria based on questions such: What flaw parameter will be studied? Which flaw size range will be investigated? Moreover, how many intervals within this range will be investigated?. Once these questions are answered, samples with convenient flaw sizes and types should be prepared. Then, the inspection of those specimens should be carried out under specific conditions and selected NDT method. Related results should be recorded as a function of the selected flaw parameter. Finally, the results should be plotted as a POD curve. The cost associated with the generation of POD curves is considerably high since a large number of experiments is needed to achieve reliable statistics. In practice, for a system which provides an only binary *hit/miss*[1] response, it is recommended to have either a minimum of 29 flaws within every flaw size interval according to [21], or a minimum of 60 inspected flaws distributed in the whole parameter range as published by [22, 23]. For

[1] *hit/miss* is a binary data type to produce POD curves as a function of the flaw size *a*. *hit/miss* expresses the reliability of an NDT method in terms of whether the flaw was detected or not.

instance, if an amount of five flaw size intervals is established for a single parameter, that entails the manufacture of 145 flaw specimens and the same number of flawless samples, which will be overall randomly inspected.

In general, ILI systems are responsible for the detection, location, identification, and sizing of each type of anomaly or characteristic in pipelines. As data from every ILI tool contains measurement errors due to its physical limitations, it is necessary to include proper correctness by defects assessment. Variables as the probability of detection (POD), probability of identification (POI), sizing accuracy and sizing capability, should be statistically calculated for every defect type characterised by a specific tool, in order to obtain reliable information [26].

2.2 NDT Methods

Currently, the inspection vendors offer a wide assortment of tools for pipeline assessment. Many of them combine diverse inspection techniques in order to find different types of defects and to increase results accuracy. The selection of a specific NDT method for pipeline inspection depends on different parameters such as the pipeline historical data, expected pipeline failures and operator's targets.

The most used NDT methods for in-line inspection are the ones based on magnetic flux leakage (MFL) and ultrasonic (UT) technics. From these two, the magnetic solution is which reaches the first place due to its lower cost compared with other techniques and its measure reliability, especially the last high resolution (HRMFL) version. However, the pipeline inspection market offers also alternative solutions for defect characterisation, considering that no NDT technology can be applied in all cases and neither be optimal for all defect types. Existing techniques as the electromagnetic acoustic transducer (EMAT), radiographic testing (RT), Eddy current (ET), magnetic particle (MT), dye penetrant (PT) are also available and recommended by current standards for specific applications [27–31]. A summarised description of previously mentioned techniques follows as a reference for comparison. The list begins with the basis of the MFL technique since it is the method of interest at the present research. A detailed study of MFL, however, is introduced in Section 2.4.

2.2.1 Magnetic Flux Leakage (MFL)

MFL applications use a magnetic circuit to magnetise a segment of the tested object. The circuit is composed basically of a pair of permanent magnets, a pair of coupling shoes, a yoke, a magnetic sensor array and an electronic system (hardware and software) to control the system and to record and save the data. Acquired MFL signals after a run through kilometres of a pipeline are analysed to characterised features present in them.

MFL tools can accurately detect metal losses, deformations and metallurgical flaws due to changes in the magnetic flux behaviour of the pipe wall. Flux lines will leak out the pipe wall where defects are located. This leaked field can be easily measured with a sensor array as it passes over the flaw. MFL can also detect and size crack-like features but only under specific design structure and for restricted flaw sizes. That is the case of the *ROCORR MFL-C SERVICE* tool developed by the Rosen–Group company. In general, detection capabilities in currently MFL tools depend basically on the number of sensors in the array. So that, inspection companies have available low resolution, high-resolution, and super high-resolution tools. The provided detection capability reaches even 10% of the wall thickness at 80% certainty. Primarily on an MFL application, operating and performance specifications and sizing capabilities depend on the tool model and defect dimensions.

2.2.2 Ultrasonic Testing (UT)

Ultrasonic testing takes the advantages of sound waves, which propagate along with a medium by the vibration of atoms and molecules. The mechanical properties of the material define the velocity of the wave displacement. Most applications use a range of wavelengths from 1 to 10 mm, high frequencies from 0.1 to 15 MHz and sound velocities from 1 to 10 km/s [27]. The incident wave reaches the specimen wall side through a couplant; it will propagate along with the material until it reaches the opposite wall side where the wave is reflected at the boundary. Then, the thickness of the pipeline wall can be calculated using the travelling time of the reflected wave. The wave will be scattered and reflected earlier if a discontinuity or anomaly is located on the travel path, enabling the feature detection. Available ultrasonic transducers are based on different principles, among others: piezoelectric, ferroelectric, magnetostriction effect or laser generation.

The advantages of the ultrasonic inspection include the ability to measure the wall thickness directly (although measurement accuracy is highly dependent on surface condition), the reliability of defect sizing and the capability to characterise a considerable number of defect types including cracks. A significant drawback of the system is the necessity to transmit a maximum energy pulse to the test piece, which requires the use of a couplant and the smoothness of the material surface. Particular attention should be paid to conserve the couplant layer thin to keep the direction of the ultrasonic beam constant, which cannot always be guaranteed. On the other hand, it is hard to detect anomalies oriented parallel to the sound beam which are significantly narrow.

Currently, UT tools offer tolerances of 1 mm in the case of high-resolution and 0.5 mm for super high-resolution, both of them at 95% confidence interval [26]. In fact, performance specifications depend on the tool design and defect type. The EVO series from the NDT Global company, for instance, offers the UMp 1.0 tool for metal loss inspection in pipelines transporting liquids. It has a wall thickness determination of ± 0.4 mm and a depth sizing of ± 0.4 mm, according to API 1163[2].

[2]The API 1163 is a standard for In-line Inspection System Qualification developed by the American Petroleum Institute (API). Further discussion on this topic can be found in Section 2.4.4.

2.2.3 Electromagnetic Acoustic transducer (EMAT)

EMAT is not a different NDT technique. The designation of EMAT refers to the principle applied for the transducer to generate sound waves to inspect metals or ferromagnetic materials. It contains essentially two components, a magnet and a coil. The induction coil is excited with alternating current, which generates electromagnetic oscillations and induces Eddy current as the coil moves close enough to the inspected material. Consequently, the Eddy currents present at the material's surface together with the magnetic field from the magnet will create sound waves thanks to Lorentz force. In the case of ferromagnetic materials, sound waves also result due to the magnetostriction.

The remarkable benefit of EMAT over conventional piezo-UT is that a couplant is not required to apply the test. Nevertheless, an EMAT as a sensor, based on the electromagnetic induction principle, is strongly disturbed by the lift-off effect, which is wavelength dependent. The lift-off of one wavelength has, as a result, an attenuation of the signal of 80dB. Therefore, an EMAT has to be always located near the surface. A lift-off of 500 μm or less is common if permanent magnets are in use. If electromagnets are employed, the signal loss due to lift-off can be compensated by a higher electromagnetic power. However, this measure cannot be applied in pipeline ILI because of its high power consumption. Furthermore, EMAT's applications are also limited in frequency.

2.2.4 Eddy Current Testing (ET)

Eddy current testing is an NDT technique only applicable to conductive materials due to its electromagnetic principle. A conventional eddy current system works as follows: an alternative current excites a coil which generates a varying magnetic field. The range of frequencies used for ET varies from few kHz to more than 5 MHz. The presence of the magnetic field close to the tested specimen induces eddy currents in its surface. Eddy currents, in turn, generate a second magnetic field that opposes the change in the exciter field. As a result, a change in impedance can be measured. Discontinuities located in the tested material will alter eddy currents, and consequently, phase and amplitude will be modified, reporting the presence of an anomaly.

Eddy current testing is, in general, more sensitive to small flaws in particular diminutive cracks than other techniques. It can accurately detect superficial and near-surface anomalies from different types. An ET equipment can be portable, allowing the inspection of specimens with complex geometries. ET is not extensively used in PIG applications due to different limitations of the technique. Unfortunately, ET in pipeline inspection is only able to detect inner-surface defects (ID) because the penetration depth[3] of eddy currents is limited.

[3]Depth of penetration depends on applied frequency, material conductivity and material permeability.

2.2.5 Radiographic Testing (RT)

Radiographic testing is one of the oldest NDT methods, where the tested specimen is exposed to penetrating radiation. The inspected material is positioned between the radiation source and the detector. Commonly RT applications use x–rays or gamma–rays for inspection. As a result, RT technique delivers a shadow image of the solid. It presents a contrast in the projection of the object depending on the level of ray absorption. Some characteristics of the specimen can modify its degree of absorption, namely material thickness, chemical composition, material density, scattering processes, and located anomalies. Currently, radiographic methods include film radiography, real-time radiography (RTR), computed tomography, digital radiography, and computed radiography.

Radiographic inspection is highly recommended to confirm the results obtained using other NDT techniques. It is especially advised in the case of welds, characterisation of pitted areas and sizing of small diameter pits. Nevertheless, the use of x–rays or gamma–rays is dangerous due to their high energy level. Therefore strict security precautions must be followed. RT is not always applicable; hence it requires access to the front and opposite side of the specimen. In general, it is a relatively expensive technique, and obtaining several images from different objects' views may be necessary to accurately size defects.

2.2.6 Dye Penetrant Inspection (PT)

Dye penetrant inspection or liquid penetrant inspection (LPI) is an NDT method to test surfaces of significantly smooth and non–porous materials. PT uses a coloured dye called the penetrant. It is applied thoroughly over the specimen's surface. The object should be previously cleaned and dried to avoid the presence of contaminants. After a cautious period of dwell time to allow the penetrant to seep into the flaw, the excess at the surface is removed carefully. Afterwards, a developer layer is applied evenly into the entire area. Once more a rest period is needed, the operator should wait until the developer draws the penetrant from the flaw out on to the surface. Thereupon the presence of defects will be visible.

Almost all materials can be inspected with PT. It is a low-cost and straightforward technique. Furthermore, PT is a highly efficient method to detect small discontinuities, even on objects with complex shapes. In contrast with these significant benefits, numerous features restrict the use of PT in NDT. Namely, the requirement of visual inspection by direct access to the surface, the detectability only of defects open to the surface, the necessity of a painstaking test zone preparation and the demand for chemical handling in a wet process.

2.2.7 Magnetic Particle Testing (MT)

The inspection using magnetic particles is one of the most widely used NDT methods for ferromagnetic materials. MT uses magnetic powder particles to detect anomalies. The first step to applied MT is to clean the specimen to avoid obstacles for the particle movement due to grease, dust or other components. Next, the specimen should be magnetised preferably with a field direction perpendicular to the suspected defect. Then, the magnetic particles can be applied utilising a dry or wet method on the specimen. The particles will be attracted and clustered where a defect is present due to the leaked magnetic field. The existence of such clusters will indicate the operator the presence of anomalies.

MT has a notable advantage over PT: it does not need a carefully previous cleaning of the tested surface. As PT, MT is a relatively simple method to detect surface and near-surface anomalies, specially crack-like and surface breaking. Together with these benefits, MT has however the following drawbacks: (i) it is limited to ferromagnetics, (ii) it requires a convenient level of magnetisation which in some cases can be challenging to establish, (iii) the specimen must be reachable physically and visually from an operator, (iv) its application can demand a removal of the coating, and, (v) that another cause, different to the presence of a defect, can influence the accumulation of particles. Moreover, a very critical disadvantage is that a successful inspection depends mainly on the ability and expertise of the operator.

2.3 Reliability of inspection results

The reliability of the results obtained from an inspection processes is a crucial parameter. Decisions about pipeline treatment to guarantee their integrity are based on the inspection data. As every inspection method has an inherent error, it is necessary to characterise and compensate it by all available data. Two cases are discussed in this section to emphasise the relevance of accomplished reliable information from inspection processes.

The accident on the USA nuclear facility *Three Mile Island* is presented in the book *Diagnostics and Reliability of Pipeline Systems*. This unexpected event occurred in a steam pipeline, which burst not long after conducting a routine inspection process. The result of the inspection reported perfect condition for the pipe. This example introduces in the book the statement that potential mistakes in pipeline assessment can still be an indirect cause of accidents. Presently, there are available mathematical and statistical models for error compensation in measurements and processes. However, these models involve many variables, and some of them are based on probabilities, which can not belong to a specific situation. Timashev and Bushinskaya considered that sources of such failure in the assessment as in *Three Mile Island* can be grouped in three cases: the omission of severe defects, underestimation of the defect size and wrong defect type identification. The authors in [26] presented a second event summarised in Figure 2.3 [26].

In the figure is shown an example of a systematic error causing size underestimation in most of the measurements. The graph presents λ values for 25 corrosion defects, providing information about the reliability of defect depth estimation. The parameter λ expresses the ratio between the measured depth using a verification process d_V (real value) and the estimated depth employing ILI inspection d_I. As can be seen in Figure 2.3, the ratio of measured/estimated depths on average λ_{cp} demonstrates that the information obtained with ILI tools have reported only half of the real value. Hence current standards for ILI assessment recommend correction of the estimated data considering the error compensation demand.

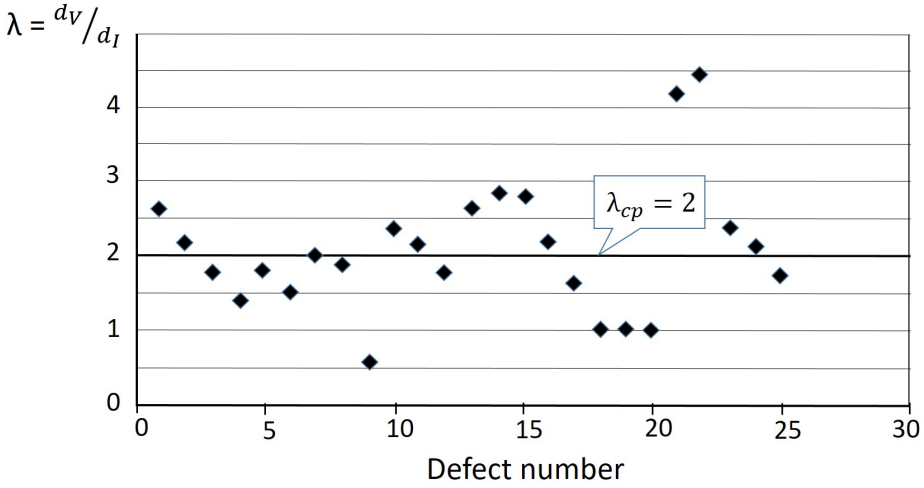

Figure 2.3: *Results of depth estimation on corrosion defects. λ expresses the ratio of measured data d_V using local methods (real value), overestimated data d_I measured by an ILI tool (Russian gas pipeline "Urengoi-Surgut-Chelyabinsk-2") [26].*

The characteristics of the error should be established according to defect type and measurement tool in order to apply a specific mathematical model. In fact, the error behaviour can be known only through measurement validation, which means that every tool should be subject to repeated pull-tests[4] for every defect type. The complexity of a real case and the amount of affecting variables suppose in some cases its confirmation directly in-situ. Moreover, an accurate result will be reached after validation, typically using a different technique.

Besides the interest on error compensation, there is in recent studies related to pipeline integrity, a demanding effort to establish quantitative relations based on defect type and defect dimensions. This interest responds to the necessity of oil and gas companies to have a more in-depth knowledge of pipeline conditions. A reliable pipeline assessment ensures the company the possibility to make the best decision concerning maintenance, repair, inspection frequency or even pipeline dismissal. All of these pro-

[4]Pull-test is a term used for a mechanism to pull the inspection tool through a test pipeline-loop, which is built-up using pipelines that contain real or artificial anomalies. This procedure is performed using a cable winch and an engine.

cesses involve significant investment for the companies; however, being unaware will implicate significant risks.

In any case, accurate defect sizing allows an unambiguous classification of defects in order to apply specific criteria from the existing regulations to determine stress loads, defect behaviour depending on time or pressure, or material degradation. Such parameters often used in pipeline integrity are required to determine residual strength, remaining pipeline life, rate of depth growth, rate of corrosion, crack critical opening, stress intensity factor, failure pressure, defect residual life and probability of non-detection of defects, to mention some of them. All of these factors are relevant to the operator, considering that this information contributes to the knowledge of the pipeline system. These parameters are all included and well defined in the fitness-for-service (FFS) standards. These regulations procure the optimisation of the decision-making process concerning the pipeline system integrity. Such quantities are calculated taking advantage of physics, mathematics, and statistics. The detection of defects and accurate defect sizing are relevant features for the proper use of standard's recommendations. Nevertheless, attaining a high probability of defect identification (POI) is also essential. An accurate defect identification allows the operator to take the maximum benefit from regulations described in standards. Besides the information obtained by the current inspection, also available information such as material features, earlier inspections outcomes, and pipeline history play a vital role to achieve reliable results.

2.4 Magnetic Flux Leakage Testing

The MFL study will be addressed here to the application on pipeline inspection gauges (PIGs). A PIG is an in-line inspection tool which travels along the pipeline to assess pipe condition. There are different NDT techniques as it was already reviewed in section 2.2; however, companies offer nowadays mostly PIGs based on MFL and UT taking advantage of their facilities. Generally, a PIG consists of an assembly of independent systems distributed in a circumferential array around a common axis. This location allows the array of sensors to scan the pipeline surface simultaneously by 360 degrees. An example of an MFL PIG is shown in Figure 2.4. This PIG is a design version from ITION-MFL tool by the Corporation for the Investigation of Corrosion CIC (Corporación para la Investigación de la Corrosión) in Colombia.

Figure 2.4: *ITION-MFL, design version from CIC.*

Typically, a PIG consists of several functionality bodies. Likewise, each body comprises different systems. For the ITION-MFL in Figure 2.4 the following systems are intended,

- Measurement systems: MFL, caliper and inertial.
- Basic systems: data storage, data processing, software platform, odometers[5], power, wraps and sealings.
- Complementary systems: speed control and tracker.

Magnetic flux leakage (MFL) technique demands four different components to provide satisfactory inspection results [33]. It requires first a magnetic circuit to magnetise the tested specimen; in this manner, flux lines will leak out the surface where a defect is located. Second, a detection system which scans along the object surface measuring the magnetic field. Third, a method for data processing in order to identify and to size the anomalies. Finally, the last component is a strategy to present the results, which should be in accordance with regulations and standards in a comprehensive report for the operator. A detailed description of these requirements follows in this section.

2.4.1 Magnetic Circuit

The magnetic structure of an MFL PIG is made up of multiple magnetic circuits which are put together around the same body as can be seen in Figure 2.5.

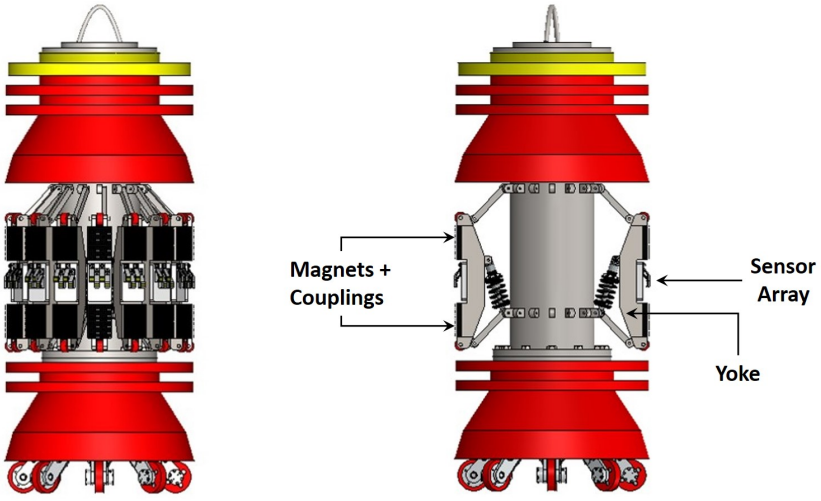

Figure 2.5: *Full and partial view of the MFL system by an ITION design version from the CIC.*

[5]The odometer is a tool which counts the revolutions of a wheel that is rolling along a surface. It is used in a PIG together with an Inertial Navigation System (INS) and a magnetic reference station as a whole system to measure distances [32].

Every magnetic circuit includes a yoke made of a material with high magnetic permeability which acts as a bridge between two powerful magnets. A pair of ferromagnetic coupling pieces are used on the opposite side of the magnets as mechanical protection. Furthermore, these couplings provide the PIG with a suitable structure to come into contact with the pipeline surface. As soon as the PIG is launched into the pipe, a closed circuit is established, and flux lines will flow along yoke, magnets, couplings and pipeline wall. A proper design of the magnetic circuit increases the reliability and sensitivity of an MFL PIG vastly [34]. Systematic errors in MFL measurements will be generated as a consequence of a non-optimal pipeline magnetisation. The insufficient field will cause fundamentally two critical sources of errors: low signal-to-noise ratio (SNR) and leakage of the magnetic field due to material stresses and strains, which will be interpreted as local metal losses. On the other hand, the overestimation of the magnetisation demands the use of bigger magnets. Furthermore, it will cause a lower MFL signal response due to the reduction in material permeability. The major drawback of bigger magnets in a PIG is not their cost, but the requirement of extra space and weight for its mechanical design. Further discussion about magnetisation strength is extensively presented in Section 6.2. Most MFL publications suggest "magnetically saturation of the pipeline wall". Unfortunately, a literature review does not reveal any discussion about the meaning of magnetic saturation. In this work, the term saturation and its impact on MFL signals are covered in detail in Sections 5.6 and 6.5.

Several variables should be carefully examined to design a suitable magnetic circuit of a PIG. Analytical approaches are based on the comparison with the electric model. Hopkinson's law and Kirchhoffs law describe the behaviour of magnetomotive force, magnetic flux and reluctance in the magnetic circuit [34, 35]. An exact analytical solution is not visible and purely experimental research is highly demanding because of the number of involved variables. As Dobmann and Höller [36] highlighted already in the eighties, the finite element method (FEM) offers the best alternative to study electromagnetic problems. Currently, the market offers different software alternatives to simulate field theory problems. In this work, COMSOL Multiphysics is used as a simulation tool. COMSOL is based on FE and is structured under different modules. Every module allows the analysis of a specific physical phenomenon. Electric, magnetic and electromagnetic applications can be developed by the AC/DC module as static or low-frequency models. A detailed description of the features of COMSOL Multiphysics can be found in Section 3.1.3.2.

The magnetic circuit of a PIG and its related parameters have been recently studied by different authors. Jansen and co-workers [34] conducted experiments and simulations to show that underestimating the pipeline magnetisation allows for the disturbance of MFL signal. Therefore, they recommend the use of a magnetic field density higher than 1.8 T. They also demonstrated through an analytical model that the pipeline reluctance should be higher as the reluctance of the PIG composition, meaning that the pipeline wall thickness to be inspected will be limited to a range. A different study published by Katoh et al. [37,38] confirms the significant influence of the air gap between the magnetic poles and the pipe wall on pipeline magnetisation. Their study is based on FEM through 2D model analysis. The results verified the relation of leakage flux density depending on the flaw breadth and on the average magnetic flux density. They also demonstrated

the possibility to calculate the magnetic field intensity on the specimen surface from magnetic flux measurements in space using the BH curve of the material. Xiao-Chun and co-workers [39] proved by 3D simulation that the magnet width has a stronger impact in the tangential component of the magnetic field density B_x compared to the dependency on magnet thickness. In addition, they showed that for longer distances between magnetic poles in a longitudinal direction, the SNR decreases notably. This is a direct consequence of the magnetic strength reduction in the specimen.

Yang et al., Li et al. and Wang and co-workers [40–42] published the velocity effects on MFL inspection in different years. Yang et al. [40] outlined a possibility to take advantage of velocity effects to detect stress corrosion cracks which are axially extended. This will be possible by means of the perturbation currents in the wall surface generated from the magnetiser movement along the pipe. The simulation showed the advisability of the proposal and experiments are recommended for future work. Li and co-workers [41] presented a 2D axial MFL numerical simulation at high speed. They concluded that arised eddy currents influence the shape and the magnitude of MFL signals. Therefore, noise suppression techniques and more robust signal processing methods should be used. Wang et al. [42] demonstrated by means of simulation and experiments that a range of velocity between 5 m/s and 55 m/s is necessary to obtain satisfactory MFL results under laboratory conditions. Parra-Raad and Roa-Prada [35] analysed numerically a two–dimensional model of a MFL circuit. They studied the behaviour of the magnetic flux density depending on yoke length, yoke thickness and lift-off. The authors in [35] implemented in Matlab an optimisation algorithm to find the proper dimensions of variables which maximise the specimen magnetisation. Experiments were carried out in order to verify the validity of the optimisation process with acceptable results. 3D simulation is suggested for more accurate comparison.

Concerning the direction of magnetisation, in-line inspection vendors offer today mainly axial and circumferential MFL PIGs. Axial magnetisation utilises a magnetic field oriented along the pipe axis. Although this orientation has been widely used since this technique appeared in the sixties, it is well known that axial MFL hardly detects narrow defects which are oriented in the axial direction. This difficulty occurs because extended narrow defects do not disrupt the magnetic flux lines significantly as it extends parallel to the field. Circumferential PIGs have been developed to avoid this problem. In this case, the magnetic field is oriented around the pipe instead of along the axis. This implementation has demonstrated successful results detecting extended narrow defects, axially oriented. However, this kind of pipe magnetisation is mechanically much more complicated. Besides its complexity, this orientation is more sensitive to velocity effects. Nestleroth [43] demonstrates after his research on circumferential MFL that a purely circumferential MFL implementation reduces the detection capabilities and sizing accuracies compared with axial MFL. Ireland and Torres [44] confirmed through simulation results the conclusion from Nestleroth. The authors suggested further research regarding sensor sensitivity, placement, calibration and manufacturing tolerances by circumferential MFL in relation to the already known axial MFL behaviour.

2.4.2 Detection System

Currently, there is a wide variety of magnetic field sensors. Every sensor type has different performance according to its physical principle. A specific sensor is selected in terms of functional purposes. Kloster [45] has extensively discussed in his doctoral research about magnetic field sensors. He defined a list of the relevant parameters for industrial applications, namely dynamics, linearity, hysteresis, operating temperature range, magnetic sensitivity, offset, temperature-offset coefficient, long-term stability, sensitivity over high magnetic field, noise, stability over environmental conditions, bandwidth, power consumption, size, sensitivity over radiation and finally, the price. Figure 2.6 summarizes current available magnet field sensors based on specific physical effects accompanied by the year of development.

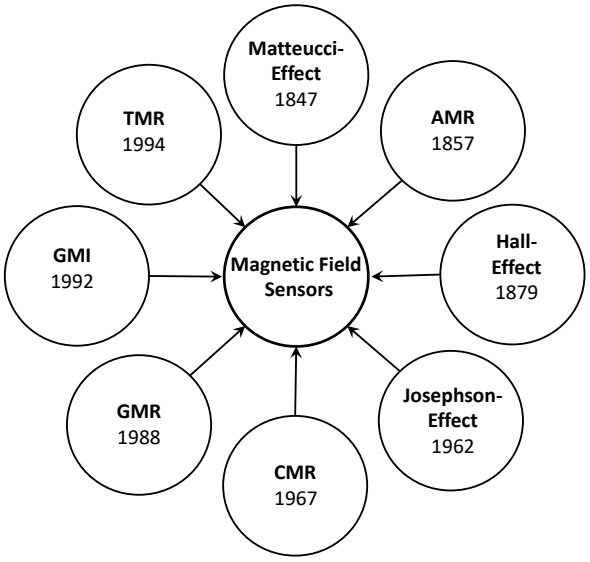

Figure 2.6: *Physical effects used for magnetic field measurements, including the year of manufacture [45].*

Hall sensors are prefered for MFL PIGs manufacture because of their applicability, lack of the hysteresis effect, low power consumption, linearity, ease in connection with other electronics and relatively small size. Hall sensors are solid-state probes based on the Hall Effect. In this process, a voltage difference is delivered at sensor output as a response of a magnetic flux perturbation. A sensor array is used in every magnetic circuit of the PIG considering that a Hall sensor is around 4 mm in width (see Figure 2.5). At present, inspection companies provide their MFL services with low, high and super high-resolution tools. The resolution parameter depends directly on the number of mounted sensors in the PIG system. A higher resolution is needed in order to reach better recognition and analysis of defects [34].

Gloria et al. [46] published the development of a sensor array for detection and sizing of internal pipeline corrosion defects. This sensing module comprises a magnet, an array of 7 Hall sensors and a small sacrifice plate. The authors in [46] argued that the main advantage conferred to this sensor array is that the magnetic saturation of the

tested material is not needed. Hence, the performance of the sensor does not depend on the wall thickness. They concluded that signals obtained with this new sensor are more straightforward as conservative MFL signals. However, against that argument, developers of in-line inspection tools prefer the ability of standard MFL to detect internal and external defects simultaneously. Novel proposals for defect recognition include the combination of several techniques. For example, Niese [1] developed in his doctoral thesis a wall thickness measurement sensor for pipeline inspection. He integrated into one sensor EMAT, MFL and Eddy current technologies. The sensor proposed by Niese showed satisfactory experimental results in the laboratory which are comparable to high-resolution tools. The main objective considered for the development of this sensor was the determination of remaining wall thickness in case of metal loss (e.g. general corrosion, pitting corrosion). Niese made use of the advantages from every employed technique, so that some of the flaw parameters may be estimated simultaneously by different methods. Proper performance of the combined sensor in a PIG test has not been published. A different study from Hwang and co-workers [47] proposed a scan-type magnetic camera to improve the detection of cracks at high speed and high spatial resolution. The camera here consists of a magnetic source, a magnetic sensors array, magnetic lens and an analogue to digital converter (ADC). Le et al. [48] presents analytical, simulated and experimental results quantifying cracks. Experimental measurements are obtained using an AC-type magnetic camera. The camera, in this case, consists of two coils, two cores, a copper sheet and a Hall sensor matrix of 1024 (32 x 32) elements. Defect images obtained experimentally in these two last works regarding the camera concept are well defined. Nevertheless, such an arrangement is not viable for MFL PIGs due to the intrinsic requirements of the magnetic camera. Although there are several studies and proposals to improved sensing performance for particular applications of the MFL technique, a Hall sensor array remains the most popular option for the MFL PIG detection system.

2.4.3 Data Processing

After having been collected, MFL signals should be analysed and interpreted. As pioneers, Zatsepin and Shcherbinin [49, 50] published analytical and experimental studies on magnetic leaked field signals in 1966. Since then, this proposal has been broadly used, known as the dipole model. The authors in [49, 50] derived equations for the axial and radial components of the magnetic field in a 2D approach of a line and a strip (see Section 3.1 for further discussion on this topic). Subsequent work, including further studies from Shcherbinin and Pashagin [51], has optimised the application of the model adding more parameters and reducing discrepancies between theoretical and experimental results published in 1966. Lord and Hwang [52] were pioneers applying finite element analysis to the calculations of magnetic leakage fields. A two-dimensional model was considered to model circumferential cracks or grooves in pipelines. Later, Dobmann and Höller [36] underlined the importance of computational development which allows numerical analysis to solve complex field problems. In particular, the case of magnetic leakage phenomena in 3D involves complex mathematical relations and a considerable amount of variables making an exact solution unfeasible [53]. Recent authors [13, 54–61] agree that two main processes fully describe the MFL problem:

- a forward problem, which correlates the features of the MFL signal with defect characteristics, and
- an inverse problem, which develops a strategy for defect reconstruction based on MFL signal properties.

Different approaches to solve forward and inverse problems have been developed in order to take advantage of the MFL technique. Accuracy on pipeline assessment is currently at a satisfactory level; nevertheless, pipeline integrity operators urge inspection vendors to increase the capacity on defect reconstruction based on MFL signals. Figure 2.7 shows the overview flowcharts of the most common processes to solve MFL forward and inverse problems hitherto.

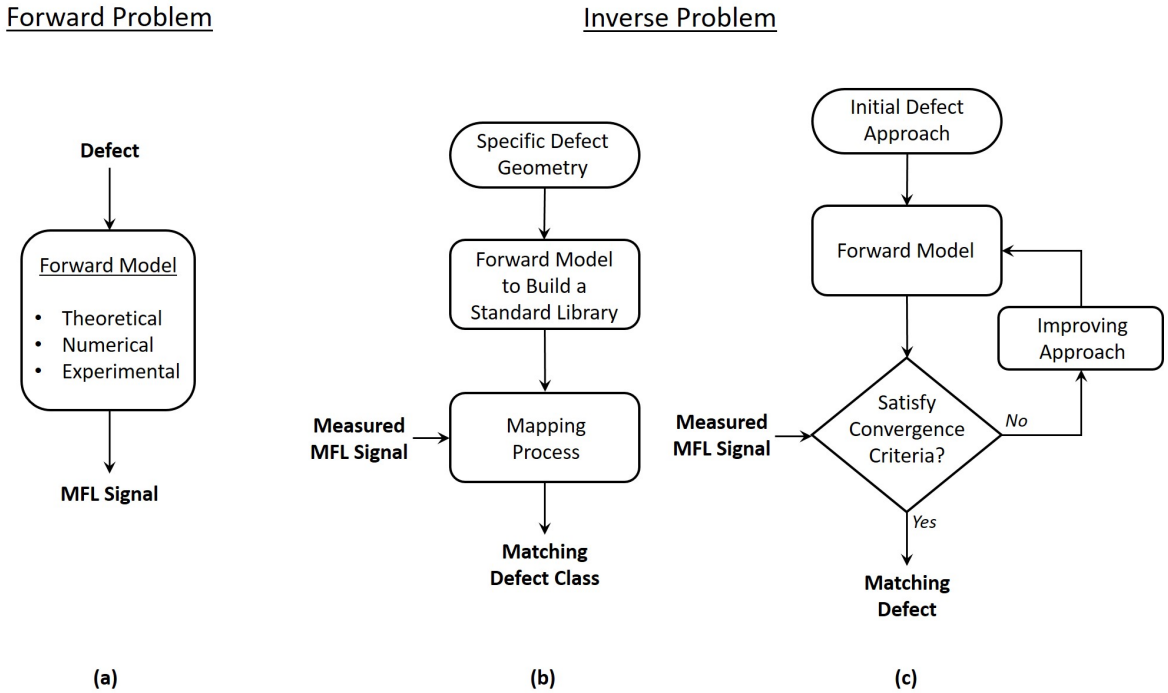

Figure 2.7: *Schematic representation of prevailing solutions by the MFL technique. a) Forward problem. b) Open-loop to solve the inverse problem. c) Closed-loop to solve the inverse problem.*

The input by the forward problem is a well-defined defect located inside a magnetised domain. The presence of the defect will cause a magnetic field perturbation. Models to calculate the leakage field have been developed so far based on analytical formulas and numerical simulations [49, 52, 53, 55–57, 62, 63]. The output of the forward problem is the corresponding MFL signal, which can be alternatively obtained by means of experiments. On the other hand, the inverse problem has been proposed mostly as a mapping or iterative process which compares the measured MFL signal (input) with the characteristics of an assumed defect [13, 58, 59]. In this perspective, the inverse process includes itself a forward solution in order to previously establish the leakage field from selected defect types, as illustrated in Figure 2.7. By the iterative method, in particular, an initial assumption is used as a starting approach; if convergence criteria

are met, defect identification and sizing are delivered as output. Otherwise, an improved defect approach is selected from a database. Three different types of methods are used to implement the inverse problem according to a more general classification published in [61], namely: neural networks, gradient-based optimisation of deterministic category, and metaheuristic optimisation of stochastic category. Afterwards, Huang and Zhao split the inversion problem into direct and indirect methods [13]. A detailed review of the most recent studies addressed to improve solution methods for the forward and inverse MFL problems follows. Later in Section 3.1 the fundaments of MFL signal modelling which have provided bases of the current methods are thoroughly discussed.

2.4.3.1 Forward Problem

Lukyanets et al. [64] used an integral equation to express the density of surface charges for an anomaly with smooth edges. They reported an analytical and numerical agreement. Constant permeability was assumed in order to demonstrate that the surface shape of the defect has a direct relation with the density of defect–induced magnetic charges. Further research is expected considering non-constant permeability. Katoh et al. [65] studied the influence of the BH curve on the magnetic flux leakage density numerically. They demonstrated that there are two significant parameters: initial permeability and the magnetic flux density in the saturation state. Zuoying and co-workers [66] reported an FE study of MFL signal pattern in relation with defect characteristics. The authors chose length, width, depth and lift-off as parameters to conduct the analysis. A 3D model was simulated with ANSYS finite elements software. They confirmed that the FE approach is a reliable procedure for MFL analysis. Li et al. [17] published the experimental and numerical results of an MFL defect characterisation study. They showed that using redundant information improves the detection and characterisation capabilities of irregularly shaped defects. Redundant data is obtained through the three components of the magnetic field density. Romero Ramirez and co-workers [15] presented an experimental study of MFL signals from a tank floor. They concluded that the MFL technique does not allow to identify if the defect is located on the inner or outer wall surface (see Figure 5.11 to clarify defect location definitions). This difficulty is justified due to the similarity of measured MFL signals in either of the two cases. Snarskii et al. [67] proposed three-dimensional integral equations to calculate the magnetic field of a defect while assuming constant permeability. They found that this assumption is invalid for defects deeper as 25% of the wall thickness. However, good agreement was found for defect depths until 25% of the wall thickness.

In general, analytical methods are swift. However, results accuracy is affected by the mandatory assumptions which are necessary to simplify mathematical expressions. On the other hand, numerical solutions deliver accurate results. Nevertheless, they have the disadvantage of a high computational cost and limitations on complex geometries. Besides those, the empirical methodology provides an accurate solution. However, its implementation is highly demanding in order to allow parameter variation.

2.4.3.2 Inverse Problem

It is worth mentioning that a detailed study and understanding of the forward problem is meaningful to solve the inverse problem. The reason is not only because a forward model stage is required for the inverse process solution, but also because the comprehension of the MFL phenomena provides the researcher with a background on related physics. However, some studies reported the forward problem stage as a black box, which contains the required database as represented in Figure 2.7. In such studies, the optimisation of the matching algorithm has prevailed over the understanding of MFL physical behaviour.

The inverse problem by in-line inspections using the MFL technique had only been investigated since 2000. Even though related investigations on defect sizing utilising statistical recognition and artificial neural networks (ANN) technology had already begun a decade earlier in other research fields [13]. Indeed, the reconstruction of defects based on MFL signals is a very complex issue due to the lack of information regarding defect features and specimen magnetisation. This difficulty is explained analytically by Shur and co-workers in [60] based on the formulation of the forward and inverse problem by the equation:

$$A\,z(s,x) = u(x), \tag{2.1}$$

where A is an operator defined depending on the form of the ferromagnetic surface. For the forward problem, A as well as the function $z(s,x)$ are known. Then, the only unknown $u(x)$ has to be calculated. Whereas in the inverse problem $u(x)$ is a known function obtained through a finite number of measured points, while, A and $z(s,x)$ are unknowns. Consequently, a unique solution by the inverse problem is unfeasible, considering that the following parameters are unknown: the magnetisation inside and at the surface of the specimen, the shape of the defect and its dimensions. For this reason, it is required to make some assumptions. Shur et al. have solved the inverse problem employing mathematical tools developed in the geophysics field. They have claimed based on their results that a mathematical solution is possible for superficial internal defects since the specimen surface containing the defect is known.

Existing strategies to solve the inverse problem can be classified according to [13] into mapping, iterative and signal classification methods. The mapping method is often called a pattern matching method, which is performed as an open-loop process as the one illustrated in Figure 2.7b. It makes use of a standard library with signals earned from specific defect kinds which were implemented employing magnetic dipole model, finite element model or even experiments. The mapping process between the test signal with recorded signals is carried out by a statistical method or neural network method. As a result, the defect type and its dimensions are provided. Likewise, the iterative method solves the problem utilising the solution of a forward model, as shown in Figure 2.7c. However, it involves a closed-loop process. Then, the solution will be delivered once the convergence criteria are fulfilled. On the other hand, the third class known as signal classification or pattern classification method consists in dividing the problem into an specific number of solutions for a limited number of categories. This classification depends basically from the defect type and it is conducted for example using a filter for identification. In the third group, the feature-based classification method is also included,

which is addressed to compress data and variables by means of signal feature extraction. Additionally, the neural network method or clustering method was utilised in the process for defect classification. In general, the authors in [13] identified the limitations of current methods with the inaccuracy on prediction and therefore, by defect sizing. They claimed that depending on the method used, any of these two constraints prevent achieving high precision results by complex geometries, which are common by corrosion phenomena.

The intention to highlight next studies leads to provide an overview of the research evolution related to the inverse problem based on MFL signals. Under no circumstances the aim here is to delve into any of the published works. The following are the most relevant proposals published lately. Mandayam et al. [68] proposed permeability compensation of MFL signals through a wavelet basis functions network. The method eliminates changes in permeability from undesirable sources (e.g. pipe wall thickness, stress level), preserving the sensitivity to defect depth. Results were satisfactory for simple defect types, nevertheless for more complex anomalies could be non-functional due to the constrained database. Employing a painstaking experimental study, Schifini and Bruno [69] demonstrated that their 3D numerical model reports good agreement with experimental outcomes. They assumed the superficial defect shape as known for numerical treatment in an iterative procedure. Their results deliver errors below $\pm 25\%$ for the three kinds of superficial flaws studied.

Carvalho et al. [70] published successful results on defect classification based on MFL signals. Anomalies in pipe welded joints were sorted as external corrosion, internal corrosion and lack of penetration[6]. MFL signals were obtained with a PIG, and pre-processing techniques (Fourier analysis, moving-average filter, wavelet analysis and Savitzky-Golay filter) were applied to facilitate the identification. This work proposed artificial neural networks as a suitable method for pattern recognition. Carvalho et al. concluded that more accurate results could be obtained as more training data are introduced. Accodingly, the correctness of results can decrease due to the use of trained data from a different specimen as the tested object. Zhang et al. [71] proposed the particle swarm optimisation algorithm for reconstruction of rectangle cracks in MFL testing. The authors in [71] presented simulation results from two cases where the maximum error is 15%. Ravan et al. [59] published a procedure to estimate the shape of the opening and the depth profile of a defect using MFL signals. They combined FEM and an analytical approach to get the best from every method. The authors in [59] had tested the method with two arbitrary real defects. Results showed that the accuracy of the method is affected with the lack of sharp variations in the signals. Nevertheless, maximum depth of defects was accurately reported. Mukherjee et al. [72] developed a new algorithm to preprocess MFL signals before defect characterisation. The algorithm is based on adaptive channel equalisation. Their results demonstrated the cancellation of the noise and consequently, a signal-to-noise ratio improvement. In the same year, Kathirmani et al. [73] published an algorithm for real-time data compression of MFL signals. Related results showed high compression ratios with minimal loss of information. The applicability of the method for a specific case should be evaluated. Computational complexity and the risk of losing vital information can invalidate the method. Mukherjee et al. [74] reported

[6]The lack of penetration is defined as the difference between the actual and nominal penetration by a weld joint.

a 2D partial time-varying model for inverse mapping of MFL signals to estimate shape, length and width of metal loss defects. The authors proposed future studies to apply the successful model in 3D profiles.

In this subsection, only a selected number of papers to show the progress of data processing in MFL testing has been mentioned. These studies verify the necessity of a reliable method to reconstruct defects based on MFL signals still to be developed. Current solutions are limited to a specific geometry or condition, making their general use unfeasible. Lack of a more accurate method remains.

2.4.4 Results Report

A pipeline system can be considered as a whole, including its surroundings, taking advantage of current developed technologies and processes. It means, today it is not enough to only detect and size isolated defects. Historical data including all parameters which can affect pipeline functionality (e.g. presence of stresses or corrosive materials in the surroundings) should be taken into account. In this manner, pipeline deterioration and damage can be foreseen and prevented. For this reason, pipelines must operate under an integrity management program with consistent criteria regarding assessment techniques and tools. Pipeline integrity management is not a primary objective in this work; nevertheless, an overview follows as a reference and primarily seeks to highlight the importance of delivering accurate and intelligible results by pipeline inspections. In general, the oil and gas industry needs a robust infrastructure. Thompson in [75] divided the system into three major sectors, namely pipelines, production and facilities. Likewise, the pipeline sector is split into two groups: natural gas and hazardous liquids. A schematic of the proposed transmission pipeline system by Thompson is shown in Figure 2.8.

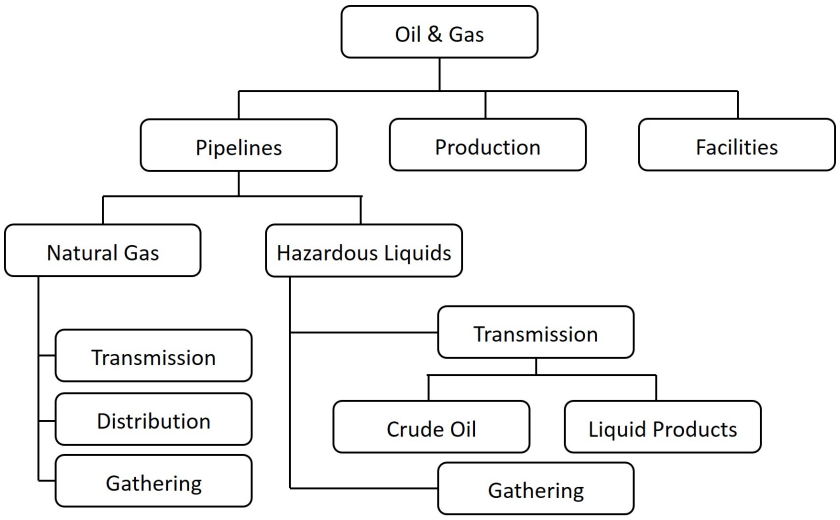

Figure 2.8: *Transmission pipeline sector [75]*

The author in [75] reported corrosion costs related to the transmission pipeline industry in the United States of about $5.4 and $8.6 billion per year. He underlined the

importance of improving risk assessment strategies and pipeline integrity management programs in order to reduce maintenance inversions and increase pipeline safety.

Currently, the American Society of Mechanical Engineers (ASME) offers standards as a guide to improve pipeline safety integrity management. The *ASME B31.4 Pipeline Transportation Systems for Liquid Hydrocarbons and Other Liquids* [76] is a code which formulates the requirements involved in processes such as design, material selection, construction, assembly, inspection, and testing of piping transporting liquids. The carried substance can be crude oil, natural gasoline, natural gas liquids, liquefied petroleum gas, carbon dioxide, liquid alcohol, liquid anhydrous ammonia and liquid petroleum products. On the other hand, the *ASME B31.8S Managing System Integrity of Gas Pipelines* [77] includes the recommendations for on-shore gas pipeline systems constructed with ferrous materials such as pipes, valves, appurtenances attached to a pipe, compressor units, metering stations, regulator stations, delivery stations, holders and fabricated assemblies. Likewise, there are also other available standards which are developed by different entities around the world. That is, for example, the case of the United Kingdom with its own code for gas pipelines, named IGE/TD/1 initially and since 2004 known as PD8010 [78].

A fundamental stage on the ASME B31.8S development [79] has been the identification of the threats from possible defect types in pipelines and their suitable treatment. Currently, the standard recommends the company to identify pipeline threats and classifies them in three time-behaviour categories: time-dependent, stable and time-independent. Details of every category are provided in Appendix C, Table C.1. Besides, the ASME B31.8S includes risk assessment, integrity assessment, responses to integrity assessment and mitigation (repair and prevention).

Ordinarily, the integrity management process for a pipeline system has three main phases: first, it is necessary to consider the whole pipeline system and identify its susceptibility regarding each threat found. Second, the prioritisation of the system segments depending on the risk of threats. In any case, every flaw must be considered individually as well as a part of a global risk assessment. Furthermore, based on the risk study, the third stage requires integrity assessment or inspection using assessment tools. Figure C.1 in Appendix C presents the integrity assessment process divided into actions, results and categories.

The ASME B31.8S standard acknowledges three assessment methodologies for integrity management in gas pipelines: pressure testing, direct assessment (DA) and in-line inspection. Assessment methods are applied depending on the conditions of the pipeline, and their use is advisable in specific periods of the pipeline life cycle. The discussion here focusses on in-line inspection as this is the subject of interest. Regarding in-line inspection, three standards are recommended in ASME B31.8S:

- API STD 1163, In-line Inspection Systems Qualification Standard
- NACE SP0102, In-Line Inspection of Pipelines
- ANSI/ASNT ILI-PQ, In-line Inspection Personnel Qualification and Certification

The American Petroleum Institute (API) defines the API 1163 standard [80] as an "umbrella document" containing procedures, personnel, equipment, and associated software related to ILI systems. It includes requirements for utilising ILI systems both onshore and offshore, for gas and hazardous liquid pipelines. The API 1163 can be utilised for existing as well as for developing technologies. This standard implicates the use of the NACE SP0102 and ASNT ILI-PQ standards as a supplement. The SP0102 (formerly RP0102) [81] is a standard provided by the National Association of Corrosion Engineers (NACE). It is a guide for organising, planning and executing ILI projects and programs. It can be used by individuals or teams conformed by engineers, operations and maintenance personnel, technicians, specialists, construction personnel, and inspectors. NACE SP0102 includes tool selection and usage, as well as recommendations about data management and data analysis. On the other hand, the American Society of Nondestructive Testing (ASNT) developed the ILI-PQ standard [82], which was approved by the American National Standards Institute (ANSI). ILI-PQ standard defines the minimum requirements for personal qualification and certification of workers who are involved with in-line inspection processes. The standard establishes three levels of qualification and certification: I, II and III. This categorisation exits for tool operators as well as for data analysts.

Undoubtedly, ILI systems are preferred and widely used for pipeline assessment. This methodology has demonstrated robustness and efficiency for inspection, especially along kilometres of difficult access areas. Deterioration of pipelines is strongly influenced by the presence of physical and geometrical defects. Therefore, the purpose of the ILI tool is primarily to define defect parameters such as depth, length, width, position and orientation. Once defect size is known, it is also relevant to establish how these detected anomalies change with time. Defect modifications in time cannot be directly measured by ILI tools but can be calculated from the information obtained by current and previous inspections. Well defined methodologies and processes are available today in the standards to take benefit of ILI data. The treatment of ILI results should also include error measurement compensation, as discussed in section 2.3. It is an essential parameter in standard recommendations; nevertheless, still, research is subject to enhance.

Timashev and Bushinskaya asserted "the results of defect parameters measurements are just an approximate evaluation of the true values." [26]. They also listed the next factors as possible causes of control reliability failure:

- physical limitations of the measurement tool
- quality and integrity of the instrument being used
- state of the objects' surface in the control zone
- conditions of control
- time of control
- visual acuity and physical condition of the inspector/diagnostician
- qualification and the psycho-physiological condition of the inspector

3

Fundamentals

A general mathematical formulation concerning the MFL phenomena introduces this chapter. Then, the fundamentals of theoretical and numerical modelling are discussed, in particular, the COMSOL Multiphysics software as a simulation tool. Indeed, a thorough study of the remarkable strategies to model the MFL signal is essential to understand the complexity of this task. This review will help to understand the evolution of the techniques in time. Moreover, the strengths and weaknesses of every method become accessible, revealing why it is still a relevant subject of investigation.

3.1 MFL Signal Modelling

For over three decades, experimental work has been mentioned as the most published literature concerning MFL. Theoretical and numerical modelling were the two new solutions at that time [36]. Although this modelling classification remains valid, only a few publications deal today with the theoretical analysis. Most of the recent studies still take advantage of the dipole model [49, 50]. Experiments are seldom employed today since it entails an impractical and high demanding process.

On the other hand, numerical modelling has been intensively utilized to understand the phenomena, becoming an advisable tool for model development nowadays. However, hitherto, numerical analysis has been predominantely used for two-dimensional modelling. Furthermore, although different approaches are currently applied based on the so-called non-numerical methods, among them wavelet, Hilbert and Hilbert-Huang transforms [12], any of them have been able to contribute in the understanding of the relationship between MFL signals and related defect dimensions. In this chapter, a review of theoretical, numerical and experimental modelling will be thoroughly presented since their application have been essential to achieve the objectives of the current study.

3.1.1 Static Leaked Flux Problem Formulation

The mathematical formulation of the leaked field phenomena, in general, is presented here based on the publication of Dobmann and Münnich [83]. The authors characterised the problem in two primary regions. The inner region is defined for a volume V of ferromagnetic material, which is delimited by the surface S according to Figure 3.1.

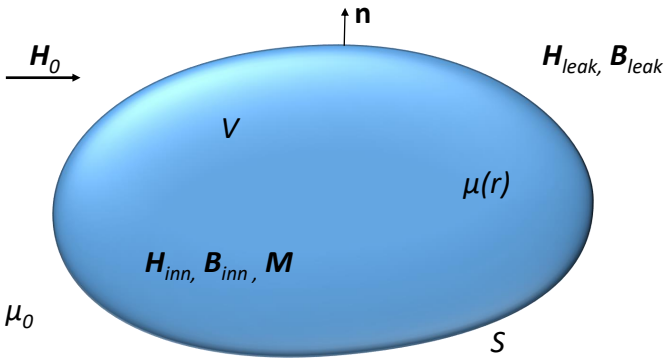

Figure 3.1: *Mathematical formulation of the static leaked field [83].*

The body in Figure 3.1 is described by the permeability $\mu(r)$ dependent on position, considering that r is defined as the position vector. V is magnetised by a static incident field $\mathbf{H}_0$ of which the magnitude and direction are known. The complementary volume of V defines the outer region, where $\mathbf{H}_0$ is generated. The permeability of the exterior is assigned as the vacuum permeability, μ_0. In the outer region results a magnetic leaked field $\mathbf{H}_{leak}$ due to the interaction of the applied field with the ferromagnetic body. In addition, an induced field $\mathbf{H}_{inn}$ emerges in the volume V through the spontaneous magnetisation $\mathbf{M}$.

Both field fractions $\mathbf{H}_{leak}$ and $\mathbf{H}_{inn}$ satisfy Maxwell equations. The solution of the leaked field problem comprises the solution of the inner and outer region problems together with the observance of the boundary conditions. If Φ_{leak} and Φ_{inn} define the scalar magnetic potentials, it can be found that,

$$\nabla^2 \Phi_{leak} = 0 \tag{3.1}$$

$$\nabla^2 \Phi_{inn} = \frac{\nabla \Phi_{inn} \cdot \nabla \mu(r)}{\mu(r)} \tag{3.2}$$

which is equivalent to:

$$\nabla^2 \Phi_{inn} = \nabla \cdot \mathbf{M} \tag{3.3}$$

if the vector $\mathbf{n}(r_s)$ is introduced as the outer normal at the point r_s in surface S of the volume V, it can be stated for both field regions that

$$\mathbf{n}\,(\mathbf{r}_s) \times \big(\,\mathbf{H}_{out}(\mathbf{r}_s) - \mathbf{H}_{inn}(\mathbf{r}_s)\,\big) = 0 \tag{3.4}$$

$$\mathbf{n}(\mathbf{r}_s) \cdot \big(\,\mathbf{B}_{out}(\mathbf{r}_s) - \mathbf{B}_{inn}(\mathbf{r}_s)\,\big) = 0 \tag{3.5}$$

where, $\mathbf{H}_{out} = \mathbf{H}_0 + \mathbf{H}_{leak}$ and $\mathbf{B}_{out} = \mathbf{B}_0 + \mathbf{B}_{leak}$.

The problem of the outer region is described by the Laplace Equation 3.1. While, the inner region is defined as a non-linear differential problem due to the hysteresis behaviour of the material, Equation 3.2 and Poisson Equation 3.3. The divergence of $\mathbf{M}$ describes the source of the scalar potential as in Equation 3.3. Then, the problem can be solved, making use of proper boundary conditions. To fulfil this requirement, Equations 3.4 and 3.5 formulate the continuity of two field components across both regions, the axial component of the magnetic field and the radial component of the magnetic density flux.

The detailed solution of a two-dimensional case is presented in Section 5.1 in order to provide an example of the leaked flux problem analysis. That model consists of an infinitely long ferromagnetic cylinder excited through a homogeneous magnetic field. The example allows the magnetic behaviour study of a ferromagnetic specimen and its surroundings employing a simplified case. It is worth to mention that analytical solutions are so far feasible only for simplified geometries.

3.1.2 Theoretical Modelling

The theoretical modelling of the leaked flux problem is based on the theory of potential distributions. It allows determining scalar distribution functions for both the two-dimensional and three-dimensional cases [36]. First, the two-dimensional approach will be presented to introduce the dipole model from Zatsepin and Shcherbinin. Afterwards, the three-dimensional case on vector fields will be reported.

Potential distributions are representations of a function $U(\mathbf{r})$ which for the two-dimensional case is twice differentiable in an area F and its boundary, the curve C:

$$U(\mathbf{r}) = -\iint_F df' \rho(\mathbf{r}') \, \phi(\mathbf{r},\mathbf{r}') + \int_C ds' \sigma(\mathbf{r}') \, \phi(\mathbf{r},\mathbf{r}') - \int_C ds' \chi(\mathbf{r}') \, \mathbf{n} \cdot grad' \, \phi(\mathbf{r},\mathbf{r}') \quad (3.6)$$

where $\rho(\mathbf{r}')$ is a flat distribution, $\sigma(\mathbf{r}')$ a line distribution, $\chi(\mathbf{r}')$ is a line double distribution. The term $\phi(\mathbf{r},\mathbf{r}')$ formulates the Green's function of the Laplace equation in two-dimensional free space, which is defined as,

$$\phi\,(\mathbf{r},\mathbf{r}') = \log \frac{1}{|\ \mathbf{r} - \mathbf{r}'\ |}$$

Following additional conditions must be fulfilled in order to determine the distribution functions:

$$\begin{aligned}
\rho(\mathbf{r}) &= \frac{1}{2\pi} \nabla^2 U(\mathbf{r}) \qquad in\ F, \\
\sigma(\mathbf{r}) &= \frac{1}{2\pi} \mathbf{n} \cdot grad\, U(\mathbf{r}) \quad on\ C, \\
\chi(\mathbf{r}) &= \frac{1}{2\pi} U(\mathbf{r}) \qquad on\ C.
\end{aligned}$$

Therefore, the Equation 3.6 is only valid if $U(\mathbf{r})$ in F is the solution of the Poison equation $\nabla^2 U(\mathbf{r}) = 2\pi\, \rho(\mathbf{r})$. While, $\sigma(\mathbf{r})$ is established by the boundary values of the

derivation of $U(\mathbf{r})$ in the direction of the outer normal $\mathbf{n}$, namely $\mathbf{n} \cdot grad\, U(\mathbf{r}) = 2\pi\, \sigma(\mathbf{r})$ and, $\chi(\mathbf{r})$ by the boundary values belonging to $U(\mathbf{r})$ as $U(\mathbf{r}) = 2\pi\, \chi(\mathbf{r})$ on C.

The first authors to published a mathematical description of the magnetic leaked field due to a surface-breaking defect were Zatsepin and Shcherbinin [49, 50]. They assumed special distribution functions and compared resulting potentials and fields with leakage fields obtained experimentally with real defects. Zatsepin and Shcherbinin concluded that the topography of the magnetic field caused by a defect which depth is significantly smaller than its width, might be calculated through the field of a linear magnetic dipole. While the magnetic strip dipole can be used to describe the field behaviour of defects with its depth approximately equal or greater than their width. The authors in [49, 50] obtained mathematical expressions for the leaked field according to:

$$\mathbf{H}^{leak} = -\, grad\, U(x,y)$$

Figure 3.2a illustrates the parameters to establish the leaked field of a line dipole. The infinite line distributions A_1 and A_2 are located perpendicular to the x-y plane and separated 2b from each other. Magnetic field components H_x^{leak} and H_y^{leak} of a line dipole are then expressed by Equations 3.7 and 3.8.

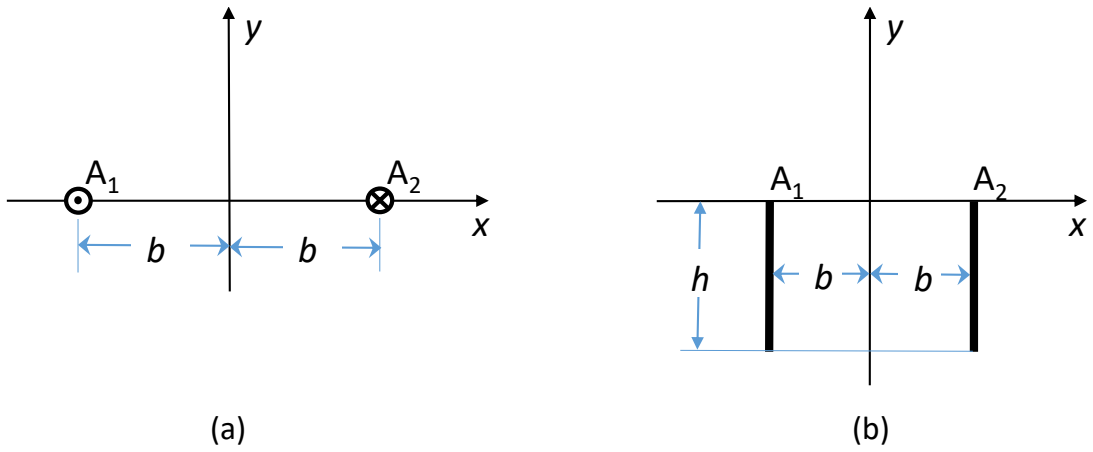

Figure 3.2: *Illustration of: (a) A line dipole and (b) A strip dipole [49, 50].*

$$H_x^{leak} = 2\,\sigma_1 \left[\frac{x+b}{(x+b)^2 + y^2} - \frac{x-b}{(x-b)^2 + y^2} \right] \tag{3.7}$$

$$H_y^{leak} = 2\,\sigma_1 \left[\frac{y}{(x+b)^2 + y^2} - \frac{y}{(x-b)^2 + y^2} \right] \tag{3.8}$$

where σ_1 is the magnetic charge on the line.

Similarly, the leaked field in two dimensions of an infinitely long surface defect is comparable with the magnetic charge of a rectangular strip dipole. Figure 3.2b shows

the strip dipole with a width of 2b and a depth of -h. The calculation of the respective field components can be determined by the Equations 3.9 and 3.10.

$$H_x^{leak} = 2\,\sigma_s \left[\arctan \frac{h(x+b)}{(x+b)^2 + y(y+h)} - \arctan \frac{h(x-b)}{(x-b)^2 + y(y+h)}\right] \tag{3.9}$$

$$H_y^{leak} = \sigma_s \ln \frac{[(x+b)^2 + (y+h)^2]\;[(x-b)^2 + y^2]}{[(x+b)^2 + y^2]\;[(x-b)^2 + (y+h)^2]} \tag{3.10}$$

assuming a constant surface magnetic charge density σ_s for the strip along h.

Subsequently, Zatsepin and Shcherbinin [50] reported subsequently plots comparison, including analytical and experimental results from different types of defects. Agreement on results has shown that the proposed two-dimensional method is an accurate approximation to determine the leaked field for defects which are infinitely long and have elementary cross-section geometries. However, it is not suitable for the calculation of leakage fields produced by complex geometry flaws. Moreover, the method does not provide a means for defect reconstruction.

3.1.3 Numerical Modelling

The theoretical modelling is in general suitable to provide an exact solution only for problems which involve specimens with elementary geometries. Unlike, Hwang and Lord introduced a different approach to solve the problem in the non-destructive testing field. They solved the MFL problem utilising the finite element method. The advantage of numerical methods is in general that, they can provide a reliable solution for non-linear problems without limitations on sample geometry.

The numerical modelling process requires the establishment of a mathematical model as an initial step. This mathematical model describes the physical system of interest and simultaneously, it provides equations and conditions to be fulfilled in order to find the solution. This section introduces three different numerical strategies to solve the MFL problem, namely in chronological order: Dobmann and Münnich [83], Dutta et al. [16,84] and Dyakin et al. [88]. These strategies are selected as an example from remarkable proposals in the last decades. The basis of the finite element method is introduced at the end of the section. In addition, the section also includes a review of the process used by COMSOL multiphysics since it has been an essential tool used in this research.

Dobmann and Münnich [83] published an approach to describe the MFL phenomena in 3D through distribution functions. They used the Green's theorem for a vector field to formulate the leaked field problem under Equations (3.1) to (3.5). The authors defined $\mathbf{P}(\mathbf{r})$ as a twice continuous differentiable vector function in a volume V and its surface

S according to Figure 3.1. For the three-dimensional case applies that,

$$\left.\begin{array}{ll}\mathbf{r}\in V: & 4\pi\mathbf{P}\\ \mathbf{r}\in S: & 2\pi\mathbf{P}\\ \mathbf{r}\in \overline{V}: & 0\end{array}\right\} = \iiint_V dv'\,[div'\,\mathbf{P}\,grad'\phi + rot'\,\mathbf{P}\times grad'\phi] - \oiint_S df'\,[(\mathbf{n}\cdot\mathbf{P})\,grad'\phi + (\mathbf{n}\times\mathbf{P})\times grad'\phi] \quad (3.11)$$

where, $\overline{V}$ indicates the complement of V, namely the outer space. While, $\phi\,(\mathbf{r},\mathbf{r}')$ expresses the Green's function of the Laplace equation in three-dimensional free space. $\phi\,(\mathbf{r},\mathbf{r}')$ represents the potential response observed at point $\mathbf{r}$ caused by a potential source released at point $\mathbf{r}'$:

$$\phi = \phi\,(\mathbf{r},\mathbf{r}') = \frac{1}{|\,\mathbf{r}\,-\,\mathbf{r}'\,|}$$

Equation 3.11 includes integrals and differentials related to the prime coordinates. The volume integral provides the field derives from div $\mathbf{P}$ and rot $\mathbf{P}$ as sources of $\mathbf{P}$ located in V. On the other hand, the surface integral comprises the field in V resulting from sources and rotations in $\overline{V}$ described by $\mathbf{n}\cdot\mathbf{P}$ and $\mathbf{n}\times\mathbf{P}$ at S. So, the vector field $\mathbf{P}$ consists of these two fundamental parts.

Integral equations for related magnetic fields and flux densities can be derived applying 3.11 to the fields. Using the nomenclature from Equations (3.1) to (3.5) applies that,

$$4\pi\mathbf{H}_{out} = 4\pi\mathbf{H}_0 + \oiint_S df'\{(\mathbf{n}(\mathbf{r}')\cdot\mathbf{H}_{out})\,grad'\phi + (\mathbf{n}(\mathbf{r}')\times\mathbf{H}_{out})\times grad'\phi\} \quad (3.12)$$

$$4\pi\mathbf{B}_{out} = 4\pi\mathbf{B}_0 + \oiint_S df'\{(\mathbf{n}(\mathbf{r}')\cdot\mathbf{B}_{out})\,grad'\phi + (\mathbf{n}(\mathbf{r}')\times\mathbf{B}_{out})\times grad'\phi\} \quad (3.13)$$

$$4\pi\mathbf{H}_{inn} = -\iiint_V dv'\,\frac{\mathbf{H}_{inn}\cdot grad'\mu(\mathbf{r}')}{\mu(\mathbf{r}')}\,grad'\phi - \oiint_S df'\{(\mathbf{n}(\mathbf{r}')\cdot\mathbf{H}_{inn})\,grad'\phi + (\mathbf{n}(\mathbf{r}')\times\mathbf{H}_{inn})\times grad'\phi\} \quad (3.14)$$

$$4\pi\mathbf{B}_{inn} = -\iiint_V dv'\mu_0(\mathbf{H}_{inn}\times grad'\mu(\mathbf{r}'))\times grad'\phi - \oiint_S df'\{(\mathbf{n}(\mathbf{r}')\cdot\mathbf{B}_{inn})\,grad'\phi + (\mathbf{n}(\mathbf{r}')\times\mathbf{B}_{inn})\times grad'\phi\} \quad (3.15)$$

Equations (3.12) to (3.15) are valid for an observation point $\mathbf{r}$, which is located either in the inner space V or in the outer space $\overline{V}$. However for an observation point at the interface S, the 4π factors in the equations should be replaced for 2π.

The authors in [83] defined χ_v and $\mathbf{j}_v$ as the spatially distributed static dipole and current distribution, respectively. Besides them, χ_s and $\mathbf{j}_s$ determine the surface dipole

and current density distribution for the surface integrals. Hence,

$$\begin{aligned}
\chi'_v := \chi_v(\mathbf{r}') &:= \frac{\mathbf{H}_{inn}(\mathbf{r}') \cdot grad'\mu(\mathbf{r}')}{\mu(\mathbf{r}')} &&= div'\,\mathbf{M}' \\
\mathbf{j}'_v := \mathbf{j}_v(\mathbf{r}') &:= \frac{\mathbf{H}_{inn}(\mathbf{r}') \times grad'\mu(\mathbf{r}')}{\mu_0} &&= -\,rot'\,\mathbf{M}' \\
\chi'_s := \chi_s(\mathbf{r}') &:= \mathbf{n}(\mathbf{r}') \cdot \mathbf{B}_{inn}(\mathbf{r}') \\
\mathbf{j}'_s := \mathbf{j}_s(\mathbf{r}') &:= \mathbf{n}(\mathbf{r}') \times \mathbf{H}_{inn}(\mathbf{r}')
\end{aligned}$$

Equation 3.13 and Equation 3.15 are used to establish an integral relation for the axial component of the magnetic field strength at the interface. Considering the boundary conditions in 3.4 and 3.5, the following applies:

$$\begin{aligned}
\mathbf{j}''_s = \frac{2\mathbf{n}'' \times \mathbf{H}''_0}{\mu'' + 1} &- \frac{1}{2\pi(\mu'' + 1)} \iiint_V dv'\, \mathbf{n}'' \times (\mathbf{j}'_v \times grad'\phi) \\
&- \frac{1}{2\pi(\mu'' + 1)} \oiint_S df'(\mu' - 1)\, \mathbf{n}'' \times (\mathbf{j}_s{}' \times grad'\phi)\,; \quad \mathbf{r}', \mathbf{r}'' \in S
\end{aligned} \tag{3.16}$$

where, $\mu'' := \mu(\mathbf{r}'')$ and $\mathbf{n}'' := \mathbf{n}(\mathbf{r}'')$. Likewise, Equations 3.12 and 3.14 are utilised to determine an integral relation for the radial component of the flux density at the interface. As a result, taking into account the boundary conditions in 3.4 and 3.5 results:

$$\begin{aligned}
\chi''_s = \frac{2\mu_0\mu''}{\mu'' + 1}\, \mathbf{n}'' \cdot \mathbf{H}''_0 &- \frac{\mu_0\mu''}{2\pi(\mu'' + 1)} \iiint_V dv'\, \chi'_v\, \mathbf{n}'' \cdot grad'\phi \\
&+ \frac{\mu''}{2\pi(\mu'' + 1)} \oiint_S df'\, \frac{\mu' - 1}{\mu'}\, \chi'_S\, \mathbf{n}'' \cdot grad'\phi\,; \quad \mathbf{r}', \mathbf{r}'' \in S
\end{aligned} \tag{3.17}$$

Equations 3.16 and 3.17 arise as non-linear Fredholm integral equations of the second kind for solving χ_s and $\mathbf{j}_s$. Furthermore, once χ_s and $\mathbf{j}_s$ are known, Equation 3.12 and the set of boundary conditions can be considered for solving the leakage problem $\mathbf{H}_{leak}$ based on:

$$\mathbf{H}_{leak} = \frac{1}{4\pi\mu_0} \oiint_S df'\, \{\chi'_s\, grad'\phi + \mu_0\, \mathbf{j}'_s \times grad'\phi\} \tag{3.18}$$

Dobmann and Münnich also presented experimental results. Their set-up consists of a cylindrical bar of steel with a saw cut, which extends longitudinally along the axial coordinate. Several defect widths (circumferential direction) and depths (radial direction) were considered. Axial and radial components of the leaked field were recorded for an applied field range between 2.5 kA/m and 32 kA/m. Changes in the applied field imply the variation of the relative permeability from 300 to 50. Experiments showed that the maximum of the radial component increases linearly for applied fields higher than 8 KA/m, while for lower applied fields the behaviour is no-linear. According to this result, the permeability gradient and thereby the volume integrals in Equations 3.16 and 3.17 can be neglected since the applied field of interest lies on the linear range. This assumption allows the decoupling of the two integral equations and their independent solution from each other.

Dobmann and Münnich carried out further works for an applied field of 12.7 kA/m, namely a relative permeability of 100. Under this condition, the contribution from $\mathbf{j}_s$

can be disregarded comparing with that from χ_s since according to the law of refraction, current distributions are μ times lower than dipole distributions. Hence, the numerical problem reduces to the solution of the integral equation,

$$\chi_s'' = \frac{2\mu_0\mu}{\mu+1}\,\mathbf{n}''\cdot\mathbf{H}_0'' + \frac{\mu-1}{2\pi(\mu+1)}\oiint_S df'\,\chi_s'\,\mathbf{n}''\cdot grad'\phi\,;\quad \mathbf{r}',\mathbf{r}''\in S \tag{3.19}$$

and to determine the magnetic leaked field,

$$\mathbf{H}_{leak} = \frac{1}{4\pi\mu_0}\oiint_S df'\,\chi_s'\;grad'\phi \tag{3.20}$$

The authors in [83] identified these integral equations being of the form:

$$y(x) = g(x) + \lambda\int dx' K(x,x')\,y(x')$$

and suggested to solve them through successive iterations according to Fredholm Theory. After every iteration process, the permeability will be corrected according to the known material hysteresis curve. The initial value selected to begin the iteration process is the inhomogeneity case:

$$\chi_s^{(0)\,\prime\prime} = \frac{2\mu_0\mu}{\mu+1}\,\mathbf{n}''\cdot\mathbf{H}_0''$$

and for n iteration steps was achieved:

$$\chi_s^{(n)\,\prime\prime} = \chi_s^{(0)\,\prime\prime} + \frac{\mu-1}{2\pi(\mu+1)}\oiint_S df'\,\chi_s^{(n-1)\,\prime}\,\mathbf{n}''\cdot grad'\phi \tag{3.21}$$

Then, the sequence converges if a fixed $\varepsilon > 0$ and an integer n_0 exist, for which the following applies:

$$\|\,\chi_s^{(n)\,\prime\prime} - \chi_s^{(n-1)\,\prime\prime}\,\| < \varepsilon$$

for all $\mathbf{r}''\in S$ and all integers $n \geq n_0$.

The authors in [83] claimed that the iteration method converges in about 36 iterations with an approximated ε value of 10^{-4}, including the regions with highest dipole distribution gradient. The main advantage of the integral equation method is the fact that a three-dimensional problem is reduced to a two-dimensional formulation.

Dutta et al. [84] published a more recent proposal. Although the scope of this recent study is not comparable regarding the study from Dobmann and Münnich, it involves an accepted model. Dutta et al. derived elementary expressions for the components of a MFL signal respect to the spatial behaviour. A three-dimensional analytical model is developed, allowing the estimation of the leaked field. In this case, the field leaks out as a result of the presence of a surface-breaking defect. Constant permeability is assumed neglecting the volume magnetic charge in order to include only surface integrals in the model. A high magnetic field for excitation is considered with the objective of reaching saturation of the material. The shape of the defect is assumed to be elliptical achieving uniform magnetic field in it. Figure 3.3 shows the geometry and pole distribution of the defect.

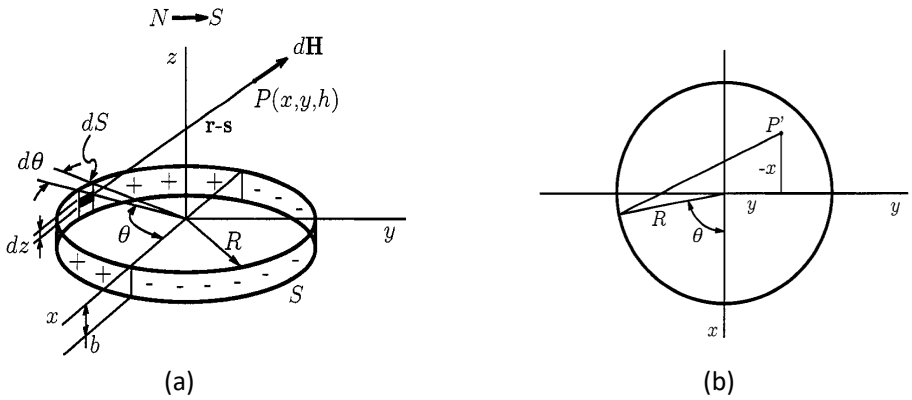

Figure 3.3: *Representation of a three-dimensional dipole model for a cylindrical hole defect [84]: (a) Three-dimensional and (b) Planar geometry*

.

The authors in [84] stablished Equations 3.22 and 3.23 to obtain the leaked field at any point $P(x,y,h)$ in Figure 3.3. In the equations, M refers to the magnetisation magnitude. H_x, H_y and H_z are the components of the MFL field.

$$\mathbf{H}(\mathbf{r}) = \frac{M\,R}{4\,\pi} \int_0^{2\pi} \int_{-b}^{0} \frac{r_x\mathbf{i} + r_y\mathbf{j} + r_z\mathbf{k}}{(r_x^2 + r_y^2 + r_z^2)^{\frac{3}{2}}} \sin\theta\, dz\, d\theta \tag{3.22}$$

$$\mathbf{H}(\mathbf{r}) = \mathbf{H}_+ + \mathbf{H}_- = H_x\mathbf{i} + H_y\mathbf{j} + H_z\mathbf{k} \tag{3.23}$$

The vector $\mathbf{r}$ is defined as in Equations 3.24 and 3.25. Plus and minus signs are used in these Equations as subscripts to indicate north and south polarity regions.

$$\mathbf{r}_\pm = r_x\mathbf{i} + r_{y\,\pm}\mathbf{j} + r_z\mathbf{k} \tag{3.24}$$

$$\mathbf{r}_\pm = (x - R\,cos\,\theta)\mathbf{i} + (y \pm R\,sin\,\theta)\mathbf{j} + (h - z)\mathbf{k} \tag{3.25}$$

Dutta et al. [16] published simulated results of cylindrical and cuboidal defects. The authors presented a discussion about the signal characteristics of the orthogonal components of the MFL signal, primarily respect to lift-off. They demonstrated that the model is scale-invariant regarding the spatial properties of the MFL signal. Specific attention is paid in their work to the circumferential component of the leaked field. They considered this component fundamental to characterise the defect in the circumferential direction. Finally, Dutta et al. also proposed a compensation technique to correct lift-off dependency on the determination of radius and depth for a cylindrical defect.

In the last years, a different approach was published by Dyakin et al. as a series of articles [85–92]. They calculated the magnetic field behaviour for different defective specimens. In every case, the sample possesses a flaw inside of it. The first publication consists of a finite defect in a three-dimensional half-space, assuming a uniform external field. Dyakin et al. solved the problem based on the integrodifferential equation of magnetostatics [85]. The same study was conducted placing the defect in a semispace instead of a half-space [86]. Dyakin and co-workers considered, in the third publication [87], the case of a spherical defect in a semispace magnetised by an inhomogeneous external field.

A turn carrying a current produces the related incident field. Using the same technique, the authors also provided equations to calculate the leaked field due to the presence of a finite defect inside different bodies: a plate, a sphere, a cylinder and a pipe [88–92].

The equation system obtained in the case of a spherical defect located in a plane-parallel plate [88] is singularly presented here because this specific geometry is particularly meaningful in this research. Figure 3.4 shows the selected variables to formulate the problem. A cavity full of air is located inside a plate with permeability μ different to 1. The plate is limited by a plane located at $z = -d_1$ and a plane at $z = d_2$. The set of points located in the plate apart from those inside the cavity are represented by Ω. The cavity surface is designated as S and the related sphere radius as r_0.

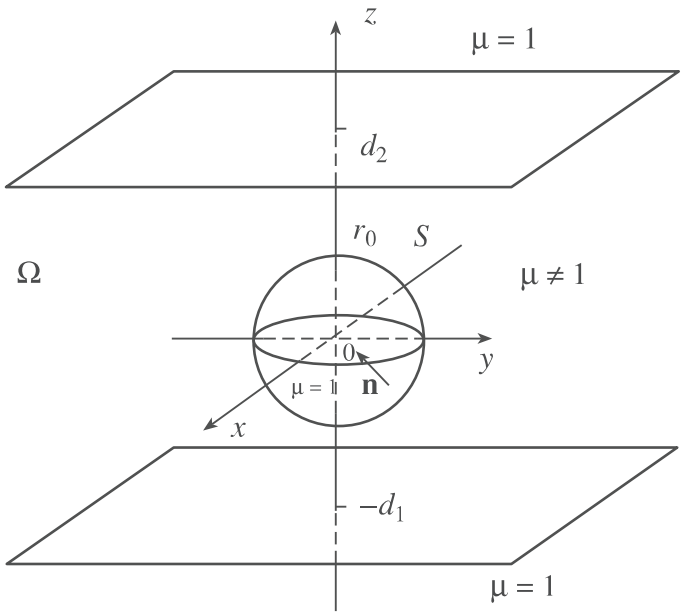

Figure 3.4: *Spherical defect located in a magnetised plate [88].*

The authors in [88] defined an uniform external field $\mathbf{H}^0 = \{H^0,0,0\}$ and the parameter λ equal to $(\mu-1)/(\mu+1)$. Expressions for the resulting magnetic field on the plate surfaces are formulated as H_x, H_y and H_z:

$$\frac{H_x(\xi,\zeta)}{H^0} = 1 + \frac{2\lambda\,(1+\lambda)}{\xi^2+\zeta^2}\sum_{l=1}^{\infty} Q_l \left\{ \frac{g_l^x(\xi,\zeta,\eta)}{\omega^{l+2}} + \lambda\sum_{n=0}^{\infty}\frac{\lambda^{2n} g_l^x(\xi,\zeta,\eta_1(n))}{\omega_1^{l+1}(n)} + \sum_{n=1}^{\infty}\frac{\lambda^{2n} g_l^x(\xi,\zeta,\eta_2(n))}{\omega_2^{l+2}(n)} \right\}$$

$$\frac{H_y(\xi,\zeta)}{H^0} = \frac{2\lambda\,(1+\lambda)\xi\zeta}{\xi^2+\zeta^2}\sum_{l=1}^{\infty} Q_l \left\{ \frac{g_l^y(\eta)}{\omega^{l+2}} + \lambda\sum_{n=0}^{\infty}\frac{\lambda^{2n} g_l^y(\eta_1(n))}{\omega_1^{l+2}(n)} + \sum_{n=1}^{\infty}\frac{\lambda^{2n} g_l^y(\eta_2(n))}{\omega_2^{l+2}(n)} \right\}$$

$$\frac{H_z(\xi,\zeta)}{H^0} = 2\lambda\,(1+\lambda)\,\xi\sum_{l=1}^{\infty} l\,Q_l \left\{ \frac{g_l^z(\eta)}{\omega^{l+3}} - \lambda\sum_{n=0}^{\infty}\frac{\lambda^{2n} g_l^z(\eta_1(n))}{\omega_1^{l+3}(n)} + \sum_{n=1}^{\infty}\frac{\lambda^{2n} g_l^z(\eta_2(n))}{\omega_2^{l+3}(n)} \right\}$$

where, $\xi := \dfrac{x}{d_2}$, $\zeta := \dfrac{y}{d_2}$ and $\varepsilon := \dfrac{r_0}{d_2}$

and the coefficient $Q_l := \dfrac{h_{l,1}\varepsilon^{l+2}}{\sqrt{\pi l(l+1)(2l+1)}}$ using the function h to provide the representation of an unit sphere with the center at the origin of coordinates into an orthonormalised system of functions defined on S by means of a expanded series.

Additionally, next functions are defined with P_l as Legendre polynomials,

$$\begin{aligned} g_l^x(\xi,\zeta,\eta) &:= ((l+1)\xi^2 - \zeta^2)P_l'(\eta) - l\xi^2\eta P_{l+1}'(\eta), \\ g_l^y(\eta) &:= (l+2)P_l'(\eta) - l\eta P_{l+1}'(\eta), \\ g_l^z(\eta) &:= P_{l+1}'(\eta) \end{aligned}$$

taking into account that:

$$\omega := \sqrt{\xi^2+\zeta^2+\tau^2}, \qquad \eta := \frac{\tau}{\omega}, \qquad \omega_1(n) := \sqrt{\xi^2+\zeta^2+\tau_1^2(n)},$$
$$\eta_1(n) := \frac{\tau_1(n)}{\omega_1(n)}, \qquad \omega_2(n) := \sqrt{\xi^2+\zeta^2+\tau_2^2}, \qquad \eta_2(n) := \frac{\tau_2(n)}{\omega_2(n)}.$$

Where the parameters τ are defined depending on which surface the field to be calculated is selected:

for $z = -d_1$:

$$\tau := -\delta, \qquad \tau_1(n) := 2(n+1) + (2n+1)\,\delta, \qquad \tau_2(n) := -(2n + (2n+1)\,\delta)$$

and, in the case of $z = d_2$ applies:

$$\tau := 1, \qquad \tau_1(n) := -(2n+1+2(n+1)\,\delta), \qquad \tau_2(n) := 2n+1+2n\delta.$$

with $\delta := \dfrac{d_1}{d_2}$.

The authors in [88] implemented the equations in an algorithm developed under FORTRAN programming language in order to solve the problem. The same procedure was carried out with other investigated body geometries. Related fields for simple geometries were calculated with the aim to compare them with exact results found analytically. The convergence of the numerical results to the exact solutions was verified. They claimed that a solution for the magnetostatic problem applied to different samples and defect geometries remains a challenging task for practical use of magnetic testing methods.

Hitherto in this section, different numerical proposals to solve the MFL signal problem have been reviewed. These previous models entail a demanding mathematical component as has been shown. In the next section, the finite element method (FEM) will be introduced, which is the most common numerical technique used today.

3.1.3.1 Finite Element Analysis

The finite element analysis (FEA) is based on the laws of conservation, electromagnetism and classical mechanics. A discretisation process is used as a first step to enable these

models for numerical evaluation and their respective implementation on computers. Once the problem is discretised on a fixed number of elements over the domain, an extensive system of simpler equations is obtained. Then, an approximated solution is established employing a variational method, which considers the minimisation of the associated error function [93]. The FE mathematical approach and notation presented below is according to [36].

The finite element method consists of a particular numerical projection method, which can be described by linear operators, whereby:

$$\mathbf{L}\,U(\mathbf{r}) = g(\mathbf{r})$$

assuming that the differential or integral operator is represented by $\mathbf{L}$, the solution function by $\mathrm{U}(\mathbf{r})$ and the imposed function by $\mathrm{g}(\mathbf{r})$. Besides, for the boundary or transition condition applies:

$$\mathbf{R}\,U(\mathbf{r}) = h(\mathbf{r})$$

in which the function class of $\mathrm{U}(\mathbf{r})$ can be found from a Hilbert space trough mathematical projection methods as follows,

$$U(\mathbf{r}) \approx \hat{U}(\mathbf{r}) = \mathbf{P}\,U(\mathbf{r}) = \sum_{i=1}^{n} \alpha_i\,\phi_i(\mathbf{r}) \tag{3.26}$$

where $\mathbf{P}$ is a projection operator employed to establish $\hat{\mathrm{U}}(\mathbf{r})$ as an image of $\mathrm{U}(\mathbf{r})$, obtaining an approximation of the solution function. $\phi_i(\mathbf{r})$ denotes the basis functions and α_i denotes the coefficients of the functions that approximate $\mathrm{U}(\mathbf{r})$ with $\hat{\mathrm{U}}(\mathbf{r})$.

The functional of the field energy can then be established using the corresponding integral formulation in agreement with the Ritz method, hence:

$$\mathbf{X}\,[U] = \tfrac{1}{2}\left\langle \mathbf{L}\,U, U\right\rangle - \left\langle g\,,\,U\right\rangle$$

and the minimum of the functional can be determined by,

$$\frac{\partial}{\partial \alpha_j}\,\mathbf{X}\,[\hat{U}] = 0, \qquad j = 1,\,...,\,n$$

Using the integral form $\langle\ ,\ \rangle$ for a scalar product in the Hilbert space of the j functions of $\hat{\mathrm{U}}$ and applying Equation 3.26 can be obtained:

$$\tfrac{1}{2}\left\langle \alpha_j \mathbf{L}\phi_j(\mathbf{r})\,,\,\hat{U}(\mathbf{r})\right\rangle + \tfrac{1}{2}\left\langle \mathbf{L}\hat{U}(\mathbf{r})\,,\,\alpha_j\phi_j(\mathbf{r})\right\rangle - \left\langle g\,,\,\alpha_j\phi_j(\mathbf{r})\right\rangle = 0, \qquad j = 1,\,...,\,n \tag{3.27}$$

And assuming that the operator $\mathbf{L}$ owns the characteristics of self-adjointment, it is possible to establish the following,

$$\left\langle \mathbf{L}\,U\,,\,v\right\rangle = \left\langle U\,,\,\mathbf{L}\,v\right\rangle$$

Consequently, Equation 3.27 is equivalent to,

$$\left\langle \mathbf{L}\,\hat{U}(\mathbf{r})\,,\,\phi_j(\mathbf{r})\right\rangle - \left\langle g\,,\,\phi_j(\mathbf{r})\right\rangle \equiv 0, \qquad j = 1,\,...,\,n$$

hence,

$$\left\langle \mathbf{L}\,\hat{U}(\mathbf{r}) - g\,,\,\phi_j(\mathbf{r}) \right\rangle \equiv 0, \qquad j = 1,\,...,\,n \tag{3.28}$$

So the error caused when U is replaced by $\hat{U}$ can be quantified by means of a residual ε as,

$$\varepsilon := \mathbf{L}\hat{U} - g \tag{3.29}$$

This error is derived on the orthogonal space from all $j = 1, ..., n$ basis functions $\phi_j(\mathbf{r})$ as declared when the functional of the energy is reduced to a minimum.

In general, a mathematical model can be used for numerical simulation only if it is well-posed. That means that all necessary data to define the model is provided, and consequently, a unique solution is feasible. As mentioned above, the solution delivered from the simulation process is an approximation of the exact solution. The error arises because the infinite terms of the Taylor series are approximated to a finite sum to establish the equation system. It is known as a truncation error. According to this, the solution provided converges to the exact solution as long as the truncation error approaches zero. This condition is achieved if the numerical model possesses two characteristics: stability and consistency [93].

3.1.3.2 COMSOL Multiphysics

COMSOL Multiphysics is a specialised software to build up models in different fields in physic and to solve them employing the finite element method. COMSOL fundamentals will be reported here based on COMSOL Multiphysics guides [93, 94]. Figure 3.5 summarises the main workflow of the simulation process by COMSOL, which consists of two main stages: the model definition and the FEM performance. The model definition step permits the set up of the model environment. It includes the selection of the space dimension, the statement of symmetries if they exist, the definition of the physical interfaces according to the physics field, and also the study type in relation with time and frequency dependencies. Next, it is necessary to build, synchronise or import the geometry. After the model is achieved, material properties should be specified for every domain. Subsequently, governing physics for domains, boundaries, edges and points must be configured as well as initial values and boundary conditions. Once the model is fully defined, the finite element analysis can be conducted.

COMSOL establishes the corresponding set of partial differential equations (PDE) for the model according to the previously selected physics field. The main objective of the COMSOL simulation is to find an approximated solution to the PDEs, which allows the construction of a mathematical model equation. The so-called weak formulation achieves this aim through the following sequence:

- Integration of the PDE over the entire domain, so numerical problems related to discontinuities are discarded.
- Insertion of a set of test functions into the integral in order to sample the expected PDE solution. This sampling is carried out by multiplying the PDE and the test

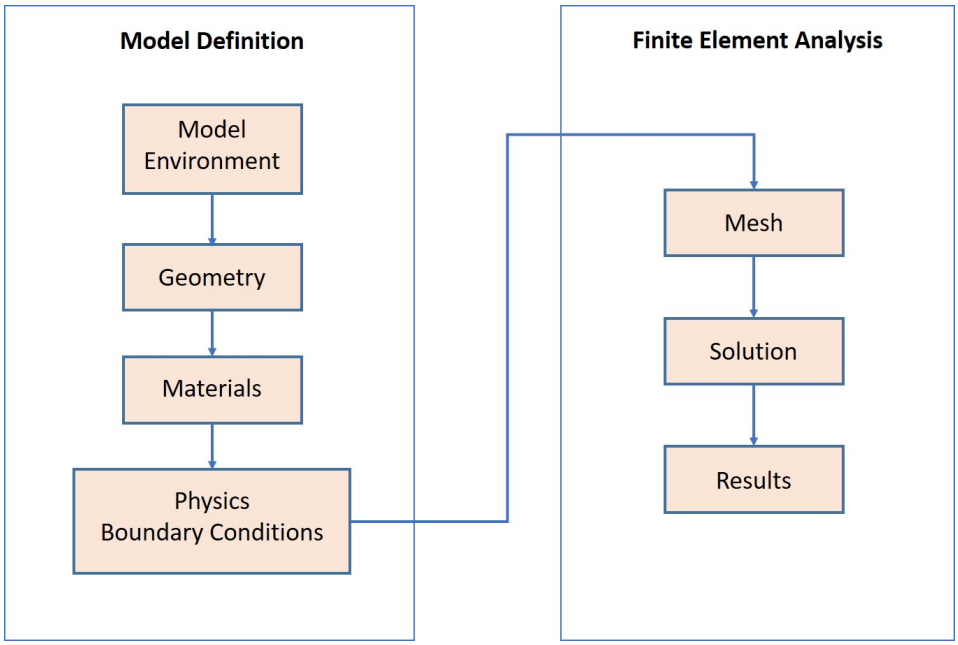

Figure 3.5: *Simulation workflow by COMSOL Multiphysics.*

vectors. Every test function is non-trivial only in an arbitrary narrow range so that the entire set of functions covers the whole domain. The test functions and the solution is assumed to belong to Hilbert spaces.

- Reduction of the integrand differentiation order making use of the divergence theorem. Thereby, the derivative is removed from the dependent variable to the test function.
- Insertion of natural boundary conditions, also called Neumann boundary conditions for specified fluxes at domain boundaries.
- Introduction of fixed boundary conditions, also known as Dirichlet boundary conditions. By that means, particular values of the sought variable are provided at specific boundaries. Fixed boundary conditions claimed for a unique solution by means of a well-posed problem. Those can be introduced straight away into the equation with the aid of additional test functions.

The model equation obtained as a result of the weak formulation is then discretised in order to acquire the numerical model equation. The discretisation is accomplished by, for example, the Galerkin method. This aim is attained using an approximated solution of the weak formulation, which consists of a linear combination of basis functions. This approximated solution belongs to a finite-dimensional subspace within the Hilbert space for which Equation 3.26 is valid. The discretisation of the model in COMSOL is carried out through a computational mesh. Each mesh element has a related number of nodal points. Every node implies a set of basis functions. The default functions used by COMSOL are of the type, second-order Lagrange elements for most physics. These functions constrain the coefficients to be continuous across the boundaries between adjacent elements.

After the geometry is subdivided into smaller pieces, the set of functions obtained from Equation 3.26 can be substituted into the weak formulation. This operation results in an expression with n coefficients α_i, including the unknown terms used to establish the boundary conditions. All these unknowns together are called the degrees of freedom (DOF). The set of all these discrete degrees of freedom is called the vector of unknowns. An equivalent number of equations is needed to solve the problem; those are obtained from the test functions ϕ_j as in Equation 3.28. Relations to meet the boundary conditions are also included. As the purpose of a test function is to sample the equation locally, COMSOL substitutes the set of test functions for the set of basis functions which are already localised functions, so that the entire domain is covered. Every emerged equation after the substitution has a small number of terms owing that the chosen functions are localised. A system of algebraic equations results after the model is discretised and the boundary conditions are imposed, this system has the form:

$$\mathbf{A}\,\mathbf{c} = \mathbf{b}$$

where $\mathbf{c}$ is the vector of unknowns. $\mathbf{A}$ is a square matrix known as the stiffness matrix. It contains the coefficients α_i in each equation j. Moreover, $\mathbf{A}$ is a so-called sparse matrix meaning that most of the elements A_{ij} are zero. This benefit results from the use of localised basis functions, and it enhances the efficiency of numerical methods to solve the system. The vector $\mathbf{b}$ is usually called the load vector.

As already emphasised, the solution of the equation system provides an approximation of the PDE solution, Equation 3.26. In a stable and consistent posed problem applies that: the denser the mesh, the smaller the difference between the approximate solution and the exact solution. This error is expressed as the residual ε in Equation 3.29. In numerical analysis, there are two fundamental sources of error, one associated with the discretisation of the geometry and the second with the discretisation of the solution. The error caused by geometry discretisation is in general dominant. COMSOL also offers the possibility to increase the element order as an alternative to minimise the error, besides to shrink the element size. However, a compromise should be reached since the use of denser meshes or higher elements order demand higher computational requirements. Once a previously specified error tolerance is achieved, the solution of the equation system is delivered. As the exact solution is unknown, COMSOL recommends performing a mesh refinement study in order to check the convergence of the simulation results assuring the accuracy of modelling.

In order to solve the problem, COMSOL uses several methods based on the numerical model. In the case of systems of linear equations, there are two classes of algorithms to deal with: direct and iterative methods. Direct solvers are based on LU decomposition (Lower Upper decomposition, also called LU factorisation). These types of solvers approach the solution in one large computational step after the functional of the system is established through the Newton-Raphson method. Iterative methods, as opposed to direct methods, approach the solution in several steps. Hence, the reduction of the calculated error can be appreciated as the number of interactions raises for well-posed problems. In general terms, direct solvers can be more robust, but they demand considerably more memory for the same problem as iterative solvers. However, iterative solvers can require specific settings according to the nature of physic laws which govern

the model. In fact, the selection of the best solver settings by COMSOL is implemented by default for every physic interface.

In the case of non-linear equations system, the solution is based on the damped Newton-Raphson method. Multiple iterations are applied to find the solution until it converges to within the established tolerance or until a maximum number of iterations is reached. This method uses a damping factor, which provides two advantages to the process: first, the minimisation of the number of Newton-Raphson steps and second, it prevents the search in regions where the problem does not have a solution. Nevertheless, it is still possible that non-linear systems may not converge. The reasons can be summarised in three cases: the assumed initial condition is too far away from the solution, the problem itself does not have a solution, and finally, the material properties are discontinuous and non-differentiable. A more robust approach is employed by COMSOL to solve non-linear problems using the so-called load ramping technique and the continuation method. This strategy increases the load of the current model gradually, starting with a magnitude infinitesimally larger than zero until the wanted load is achieved. This algorithm provides advisable initial conditions to carry out the Newton-Raphson iterations in order to solve the problem. In addition, it supplies the possibility to find an approximated failure load value for problems which do not have a solution. For this purpose, the algorithm makes use of results successfully obtained for previous load values. The report of the whole process is displayed in COMSOL on a log file allowing the user to get a better knowledge about the system. For those cases where the load ramping technique is still inefficient, COMSOL uses nonlinearity ramping for convergence improvement. However, if the solution is expected to oscillate between different regions as the Newton-Raphson method is applied, COMSOL has a trust region solver known as the Double Dogleg non-linear solver available, which can offer better performance.

3.1.4 Experimental Verification

The experimental study of MFL is, in general, highly demanding and expensive if the set-up entails changes in parameters, as it is typical for empirical analysis. Figure 3.6 shows the MFL principle consisting of a yoke, a pair of permanent magnets, a pair of pole shoes and a test specimen. Besides the magnetic circuit, there is a sensor to measure the magnetic field. It is located between the pole shoes as close as possible to the sample surface. The path for magnetic flux lines is highlighted, Figure 3.6a presents the flux behaviour for a flawless specimen and Figure 3.6b the case for a sample containing a thickness reduction. In this case, the magnetic field leaks out owing to the local reduction of the ferromagnetic material. In addition to the components in Figure 3.6, the set-up for an experimental study needs the implementation of the motion system, data acquisition unit and data processing system. Despite the simplicity of the magnetic component, the following limitations were found as the first tests were conducted:

- Fixed magnetic field.
- Unique sensor permitting the measurement of only one field component at a time.

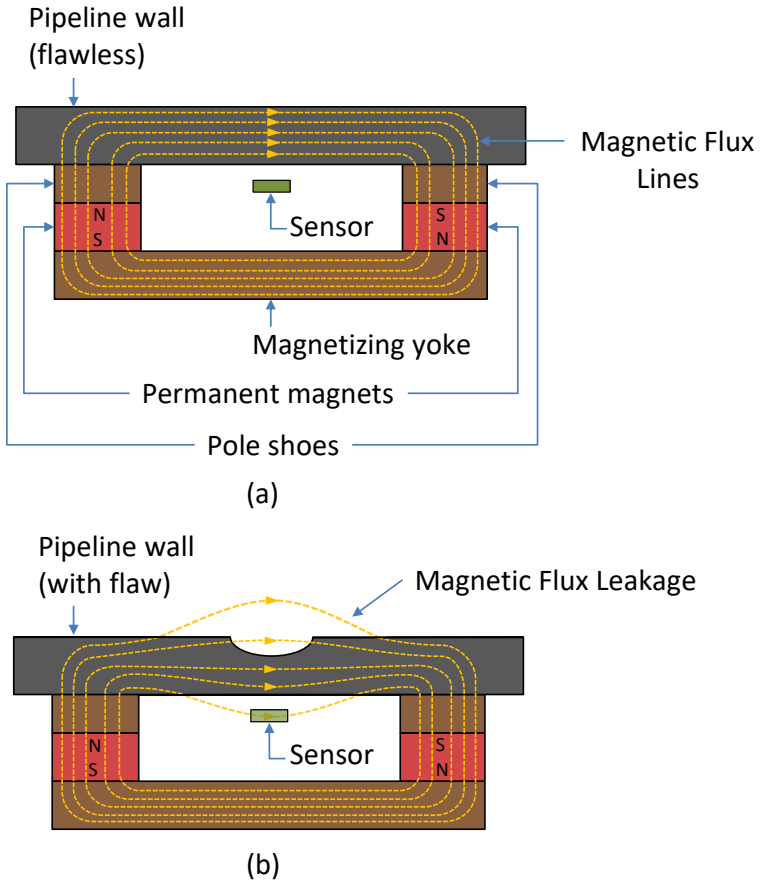

Figure 3.6: *MFL Principle: (a) Magnetic flux lines for a flawless specimen. (b) Magnetic flux leakage as a consequence of a thickness reduction in the sample.*

- Risky manipulation of the samples due to the high magnetisation and the inability to switch off the magnets.

In order to improve the initial set-up, next upgrades were included:

- An electromagnet is used to magnetise the specimen, with the possibility to modify the applied magnetic field.
- The development of a sensor consisting of two Hall sensors in an array allowing the measurement of tangential and normal components of the magnetic field simultaneously.
- The implementation of the set-up on an automated scanner to allow sensor displacement on defined areas with high measurement resolution, and a guaranteed constant lift-off.
- The possibility of switching off the electromagnet during sample exchange, which reduces accident risk.

3.2 Magnetic saturation

In general terms, magnetisation can be modified by two mechanisms, domain wall displacement and domain rotation. Both of them can occur in the material simultaneously. Nevertheless, it is expected without certainty so far, that displacements of domain walls contribute to the total magnetisation mainly before the knee of the MH curve. While domains rotation is mostly responsible for increases on magnetisation after the knee and along the saturation branch [95]. In fact, the predominant mechanism from these two will define the shape of the Hysteresis loop. Hitherto, it has been impossible to deduce a single function for magnetisation in terms of **H** defining the non-linear MH-curve because the factors involved are still not well known. The behaviour of the magnetisation process as the applied field reaches relatively high magnitudes was studied in [95, 96]. The related authors describe this process under the denotation of the so-called, *law of approach to saturation*. They coincide that there are still disagreement and unsatisfactory understanding from research which allows defining saturation strictly. Here is the currently publishing state as an overview of corresponding mechanisms presented. Chikazumi and Graham published in [96] a mathematical demonstration establishing the following expression to calculate rotation magnetisation for a polycrystalline-cubic anisotropic material in the saturation branch,

$$M = M_s \left(1 - \frac{b}{H^2} - ...\right) \tag{3.30}$$

with,

$$b = 0.0762 \frac{K_1^2}{M_s^2} \tag{3.31}$$

where K_1 is a cubic anisotropy constant. In particular, cubic anisotropy constants depend on composition and temperature. They have dimensions of energy per unit volume [1].

On the other hand, the law of approach to saturation is experimentally defined in [96] as,

$$M = M_s \left(1 - \frac{a}{H} - \frac{b}{H^2} - ...\right) + \chi H \tag{3.32}$$

where, the term χH considers the increment on spontaneous magnetisation [2] due to the presence of an external magnetic field. The term b/H^2, as explained previously, is the contribution of a uniform magnetisation rotation. Furthermore, the first term a/H takes into account the inhomogeneity of the magnetic material with a lack of consensus from research. Interpretations of it include dislocations generating stress fields, non-magnetic inclusions and voids.

[1] For iron at $20°C$, $K_1 = 4.72x10^5 erg\,cm^{-3}$

[2] Spontaneous magnetisation is one of the Weiss'postulates. It states the effective magnetisation induced in the material below its Curie temperature by spin order, even in the absence of an applied field.

4

Statement and Approach

As introduced in Chapter 1, corrosion has been statistically placed as the primary cause for pipeline failures well beyond other factors. The inability to accurately size corrosion defects located in pipelines can result in erroneous integrity strategies with fatal consequences, even when appropriate inspection processes have been conducted (see Section 2.3). Consequently, being able to provide reliable defect dimensions based on data acquired using in-line inspection techniques is crucial in order to achieve a safe, reliable and sustainable pipeline operation. Figure 4.1 presents a general conceptual overview to guarantee pipeline integrity focused on wall-part defects problematic.

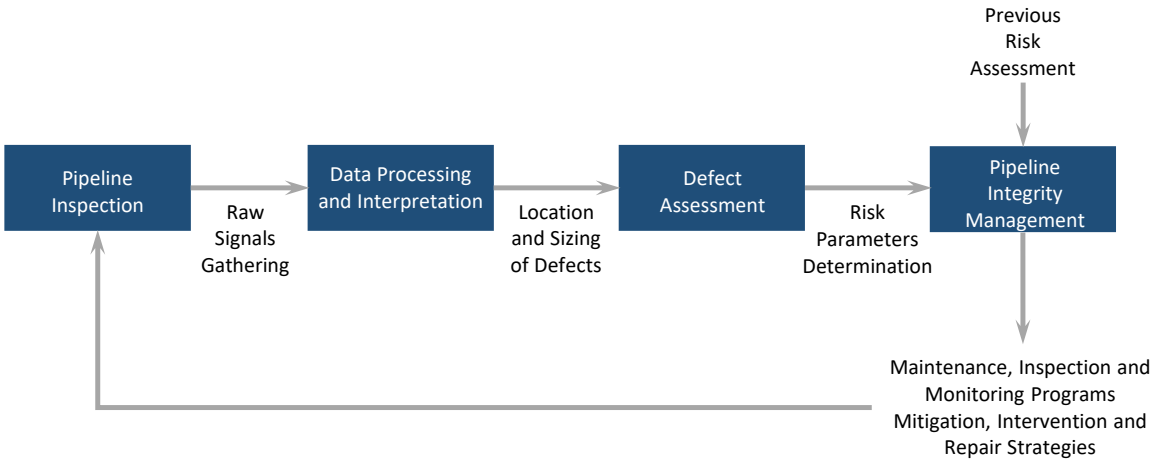

Figure 4.1: *Conceptual overview of the pipeline assessment process addressed to wall-part defects problematic in order to guarantee pipeline integrity.*

The whole process in Figure 4.1 comprises four main stages. The first block requires a selection of a specific technique for pipeline inspection. The best technique is chosen based on the particular assessment aims and pipeline conditions, as discussed in Section 2.2. According to the nature of the signals acquired in the first stage, the most accurate data processing and interpretation method available is selected to locate and size the identified defects. Once this information is delivered, a defect assessment method is chosen depending on defect type. The results obtained from the current inspection,

together with previous outcomes, serve to define advisable programs and strategies to implement in the inspected pipeline system through a pipeline integrity management process.

A Pipeline Defect Assessment Manual (PDAM) has been published as a result of a Joint Industry Project [97]. Its main aim focuses on providing suitable standards and programs regarding pipeline integrity management. PDAM includes a guide to the use of assessment methods according to the defect type. Such methods are symbolised in the third block of Figure 4.1, which require defect dimensions and location as input. Specifically for corrosion defects, PDAM published available empirical and semi-empirical methods. Most of these methods are based on the general form of the NG–18 equation[1], which consists of the so-called *part–wall failure criterion*. Even though other alternatives are already developed, the general form is recognised as the best approach. Nevertheless, differences between the methods are related to the assumptions and simplifications on flow stress definition, geometry correction factor and defect profile. Although, available data in published literature is not sufficient to conduct a thorough comparison of the methods, comparing experiments and predictions permits the clasification of the methods as conservative or unconservative [98]. Related information on assessment methods has already been published in detail; therefore in this section, an overview of the modified B31G is provided only as an example to emphasise the importance of accurately sizing detected defects (refer to Section 2.4.4 for further contextualisation). The NG–18 equation is utilised to evaluate the burst strength of a corroded area subject to internal pressure loading, which is given by the following equation in case of a corroded area extended longitudinally:

$$\sigma_\theta = \bar{\sigma} \left[\frac{1 - \frac{d}{t}}{1 - \left(\frac{d}{t}\right) \frac{1}{M}} \right] \tag{4.1}$$

According to Cosham and Hopkins in the PDAM [97] *"$\bar{\sigma}$ is the flow stress, which is an empirical concept intended to represent the stress at which unconstrained plastic flow occurs in a strain hardening elastic-plastic material via a single parameter."*. d represents the maximum defect depth, while the nominal wall thickness is symbolised by t. M is known as the bulging factor or Folias factor. Since a particular defect shape is assumed to establish the equations in every method, M definition varies according to this assumption. For instance for the modified B31G method,

$$M = \sqrt{1 + 0.6275 \left(\frac{2c}{\sqrt{Dt}}\right)^2 - 0.003375 \left(\frac{2c}{\sqrt{Dt}}\right)^4} \tag{4.2}$$

where $2c$ corresponds to the maximum allowable longitudinal extent of the corroded area and D describes the nominal outside diameter of the pipe.

As can be observed, equations 4.1 and 4.2 include, apart from flow stress and nominal pipeline features, only defect length and depth as input. Such equations deliver essential information to a complex flowchart decision diagram considering different issues in order

[1]The so-called *general form* corresponds to the basic equation of the part-wall NG-18 failure criterion.

to determine, e.g. the maximum allowable operating pressure (MAOP). Furthermore, parameters such as the corrosion growth rate can be defined based on defect dimensions in order to establish an inspection program. Models to determine corrosion growth rate are either deterministic or probabilistic [99]. In general, these models require high accuracy by the input data, namely defect length and depth. In fact, the underestimation or overestimation of defect dimensions, and consequently misinterpretation of the pipeline conditions risk, have both unfortunate consequences. The underestimation will permit pipeline failures and the overestimation, unnecessary assessments.

Specifically, the primary aim of this work is dedicated to the second block in Figure 4.1. Thus, data obtained from an in-line inspection using magnetic flux leakage (MFL) technique need to be processed to locate and size detected defects. MFL has been utilised for decades, and it is still today the most widely used inspection method in the oil and gas industry due to procedural and financial advantages compared with other alternatives (see Section 2.2). Furthermore, MFL has demonstrated high performance in the detection of corrosion problematic. Therefore, these benefits will be exploited, assessing corrosion type defects in this research. Despite the broad acceptance of the MFL technique, a model capable of solving the inverse problem is still urgently required, as demonstrated in Section 2.4.3. The primary concern is to be able to deliver flaw length and depth based on MFL signals accurately since these parameters provide pivotal information to make correct decisions to guarantee pipeline integrity.

Several strategies for defect sizing based on MFL signals have been developed in recent years, as discussed in-depth in Section 3.1. In this respect, existing literature can be classified into three main categories according to [12]: first, numerical techniques to establish defect dimensions [16, 54, 58, 59, 84–92, 100] reporting satisfactory results for simple geometries; however they are not applicable for arbitrary shapes. Second, non-numerical techniques to detect and locate defects without defect sizing [72–74]. And third, non-numerical techniques to detect, locate and/or determine the opening length of defects [68, 70, 71]. In addition to these three categories, the authors in [12] claimed to be the single group proposing a technique which detects, locates and determines defect length and depths based on non-numerical methods. However, the techniques which involve defect sizing are limited because they consider only: (i) 2D approaches; (ii) solely simple shapes; or, (iii) in spite of considering 3D models and more complex geometries as in [12], results are only acceptable for patterns which have previously been included as reference during the machine learning step.

This research makes a solid contribution to a well-founded understanding of the relationships between MFL signal features and defect length and depth, see Figure 4.2. A careful study is conducted in 3D to determine the behaviour of the factors which modify MFL signals in relation to the defect dimensions. Advantages of analytical, numerical and experimental approaches are exploited in order to understand, in particular, the relationship between defect depth and the features of MFL signals, which has hitherto been recognised as an unsolved problem [12, 16, 54, 59, 84, 101, 102]. The model proposed here considers for the first time in a publication the location of the defect (see Figure 5.11 for definitions), since acquired MFL signals from inner and outer defects report different behaviour. Features of the research conducted in this thesis are summarised

in Figure 4.2. Importantly, the proposed model as a whole is a novel solution which provides calibration curves to accurately determine the length and depth of a single defect, which has been unfeasible hitherto.

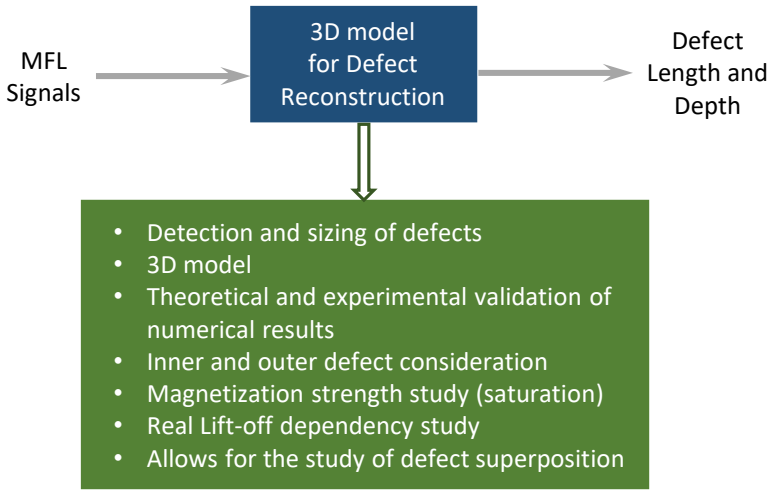

Figure 4.2: *Conceptual overview of the current model development for the reconstruction of 3D defects based on MFL signals.*

In order to solve completely this current problem urged by the carbon steel industry, the current study proposes two stages. Firstly, the development of a model for defect reconstruction based on MFL signals in the case of a single calotte-shaped flaw, which closely represents corrosion defects. Secondly, the study of adjacent defects interaction on resulting MFL signal. This strategy will allow for the division of complex corroded areas into individual calotte-shaped defects permitting their treatment through signal superposition. The first stage corresponds to the main objective of this research, and the second will be solved in future investigation. In this context, a previous assessment on MFL signals obtained from clustered flaws is performed in order to verified signal superposition. The work from Mandache and Clapham [103] can be highlighted in this respect. It develops an analytical model based on the dipolar magnetic charge (DMC)[2] definition accounting for neighbouring circular defects. They showed very good agreement between analytical and experimental results from the radial component of the leaked field caused by adjacent defects.

Specifically, at the beginning of this research, the interaction of neighbouring defects was simulated using 2D and 3D models. Figure 4.3 illustrates the sort of sample used to carry out the corresponding assessment.

[2]DMC defines the generation of opposite magnetic polarities on the walls of, for example, a corrosion pit due to the divergence of the most flux lines around the defect. This effect is caused by the high magnetic reluctance resulting from the flaw presence in a magnetised material [103].

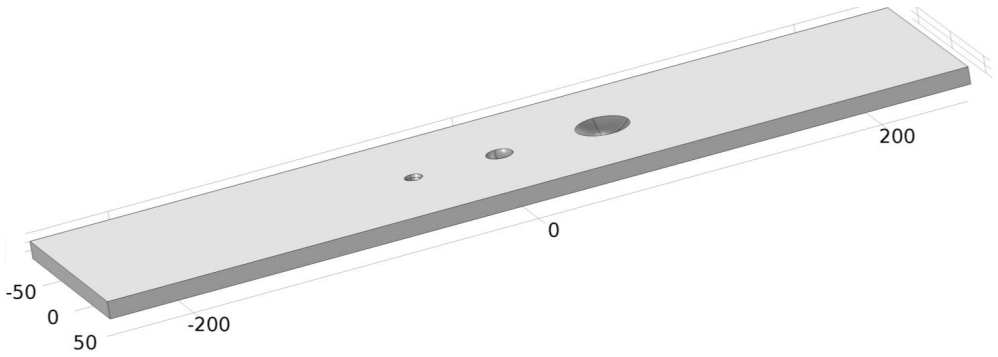

Figure 4.3: *Sample features in mm to conduct signal superposition assessment.*

Results obtained from the simulation are compared with experimental data published from Niese in [1]. Simulated and experimental results agree very well, as can be seen in Figure 4.4. The blue line parallel to the position coordinate in Figure 4.4b reports the absence of a defect and thereby the length of the sample. The signal peaks which appear at the ends of the sample are generated due to the electromagnet poles, where the sample lies.

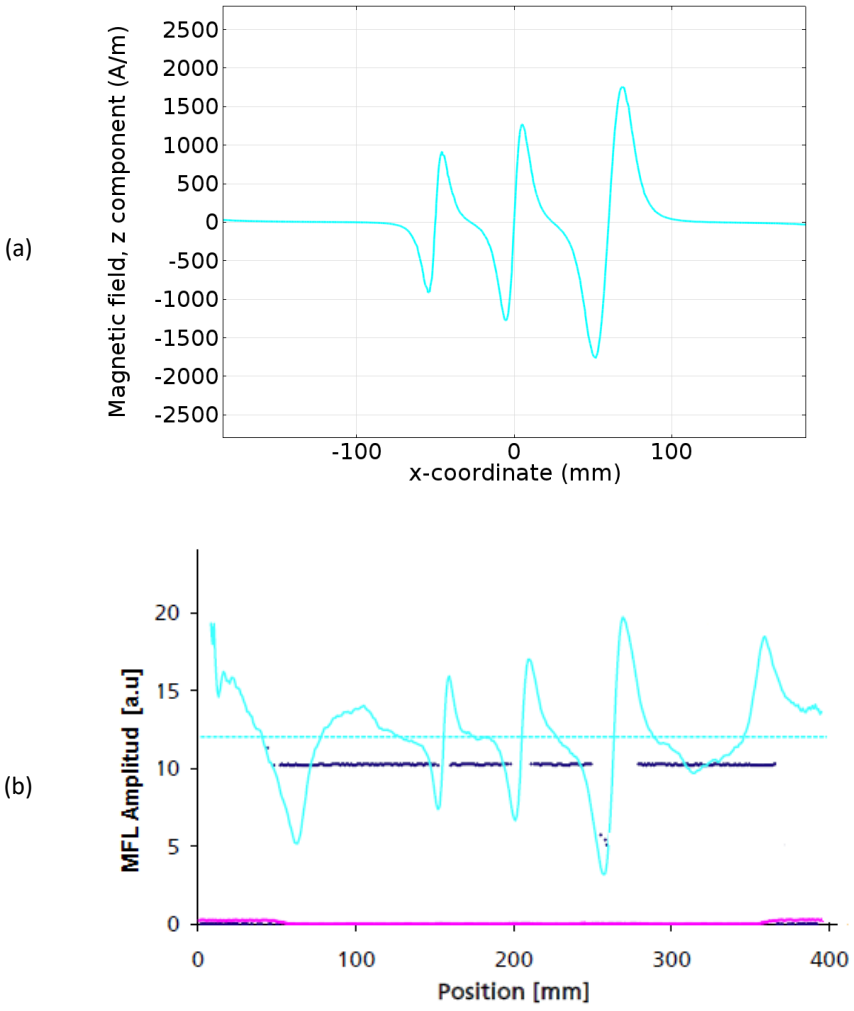

Figure 4.4: *Comparison of superposed MFL signals resulting under: a) Simulation and b) Experiments [1].*

The superposition of MFL signals resulting from single defects moving closer and interacting has been proved. In this respect, a detailed report can be found in Appendix D. Consequently, the consideration of a corroded area as an arrangement of single superimposed defects provides a proper approach in order to reconstruct such defects present in carbon steel structures.

5

Methodology

Currently, there is a need to deepen understanding the magnetic flux leakage signals and magnetic mechanisms in general. Three different research methods have been required to fulfil the objectives of this study due to the physical complexity. These approaches are namely analytical, numerical and experimental analysis. Fundamentals of every method are presented in Section 1, including the corresponding benefits and drawbacks. The results obtained from every method complement the others so that the strengths of each method are exploited. The discussion about the different approaches is addressed in that section, mainly to MFL signal modelling. This review provides the fundamentals but primarily, it sets out the necessity to combine the advantages of every method in order to implement a model for defect reconstruction.

On an overall basis, the methodology in this research starts with a qualitative assessment of MFL signals, and it delves into the defect reconstruction through a quantitative analysis. Every parameter which alters the MFL response is quantitatively assessed. This procedure allows a competent interpretation of the phenomena and the achievement of a robust model for defect sizing. Therefore, dimensions of the defects can be accurately determined based on the information obtained from MFL signals. Along with the chapter, the executed methodology to reach the aim of this research is stepwise described. Besides, it provides necessary fundamentals and modelling requirements for a student or researcher interested in performing further investigation in this subject.

The overview chart in Figure 5.1 summarises the methodology followed in this research. The MFL signal assessment begins with the study of a specific case modelled in 2D. This geometry simplification allows for a complete theoretical and numerical analysis. In this perspective, simulation results are compared with those obtained from theoretical analysis in order to validate the 2D model. After that, the 2D case is further discussed to verify the necessity of 3D simulations since real defects are considered in the main aim of this research. In this respect, a ferromagnetic cylinder surrounded by air is selected as the specimen for the assessment. At first, the cylinder is considered infinitely long for 2D analysis. Afterwards, the cylinder length is limited in order to carry out the numerical study in 3D. The results have proven the need for 3D simulation to perform this research, as illustrated in Figure 5.1.

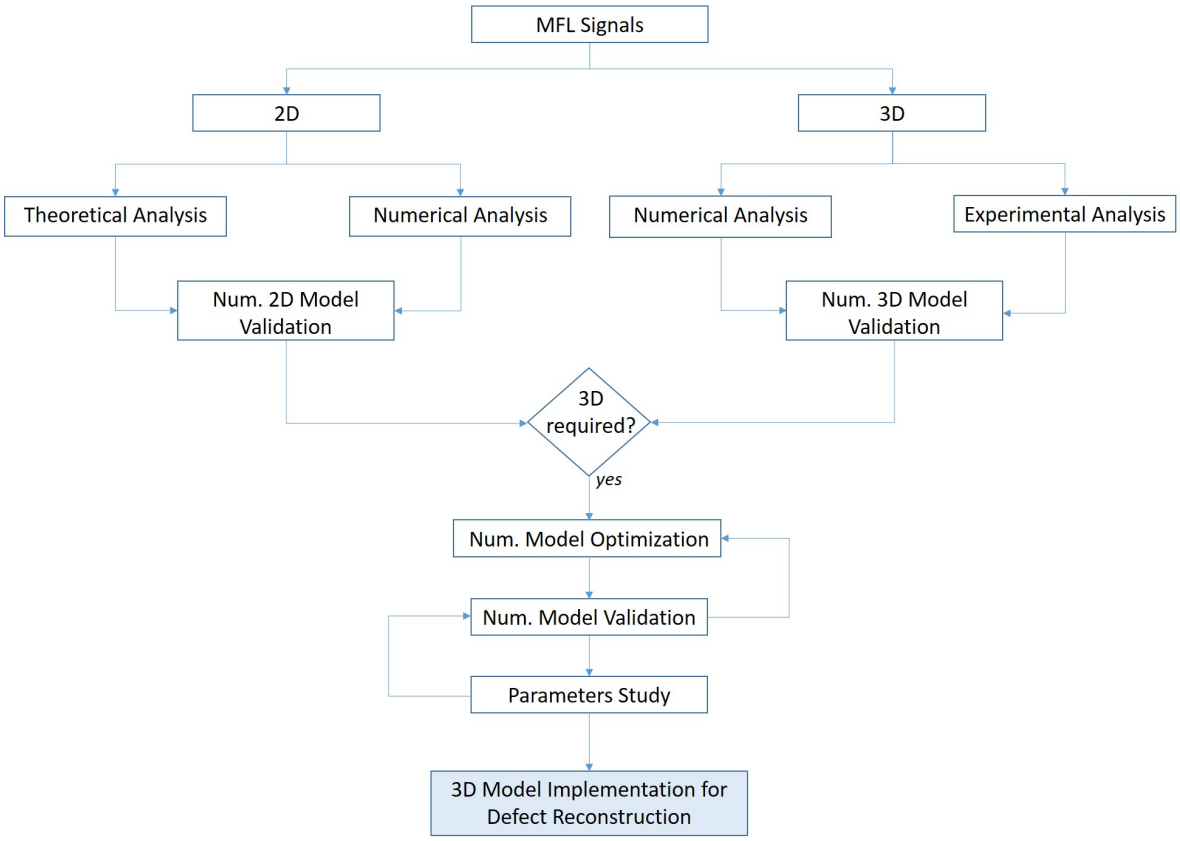

Figure 5.1: *Flow diagram of the applied methodology*

According to the findings, the simulation model is improved to establish a 3D arrangement which permits the acquisition and analysis of MFL signals. In fact, a detailed study of the theoretical approach for MFL modelling is fundamental to conduct this process. Consequently, a strict command of physics and parameter behaviour enables the establishment of a consistent simulation model. From this point forward, the chosen specimen for 3D simulations and experiments will be a plate of steel containing a hole with calotte shape which acts as a typical corrosion flaw. Besides, a similar experimental set-up is arranged to perform different tests. In general, the experimental approach is used in the first instance to optimise and validate the simulation model. Then, a rigorous study is conducted, including all parameters which affect quantitatively and/or qualitatively MFL signals. Such analysis requires an extensive assessment of numerical and experimental results as will be described below. As a result, a robust model for single defect sizing is implemented based on the parameter evaluation. To conclude this study, the proposed model is applied to MFL signals obtained experimentally.

In general, the methodology covered in this chapter is divided into four sections. The first part answers the question, how are the advantages offered by every research approach in the MFL signal study exploited? The second part reports, how are the results presented? The third part includes, how is the model based on the parameter study developed? Furthermore, to close the chapter, the meaning of the term magnetic saturation is discussed. A short description of every section follows,

1. Theoretical, numerical and experimental approaches are prepared and tuned for the MFL study. Specific requirements for each approach method are taken into account in order to fulfil the objectives successfully.

2. The selected coordinate system for the set-up, the assignment of the magnetic field components and the different type of plots reported in Chapter 6 are considered seeking to clarify the reported results.

3. Parameter assessment through a theoretical, numerical and experimental study is presented linking every step with the results in Chapter 6. Identification of the MFL signal characteristics is concretely established distinguishing between inner and outer defects.

4. Magnetic saturation concept, which is often used in publications regarding MFL technique, is deeply discussed making a benefit from the three assessment methods: analytical, numerical and experimental.

5.1 Theoretical Approach

The current theoretical approach illustrates a 2D-problem solved by Maxwell [104], which considers a paramagnetic case assuming the permeability as a constant. It is a useful approach since it allows for the establishment of field equations. To achieve this objective, an infinitely long cylinder is selected as the sample. The field behaviour of the magnetised cylinder is studied in detail in this section through purely theoretical analysis. For that purpose, Maxwell equations are solved assuming a two-dimensional approach. Distribution of the magnetic field inside and outside the sample is determined to assume a uniform applied field. Equations for the magnetic field, flux density, effective permeability and surface pole density are reported. This example permits the understanding of the magnetic phenomena and serves for later comparison between theoretical and numerical analysis.

Figure 5.2 illustrates the cross-section of the infinite cylinder with radius a and permeability μ_C. It is placed in an air domain under a uniform magnetic field $\mathbf{H}_0$ parallel to the x-coordinate. The distance r defines the separation from the cylinder axis to the observation point.

Assuming a magnetostatic case, from Ampere's law applies that,

$$\nabla \times \mathbf{H} = 0$$

Since $\mathbf{H}$ is irrotational in the absence of free currents, the general solution is given by

$$\mathbf{H} = -\nabla \Phi \tag{5.1}$$

where Φ is the magnetic scalar potential. According to Gauss's Law for magnetism $\nabla \cdot \mathbf{B} = 0$, the flux lines of $\mathbf{B}$ have neither a beginning nor an ending in the finite space, only in the infinite, or are closed lines, ending is beginning. Considering that inside the

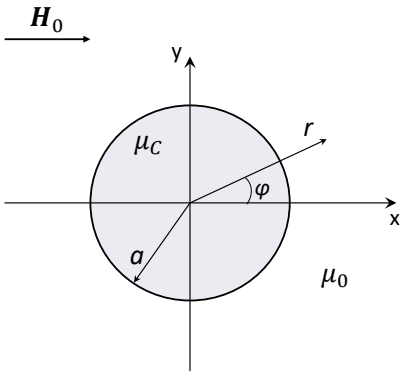

Figure 5.2: *Cross-section of an infinitely long cylinder assuming a uniform magnetic field.*

sample governs $\mathbf{B} = \mu_0(\mathbf{H}+\mathbf{M})$ with $\mathbf{M}$ as the magnetisation field, it can be established that

$$\nabla \cdot \mathbf{H} = -\nabla \cdot \mathbf{M}$$

substituting $\mathbf{H}$ from Equation 5.1 emerges a Poisson's equation, which in this case is given by

$$\nabla^2 \Phi_m = \nabla \cdot \mathbf{M} = -\rho_m$$

where ρ_m is the source for the scalar potential Φ_m and can be designated as an equivalent magnetic charge density. $\rho_m = Q_m/V$ with units $Amp - m/m^3$. Q_m defines the pole strength of a short magnet. Another contributor to Φ_m is ρ_{ms}, the equivalent magnetisation surface charge density. $\rho_{ms} = Q_m/S$ hence expressed in Amp/m [104].

Taking into account that the normal component of $\mathbf{H}$ at the boundary between a ferromagnetic material and air is discontinuous and assuming $\mathbf{n}$ as the unit vector normal to the surface, it can be stated that

$$\mathbf{n} \cdot (\mathbf{H}_{air} - \mathbf{H}_{fer}) = \mathbf{n} \cdot \mathbf{M} = \rho_{ms} \tag{5.2}$$

For the case in Figure 5.2, the total magnetic potential can be calculated as,

$$\Phi = \Phi_0 + \Phi_i \tag{5.3}$$

where Φ_0 is the applied magnetic potential and Φ_i is the induced magnetic potential. According to Figure 5.2, the applied field $\mathbf{H}_0$ and the corresponding potential can then be expressed as,

$$\mathbf{H}_0 = H_0\,\mathbf{a}_x = \frac{B_0}{\mu_0}\,\mathbf{a}_x = -\nabla\,\Phi_0 \tag{5.4}$$
$$\Phi_0 = -H_0\,x = -H_0\,r\,cos\varphi$$

The induced magnetic potential must satisfy Laplace's equation considering that there is no field generation or source of ρ_m in the volume,

$$\nabla^2 \Phi_i = 0$$

expressing it in cylindrical coordinates:

$$\nabla^2\Phi_i = \frac{1}{r}\frac{\partial}{\partial r}\left(r\frac{\partial\Phi_i}{\partial r}\right) + \frac{1}{r^2}\frac{\partial^2\Phi_i}{\partial\varphi^2} + \frac{\partial^2\Phi_i}{\partial z^2} = 0$$

The induced magnetic field is in this case independent of z since the axis of the cylinder coincides with the z-axis. Its structure is uniform along z, and the applied field is independent of the z-coordinate. Hence, applying the method of separation of variables leads to,

$$\Phi_i(r,\varphi) = f(r)\, g(\varphi)$$

Subject to the current conditions, the solutions to these equations are,

$$g = A_1 \sin n\varphi + A_2 \cos n\varphi$$
$$f = B_1 r^n + B_2 r^{-n}$$

and for the induced magnetic potential applies,

$$\Phi_i = fg = \begin{cases} \sum_{n=0}^{\infty} \left(A_n \cos n\varphi + B_n \sin n\varphi\right) r^n, & r \le a \\ \sum_{n=0}^{\infty} \left(C_n \cos n\varphi + D_n \sin n\varphi\right) r^{-n}, & r \ge a \end{cases}$$

Due to orthogonality, the coefficients A_n, B_n, C_n, D_n, except for A_1 and C_1, all become zero, then

$$\Phi_i = \begin{cases} A_1 r \cos\varphi, & r \le a \\ C_1 r^{-1} \cos\varphi, & r \ge a \end{cases}$$

It results that the induced potential will have the same φ dependence as the applied potential. Then, from Equation 5.1 the induced magnetic intensity $\mathbf{H}_i$ can be deduced as,

$$\mathbf{H}_i = \begin{cases} -A_1 \left(\cos\varphi\, \mathbf{a}_r - \sin\varphi\, \mathbf{a}_\varphi\right), & r \le a \\ \frac{C_1}{r^2} \left(\cos\varphi\, \mathbf{a}_r + \sin\varphi\, \mathbf{a}_\varphi\right), & r \ge a \end{cases} \tag{5.5}$$

The total potential Φ from Equation 5.3 must be continuous at $r = a$. Hence, appropriate boundary conditions can be applied. Thus, the total radial component of $\mathbf{B}$ and the total tangential component of $\mathbf{H}$ must be continuous at $r = a$. Then,

$$\mu_c\, \mathbf{a}_r \left(\mathbf{H}_0 + \mathbf{H}_{i\,r<a}\right) = \mu_0\, \mathbf{a}_r \left(\mathbf{H}_0 + \mathbf{H}_{i\,r>a}\right), \qquad r = a$$
$$\mathbf{a}_\varphi \left(\mathbf{H}_0 + \mathbf{H}_{i\,r<a}\right) = \mathbf{a}_\varphi \left(\mathbf{H}_0 + \mathbf{H}_{i\,r>a}\right), \qquad r = a$$

Consequently, A_1 and C_1 can be found solving the boundary equations. In addition, considering the relative permeability of the cylinder material $\mu = \frac{\mu_c}{\mu_0}$, these coefficients become,

$$A_1 = \frac{\mu - 1}{\mu + 1} H_0 \qquad C_1 = \frac{\mu - 1}{\mu + 1} a^2 H_0$$

Provided that the total magnetic field inside and outside of the cylinder consists of the sum of applied and induced fields, related equations can be established considering

expressions in cartesian coordinates of Equations 5.4 and 5.5. It delivers for $r < a$ and $r > a$ respectively,

$$\mathbf{H} = H_0\,\mathbf{a}_x - \frac{\mu-1}{\mu+1}\,H_0\,\mathbf{a}_x\,, \qquad r < a \tag{5.6a}$$

$$\mathbf{H} = H_0\,\mathbf{a}_x + \frac{\mu-1}{\mu+1}\,H_0\,\frac{a^2}{r^2}\,(cos\,2\varphi\,\mathbf{a}_x + sin\,2\varphi\,\mathbf{a}_y)\,, \qquad r \geq a \tag{5.6b}$$

Equations 5.6a and 5.6b are given in rectangular coordinates. The first term corresponds to the applied field $\mathbf{H}_0$ and the second term establishes the induced field $\mathbf{H}_i$. The induced field inside the cylinder ($r < a$) is uniform and acts opposite to the applied field. This field depends in general on different parameters, namely the applied field, the relative permeability, and the geometry of the specimen. The resulting field for $r > a$ as in Equation 5.6b depends on φ, the cylinder radius and the observation distance r, besides on the applied field, the relative permeability, and the geometry of the specimen. In fact, as the induced field component is inversely proportional to the square of the observation distance, it then vanishes in the far field, with $\mathbf{H}_0$ only remaining.

The calculation of the demagnetising field for the cylinder case in 2D is discussed next. This analysis allows for an extensive understanding of the magnetic behaviour inside the cylinder. The induced field for $r < a$ is hereinafter named as $\mathbf{H}_c$. Considering the relative permeability of the cylinder material μ can thus be expressed from Equation 5.6a as,

$$\mathbf{H}_c = \frac{2}{\mu+1}\,H_0\,\mathbf{a}_x \tag{5.7}$$

Considering that inside the cylinder is satisfied relation

$$\mathbf{B} = \mu\,\mu_0\,\mathbf{H} \tag{5.8}$$

it results that,

$$\mathbf{B}_c = \frac{2\,\mu\,\mu_0}{\mu+1}\,H_0\,\mathbf{a}_x \tag{5.9}$$

$\mathbf{M}_c$ can then be achieved from the relation $\mathbf{B} = \mu_0(\mathbf{H} + \mathbf{M})$ including the expressions above for $\mathbf{H}_c$ and $\mathbf{B}_c$ as,

$$\mathbf{M}_c = 2\left(\frac{\mu-1}{\mu+1}\right)\,H_0\,\mathbf{a}_x \tag{5.10}$$

Relating Equations 5.6a and5.10 allows $\mathbf{H}_c$ to be expressed as,

$$\mathbf{H}_c = \mathbf{H}_0 - \frac{\mathbf{M}_c}{2}$$

For the general case, the true field acting in the specimen can be found from the relation

$$\mathbf{H} \;=\; \mathbf{H}_0 - N_D\,\mathbf{M} \tag{5.11}$$

where N_D is 1/2 for an infinitely long cylinder. In general, N_D is called the demagnetisation factor. It depends primarily on the shape of the specimen as well as its permeability,

susceptibility, applied field and direction of magnetisation. A field equal to $N_D\mathbf{M}$ is induced inside the magnetised material, which opposes to the applied field. This field is called the demagnetisation field, $\mathbf{H}_D$,

$$\mathbf{H}_D = N_D\,\mathbf{M} \tag{5.12}$$

From Equation 5.11 the magnetic field for a general case can be expressed as,

$$\mathbf{H} = \frac{\mathbf{H}_0}{1 + N_D\,(\mu - 1)}$$

and hence

$$\mathbf{B} = \frac{\mu\,\mu_0\,\mathbf{H}_0}{1 + N_D\,(\mu - 1)}$$

The relation between magnetic flux density in the sample and applied field provides the effective permeability, μ_{eff}, which will be higher as long as $\mathbf{N}_D$ becomes smaller:

$$\mu_{eff} = \frac{\mu\,\mu_0}{1 + N_D\,(\mu - 1)} \tag{5.13}$$

Particularly for the cylinder case considered above, the magnetic pole density generated at the surface can be calculated from Equation 5.2 as,

$$\rho_{ms} = M\,\cos\varphi \tag{5.14}$$

Although $\mathbf{M}$ is uniform at every point inside the specimen due to the circular shape of the sample, the surface poles appear according to Equation 5.14.

The case discussed in this section sets out the high dependency of the magnetic field behaviour inside of the magnetised cylinder as well as around it on the applied field and permeability. A thorough consideration of their effects on the MFL technique application is included in the next section.

5.2 Numerical Approach

The cylinder case studied in the last section is the next numerical case assessed taking advantage of the finite element method. Simulations were carried out first as a 2D model. This model is validated by utilising the theoretical results already discussed. In order to verify the requirement of a 3D simulation to fulfil the objectives of this research, the cylinder case is then implemented in 3D. In this context, a suitable model for the MFL signal study thereby the complexity of the current arrangement needs to be increased. As domain dimensions and mesh size became more demanding due to the complexity, a convergence study was required. Convergence results are reported at the end of this section.

As already mentioned in Section 3.1.3 the numerical analysis in this work will be performed using COMSOL Multiphysics. The model definition and the finite element analysis are conducted taking advantage of COMSOL attributes (refer to Section 3.1.3.2).

One of the facilities offered by COMSOL is the possibility to create customised materials. In this study, the BH curve of the selected steel is experimentally obtained and implemented as a customized material for simulations. Additionally, a study to define a suitable strength field to be applied is also conducted carefully. Both issues, the BH curve behaviour and the advisable magnetisation strength, are discussed in this section before continuing with the simulation methodology, considering that these aspects are relevant variables in the MFL technique.

5.2.1 Model Definition

A structural steel identified as S235JR complying with European Standard EN 10025[1] was chosen as the ferromagnetic material to perform experiments and simulations along with this research. Figure 5.3 shows the set-up used to characterise the magnetic behaviour of the selected material accurately. A piece of the steel sample was extracted and rounded to get a cylindrical shape which joins correctly into the electromagnet poles. A sinusoidal signal was used to excite the electromagnet with a fixed frequency of 0.1 Hz and voltages from 0.1 Vpp to 1.9 Vpp in increments of 0.1 Vpp. A cylindrical coil is located around the sample as a magnetic field sensor. The signal from the coil is conducted to an integrator, which delivers the voltage to calculate the magnetic flux density. These measurements were plotted as hysteresis loops, as can be observed in Figure 6.1. Additionally, the resultant virginal curve obtained experimentally can be appreciated in Figure 6.2.

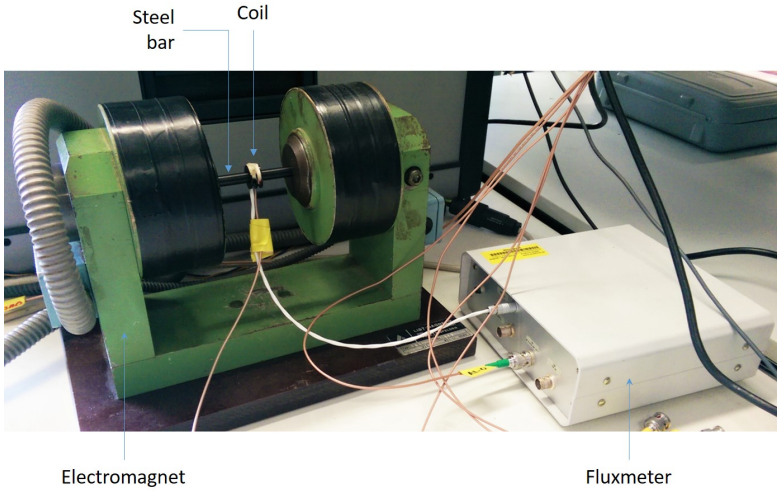

Figure 5.3: *Set-up for hysteresis measurements of the selected steel.*

Another relevant parameter in MFL inspection technique is the magnetisation strength. An appropriate magnetic field should be applied to the specimen in order to obtain suitable signals as a response. In fact, only some hundreds of amperes per meter are necessary as excitation to get field leakage in case of anomalies. However, more than

[1]EN 10025 refers to the set of standards which specifies the technical delivery conditions for hot rolled products of structural steels.

16 kA/m are recommended for pipeline inspection as will be discussed below. Figure 5.4 reports on a comparison of virginal curves and permeabilities from widely used weldable steels published in the handbook on the magnetic examination of welds [105]. The maximum permeability of a ferromagnet occurs at a relatively low level of magnetisation as can be observed in Figure 5.4b. These materials reach their maximum permeability at fields lower than 2 kA/m. Furthermore, the deviation of the virginal curve and permeability from one material respect to the others decreases as the magnetisation strength increases.

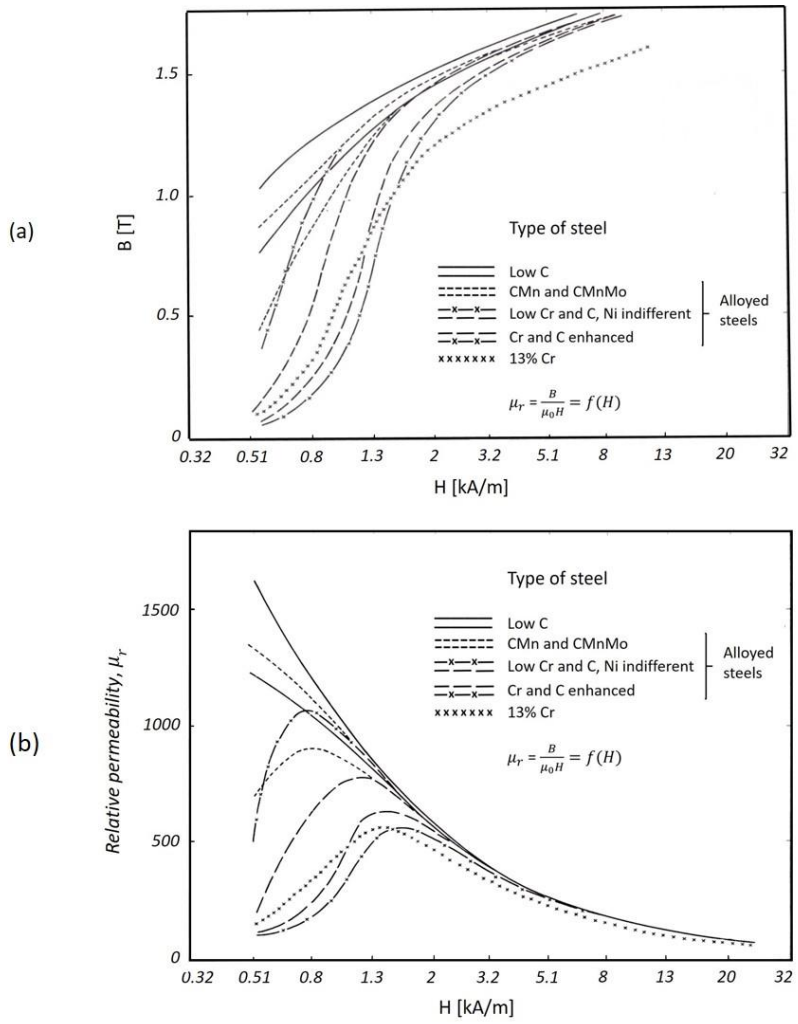

Figure 5.4: *Weldable steels, a) Virginal curves and b) relative permeabilities [105].*

The features on Figure 5.4 report a significant advantage by the MFL implementation because the assessment can be conducted independently on specific magnetic properties of the inspected material, provided that a relatively high magnetisation is applied. Additionally, there are two more advantages to raise the applied field for MFL testing: first, to achieve an advisable SNR in MFL signals, especially in applications under elevated noise. The second reason is to attenuate the influence of the mechanical conditions intrinsic to the material on its magnetic behaviour. Despite that, careful design is unavoidable considering that a higher magnetisation also entails drawbacks such as higher investment in the structure, namely additional costs but especially broader

space in the arrangement. The International Institute of Welding emphasises from the results achieved in Figure 5.4 that the behaviour of the analysed steels converges for $\mathbf{H} > 3\,\mathrm{kA/m}$. These results are notable for MFL application in pipeline inspection. Hence pipelines can be made from different types of weldable steels, and a preliminary material characterisation by an inspection process is not viable.

Besides the dependence of the magnetic properties on the applied field, it is well known that material stresses and strains also have a significant effect. As a consequence, the presence of mechanical deformations on the material affects the MFL signal response strongly if weak magnetisation is used in the inspection. Crouch and co-workers [106] published results from different sets of experiments involving defective pipelines. The authors found that tensile and compressive stresses have different effects on MFL signals. Indeed, tensile effects had the opposite slope when compared to the compressive ones as $\mathbf{H}$ increases. They concluded that applying a magnetic field beyond 16 kA/m delivers an MFL response independent of pipe-wall stress. Changes in the BH curve of the test material depending on its mechanical conditions was verified in this research. The BH curve and the permeability of the selected steel were measured under two different conditions, initially, for the specimen containing residual stresses and subsequently, after the conduction of a thermal treatment[2] which eliminates the presence of mechanical deformations in the material. Related BH and permeability curves are reported in Figure 6.4 for both conditions.

Further experiments were conducted with the purpose to recognise the effect of mechanical deformations on MFL signals under different magnetisation strengths. The chosen sample consists of a steel plate which has a length of 60 cm, a width of 25 cm, and a height of 1.2 cm. A superficial bored defect is located symmetrically in the middle of the plate (x-y plane). The defect has a cylindrical shape with 10 mm of diameter and 20% wall-thickness reduction. Scans of the plate surface (x-y plane) were carried out at a lift-off of 3.5 mm using a Hall sensor. Four different applied field strengths are selected to assess the axial component using the so-called C-scans[3]. The sharpness to identify the defect based on the signal increases significantly as the applied field increases, which can be observed undoubtedly in Figure 6.5. A more in-depth discussion on the MFL signal assessment is presented later in Section 5.5. The intention here is only to give an illustrative example to clearly show the effect of material stresses on MFL signal behaviour depending on magnetisation strength.

5.2.2 Finite Element Method

It can be stated in general, that simulation is a process which requires several steps. That means a simulation model needs to be modified repeatedly to get satisfactory results. It is fundamental starting with the simplest approach, which describes the physical behaviour

[2] In the thermal treatment, the sample is heated uniformly above its Curie point and then slowly cooled it in the absence of a magnetic field.

[3] A C-scan is a two-dimensional image which displays test sample features. Image colours in it represent the signal amplitude at each point of the specimen mapped regarding the position. The plane of the image is parallel to the sensor scan pattern.

correctly according to the specific problem requirements. Once the properties have been evaluated, the model has to be optimised, considering a compromise between model complexity and real behaviour. This objective is achieved through a solid background in the physical laws which govern the MFL application and their related parameters. In this section, two simulation models employed during this research will be presented. The first model consists of a ferromagnetic cylinder located in an air volume as the simplest approach to magnetic behaviour. Related results serve for comparison with the theoretical analysis discussed in Section 5.1. The second model comprises a plate housing a defect and surrounded by air, which allows the assessment of MFL signals behaviour in case of flawed ferromagnetic specimens. Simulation results obtained from the plate model are verified experimentally. The *magnetic fields, no currents* interface included in the AC/DC COMSOL module is selected in order to fulfil numerical aims. A stationary study type is assumed.

Indeed, there are several factors which can affect the model validity. The study of factors such as sample size, size of the sample surroundings, boundary effects, magnetising source, mesh size, among others have been fundamental in this research. All of these elements are further reviewed, including a results convergence study for the critical parameters.

5.2.3 Cylinder Model

Modelling and simulation of the cylinder case in Section 5.1 were conducted. In this context, a customised material was implemented in COMSOL according to the discussion in Section 5.2.1 utilising the empirical results of the BH curve from the selected material. The model was simulated in two and three-dimensional spaces, assuming a proper magnetic strength. A comparison of the simulation outcomes obtained by means of different space dimensions is presented in this section. In addition, analytical outcomes are also introduced in the discussion emphasising their features. Symmetries are not considered in this case, taking into account that this is a simplified model, and it can be solved in a matter of seconds.

The geometry for the 2D model consists of a circle of radius 1 cm, centred in a square with a side length of 80 cm. While in the 3D model is considered a cylinder with a radius of 1 cm and variable length. The cylinder length is simulated from 0.1 cm until 40 cm. It is placed in the centre of an air block with a length 60 times larger than the cylinder length. After the geometry is ready, the assignation of materials is necessary. The customised steel is assigned to the circle in the 2D case and the cylinder in the 3D case. While air is used for the square and the block domains, respectively. A homogeneous field is applied to the external boundaries of the air region (2D model) and air volume (3D model). According to the magnetisation strength discussion in Section 5.2.1, a magnetic field $\mathbf{H}_0$ of 20 kA/m is selected. $\mathbf{H}_0$ is applied perpendicular to the cylinder axis, as shown in Figure 5.2. The resulting magnetic field inside the cylinder distributes uniformly due to the spherical form of its cross-section, as will be demonstrated in Figure 6.6. Taking advantage of the results obtained from the theoretical analysis in Section 5.1, the cylinder

model for simulation is validated. Comparing the simulation and the analytical results became evident that 3D simulation is required to accomplish the objectives of this work, which will be discussed in Section 6.3.

5.2.4 Flawed Plate Model

A flawed plate is selected as sample provided that the primary goal of the current work is defect identification in the assessment of ferromagnetic sheets, tank floors and pipelines deteriorated by corrosion. A flawed plate meets the requirements to analyse the behaviour of MFL signals related to the presence of defects due to corrosion. Specifically concerning pipelines, it should be pointed out that those considered here have a diameter far larger than their pipeline wall thickness. This condition allows the estimation of a pipeline as a thick flat sheet for MFL signal study. Regarding the defect type for conducting MFL response analysis, a calotte shape is chosen since it approximates the corrosion problematic. However, some cases are also assessed with cylindrical defect shape. In all cases, the flaw is located symmetrically in the middle and opens at the surface of one of the plate biggest face as can be appreciated in Figure 5.5.

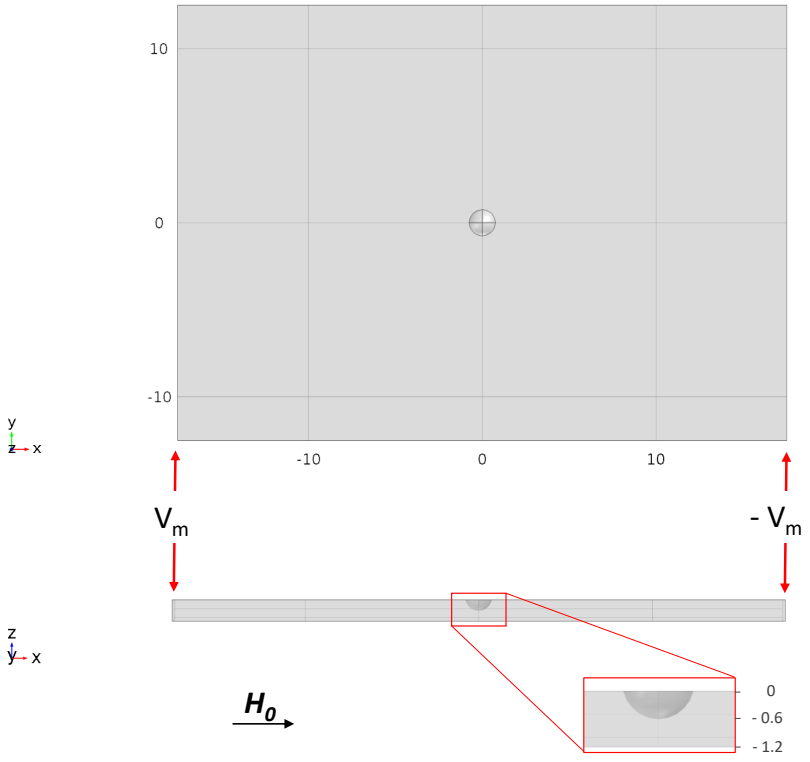

Figure 5.5: *xy and xz plane views of the flawed plate simulation model. Here, the calotte-flaw has a diameter of 1 cm and 50% of plate thickness reduction. All sample dimensions are expressed in centimetres.*

Initially, a steel plate 300 cm long, 150 cm wide and 1.2 cm high is assumed as a sample. The defect diameter is limited to 1.2 cm, 1.6 cm and 2.4 cm, while the defect

depth is defined as 30%, 50%, 70%, 90% of plate thickness reduction. The simulation model is optimised based on the results and the conducted analysis. Consequently, the plate becomes shorter with dimensions of 60 cm long and 25 cm wide, keeping the same thickness of 1.2 cm. However, the sample is simulated according to the experimental set-up with dimensions $35 \times 25 \times 1.2\,\mathrm{cm}^3$ which corresponds to the magnetised sample-section limited by the poles of the electromagnet. Defect diameters are further set to 5 mm, 10 mm and 15 mm and depths of 20%, 35%, 50%, 65%, 80% and 90% of wall thickness reduction. The length and width of the sample are defined broadly enough to avoid boundary effects on the field behaviour around the flaw. A detailed explanation of the procedures carried out is provided below in Section 5.5.

5.2.4.1 Plate Magnetisation

By the cylinder model previously, a constant magnetic field is applied to the air region boundaries to guarantee a homogeneous behaviour for sample magnetisation. However, the establishment of a homogeneous field parallel to the x-axis around the sample will cause on the flawed plate model the emergence of enormous magnetic poles at the plate ends ($x = -17.5$ and $x = 17.5$). These poles will strongly affect the plate magnetisation and lastly, the behaviour of the MFL signals. Hence, the magnetisation of the plate is achieved using a magnetic scalar potential V_m instead of an external field. This potential difference is applied to the plate ends, and it distributes along with the sample, as seen in Figure 5.6.

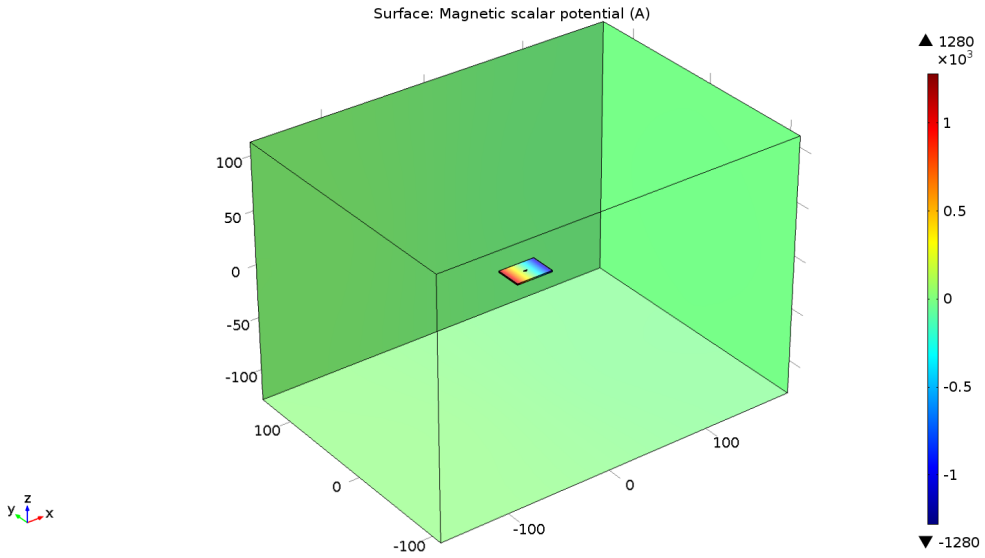

Figure 5.6: *Magnetic scalar potential at the steel plate to obtain 5.2 kA/m on the axial component of the magnetic field at 1 mm nominal lift-off. An air domain surrounds the sample.*

The plate magnetisation of the simulation model correlates closely with the magnetisation obtained in the experimental set-up as will be discussed later in Section 5.3. Henceforth, H_{x1} is established as a reference field. It expresses the axial component

of the magnetic field at 1 mm nominal lift-off over the plate. The study of the model in this section is addressed to compare numerical results with experimental behaviour (refer to Section 5.3). The resultant magnetic field is set up intentionally parallel to the x-coordinate. The magnitude of H_{x1} is defined according to Figures 5.4 and 6.4 at 5.2 kA/m. This magnetisation strength guarantees a magnetic behaviour independent not only from the weldable steel type but also from the mechanical conditions of the sample.

5.2.4.2 Air Domain Size

The ferromagnetic specimen is built inside a cubic air domain, see Figure 5.6. The effects of the air domain size on the MFL response were studied in order to prevent a wrong estimation. To this aim, the behaviour of the H_x maximum amplitude obtained at 1 mm nominal lift-off in the case of a flawed plate is monitored as the dimensions of the air volume change. For this purpose is selected the calotte defect with a diameter of 10 mm and 50% of wall thickness reduction. It is embedded in the plate as illustrated in Figure 5.5. Length, width and height of the air domain are independently studied. Figure 5.7a shows the results obtained as the air domain length increases, while the width and height are keeping constant at the values recorded in the plot. Likewise, Figures 5.7b and 5.7c reported this tendency as width and height change, respectively. Results are plotted using the same y-axis scale for comparison purposes. Indeed, the MFL signal behaviour is affected as any of the volume dimensions surrounding the plate decreases. As a result, the size of the air domain for the simulation model is defined ten times longer, ten times wider and 200 times higher as the plate dimensions, namely 350 x 250 x 240 cm^3. Changes in H_x leaked field amplitude are not significant for larger values of length, width or height, as shown in Figure 5.7. It can be deduced considering the convergence behaviour, that from these three parameters, the height of the air domain is the most critical concerning the MFL signal study.

5.2.4.3 Convergence depending on Mesh size

On the other hand, the accuracy of numerical results depends critically on the mesh size, as already mentioned in Section 3.1.3.2. Therefore, a convergence study is highly recommended for every simulation model seeking for optimisation. In particular for the current model, H_x maximum amplitude was considered as a tracked parameter while the mesh size decreases. In order to specify a mesh size, COMSOL offers nine different predefined options for the mesh size, from extremely coarse to extremely fine. However, the flawed plate model requires a customised mesh definition due to the difference in dimensions of the flaw compared with the dimensions of the plate and the air domain. For this reason, the mesh size of the flaw is defined much finer as the rest of the model. To this aim, it is taken advantage of the mesh element size settings provided by COMSOL which includes following parameters: maximum element size, minimum element size, maximum element growth rate, curvature factor and resolution of narrow regions. In this case, keeping fixed the first four parameters and modifying only the resolution of

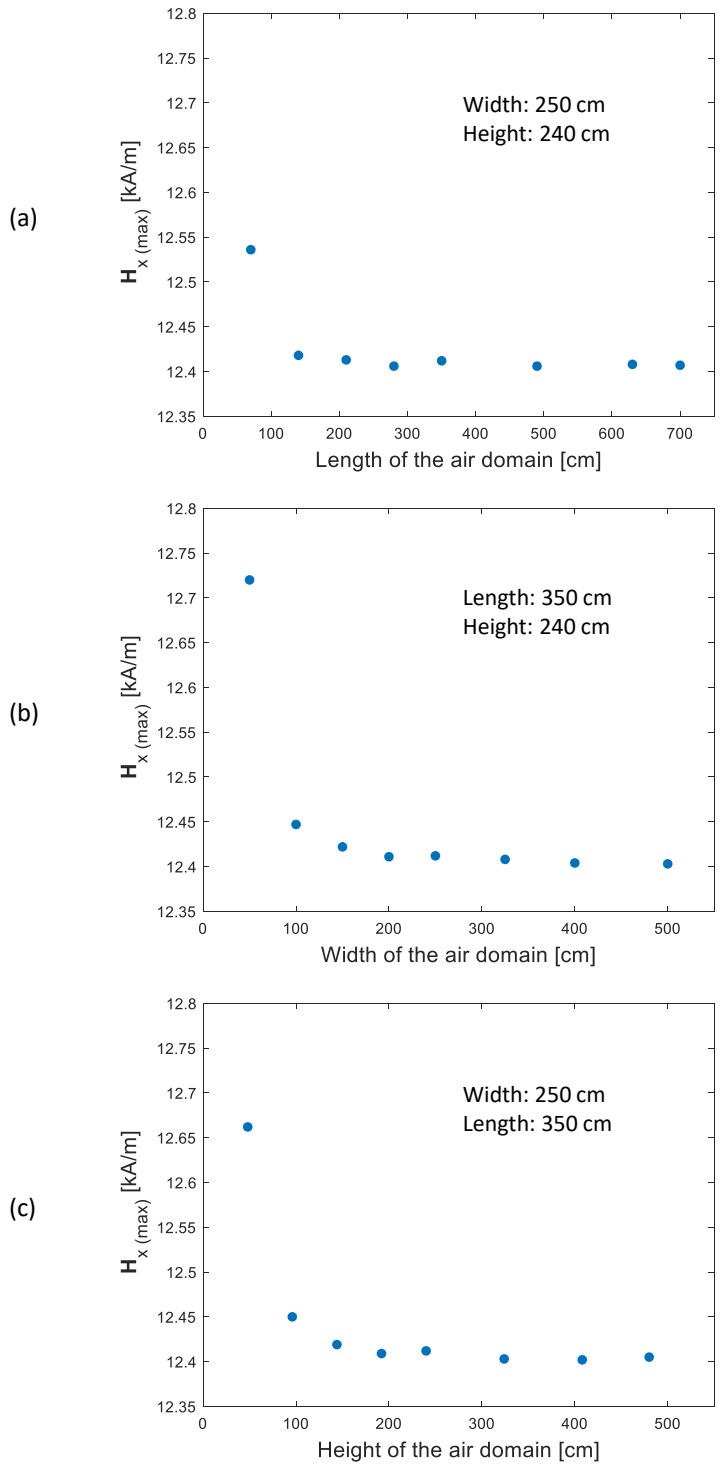

Figure 5.7: *Dependency of the H_{x1} amplitude on the air domain dimensions according to: a) Length; b) Width and c) Height.*

narrow regions has proven to be a key strategy. Figure 5.8 shows the convergence of H_x maximum amplitude as the mesh is refined; in other words, signal convergence as the number of DOFs increases. Based on these results, simulations are run for a mesh configured to get 212.146 DOFs for which the field already converges. Likewise, this strategy is applied for all simulation models.

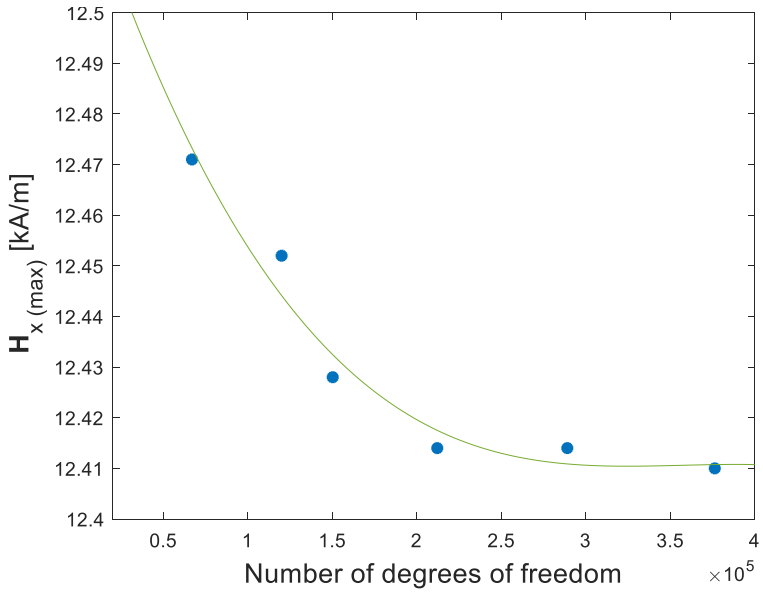

Figure 5.8: *Convergence of H_x maximum amplitude as the mesh size decreases by a simulation model of a flawed plate.*

5.3 Experimental Approach

The advantages of the experimental analysis have been exploited in this study; it provides a valuable contribution where the theoretical and numerical methods are limited. In this context, experiments have been conducted particularly under two purposes. First, to validate the simulation models and second, to verify the accuracy of the proposed model for defect reconstruction. A steel plate is used as the sample in the arrangement shown in Figure 5.9.

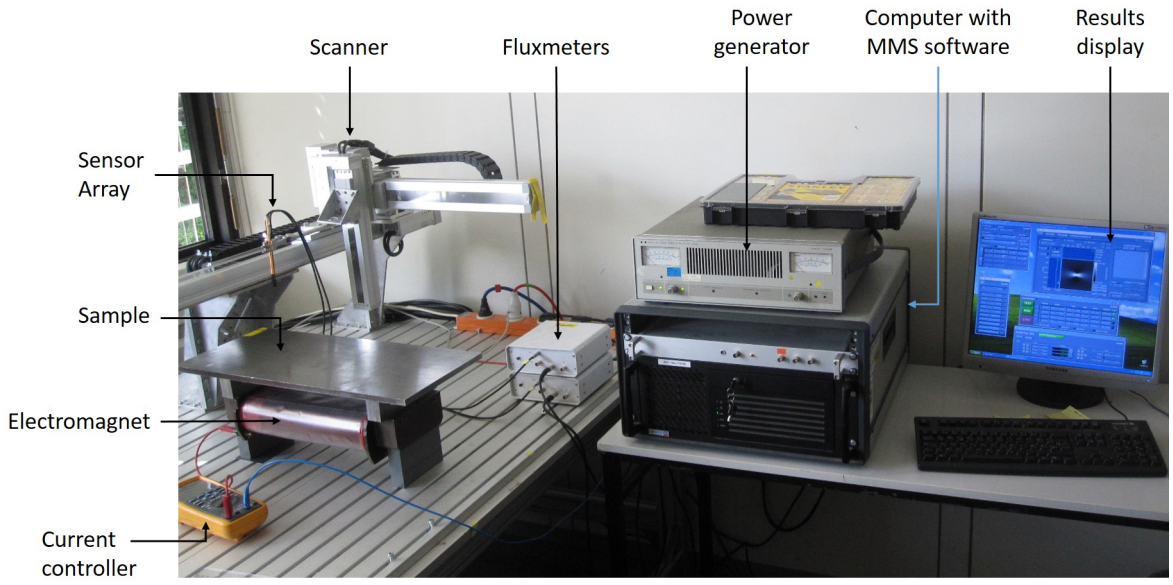

Figure 5.9: *Experimental set-up for magnetic field measurements.*

The sample is magnetised through an electromagnet to obtained the related MFL signals. Single defects are embedded in different ferromagnetic plates. These defects are machined cylindrical or calotte-shaped for specific diameters and depths, as summarised in Table 5.1.

Sample	**Diameter [mm]**	**Thickness Reduction [%]**	**Location**	**Measured H** Comp.
P1	5	20	Inner	H_x / H_z
			Outer	H_x / H_z
	10	20	Inner	H_x / H_z
			Outer	H_x / H_z
	10	50	Inner	H_x / H_z
			Outer	H_x / H_z
	15	90	Inner	H_x / H_z
			Outer	H_x / H_z
P2	5	20	Inner	H_x / H_z
			Outer	H_x / H_z
	5	50	Inner	H_x / H_z
			Outer	H_x / H_z
P3	10	50	Inner	H_x / H_z
			Outer	H_x / H_z
	10	80	Inner	H_x / H_z
			Outer	H_x / H_z

Table 5.1: *Experimental outline. Single defects are embedded in ferromagnetic plates. Features of every defect and signal acquisition are summarised.*

The sensor array consists of two Hall sensors. Every sensor acquires a component of the magnetic field depending on its orientation. One sensor is oriented to measure the axial component H_x; and the second one, the radial component H_z. The Hall sensor array can be appreciated in detail in Figure 5.10. The circumferential component is not considered since its magnitude is significantly lower than the other two.

The Hall array is installed in a three-axis scan guaranteeing accuracy in signal acquisition. The data are obtained employing the modular measurement system (MMS), which is a software package developed by the Fraunhofer Institute for Nondestructive Testing IZFP. It must be stressed that the sample is carefully demagnetised every time its magnetic or mechanical properties are modified. For instance, alterations of the sample magnetic properties can appear as the magnetisation strength decreases while mechanical modifications take place, for example, as the defect is enlarged.

According to the defect location from Table 5.1, there are two feasible categories: inner or outer configuration. This designation obeys to the practice by pipeline inspec-

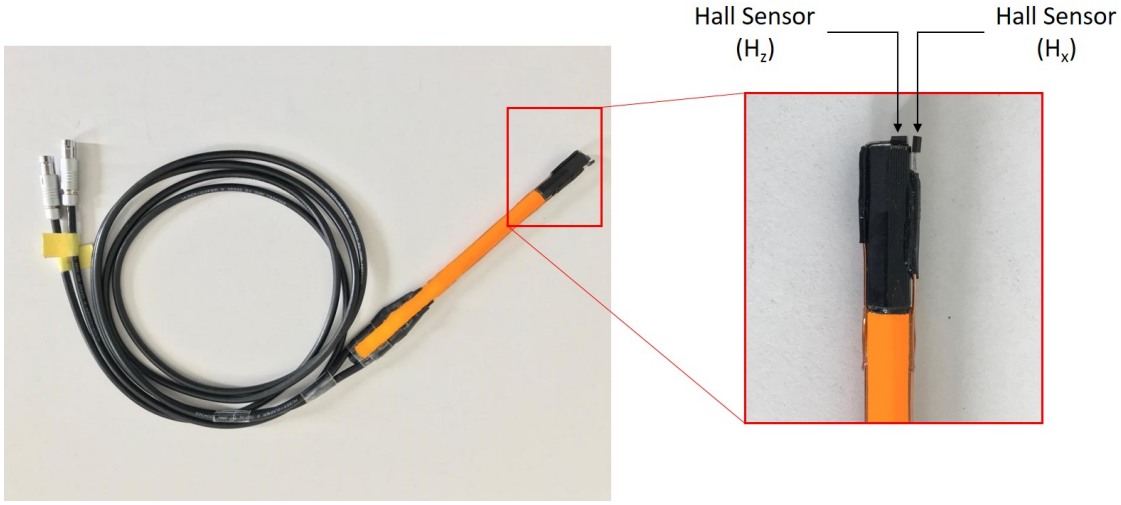

Figure 5.10: *The Hall sensor array to obtained axial and radial components of the magnetic field.*

tions, where a PIG travels inside a pipeline assessing its condition. In this perspective, a defect will be classified as an inner defect if the wall thickness reduction opens to the inner wall of the pipe, namely the scanning side. By contrast, it will be referred to as an outer defect if the wall thickness reduction opens to the outer wall; in other words, on the opposite side under scanning. Such defect classification is illustrated in Figure 5.11.

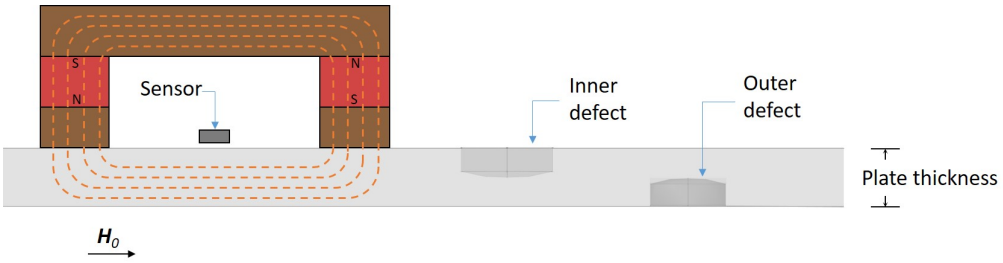

Figure 5.11: *Defect classification according to its location on plate surface respect to the scanning system.*

Nowadays, it is well known that the MFL response from inner defects differs from those resulting from outer defects. However, the differences between both conditions are rarely discussed. In the current research, the MFL signal analysis is performed depending on the location and a detailed discussion is provided independently for inner and outer defects.

The magnetisation strength of the sample is modified taking advantage of the electromagnet, which is excited under different current levels. Therefore an advisable range of data is achieved. Moreover, two different pole shoes are considered for the experimental set-up. Differences in the magnetisation strength due to the pole shoes are especially significant for the lowest applied currents, as summarised in the Table 5.2. The field behaviour at the nominal lift-off is previously established using a flawless sample. Scans are conducted between the electromagnet poles at the nominal lift-off. Results are reported for the case identified as a $H_{x(1mm)} = 5.2\,\mathrm{kA/m}$ in Figure 5.12a. A yellow line is

intentionally drawn on the plot to show the behaviour of the field where it is assumed to be homogeneous. This field is additionally plotted in Figure 5.12b.

I [A]	0.25	0.5	1	2	3
$\boldsymbol{H_{x(1mm)}}$ **[kA/m]**	0.9/1.35	1.5/1.9	2.7/3	5.2	7.4
Nominal lift-off [mm]	1	1	1	1/2/3/4/5	1

Table 5.2: *Magnetisation strength levels and corresponding lift-off for every experimental case in Table 5.1.*

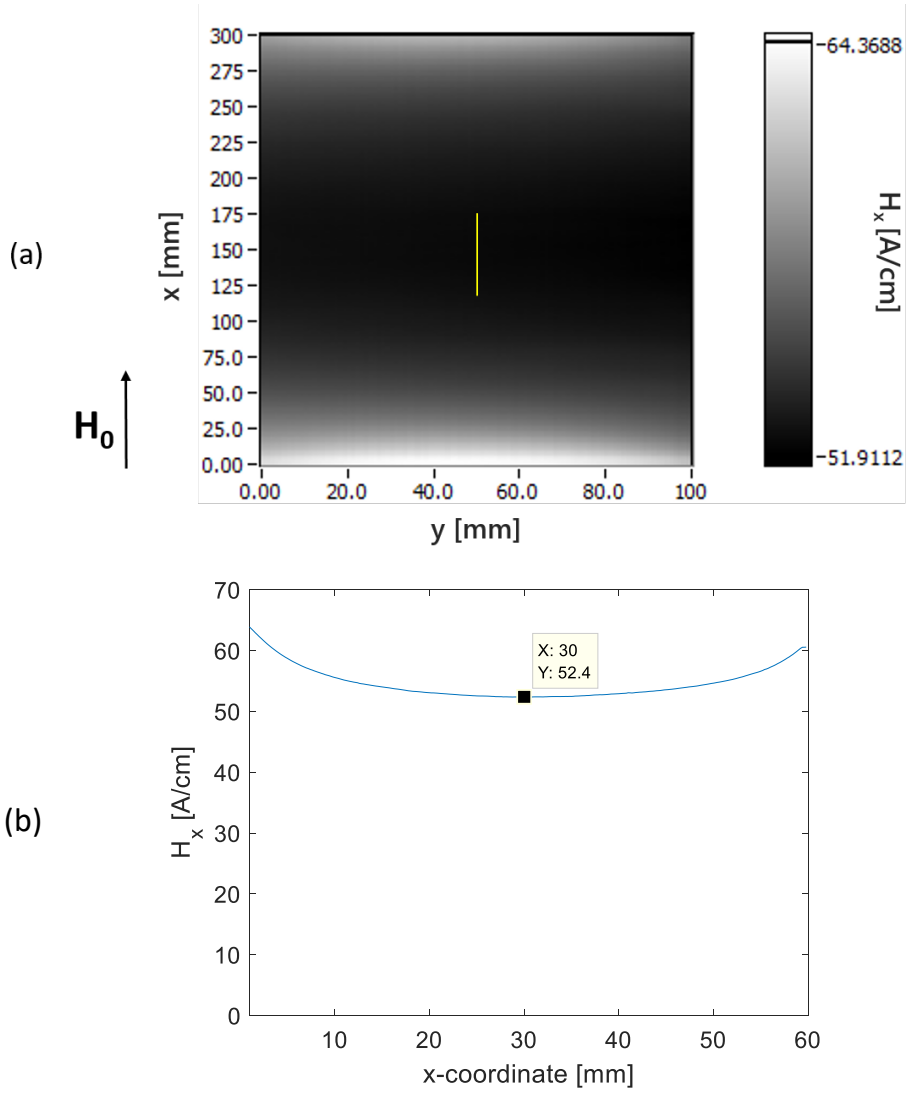

Figure 5.12: *H_x signal at 1 mm of separation between the tip of the sensor array and the plate. a) In the centre, between the poles and b) At the yellow line drawn intentionally in Figure 5.12a.*

Although Table 5.2 reports experimental data obtained at nominal lift-offs of 1 mm in most cases, H_x and H_z are measured at three different lift-off under 5.2 kA/m of

magnetisation in order to afford valuable information about the MFL signal behaviour depending on the lift-off. At first, nominal lift-offs of 1 mm, 2 mm and 3 mm were fixed. Afterwards, nominal lift-offs of 1 mm, 3 mm and 5 mm were set.

5.4 Plot Types

The coordinate system and the type of plots utilised throughout this research are reported in this section seeking to avoid misinterpretation. The coordinate system is defined based on a pipeline application, as shown in Figure 5.13. Therefore, the direction of magnetisation and the magnetic field components are established accordingly. In particular, axial magnetisation, namely parallel to the x-axis, is considered for all cases along with this research. Regarding the **H** components, they are designated here as follows: axial component H_x, circumferential component H_y and radial component H_z. This component assignment is kept henceforth for the study of the MFL signal assessment utilising a flawed plate. Concerning the experimental set-up, the Hall sensor array is oriented to obtain axial and radial component according to Figure 5.10.

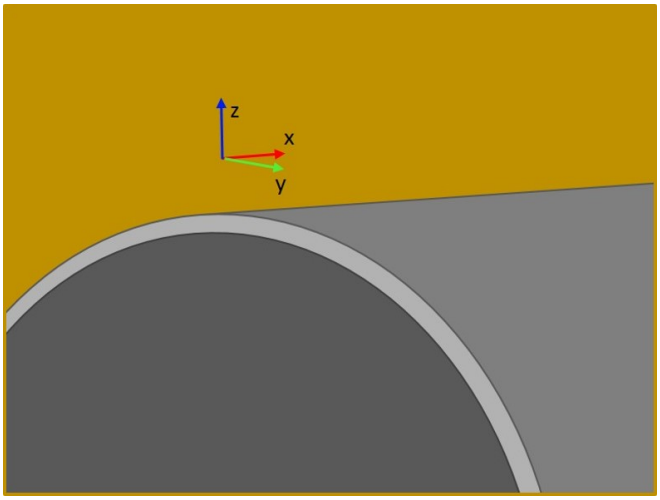

Figure 5.13: *The coordinate system definition for a pipeline under test.*

The post-processing tools provide by COMSOL are exploited in order to carry out the MFL signal assessment. In general, COMSOL allows visualising the simulation results by three kinds of graphs: 3D plots, 2D plots and 1D plots. An overview of the plot types follows, which is based on data obtained from the flawed plate model discussed in Section 5.2.4.

5.4.1 3D Plots

Figures 5.14 and 5.15 illustrate different kinds of 3D plots avoiding the air domain intentionally from the simulation model. Figures 5.14a and 5.14b show the mesh and the resulting magnetic field of a quarter of the magnetised steel plate, respectively. In

particular, a quarter of the defect can be observed at the front corner. In this figure, every plot includes its axis orientation to introduce the coordinate system graphically for the plate case under the assignment in Figure 5.13. The amplitudes are indicated on a coloured scale. Additionally, the maximum value of the plotted parameter is pointed out accompanied by an up arrow, while a down arrow indicates its minimum. Particular attention should be paid to the mesh on the flawed region, which is accurately refined as can be observed in Figure 5.14a.

(a)

(b)

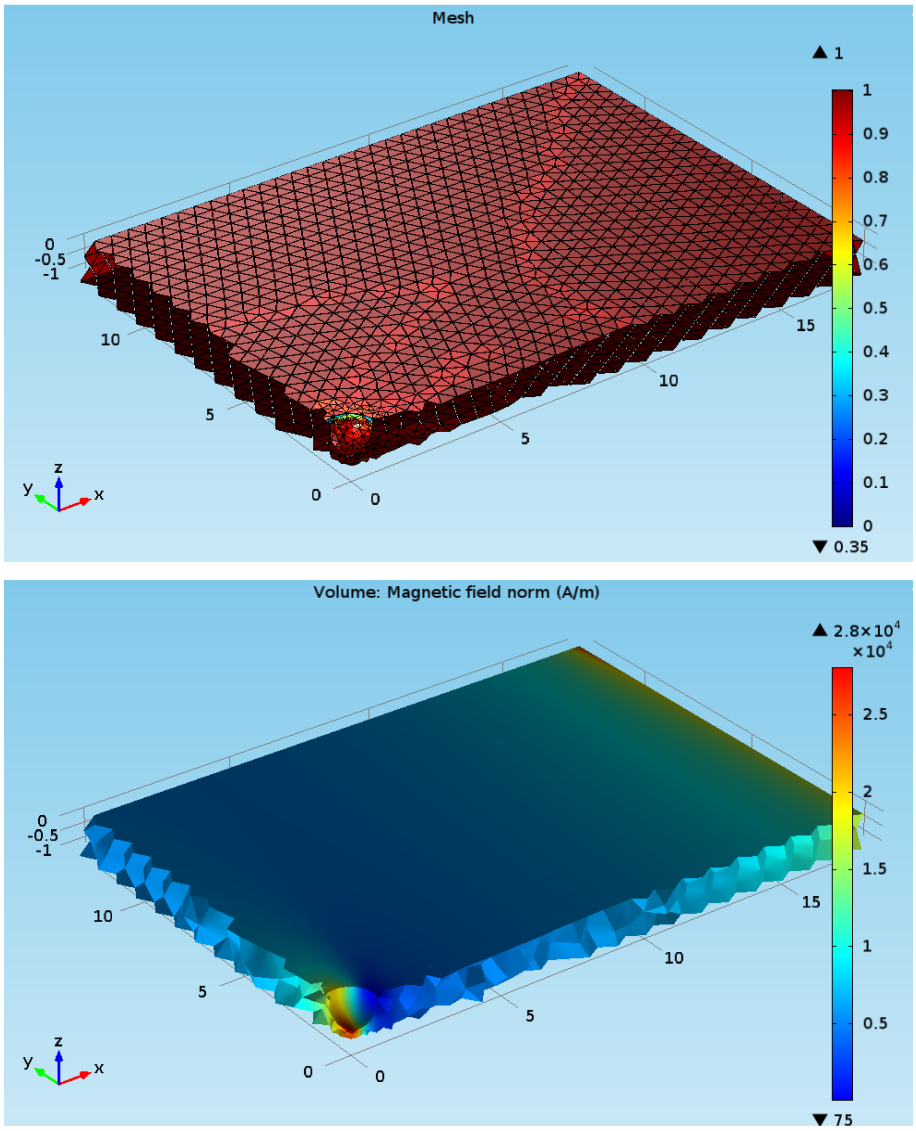

Figure 5.14: *3D plots: a) Mesh of a quarter of the plate. b) Resulting magnetic field.*

The resulting magnetic field on the volume is plotted through a colour range in Figures 5.14b, 5.15a and 5.15b. Besides, the magnetic field behaviour is emphasised using arrows in Figures 5.15a and 5.15b. The arrows in Figure 5.15a illustrate the field behaviour on an xz-plane at $y = 0$. Furthermore, Figure 5.15b considers also the field distribution inside the sample taking advantage of a transparent view. Specifically, the length and colour of the arrows indicate the magnetic field behaviour in every region.

As illustrated in Figure 5.15b, arrows are denser on the steel region under the defect tip emphasizing the highest field, and getting weaker as moves away from it.

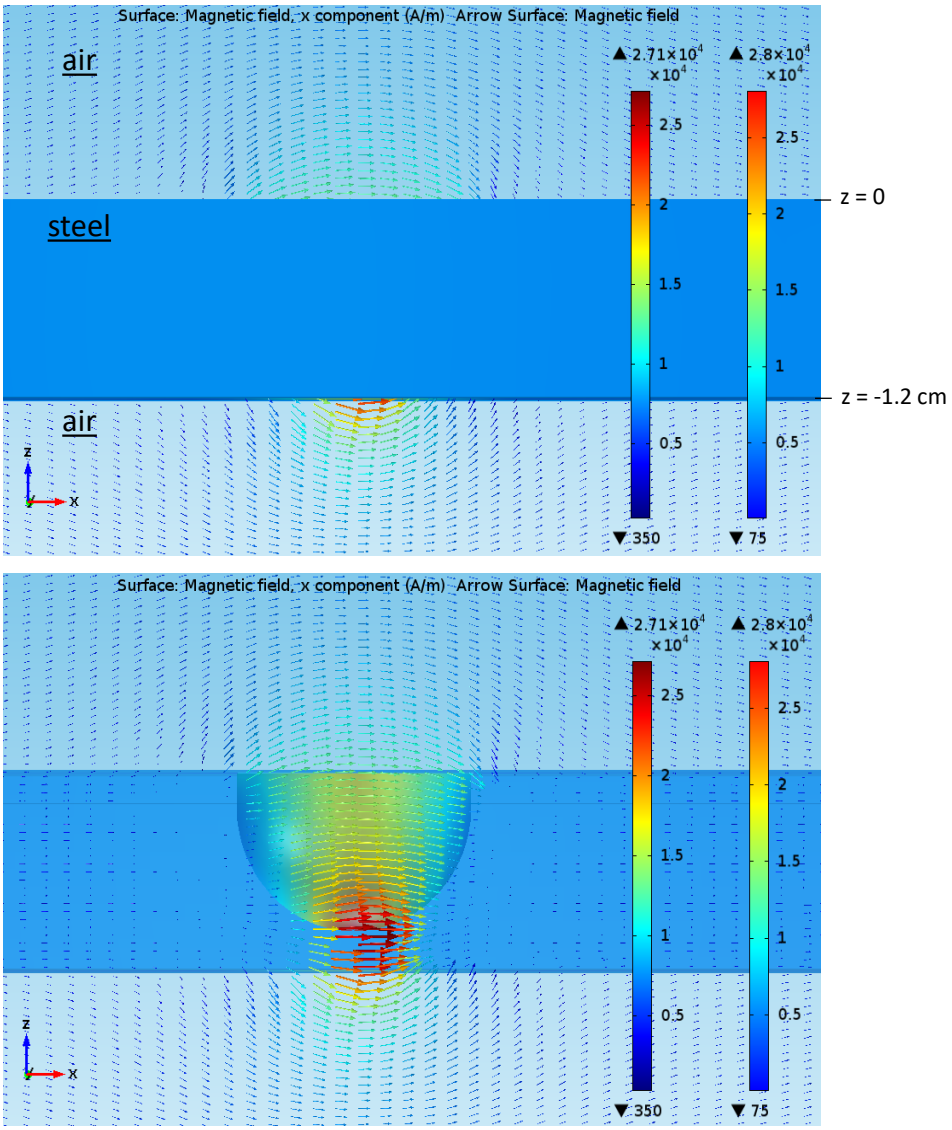

Figure 5.15: *3D plots: a) Magnetic field on the sample surface, and represented by arrows at y=0 focused on the defect region. The defect has 15 mm in diameter and 80% wall thickness reduction. b) Transparent view of Figure 5.15a.*

5.4.2 2D Plots

The so-called C-scans allow plotting the amplitude of the magnetic flux components as a top-view onto the scan area. In COMSOL, such a 2D plot is obtained by slicing a 3D plot in a specific plane to get a cross-section graph. A colour gradient will then report

the parameter of interest. Figure 5.16a presents the axial component of the magnetic field H_x as a C-scan at 1 mm separation of the plate surface, namely at $z = 0.1$ cm, refer to Figure 5.5 for the coordinate system where the sample is located. In addition, a line at $y = 0$ is intentionally introduced in the plot to have a reference for subsequent 1D plots generation.

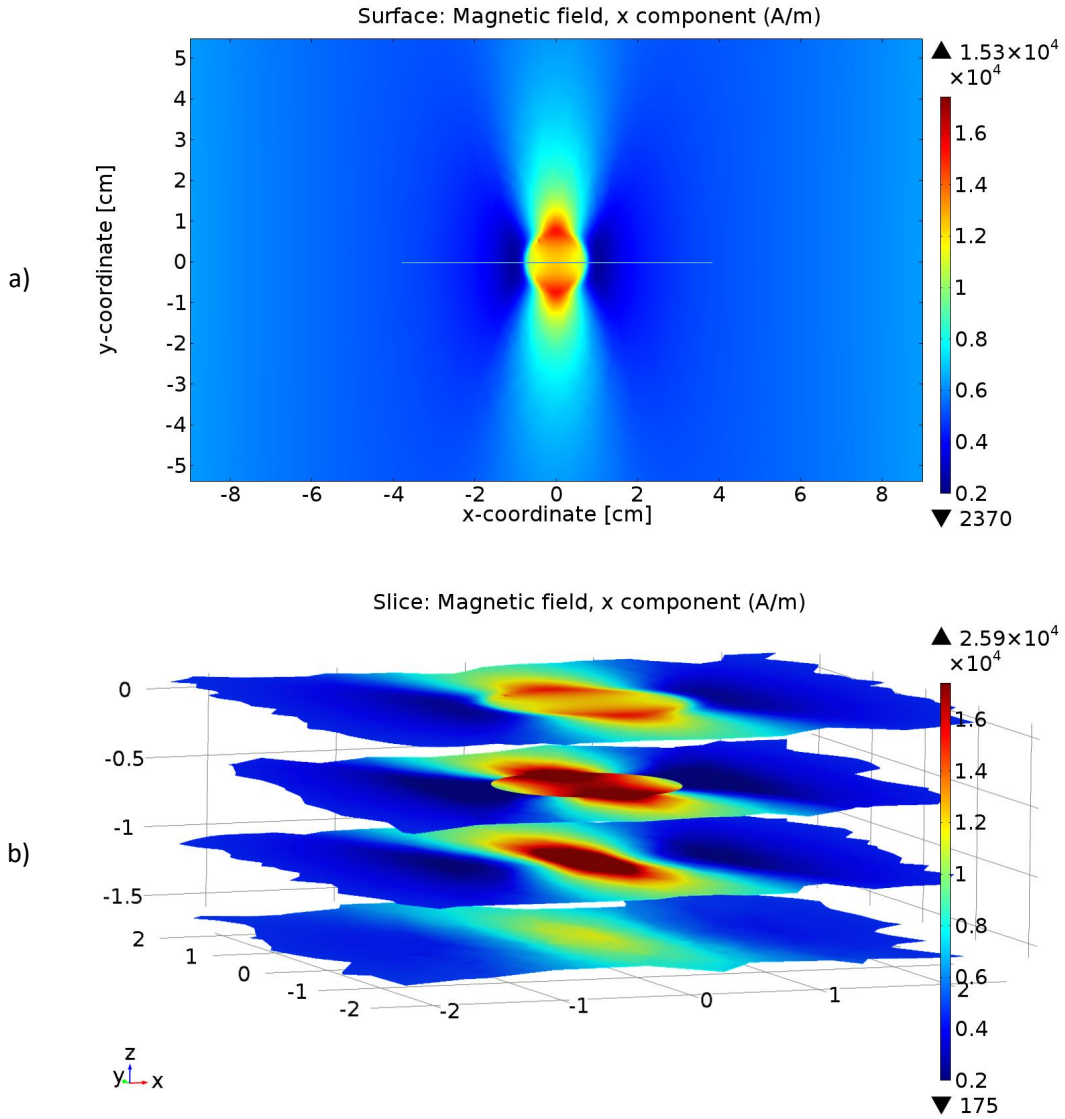

Figure 5.16: *Axial component of the leaked field: a) On a single plane at z=0.1 cm. b) On multiple planes at z=0.1 cm, -0.5 cm, -1.05 cm and -1.6 cm. A line is drawn parallel to the x-coordinate in Figure 5.16a to obtain the 1D plots in Figure 5.17.*

Figure 5.16b provides H_x leaked signal for four different planes simultaneously. The plane on the top is located at $z = 0.1$ cm on the air domain above the sample. It corresponds to the one in Figure 5.16a. The second cross section passes through the flaw at 5 mm below the surface. Further down, between the defect tip and the bottom plate surface lies the third plane in the ferromagnetic material at $z = -1.05$ cm. Finally, the fourth plane is located on the air domain, 4 mm underneath the plate. It is worth to mention that the field in Figures 5.16a and 5.16b are plotted using the same colour

gradient. However, the maximum and minimum fields at the colour legend of Figure 5.16b become higher due to the amplified fields registered at the cross-sections which pass through the ferromagnetic domain.

5.4.3 1D Plots

The information on C-scans becomes much more pronounced if amplitude locus-curves are considered plotting the MFL-components. This kind of plots is named in COMSOL as 1D plots, which illustrates the parameter behaviour along a selected line. In this work will be reported amplitude locus-curves mostly for this reference line at $y = 0$, as drawn for this purpose in Figure 5.16a. Otherwise, in case that the reference line change the location, this will be accurately stated. The corresponding H_x signal obtained for the reference line is shown in Figure 5.17a, which extends between $x = -10\,\text{cm}$ and $x = 10\,\text{cm}$. While Figure 5.17b includes the dependency of the H_x signal on lift-off. Corresponding lift-off values are detailed on the plot legend.

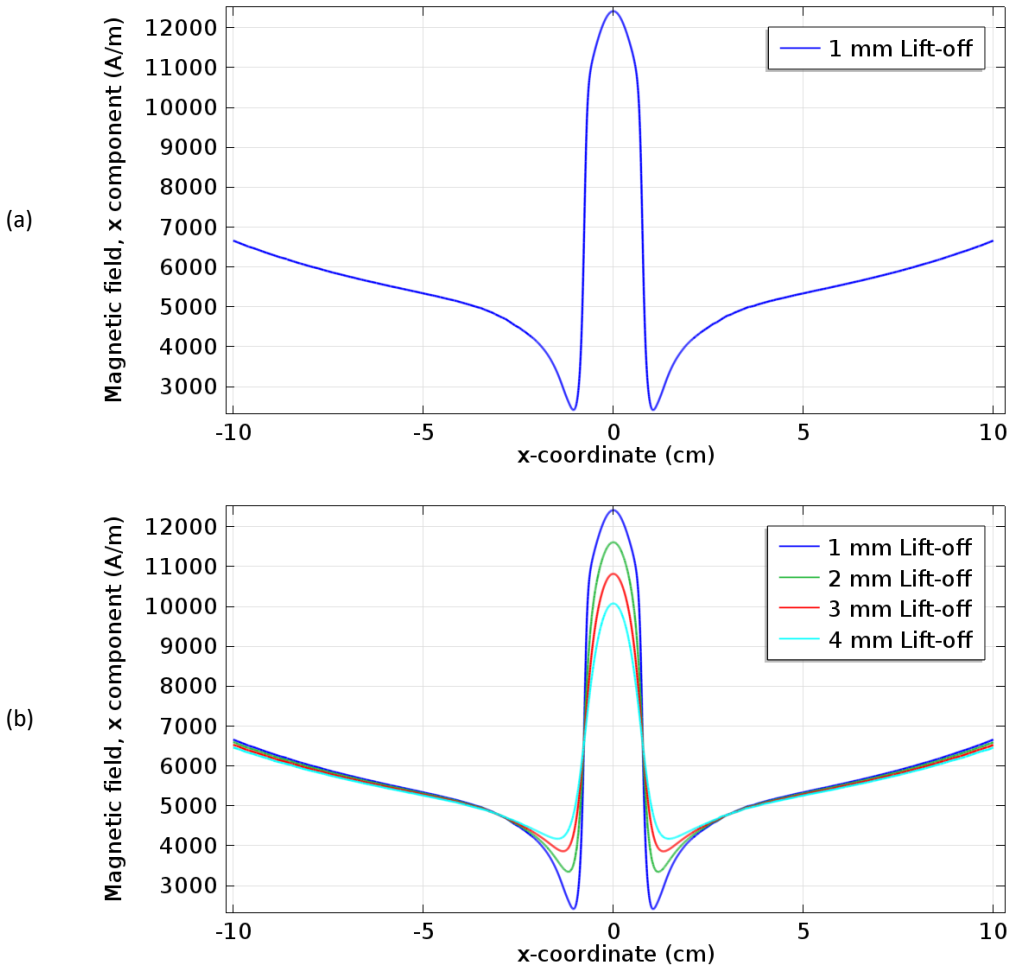

Figure 5.17: *Axial component of the magnetic field along the observation line in Figure 5.16a. a) At 1 mm lift-off. b) At different lift-offs.*

5.5 MFL Signal Assessment

The analysis of the MFL signal behaviour is conducted in this work through theoretical, numerical and experimental research approaches. At least, two of these approaches are used in the assessment of every variable which alters the signal. Consequently, results are reported making emphasis on the provenance of the data. The methodology applied in every specific case is thoroughly reported in this section.

Overall in the pipeline inspection context, inner and outer defects must be differentiated considering that inspection employing PIGs is only feasible from pipeline inside. Although most of the publications about MFL signal assessment do not distinguish defects according to their location, for this research has been fundamental to consider differences of signal parameters separately for inner and outer defects. In this regard, if an explanation of defect location terms is necessary, refer to Figure 5.11. Thus, simulation and experimental set-ups are arranged in this study to obtain MFL signals from inner and outer defect configurations using the same sample features. In fact, signals coming from each of these two configurations are qualitatively similar. However quantitatively, their behaviour differs as will be demonstrated along the next sections.

Before starting the discussion about the signal assessment, it is necessary to depict the typical behaviour of each MFL component. In this perspective, results of the axial, radial and circumferential components of the leaked field from a flawed plate are simulated (results in Section 6.4). The three components are painstakingly studied for inner as well as for outer defect cases taking advantage of the C-scans and amplitude locus curves (figures 6.8 to 6.11). Corresponding simulation set-up follows the flawed plate model introduced in Section 5.2.4. These results are obtained from a calotte shaped defect with an opening of 10 mm in diameter and 50% of wall thickness reduction. The properties of the resulting MFL components are carefully discussed. Taking into account that the main objective of this research is the assessment of MFL components amplitude and its dependency on the defect depth, henceforth this study will concentrate on the axial and radial components since the amplitude of the circumferential component is too weak compared with the other two. Despite, the information supplied by the circumferential component may not be under any circumstance neglected on the defect reconstruction process. Conversely, it can provide essential information, as discussed in Chapter 7.

Regarding the collected data obtained from simulations and experiments, it is essential to remark that they require specific treatment in order to conduct proper comparisons. In this sense, a previous review of the magnetising field is performed. The magnetisation strategy of simulation and experiments must be taken into account for the purpose of conducting a reliable analysis. In the simulation model, a magnetic potential difference is assigned to the sample ends at the respective boundaries (see Figure 5.6). While the experimental set-up includes an electromagnet, on which sample lies (refer to Figure 5.9). Consequently, poles are built at the sample extremes causing that the axial and radial components include a particular off-set level in every instance, which will be discussed in detail in Section 6.4.1. Indeed, the magnetic circuit used in an in-line

inspection tool like a PIG moves simultaneously with the Hall sensor array unlike simulation or experimental set-ups where H_x and H_z components report a constant value as long as no defect is present in the inspected sample. In fact, H_z component will register zero provided that the sensor lies equidistant to every pole.

A second necessary observation concerns the true lift-off since through simulation and experimental data comparison could be identified that the active zone of the Hall sensor is not located at the sensor tip. In this perspective should be considered that the housing dimensions of a single Hall sensor are 4.06 x 3 x 1.57 mm^3 and the separation between the sensor tip and the sample surface or nominal lift-off is defined as 1 mm. Furthermore, every sensor in the array has a different orientation, as can be observed in Figure 5.10. Hence the true lift-off for each sensor also differs depending on their specific active zone location. A detailed analysis of the experimental results was conducted to establish the true lift-off, particularly for each sensor. Firstly, a thorough matrix of experimental data and corresponding simulation results from different defect dimensions and several lift-offs are compiled. Secondly, the maximum amplitude of the axial and radial components from experimental and simulation results are contrasted simultaneously for different lift-offs. Field vs lift-off plots are obtained for every defect size considering both configurations, inner as well as outer location. Thirdly, simulation results are assumed as true values, and experimental data are shifted along the lift-off axis until the data overlapped. A defect with a diameter of 10 mm is chosen among a large number of assessed cases in order to report in this thesis an example of the process conducted for inner and outer set-up configurations (Figures 6.13 and 6.14). Plotted data are obtained from two different samples, both of them machined as calotte defects, the first flaw has 50% wall thickness reduction and the second has 80% wall thickness reduction.

True lift-offs are determined as 3.5 mm for H_x and 2.1 mm for H_z based on the results from the whole array of inner and outer defect instances. The behaviour of axial and radial components of the magnetic field assuming the true lift-off is altered, as expected, compared with the C-scans obtained at 1 mm lift-off, which can be verified in detail in Figure 6.15. Additionally, a comparison of simulation and experimental results are provided for every component and configuration through C-scans and amplitude locus curves to validate the outcomes from simulation.

The following sections report the methodology conducted to analyse three parameters which alter the MFL signal critically: applied field, defect dimensions and lift-off. More specifically, the amplitude and length of the H_x and H_z leaked components will be assessed in order to establish a reliable model for defect sizing based on the MFL technique.

5.5.1 Dependency on Applied field

Applied field is a fundamental parameter in the application of the MFL technique. Indeed, there are several aspects to take into account in this respect as those already discussed in Section 5.2.1. That review has demonstrated how the magnetisation strength

affects the MFL signal, which emphasises the advantage to use an adequately applied field to provide MFL signals free of disturbances coming from mechanical inhomogeneities in the material. Here, this section is addressed to confirm the linearity of the amplitudes of the axial and radial components of the leaked field, taking into account an applied field range suitable for MFL inspection.

The equations to solve the leakage problem are reported in Section 3.1.3 based on the theoretical approach from Dobmann et al. [36,83,107]. They describe MFL phenomena in 3D and provide the input for the implementation of numerical calculations. Additionally, the authors in [36,83,107] demonstrated experimentally that the maximum of the leaked radial component responds linearly to the applied field employing a crack type defect. This statement is needed because consequently, the integral equation system to solve the leaking field problem could be significantly simplified. Likewise, the amplitude behaviour of the axial and radial components of the MFL response to the excitation field will be introduced in this research. In this sense, two kinds of corrosion type defects were experimentally assessed, initially cylindrical shape defects and subsequently calotte shape defects. This verification will allow the description of the MFL problem through Equations 3.19 and 3.20 only if two conditions are fulfilled. The first one is a linear behaviour of the MFL components amplitudes. While the second concerns that the operating permeability is equal or higher than 100. For this purpose, a steel plate is selected to carry out the tests. It is $60\,\mathrm{x}\,25\,\mathrm{x}\,1.2\,\mathrm{cm}^3$. The preparation of the set-up starts with field measurements on the flawless plate at different magnetisation strength and also different lift-offs. These measurements will allow the determination of an advisable applied field for the simulation model. After this previous step, then, a cylindrical defect was drilled in the steel plate. The flaw is 1 cm in diameter and 6 mm deep, namely 50% of plate thickness reduction. Corresponding MFL signals resulting from experiments by the set-up configuration as inner and outer defect are thoroughly assessed. Additionally, the linearity of the axial and radial MFL components is verified in the specific case of calotte shaped defects, which is the chosen defect type for the current study. Measurements are also carried out considering both instances, inner defects as well as outer defects. The results from all the studied cases agree, thus a selection of experimental results from 5 different flaw dimensions is selected to be presented in Section 6.4.3.

As discussed in Section 3.1.3, Equations 3.16 and 3.17 can be further simplified by Equation 3.19 provided that the operating permeability is 100 or higher. As in this study, the applied field range utilised to obtained MFL signals reaches 7.4 KA/m maximum, then a sample permeability even higher than 200 is guaranteed according to the permeability curve of the test material, as can be confirmed in Figure 6.3. Hence, Equation 3.19 applies and the function $(\mu-1)/(\mu+1)$ can be also considered for theoretical analysis. In this context, the 2D case in Section 5.1 provides a straightforward example of the contribution of this term to the field outside and inside the magnetised specimen (refer to Equations 5.6). Additionally, the response of the function $(\mu-1)/(\mu+1)$ depending on applied field can be considered. It is worth to mention that the whole $\mathbf{H}_0$ range used for experiments in this research including the saturation study is analysed.

5.5.2 Dependency on Defect Size

According to the main objective in this research, a thorough study is required to establish the relation between defect dimensions and MFL signal parameters. As in previous sections, here are also assessed the defects separately for inner and outer defect configurations. In every case is studied the H_x and H_z relation to the defect length and depth. Simulations and experiments are conducted to achieve this purpose.

5.5.2.1 Initial Simulation

An initial approach is carried out using 3D simulation. The chosen defect type has calotte shape since this geometry is comparable to real corrosive wall-thinning like, for instance pitting corrosion. Three different defect diameters are included in this simulation stage: 1.2 cm, 1.6 cm, and 2.4 cm. For every diameter are considered several defect depths, namely in percentage respect to the sample thickness: 30%, 50%, 70%, 90%. Every defect is embedded individually in a plate 300 cm long, 150 cm wide and 1.2 cm high. The plate height is chosen from typical values of pipeline wall thickness which transport oil and gas. While the length and width of the plate are defined based on previous observations from simulation results, which have shown strong leakage fields occurring at the plate edges perpendicular to the applied field. This behaviour at the edges of the cubic plate disturbs the leakage field produced due to the defect presence entailing the use of a large plate as a sample in the simulation model. Consequently, the cube of air which contains the sample also has to be enlarged. The air domain is required to achieve that the total field at its boundaries converges into the driving field. So, the magnetic leakage field as the solution of the static Maxwell equations asymptotically has to tend to zero with increasing distance from the field disturbances (defect and plate edges), namely, as the air domain numerically increases. In this perspective, the cube which limits the air domain is defined as follows: 1200 cm long, 600 cm wide and 480 cm high. All these geometrical dimensions are the result of plenty of convergence trials taking into account besides the finite element mesh, i. e. mesh refinement, size and number of elements. Table 5.3 summarises the computational effort concerning the FE-approach itself. As several users in the multi-tasking mode use the server for FE calculations, the indicated computational time does not directly reflect the complexity of the mesh refinement when defect parameters are changed. The number of users calculating at the same time on the server influences the transfer times from the CPU to the storage and back; computing time is CPU-time + transfer-time. However, the number of elements applied after automated mesh refinement has not registered either a direct unique relationship to the changing complexity when the defect parameters are changed. It seems to be an individual COMSOL behaviour.

The material assigned to the plate is carbon steel, a customized material is created in Comsol introducing the virginal magnetisation curve of the test material obtained experimentally, which is described in Figure 6.2. The plate is assumed to be magnetised by a homogeneous magnetic field with a magnitude of $\mathbf{H}_0 = 20\,\mathrm{kA/m}$ in the x-direction, in other words, parallel to the plate length. This value is far in the saturation branch of

Defect		Element number of			DOF	Solving
Diam. [mm]	Depth [%]	volume	surface	line		time [s]
12	90	3863520	387212	2654	5159333	4360
	70	3017968	295948	2432	4030363	3552
	50	3419825	339442	2578	4566914	14122
	30	3441915	341798	2591	4596552	30093
16	90	900850	98498	1628	1204695	644
	70	1374573	151462	1960	1837898	1032
	50	2264702	217018	2312	3026405	2026
	30	3443904	340684	2734	4599249	3113
24	90	890280	98104	1516	1189757	8326
	70	881751	97128	1516	1178350	10121
	50	879220	96836	1508	1175015	8935
	30	1357100	150844	1846	1814413	12810

Table 5.3: *Complexity of the FE-approach as a function of the mesh refinement and solving time.*

ferromagnetic weldable steels, which starts at 2 kA/m [105]. In fact, at this applied field, even high alloyed steels with 13% Cr content have already reached permeabilities below their maximum value with a tendency to meet the value $\mu = 1$ in absolute saturation. However, this value of $\mathbf{H}_0$ guarantees to have stronger permeability gradients around the defect obtaining consequently a high MFL contrast which should be better for imaging.

The discussion here is addressed to two components of the MFL signal: axial component, namely parallel to the driving field $\mathbf{H}_0$ (parallel to x-coordinate) and the radial field component, perpendicular to the surface (parallel to z-coordinate). For this initial simulation assessment, a virtual scanning by a magnetic point-probe is assumed at 1 mm lift-off from the surface. Configurations as inner defect an outer defect are considered (results in Section 6.4.4).

5.5.2.2 Experiments

A series of experiments is conducted based on the conclusions from preliminary tests and initial simulation approach. In this context, some modifications are required concerning employed set-ups. First of all, the lowest range of applied fields reported in Table 5.2 is avoided claiming for imaging accuracy. However, 20 kA/m as used in the initial simulation is considered excessive according to the requirements in this study. Therefore, the applied field is limited to the range between 3 kA/m and 7.4 kA/m, taking into account the discussion in Section 5.2.4.1 and the practice facilities. Particularly within these applied fields, 5.2 kA/m is selected for scanning at different lift-offs. The

second consideration involves the defect size, diameters of 5 mm, 10 mm and 15 mm are selected with the purpose to include diameter smaller than the plate thickness. While, defect depths of 20%, 50% and 80% of plate thickness reduction are chosen in order to cover the whole range with three different depths limiting the experiments to a viable amount. The experimental set-up is performed as described in Section 5.3. A total of 88 different tests are accomplished, considering the features as reported in the general outline in Table 5.1. The selection of applied fields and lift-offs specifically for this part of the investigation are summarised in Table 5.4.

I [A]	1	2	3
$\boldsymbol{H_{x(1mm)}}$ **[kA/m]**	3	5.2	7.4
Nominal lift-off [mm]	1	1/3/5	1

Table 5.4: *Applied fields and chosen lift-offs for MFL signal assessment in relation to defect size, besides the features specified in Table 5.1.*

The results from this experimental phase were fundamental to verify the necessity to optimise the initial simulation model. Two different defect dimensions are chosen from the set of experiments to illustrate the inaccuracies of the simulation model. Each of these two defects has a diameter of 10 mm, while they have different defect depths: 50% and 80% of plate thickness reduction. Differences between the results under inner configuration by means of simulations and experiments will be discussed in detail at the beginning of Section 6.4.4. Although outer defects were not studied using the initial simulation model, related results will be additionally included in Figure 6.28 taking advantage of the experimental analysis at this point.

5.5.2.3 Advanced Simulation

As described above, the use of homogeneous magnetisation utilising a constant applied field at the air domain boundaries implies the consideration of extra-large dimensions for the plate and consequently for the air domain. In this perspective, an alternative for magnetisation is required to avoid the disturbances on the MFL signals resulting from severe pole generation at the plate edges perpendicular to the applied field. Therefore in the current model, the plate is magnetised through a magnetic potential difference applied directly to the plate edges. Consequently, the magnitude of this magnetic potential is assigned in order to reach the applied field required at the nominal lift-off and its direction is established as previously parallel to x-coordinate, for a detailed explanation (refer to Section 5.2.4). This way of sample magnetisation in the simulation model provides a closer distribution of the magnetic field around the sample and necessarily inside the sample as in the experimental set-up.

The relationship between the magnetic potential and the applied field requirement also depends on the sample material, geometry and size. Accordingly, this condition is used to modified the steel plate size assigning the corresponding dimensions used by experiments, namely $35\,\mathrm{x}\,25\,\mathrm{x}\,1.2\,\mathrm{cm}^3$. Accordingly, the air domain can be reduced to

a cuboid of 350 x 250 x 240 cm^3, as shown in the convergence assessment in Section 5.2.4.2. Under current model features, it is assumed a magnetic potential difference of 1280 A and -1280 A respectively in each plate edge. So, it is achieved 5.2 kA/m of applied field at 1 mm nominal lift-off.

Regarding defect size: 5 mm, 10 mm and 15 mm are the selected defect diameters seeking for comparison with experimental results. While 20%, 35%, 50%, 65% and 80% of plate thickness reduction are considered to accomplish a suitable amount of data allowing a robust assessment. In the advanced model for simulation, the axial component is obtained at 3.5 mm and the radial component at 2.1 mm, as the empirical lift-off is affected by the active zone of the sensor. Results belonging to the relation between MFL components and the defect size are reported at the end of Section 6.4.4 and in Appendix E. Due to the high amount of analysed cases, the reported results are restricted to achieve mainly two aims, firstly to permit specific subject comprehension and secondly to provide instances for comparison.

5.5.3 Dependency on Lift-off

Currently, it is well known the high dependency of the leaked field signal on the associated lift-off [108–111]. Nevertheless using MFL technique, it is still a challenge to establish the real lift-off accurately by pipeline inspection. Here, it will take advantage of simulation and experimental approaches to stablish specific relationship between H_x and H_z components under inner and outer configurations, and the lift-off used to scan the sample.

Specifically, 54 experiments were conducted to study the behaviour of H_x and H_z field components depending on lift-off. Different sample plates were used in the set-up illustrated in Figure 5.9. Signals at three different nominal lift-offs are registered for every case, namely 1 mm, 2 mm, 3 mm or 1 mm, 3 mm and 5 mm. For every experimental set is keeping constant all remainder parameters. Dimensions of the assessed defects are included in Table 5.1. Most of the studied defects have calotte shape, but also few cases are conducted with cylindrical shape defects seeking for comparison.

Fortunately, the advanced simulation model for assessing lift-off dependency can be configured to achieve MFL signals at different lift-off simultaneously. Nevertheless, the number of simulation required is more than twice the number of experiments in order to get accurate results and smooth curves. Specific aims seek first to achieve a reliable simulation model and second, to extend the data set of results. Selected lift-offs to conduct the assessment are defined in a range around empirical values, namely from 3 mm to 8 mm for the axial component and from 2 mm to 7 mm for the radial component, these ranges include the true lift-off for every field component, which will be established in Section 6.4.2.

H_x and H_z field components are obtained modelling both configurations, as an inner defect as well as an outer defect. The dependency on lift-off for a defect with a diameter of 10 mm and 50% of plate thickness reduction will be discussed as an example of the

results obtained for the whole set of analysed defects in Figures 6.37 and 6.38. Based on the results, it is understood the necessity to delve in more detailed into the dependency of defect length and defect depth of MFL signals to the lift-off. In this context, the relation of the defect length to the MFL signal duration is further studied and separately, the defect depth associated with the MFL signal amplitude as the lift-off changes. In order to keep a clear structure by results delivery, two sections will be defined: length dependency in Section 6.4.5.1 and maximum amplitude dependency in Section 6.4.5.2. Experimental results are enriched with further simulation cases seeking for a better comprehension of the relationships.

5.6 Saturation

In almost all MFL studies, sample saturation is presented as a requirement for proper technique performance. However, there is still, at least to the author's knowledge, no published discussion regarding the exact meaning of saturation affecting MFL signals. Analytical formulas exist only for the case of a paramagnetic material where the permeability is assumed as a constant, but not for materials with hysteresis character. In the paramagnetic case, for instance, looking at the 2D-problem discussed in Section 5.1, it is selected a permeable cylinder perpendicular oriented in a homogeneous magnetic field. Related saturation behaviour is governed by the function $(\mu - 1)/(\mu + 1)$ (refer to Equations 5.6). This function tends very rapidly to zero only for μ-values $<$ than 10 [102], which is clearly revealed in Figure 6.43.

H_x signal amplitude will be assessed to study the ferromagnetic behaviour as the applied field increases further from 7.4 kA/m, which was the limit to perform the assessment discussed in Section 5.5.1. This field branch is from now on referred to as near saturation region considering fields from 9 kA/m until 81 kA/m. A set of experiments and simulations are conducted using a bar from the characterised steel S235JR. The sample is 200 mm long with a rectangular cross-section of 4 mm $\times$ 2 mm, see Figure 5.18. The Figure also detailed the dimensions of the embedded flaw which is defined as a saw cut perpendicular to the length direction of the rod with following dimensions: length 4 mm $\times$ depth 1 mm $\times$ width 0.1 mm.

In order to study the effects of magnetic saturation on MFL signals, the rod is magnetised longitudinally achieving a low demagnetisation factor. Consequently, the sample reaches the near saturation region easily. The magnetisation is achieved placing the specimen in the electromagnet shown in Figure 5.3. A single Hall sensor is built in a proper structure in order to acquire the H_x component of the leaked field using the system shown in Figure 5.9. The rod is scanned lengthwise at a true lift-off of 3.5 mm. The electromagnet is excited employing dc-current with amplitude values from 0.2 A to 1.8 A providing applied fields from 9 kA/m until 81 kA/m in steps of 9 kA/m.

On the other hand, for the simulation model, length of the rod is limited to 16 mm since two main factors affect sample magnetisation: first, by the experiments, the separation between electromagnet poles is shorter as the sample length, and second, for

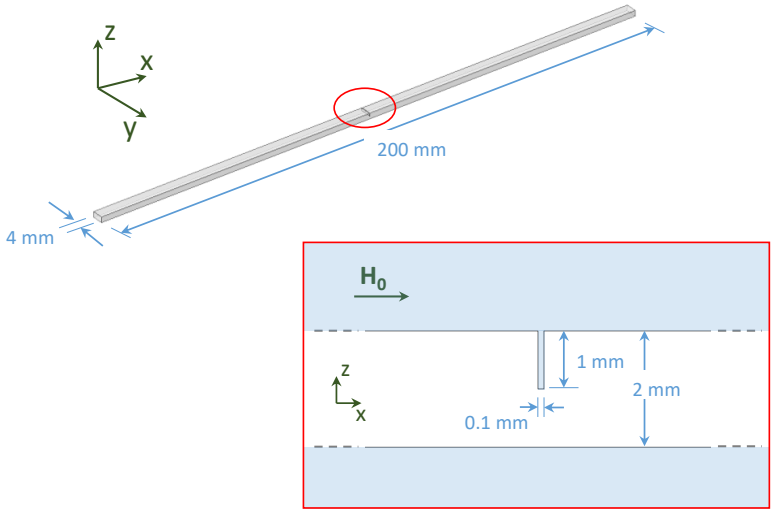

Figure 5.18: *Sample dimensions to conduct experiments and simulations related to magnetisation in the near saturation region.*

the simulation, the sample is magnetised through a magnetic potential assigned to the boundaries at rod ends as explained in Section 5.2.4.1 for the plate case. Conditions and parameters of the simulation model were modified several times until a reliable model is developed according to the experimental results. Magnitudes of the magnetic potential required to achieve desired applied fields are first established in a simulation model of the flawless rod. Afterwards, these potentials are implemented in the model of the defected rod from 13500 A to 127100 A. Related BH curve obtained experimentally for the S235JR is assumed to simulate the ferromagnetic material (Figure 6.3). Results from corresponding simulations and experiments will be reported in Section 6.5.

6

Results

Theoretical, numerical and experimental results are reported in this chapter. Those are ordered from the general to the particular, which ensures subject comprehension and progressively deepening into an innovative and robust solution. Besides the results, some observations and comparisons are also introduced. The first section reports the magnetic properties explicitly obtained for the S235JR steel selected to conduct the assessment along with this research, while the second section is focussed on magnetisation strength as a fundamental parameter on MFL inspection technique. The outcomes concerning advantages and convenience to use either 2D or 3D simulation model in order to fulfil the objectives of this research is introduced in the third section. The following section presents core results regarding defect sizing through MFL signals. Initially, the features of MFL signal components are illustrated for inner as well as for outer defect configurations. Then, the magnetising field behaviour and the active region location by Hall sensors are illustrated provided that these two parameters alter the signals significantly. At the end of section fourth, it is documented the dependency of MFL signals on the applied field, defect size and lift-off. Finally, section fifth sets out the benefit to use an applied field within the saturation range on imaging accuracy. The conducted methodology to acquire results reported in this chapter is presented in detail in Chapter 5. On the other hand, a more in-depth discussion on the relevant subjects reported here is included in Chapter 7.

6.1 Magnetic properties

Figure 6.1 illustrates the hysteresis curves obtained experimentally for a sample from the selected steel according to the methodology introduced in Section 5.2.1. These are some chosen curves from the whole range of conducted measurements. Related virginal and permeability curves are obtained from the whole set of hysteresis curves, see Figures 6.2 and 6.3. They include the response of S235JR material in the saturation branch, namely until an applied field of 86 kA/m. These extended curves allow a more in-depth analysis of the MFL response in samples which are magnetised far in the saturation region.

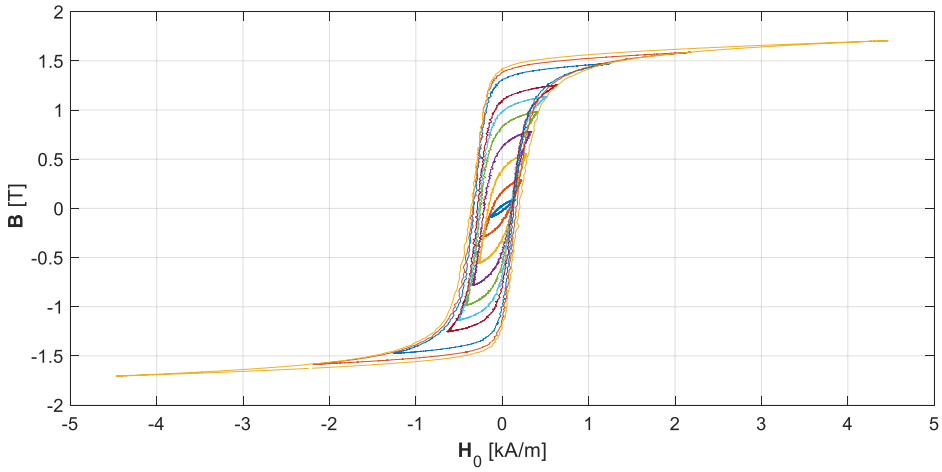

Figure 6.1: *Hysteresis loops of the test material.*

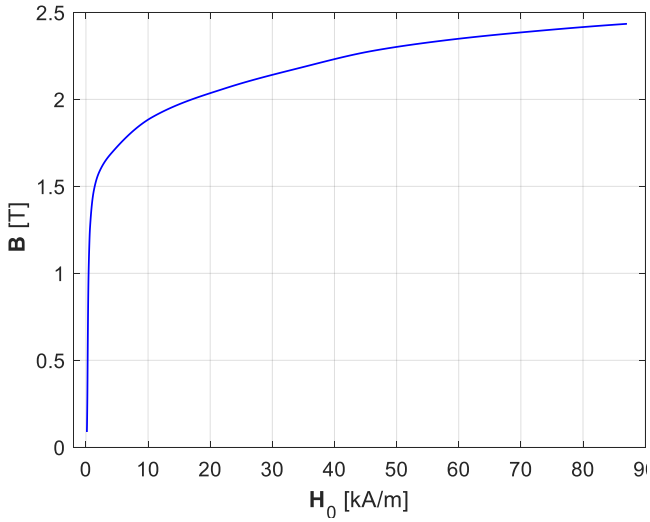

Figure 6.2: *Virginal curve of the test material.*

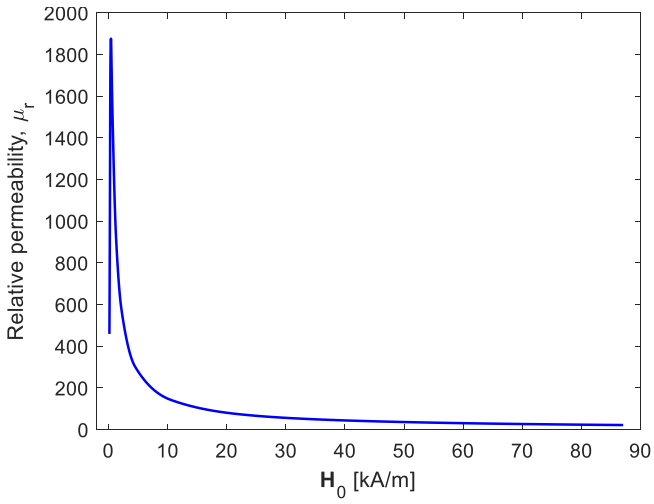

Figure 6.3: *Permeability curve of the test material.*

6.2 Magnetisation Strength

Differences in the permeability behaviour and the BH curve between two different conditions of the selected material are presented in Figure 6.4. Plots were obtained before and after a stress relief process was conducted on the steel sample. The differences are evident for lower values of $\mathbf{H}_0$. In contrast, discrepancies between signals for higher values of $\mathbf{H}_0$ tend to be insignificant. Accomplished results agree with data published in [105].

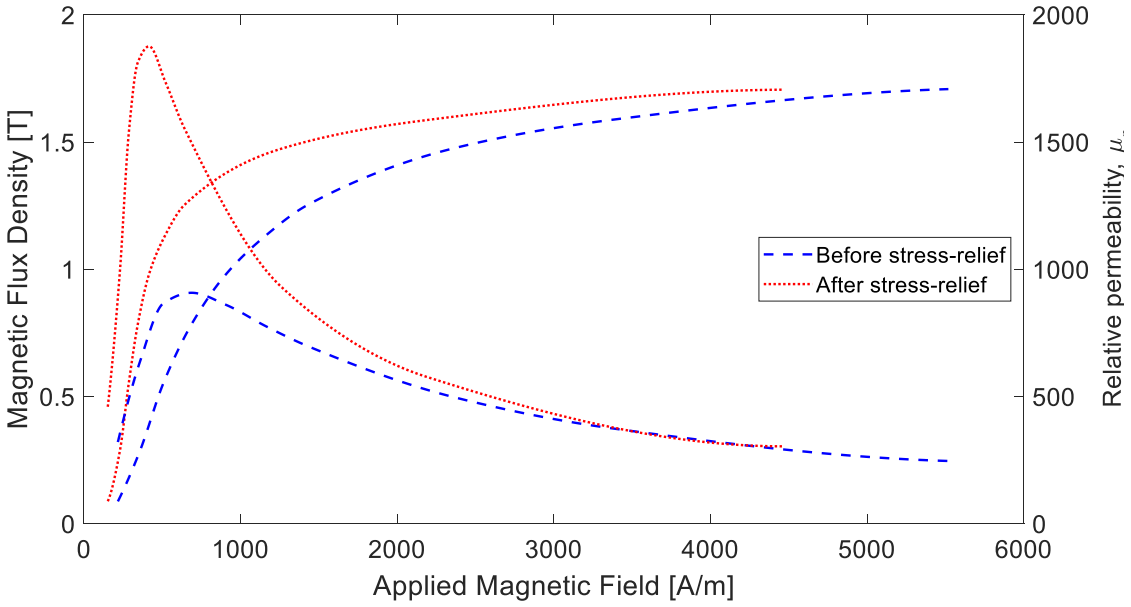

Figure 6.4: *BH curve and permeability of the selected material under two different mechanical conditions.*

Proper magnetisation strength is fundamental for successful MFL testing, as already discussed in Section 5.2. Figure 6.5 reports the tangential component of the magnetic leaked field obtained experimentally. These C-Scans are taken at 1 mm over the steel plate, known as nominal lift-off. The specimen contains a calotte defect located symmetrically on the centre of one of the largest plate surface. Fields of 0.9 kA/m, 1.5 kA/m, 2.7 kA/m and 7.4 kA/m are applied to the sample using an electromagnet. Although the plate is 60 x 25 x 1.2 cm^3, the scan area is limited to 12 x 18 cm^2, so that the defect can be registered at the centre of the plot. Here, the defect consists of a cylindrical bored hole of 1 cm in diameter and 0.24 cm deep (20% of the plate thickness). The sample is demagnetised before it is installed on the magnetic circuit to perform the experiments. As can be seen in Figure 6.5a, it is difficult to identify the gap for the lowest applied field (0.9 kA/m), due to the existence of additional field changes in the image. These changes are generated from stresses and plastic deformations located in the material around the defect. Under the same test conditions and using the same specimen, Figure 6.5b allows for effortless defect-recognition owing to a significant reduction in the signal to noise ratio. That occurs thanks to an increment in the applied field; however, image inaccuracy still exists. As can be confirmed in Figures 6.5c and 6.5d, the noise interference decreases significantly as $\mathbf{H}$ further increases.

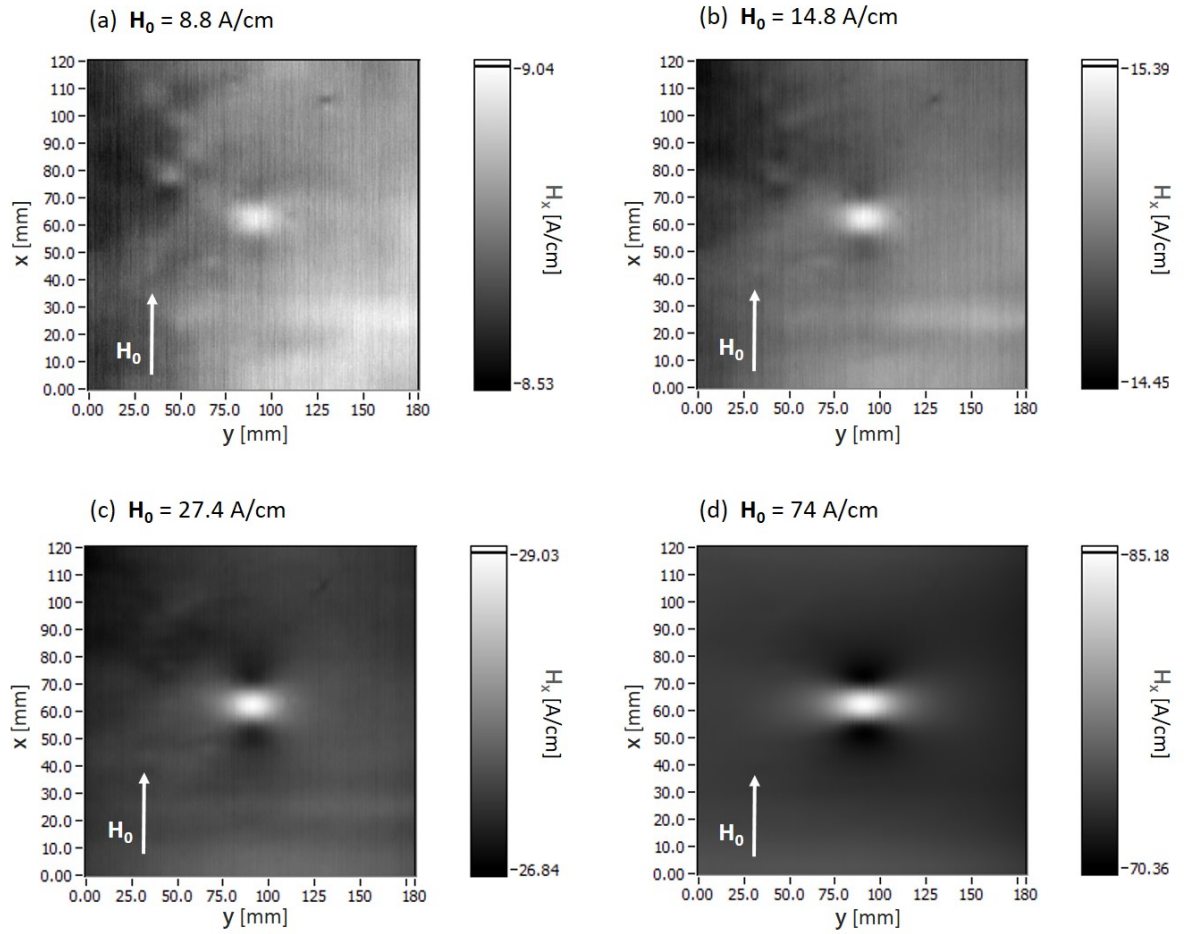

Figure 6.5: *Axial component of the leaked field from a flawed specimen magnetised under: a) 0.9 kA/m; b) 1.5 kA/m; c) 2.7 kA/m and d) 7.4 kA/m.*

6.3 Two-dimensional vs. three-dimensional simulation

The case of the infinite cylinder discussed in Section 5.1 is implemented in COMSOL. An applied field $\mathbf{H}_0$ of 20 kA/m is employed for the model. A customised material is created in the COMSOL library, including the BH curve in Figure 6.2. This material is assigned to the ferromagnetic cylinder by the simulation model. Simulation results of the magnetic field and the magnetic flux density for the magnetised cylinder can be seen in Figure 6.6. These outcomes are achieved from the two-dimensional model. Field lines are added in both cases. Comparing the plots in Figure 6.6 is evident that the resulting flux density is proportional to the magnetic field along the air domain and related through the vacuum permeability $\mathbf{B} = \mu_0\mathbf{H}$. But in the steel domain, $\mathbf{H}$ reaches its minimum due to the demagnetization factor according to Equation 5.6a, while $\mathbf{B}$ achieves its maximum due to the magnetization field by $\mathbf{B} = \mu_0(\mathbf{H} + \mathbf{M})$. Furthermore, the magnetic field inside the cylinder in Figure 6.6a is distributed uniformly in agreement with Equation 5.6a. In contrast, outside the cylinder governs Equation 5.6b.

For comparison purposes, this case is also simulated in three-dimensional space. For 3D simulation, the cylinder length is established as a variable from 0.1 cm until 40 cm. A

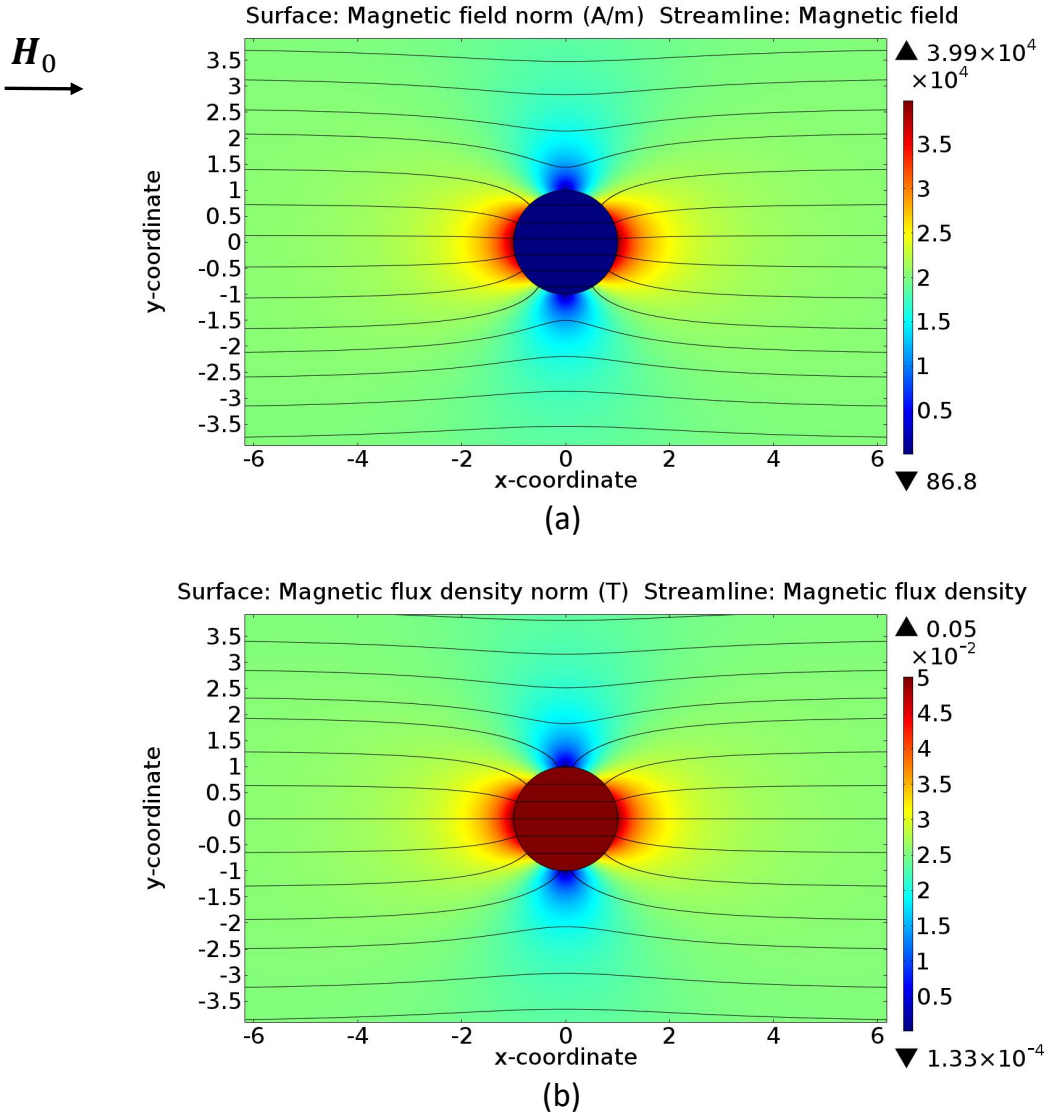

Figure 6.6: *Two-dimensional simulation results for an infinite cylinder. a) Magnetic field. b) Magnetic flux density.*

point p is chosen to observe the magnetic field behaviour as the cylinder length changes. According to the corresponding schema in Figure 5.2, p is located at $r = 1.5$ cm and $\varphi = \pi/2$.

Figure 6.7 illustrates magnetic field results obtained at point p utilising three different approaches: theory, simulation in two-dimensional space and simulation in three-dimensional space. Results show that the field calculated using Equation 5.6b and the field obtained from the 2D simulation agree. They are plotted as a constant for an assuming infinity length of the cylinder. Simulation results from the 3D simulation model tend to the same value as the cylinder reaches enough length. However, this plot allows stressing the inherent error of a 2D approach as the specimen length reduces. From Figure 6.7 can be established that the simulation in 2D reports an error of 1.83% assuming that the theoretical result is the true value of the magnetic field in point p. In fact,

the results of the 3D simulation show good agreement for a cylinder longer than 5 cm. However, for a shorter cylinder, the result obtained by 3D simulation differs considerably respect to the theory and the 2D simulation. This error increases sharply as the cylinder length approach to zero. Namely that a 2D based study for a shorter cylinder will provide inaccurate results. Consequently can be concluded that a 3D simulation is imperative to fulfil the objectives of the current work since the defect depth of interest reaches only some millimetres and the thickness of the chosen sample is 1.2 cm according to the typical pipeline wall thickness.

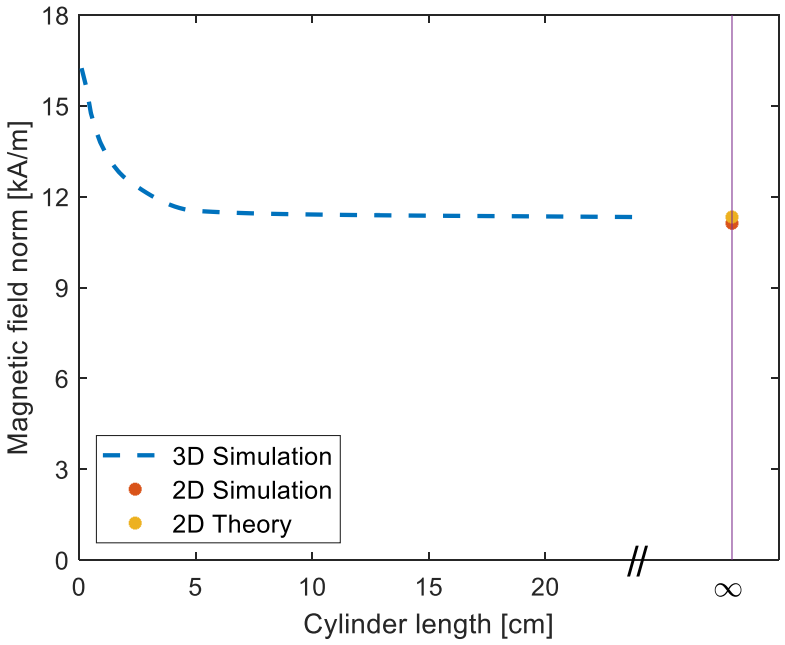

Figure 6.7: *Comparison of the magnetic field norm for a point p at $r = 1.5$ and $\varphi = \pi/2$ according to Figure 5.2.*

6.4 MFL Signals Analysis for Defect Reconstruction

The assessment of the components of the leaked field is performed mainly through two kinds of plots: C-scans and amplitude locus-curves, refer to Section 5.4. Indeed, signal interpretation is essential in this research. In this perspective, the behaviour of the MFL components accomplished from a particular defect case will be as next introduced.

Figures 6.8 and 6.9 illustrate C-scans in the case of inner and outer defects, respectively, see Figure 5.11 if clarification of terminology regarding defect location is needed. Simulated results are plotted for axial, circumferential and radial field components. These signals are taking at 1 mm lift-off for a sample as the one presented in Section 5.2.4 referred to as flawed plate case. The calotte shape defect has a diameter of 10 mm and 50% of plate thickness reduction.

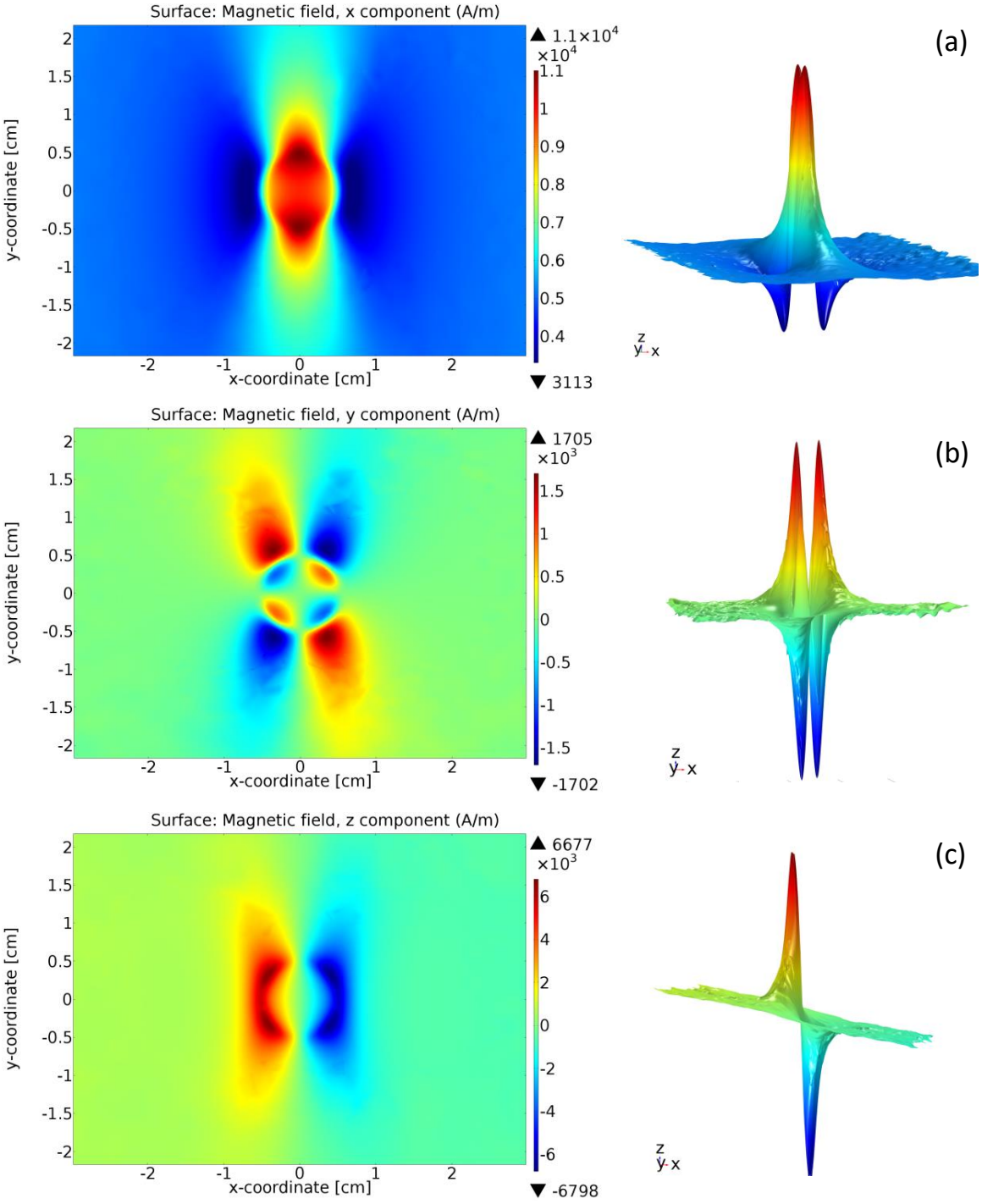

Figure 6.8: *MFL components as C-scans at 1 mm lift-off from the flawed plate model under* ***inner defect*** *configuration. The defect has a diameter of 10 mm and 50% of plate thickness reduction. a) Axial component H_x. b) Circumferential component H_y. c) Radial component H_z.*

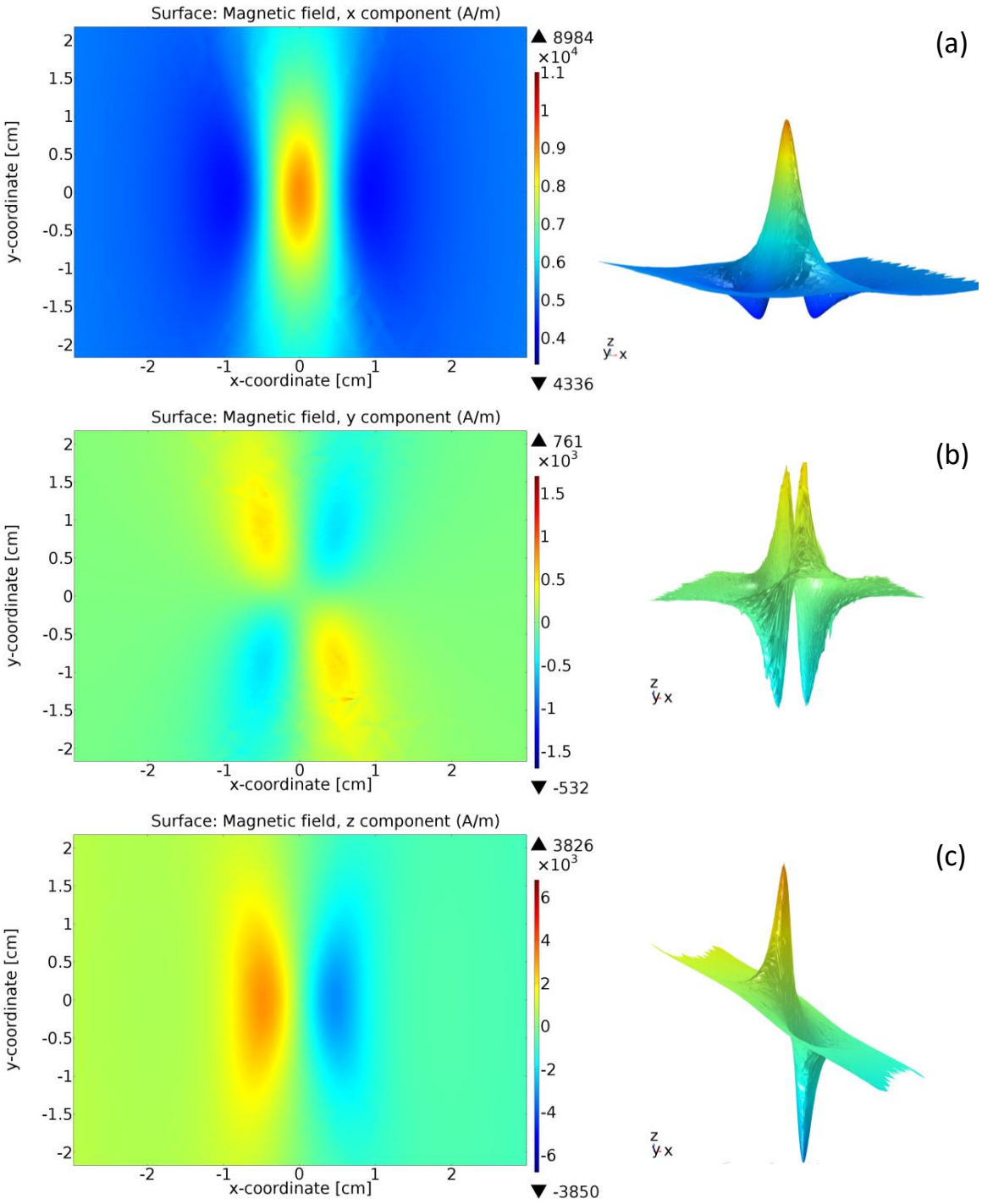

Figure 6.9: *MFL components as C-scans at 1 mm lift-off from the flawed plate model under* ***outer defect*** *configuration. The defect has a diameter of 10 mm and 50% of plate thickness reduction. a) Axial component H_x. b) Circumferential component H_y. c) Radial component H_z.*

In a general context, the data obtained by a single Hall sensor are typically reported using amplitude locus-curves. Specifically along this research is also taken advantage

of such kind of plots, as in Figures 6.10 and 6.11, which report the MFL components considering the same simulation model used previously. The signals are acquired at 1 mm lift-off, parallel to the x-coordinate at $y = 0.3$ cm. In this sense, Figure 5.16 proposes a reference line at $y = 0$ to obtained locus curves from related C-scans, otherwise here the reference is shifted in order to report a signal different to null for the circumferential component. The leaked field resulting from the outer defect case are plotted using the same coordinate scale as those utilised for the inner case to facilitate the comparison between respective components.

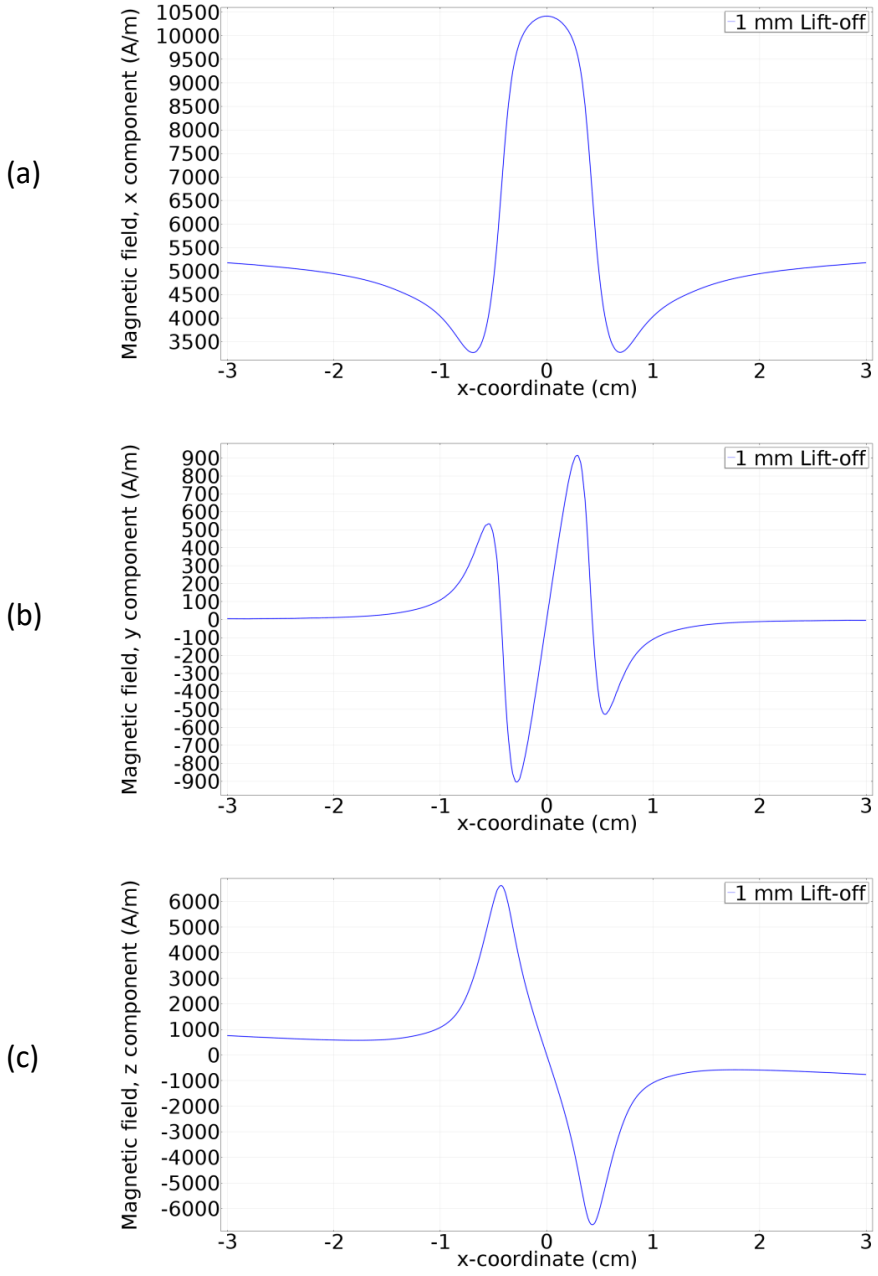

Figure 6.10: *MFL components as amplitude locus-curves obtained at $y = 0.3$ cm from the C-scans in Figure 6.8, considering an* ***inner defect*** *configuration. a) H_x. b) H_y. c) H_z.*

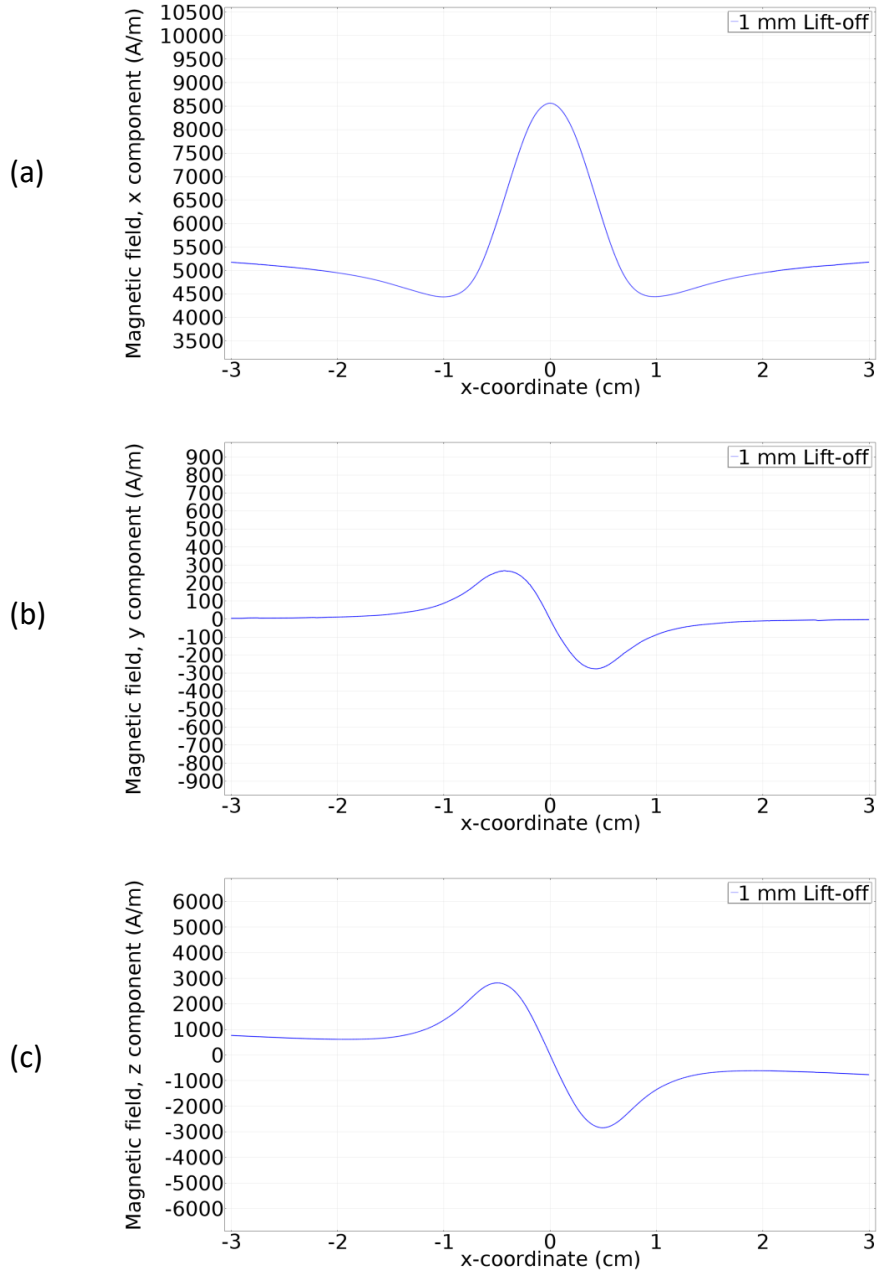

Figure 6.11: *MFL components as amplitude locus-curves obtained at $y = 0.3\,cm$ from the C-scans in Figure 6.9, considering an* ***outer defect*** *configuration. a) H_x. b) H_y. c) H_z.*

Concerning the C-scans can be stated that the contour of the defect mouth can be defined straight away and accurately through any of the MFL components for the inner defect configuration (see Figure 6.8). Conversely, the defect outline in the outer defect case is blinded by the material under the defect. This limitation contributes to loss of accurate information for direct reconstruction of the defect opening by the three components, as can be noticed in Figure 6.9. Next, the discussion is addressed to the properties of each MFL component. Although all of them contain information about

the same defective sample, it is clear from the results that every component should be independently analysed. Specifically, the axial component is shifted to a specific off-set field level, which varies with the magnetisation strength, in particular in Figures 6.10a and 6.11a can be defined the off-set as 5.2 kA/m. In general, this off-set by H_x component as long as no defect is present serves to define the applied field in a MFL assessment. Since the field changes additionally with the distance between the sensor and the sample surface, in this research, the nominal lift-off is defined as 1 mm and consequently, the applied field is established by the H_x component using flawless samples.

Considering once again Figures 6.10a and 6.11a can be claimed that the axial component has a maximum coinciding with the half-length of the defect, as well as a minimum on either side of it. Particular attention should be paid to the inner defect configuration in Figure 6.8a, which reports two peaks fitting with the defect width along the y-coordinate. Regarding the circumferential component, two lines of anti-symmetry at $x = 0$ and $y = 0$ are clearly observable by the C-scans. This information can be used to establish the symmetry axes of the defect. A relevant property of the circumferential component considering the C-scans is that eight peaks are visible by inner defect configuration, while the outer defect case reports only four peaks. In the case of amplitude locus curves are three possibilities: first, the circumferential component is equal to zero if there is no defect detection or the line scan coincides with the symmetry axis of the defect at $y = 0$. Second, the signal reports two positive peaks and two negative peaks, for instance, figure 6.10b and third, one positive and one negative peak as in Figure 6.11b.

Finally, the radial component presents a line of anti-symmetry at $x = 0$. Corresponding amplitude locus curves consist of a positive peak and a negative peak, crossing the null field precisely in the halfway of the defect length at $x = 0$. For the inner defect configuration, the peaks are defining the defect contour as the line scan moves away from $y = 0$. In contrast by the outer defect, the peak to peak distance increases despite the defect contour. Lastly, note that the amplitude of the circumferential component under both configurations in Figures 6.8 to 6.11 is considerably lower compared with H_x and H_z amplitudes.

6.4.1 Magnetising Field

Before moving on to the parameter assessment, it is necessary to underline the behaviour of the plate magnetisation in terms of H_x and H_z. For that purpose, a flawless plate will be simulated and also tested experimentally. Figure 6.12 presents simulation results as C-scans of the axial and radial component of a magnetised flawless plate.

As can be seen in Figure 6.12a, H_x signal sets a quasi-uniform field different to zero in the middle between poles while it increases as approaches any pole. Unlike, H_z signal provides a maximum in one pole and a minimum in the opposite pole, generating a field gradient. Thus, a null field is achieved at $x = 0$, as illustrated in Figure 6.12b. For a fixed set-up, the magnitude of these off-set levels depends on the applied field.

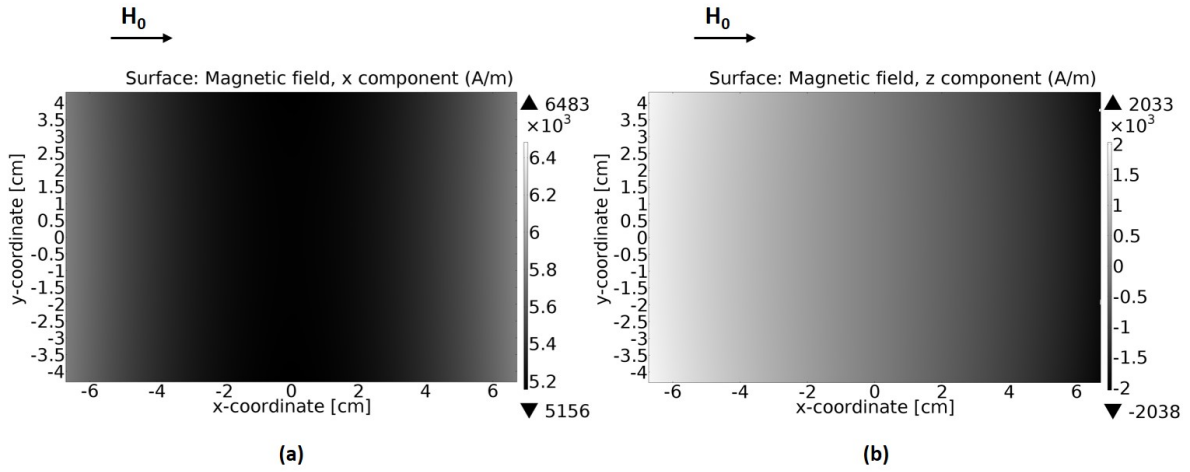

Figure 6.12: *Magnetic field C-scans obtained at 1 mm lift-off by simulation of a flawless plate model. a) H_x. b) H_z.*

Simulation results agree closely to the experimental results. The simulation model is further validated using different levels of the magnetising field, as recorded in Table 5.2.

Previously has been remarked that the plots in Figure 6.12 result from a magnetised plate without any defect. As to be expected in a flawed sample, axial and radial components of the MFL signal will be affected for the plate magnetisation. For specific cases in signal assessment can be necessary the removal of these off-set levels from the signals as illustrated by some examples in Section E.1. In this perspective, it is worth mentioning that by in-line tools like PIGs, the sensor array moves simultaneously with the magnetic system in contrast to the simulation and the experimental set-ups in the here performed study, where the magnetic system is fix and the sensor array moves independently. In consequence, as long as a PIG inspection does not detect a reduction of the wall thickness, the H_z component results in a zero field.

6.4.2 Active Region by Hall Sensors

As previously claimed in Section 5.5, the true lift-off of each sensor in the experimental set-up depends on the location of their respective active region. Figures 6.13 and 6.14 report simulation and experimental results as an example of the conducted methodology. The aim is establishing the true lift-off for the sensors which acquire the magnetic field components during scans. Related defect diameter and wall thickness reduction in percentage are set out in the legend.

It is obvious that the active (sensitive) plates of the Hall elements to measure the axial component and the radial component have a finite volume, it is impossible to have both in the same position in the array. Therefore they are placed at different lift-off positions. Due to electrical isolation reasons there exist a finite distance between the two elements too. The difference in the position of the sensors in the array can be clearly observed in the Figure 5.10. The study of all data reported experimentally reveals that

the active zone of the sensors are located with a distance of 1.4 mm apart from each other. For the nominal lift-off of 1 mm is found that the axial component was obtained at 3.5 mm and the radial component at 2.1 mm. Therefore, for 3 mm nominal lift-off results in a true lift-off of the axial component at 5.5 mm and the radial component at 4.1 mm. Besides, 7.5 mm for H_x and 6.1 mm for H_z are established as true lift-offs for the case of nominal 5 mm.

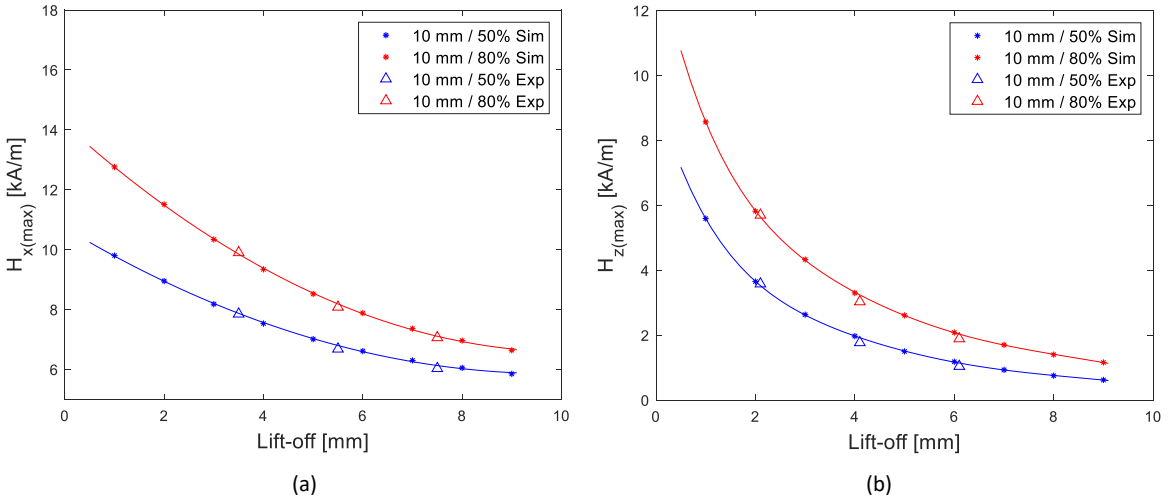

Figure 6.13: *Comparison of the signal maximum amplitude obtained by simulations and experiments at different lift-offs as* ***inner defect*** *configuration. Simulated data are interpolated. a) H_x. b) H_z.*

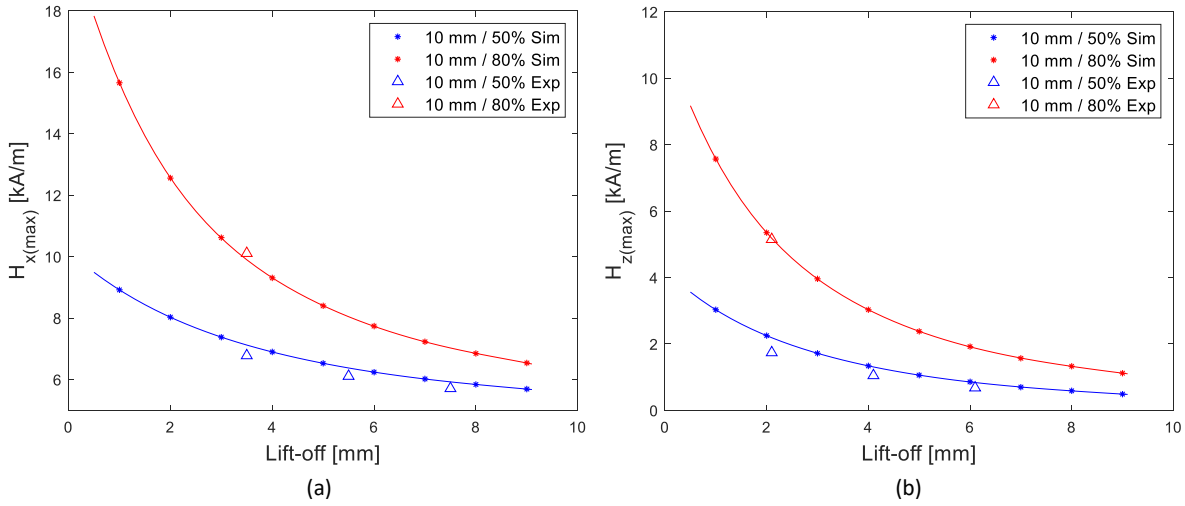

Figure 6.14: *Comparison of the signal maximum amplitude obtained by simulations and experiments at different lift-offs as* ***outer defect*** *configuration. Simulated data are interpolated. a) H_x. b) H_z.*

Accordingly, with the true lift-off found previously, H_x and H_z signals are illustrated in Figure 6.15. Simulation results are reported for axial and radial components at 3.5 mm and 2.1 mm lift-off, respectively. Each component is plotted under the same colour range for the case of inner and outer defect configuration. Thereby the quantitative differences appear straight away beside the qualitative comparison. Furthermore, these results have

been achieved from the same simulation model used to obtained data in Figures 6.8 and 6.9 to provide an instance to recognise clearly the lift-off effect on the signals.

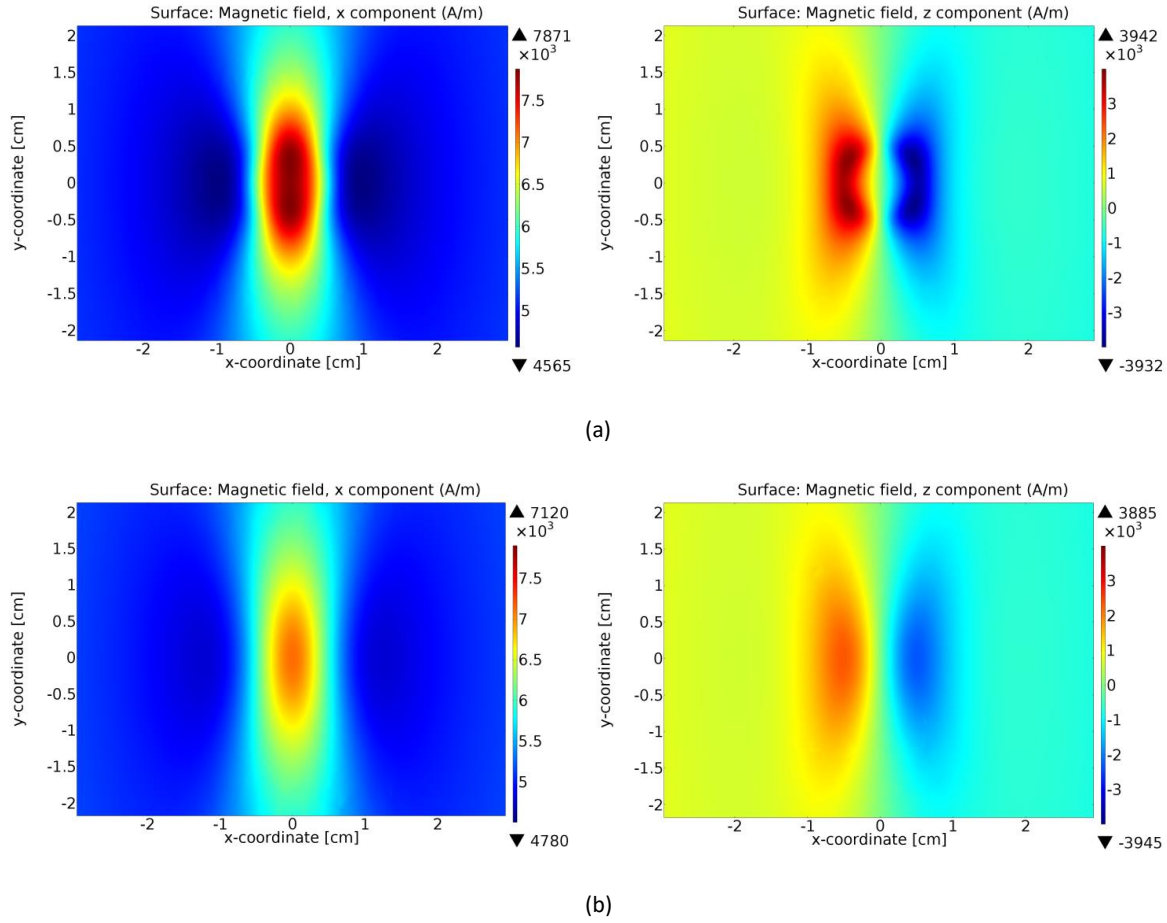

Figure 6.15: *Axial and radial components of the magnetic field at 3.5 mm and 2.1 mm lift-off, respectively. a) Inner defect. b) Outer defect.*

A comparison of simulation and experimental results for every leaked component of interest is delivered as next, continuing with the analysis of the calotte defect. This set of C-scans starts with Figure 6.16, which illustrates the axial component at 3.5 mm lift-off under inner defect configuration. Simulation outcome is limited to an area approximately of 6 cm × 4.5 cm, that includes the defect and around the defect area. Concurrently, experimental results are reported through the complete scanned area of 12 cm × 16 cm accompanied by a related zoomed plot matching the area of the simulation result.

Likewise, Figure 6.17 presents the radial component at 2.1 mm lift-off under inner defect configuration. While Figures 6.18 and 6.19 show the results for axial and radial components respectively by outer defect case. Here the results are shown in grey-scale to avoid incompatibility on the colour assignment of the scales by the required software. Attention should be paid by the magnetic field unit since for the simulation it is expressed as A/m, while for the experiments as A/cm. Also, the unit of the x-coordinate is set in cm by the simulation and in mm by the experimental full-scan.

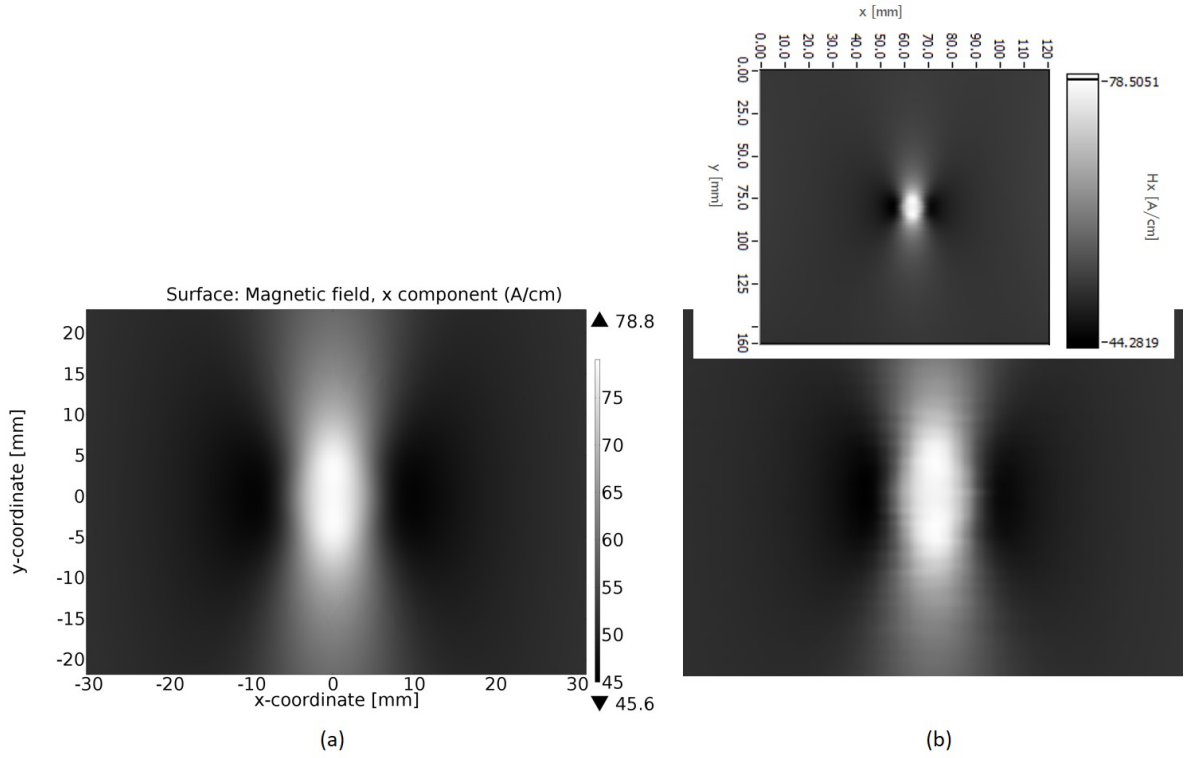

Figure 6.16: *H_x at 3.5 mm lift-off.* ***Inner defect*** *of 10 mm in diameter and 50% of plate thickness reduction. a) Simulation. b) Experiment.*

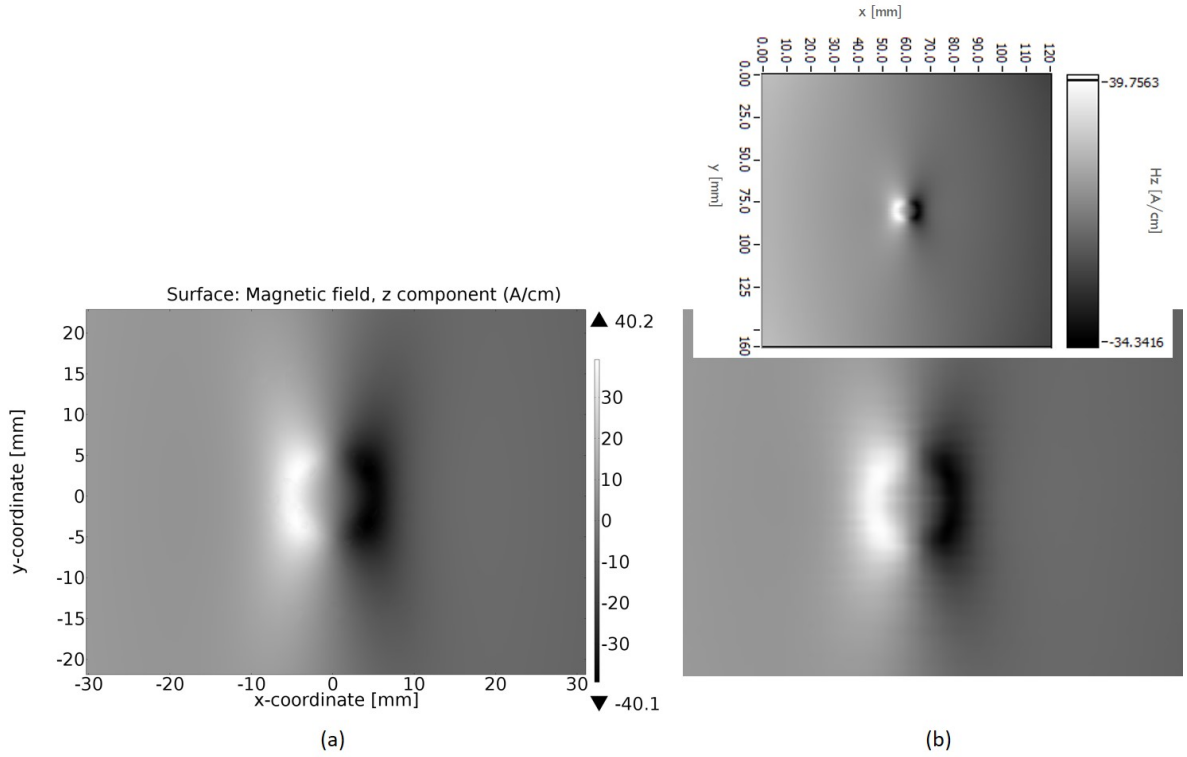

Figure 6.17: *H_z at 2.1 mm lift-off.* ***Inner defect*** *of 10 mm in diameter and 50% of plate thickness reduction. a) Simulation. b) Experiment.*

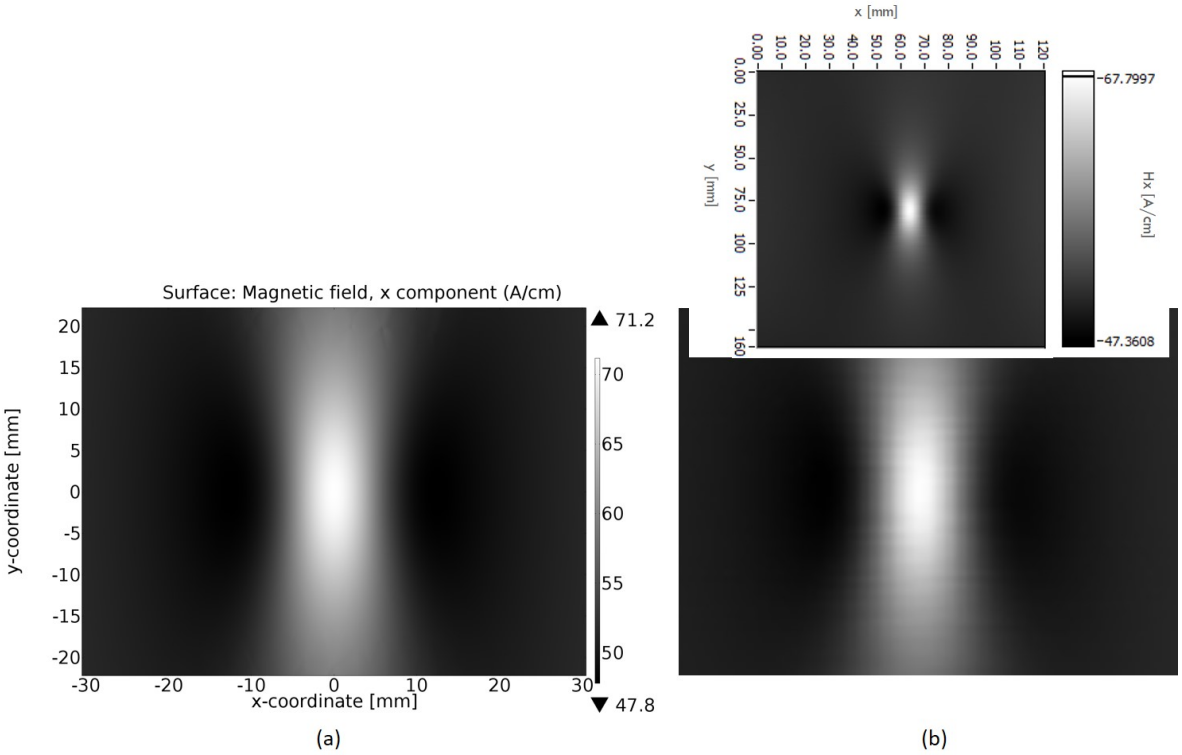

Figure 6.18: *H_x at 3.5 mm lift-off.* ***Outer defect*** *of 10 mm in diameter and 50% of plate thickness reduction. a) Simulation. b) Experiment.*

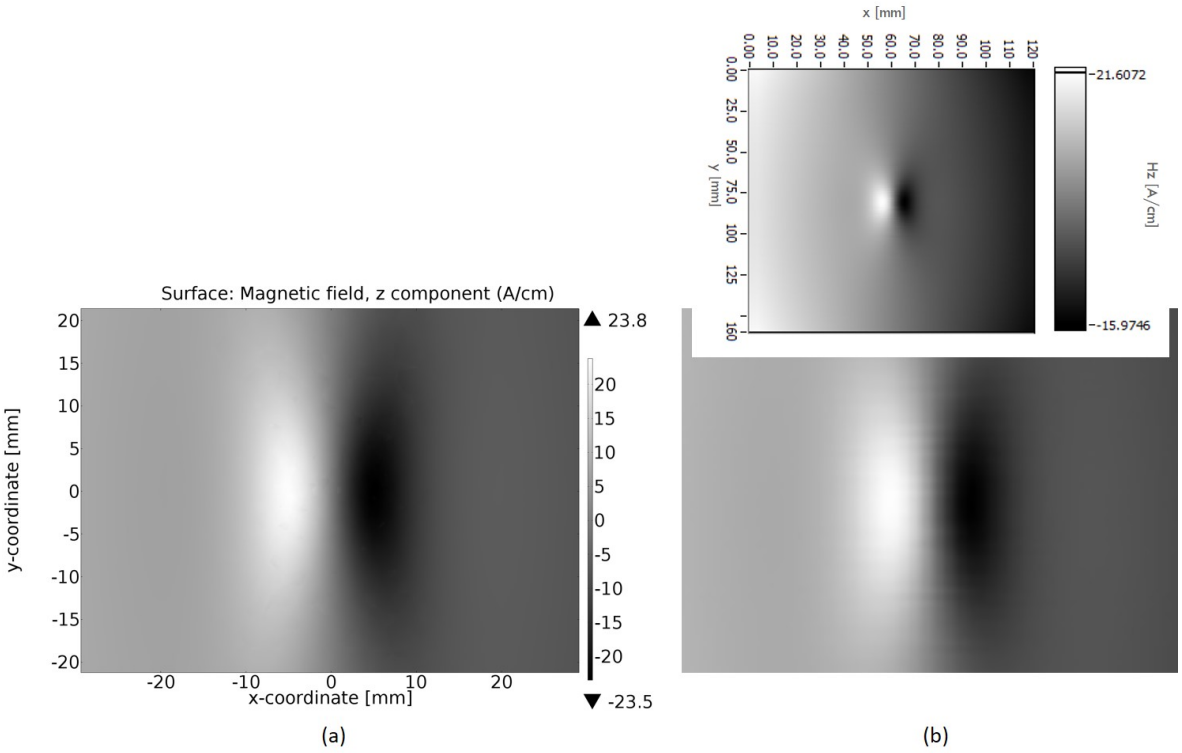

Figure 6.19: *H_z at 2.1 mm lift-off.* ***Outer defect*** *of 10 mm in diameter and 50% of plate thickness reduction. a) Simulation. b) Experiment.*

H_x and H_z signals are introduced as amplitude locus curves to facilitate the comparison between simulation and experimental results. They are obtained at the same lift-off assumed for previous C-scans providing a reference line at $y = 0$. Related signals from the inner defect configuration can be seen in Figure 6.20 and from the outer defect case in Figure 6.21.

The assessment of axial and radial components proceeds considering their dependency on the applied field, defect dimensions and lift-off as divided below into subsections. Specific requirements in order to conduct the signal analysis are exposed below for every parameter.

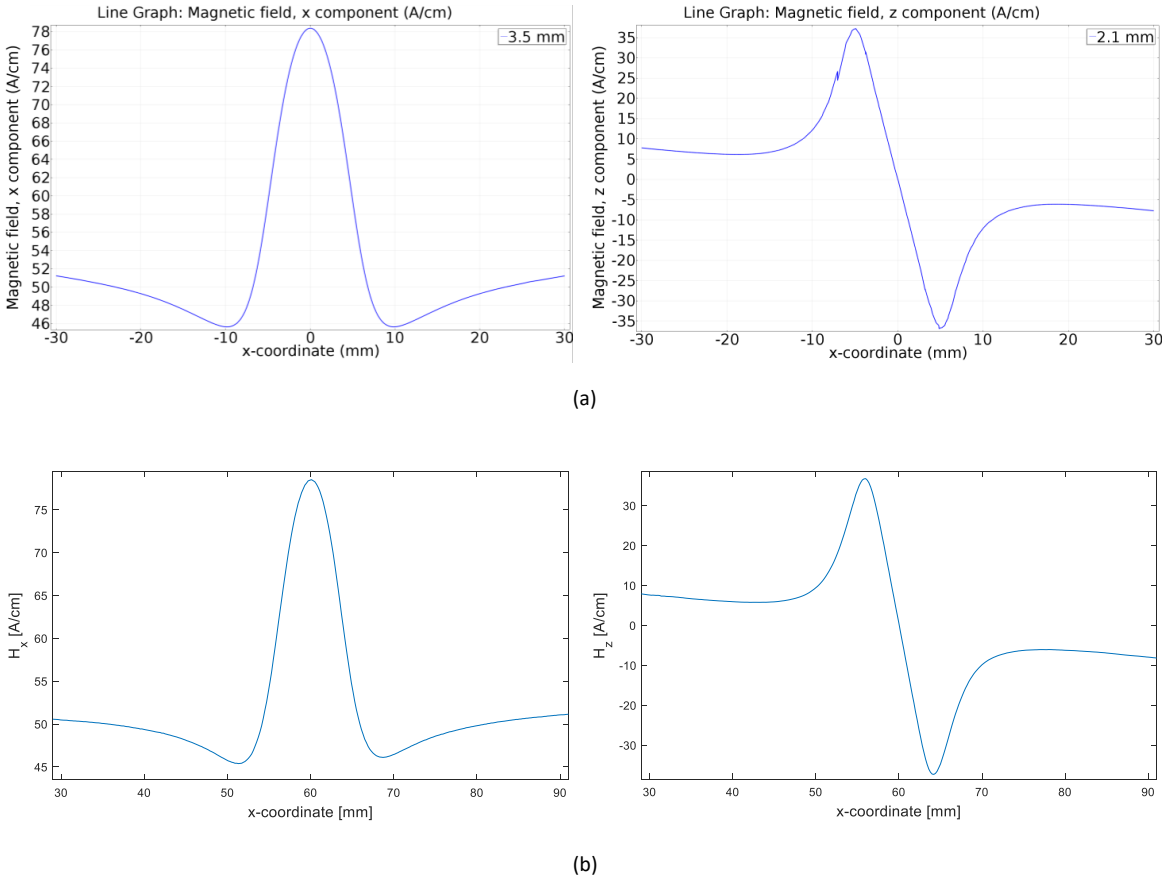

Figure 6.20: *Comparison of H_x and H_z components for the* ***inner defect*** *configuration employing amplitude locus curves obtained by: a) Simulation and b) Experiments. It should be noted the differences on the coordinate units.*

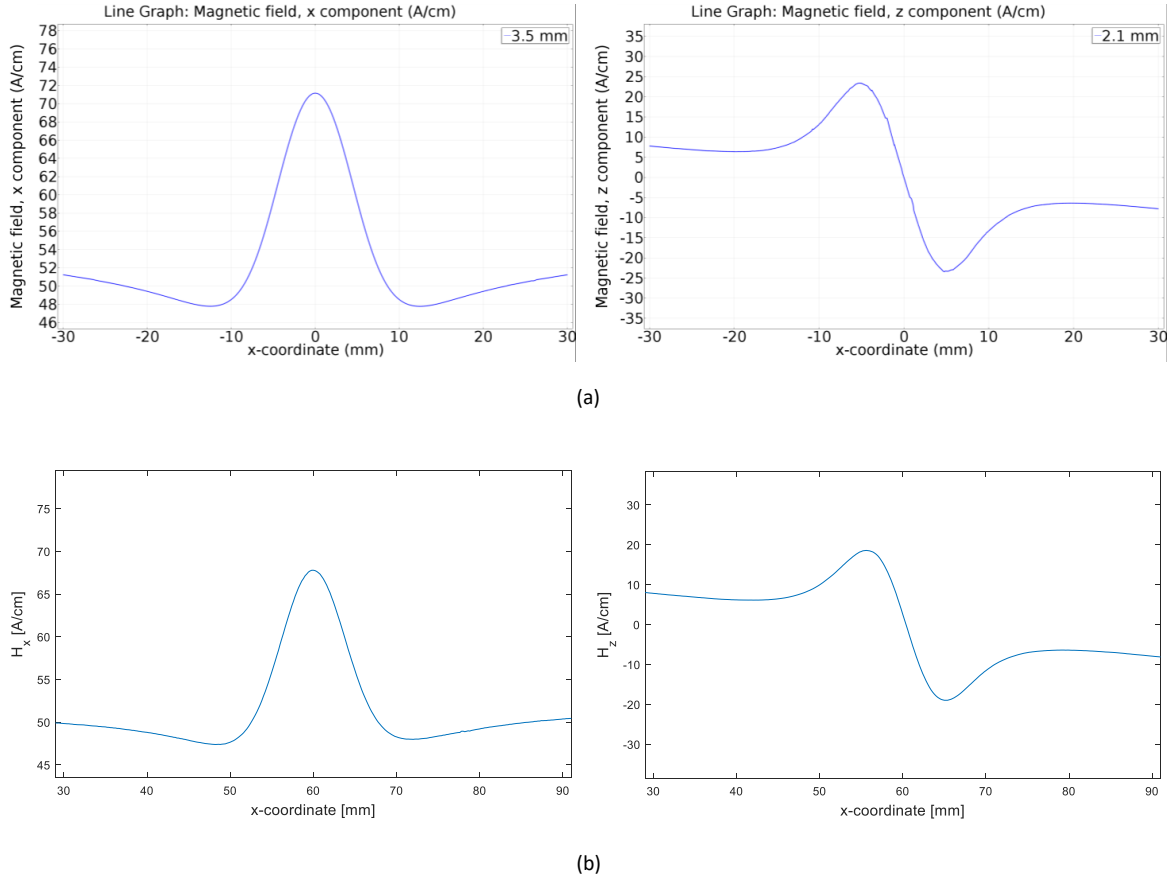

Figure 6.21: *Comparison of H_x and H_z components for the **outer defect** configuration employing amplitude locus curves obtained by: a) Simulation and b) Experiment. It should be noted the differences on the coordinate units.*

6.4.3 Dependency on Applied Field

Experiments were conducted to study the dependency of the MFL signals amplitude on the excitation field. A steel plate containing a cylindrical defect was magnetised through an electromagnet, as shown in the set-up by Figure 5.9. Excitation current to excite the electromagnet is adjusted to five different levels: 0.25 A, 0.5 A, 1 A, 2 A and 3 A achieving H_x fields at 3.5 mm lift-off of 1.35 kA/m, 1.5 kA/m, 2.7 kA/m, 5.2 kA/m and 7.4 kA/m respectively. According to experimental results in Figures 6.3 and 6.4, the permeability varies for this $\mathbf{H}_0$ range between 730 to 200, taking into account a stressed material. Figure 6.22 reports data obtained from axial and radial components of the leaked field due to the presence of a defect in the plate. The defect has a diameter of 10 mm, and its depth reaches 50% of the wall thickness. The figure illustrates the amplitude of H_x and H_z signals at 3.5 mm and 2.1 mm lift-off, respectively. It should be noticed that the off-set field inherent to the H_x component is removed before plotting. The off-set field level is defined in every instance as the axial field measured in an area where no defect is detected.

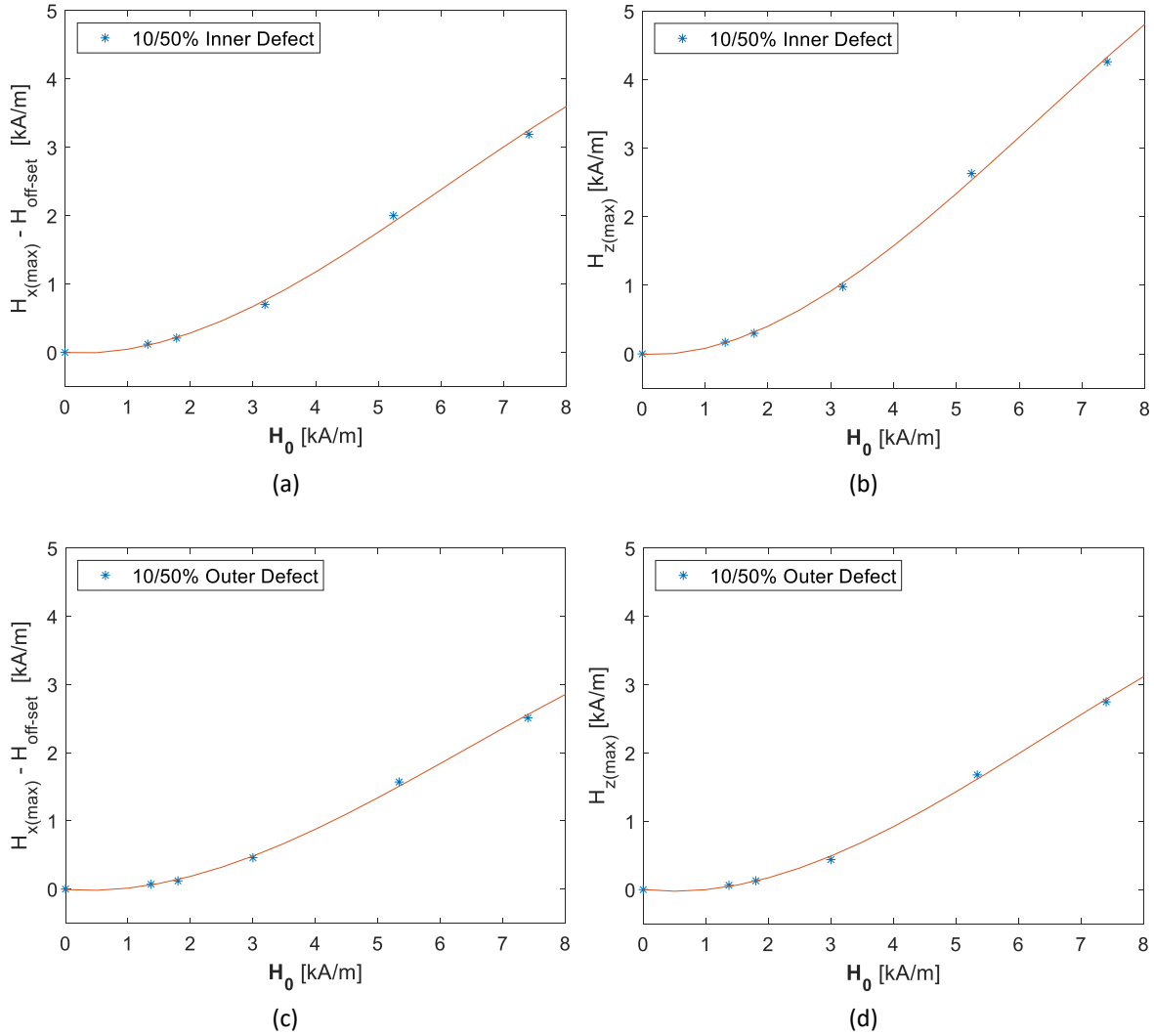

Figure 6.22: *H_x and H_z signal amplitude relationships to the applied field. The defect has a cylindrical shape with 10 mm in diameter and 50% of plate thickness reduction. a) Axial component as* ***inner defect****. b) Radial component as* ***inner defect****. c) Axial component as* ***outer defect****. d) Radial component as* ***outer defect****.*

From Figure 6.22 can be affirmed that the amplitudes of H_x and H_z raise linearly as $\mathbf{H}_0$ increases beyond 3 kA/m. This behaviour is valid in both instances, for inner defect as well as for outer defect.

Additionally, five different defects with calotte shaped were experimentally assessed in order to confirm the linear behaviour of the leaked field components respect to the applied field. This analysis is conducted because the calotte shape is chosen in this research to characterise corrosion problematic. The amplitudes of H_x and H_z are plotted in Figure 6.23, starting the magnetisation at around 3 kA/m. Diameter in mm and wall thickness reduction as a percentage are indicated for every case at the plot legend. All measurements are conducted at 3.5 mm lift-off to acquire H_x component, while a lift-off of 2.1 mm is assumed for the H_z component.

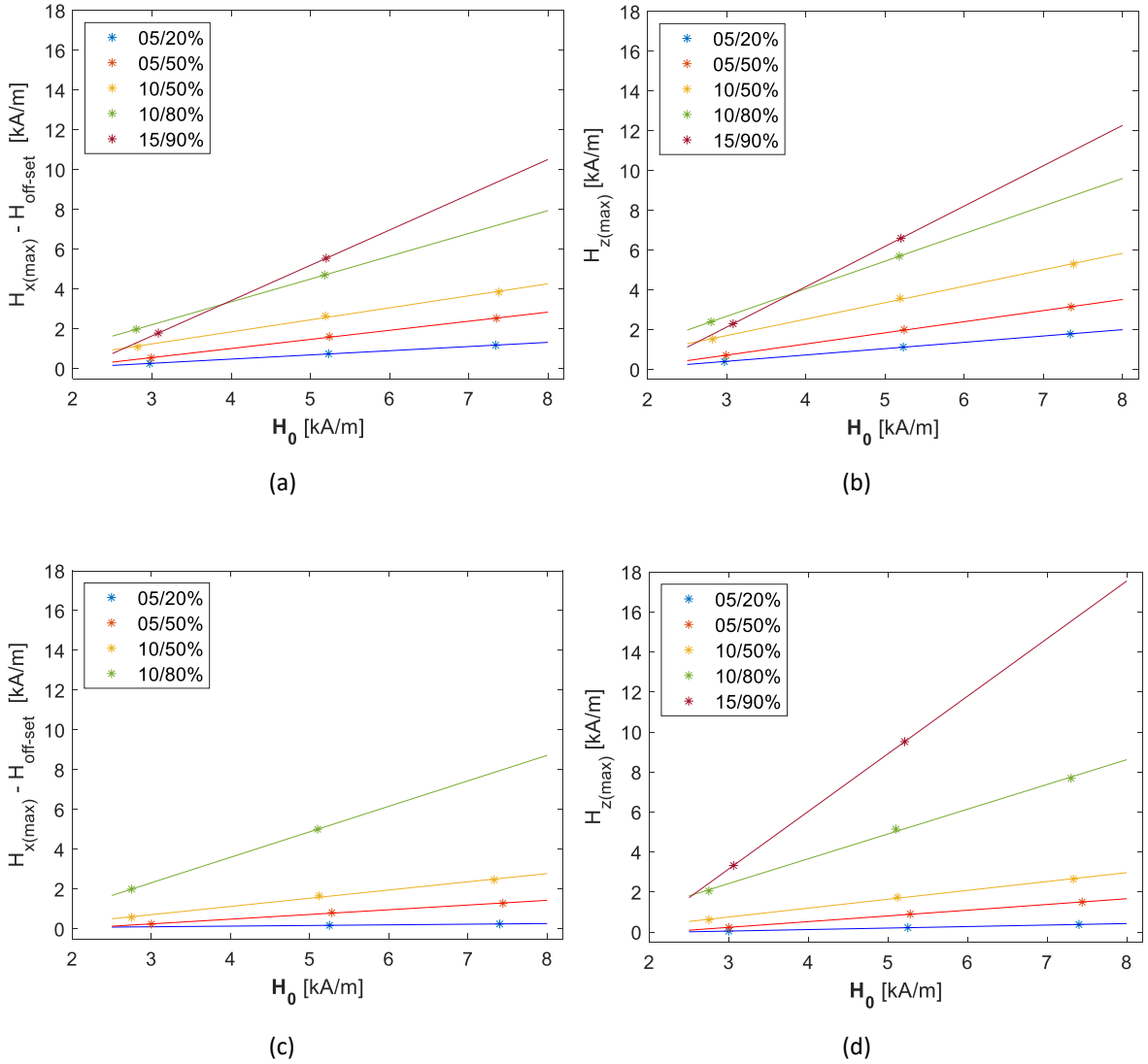

Figure 6.23: *MFL signal amplitude dependency on applied field for calotte shape defects. Defect diameter in mm and plate thickness reduction in percentage as displayed in the legend. a) H_x by* ***inner defects****. b) H_z by* ***inner defects****. c) H_x by* ***outer defects****. d) H_z by* ***outer defects****.*

Returning to the theoretical analysis, the attention is addressed to the Equation 3.21, which introduces the dependency of the MFL response on permeability through the function $(\mu-1)/(\mu+1)$. Figure 6.24 illustrates the behaviour of this term as the applied field increases. The plot includes the field range used in this study for experiments, namely from 152 A/m until 87 kA/m.

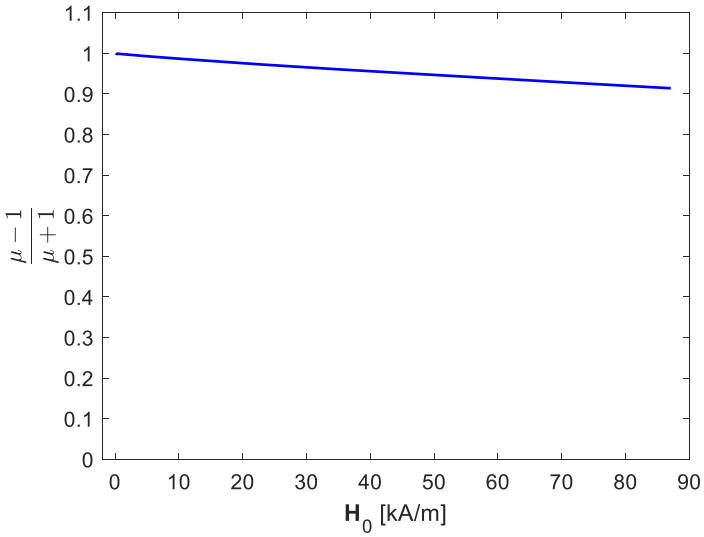

Figure 6.24: *Reliance of the term* $(\mu - 1)/(\mu + 1)$ *from Equation 3.21 respect to the applied field.*

6.4.4 Dependency on Defect Size

The methodology to conduct the study of MFL signal dependency related to defect dimensions is divided into three subsections in Section 5.5.2. This structure provides an ordered summarised view of the process. Here, in this section are reported the results of these three stages.

Model features and conditions are described for the initial simulation approach in Section 5.5.2.1. Obtained results agree qualitatively with results presented previously in Figures 6.8 and 6.10 for inner defect configuration and in Figures 6.9 and 6.11 for the outer defect case. Obviously, the contour of the defect by the C-scans can clearly be identified in all of the components. Only a contour-tracking algorithm has to be applied. In fact, as in Figure 6.8, the two maxima along the y-coordinate at $x = 0$ by the axial component seem to allow determining the defect dimension in the y-direction [102]. An example employing amplitude locus curves is as next reported in Figure 6.25, it compares H_x and H_z components as a function of the defect depth, while the defect length is kept constant.

Under inner defect configuration, as in the cases plotted in Figure 6.25, the peak-width at half-maximum (PWHM) for the axial component H_x and the peak-to-peak-distance (PTPD) for the normal component H_z are invariant against defect depth changes and only a function of the defect length. For an overview of this criterium, refer to Section E.2. Based on Figure 6.25 can be claimed that there is a unique criterion determining defect length in case of inner defects. For outer defects, this is not true because of the large lift-off from the scan-plane to the defect-plane acts like a spatial low-pass-filter and cancels-out information [102].

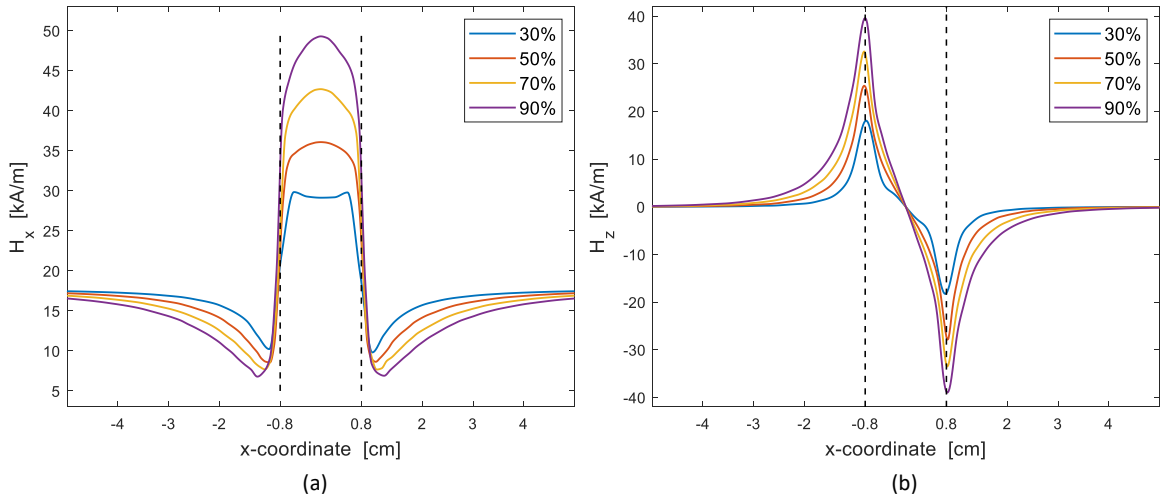

Figure 6.25: *Leaked field components at 1 mm lift-off of an **inner defect** with 16 mm of diameter and different defect depth in percentage of the plate thickness. a) Axial component. b) Radial component.*

Figure 6.26 illustrates the overall results concerning the relationship between signal amplitudes and geometry parameters. All relationships determined here are linear (see regression analysis) when defect depth varies in the parameter range as indicated. Obviously, that is not the case with defect length, where saturation effects can be observed. Furthermore, whereas H_z is increasing as the defect length increases at each defect depth value, H_x is decreasing [102]. Regarding the amplitudes, it should be considered that H_x components seem to be larger. On the contrary, they are only shifted by a field equals the applied field due to the magnetisation. In this context, can be stated that in almost all cases H_z amplitude is larger than H_x amplitude, except for the defect with 12 mm in diameter and 90% deep.

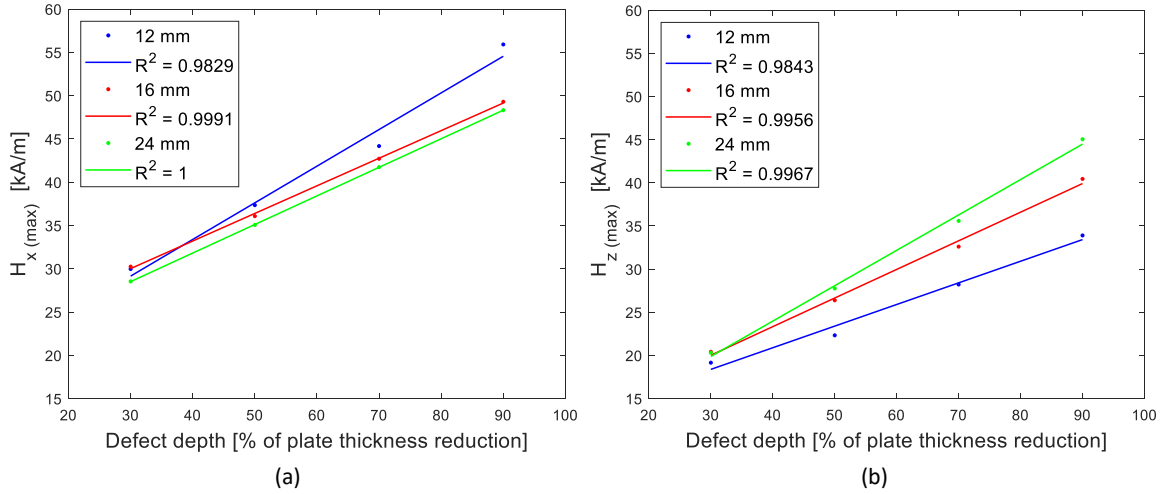

Figure 6.26: *Maximum amplitudes of H_x and H_z for **inner defects** with different depths. Defect diameters according to the legend.*

Dobmann et al. [108] documented the case of cracks and small crack width (< 1 mm). In contrast to the results here accomplished for corrosion like defects, Dobmann et al.

observed an amplitude increase by bothH_x and H_z as the defect width increases, starting from zero up to an extended saturation, then followed by a decreasing in case of larger width in the mm range and even larger.

In order to study experimentally, the behaviour of H_x and H_z amplitudes respect to the changes in defect dimensions, 88 experiments are performed under different conditions as explained in Section 5.5.2.2. A whole area is scanned at a specific lift-off between defect and sample surface. Such recording signals allow for C-scan reconstruction as considered in Figures 6.16 to 6.19. However, the resolution in a real inspection is much lower. Thus the signal assessment is addressed preferably to amplitude locus curves. Figure 6.27 illustrates the axial and radial leaked field components at 3.5 mm and 2.1 mm of lift-off, respectively. Signals resulting from two defects are reported, each has a diameter of 10 mm and the depth as states in the legend by a percentage of plate thickness reduction.

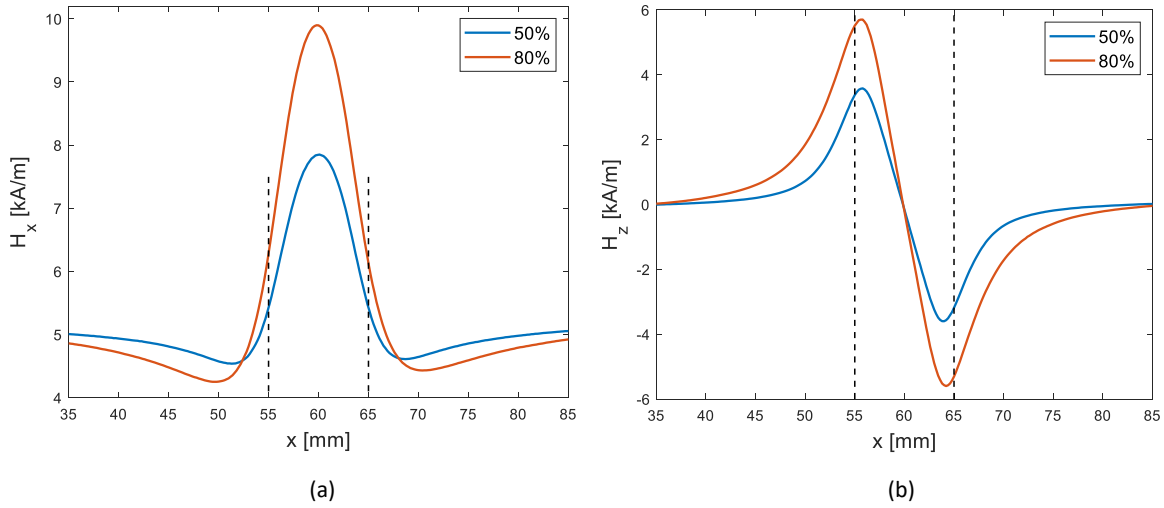

Figure 6.27: *Experimental results of the leaked field components of* ***inner defects*** *with 10 mm of diameter and different defect depth expressed in percentage of the plate thickness. a) H_x. b) H_z.*

These experimental results are reported mainly as an example to compare their behaviour with the simulation results presented in Figure 6.25. As can be observed in Figure 6.27, the PWHM for the axial component and the PTPD for the normal component are not longer invariant against defect depth changes. Although previous simulation results report the almost insignificant effect on the determination of the defect length using 1 mm lift-off, experiments in contrast report differences depending on the defect depth. This disagreement occurs because the active region of the sensors forced the lift-off to be larger than this minor nominal value, as demonstrated in Section 6.4.2. Therefore, the influence of the lift-off should also be considered by the defect length setting.

Figure 6.28 reports experimental results for two defects with 10 mm of diameter and plate thickness reduction of 50% and 80% in each case considering the outer defect configuration. The lift-off assumed for scanning is the same as for inner defects: 3.5 mm

for the axial component and 2.1 mm for the radial component.

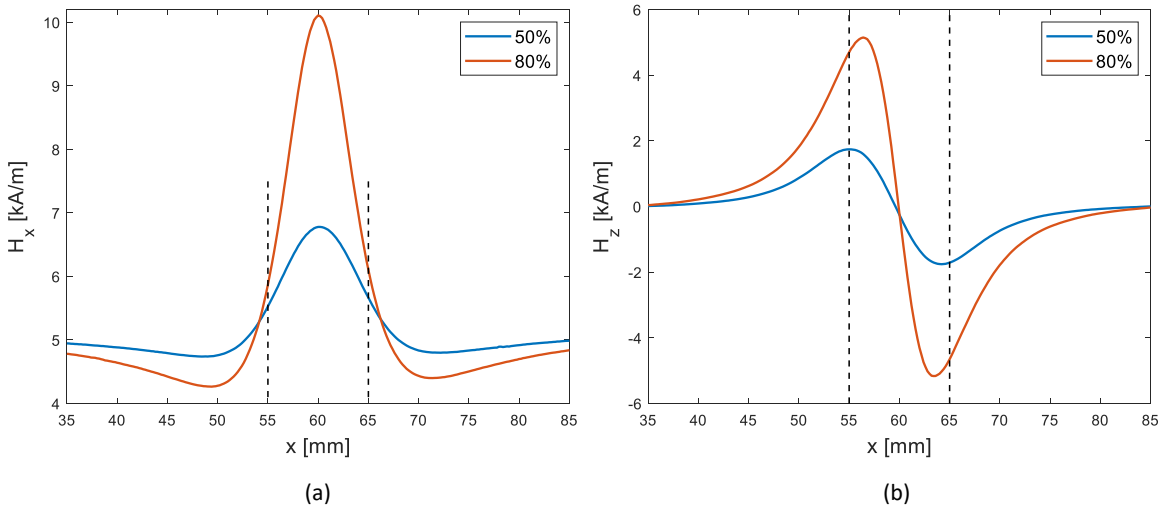

Figure 6.28: *Experimental results of the leaked field components of* ***outer defects*** *with 10 mm of diameter and different defect depth expressed in percentage of the plate thickness. a) H_x. b) H_z.*

The results achieved experimentally are exploited to optimise the simulation model entailing critical changes, as discussed in Section 5.5.2.3. In addition, the MFL signal comparison for a set of simulated defects with the same diameter and different depths are plotted in Figure 6.29 for inner defects and in Figure 6.30 for outer defects.

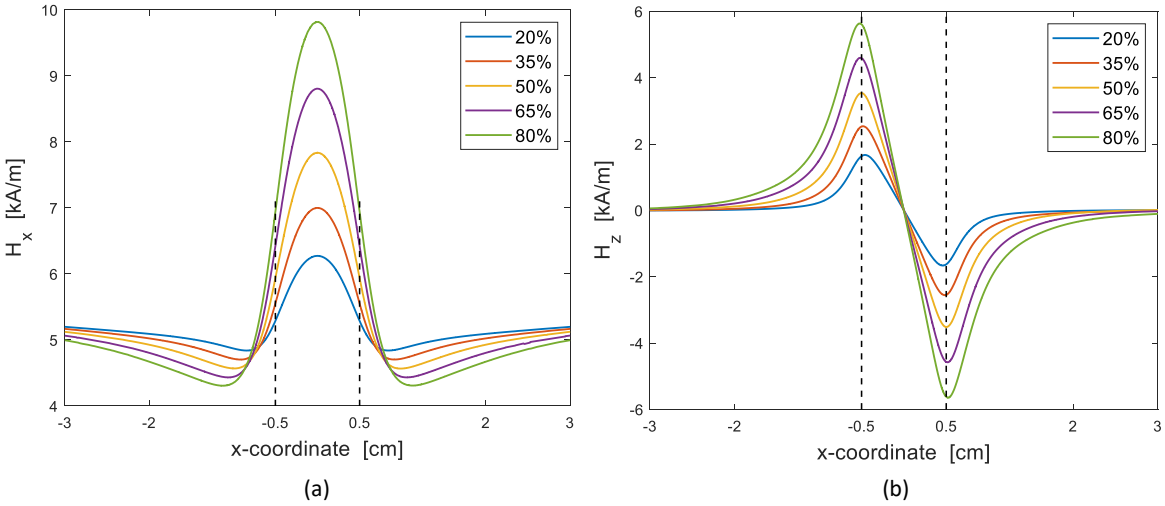

Figure 6.29: *Leaked field components of* ***inner defects*** *obtained by simulation. Defects of 10 mm in diameter and depths according to the legend in percentage of the plate thickness. Scanned lift-off at 3.5 mm and 2.1 mm respectively for: a) Axial component b) Radial component.*

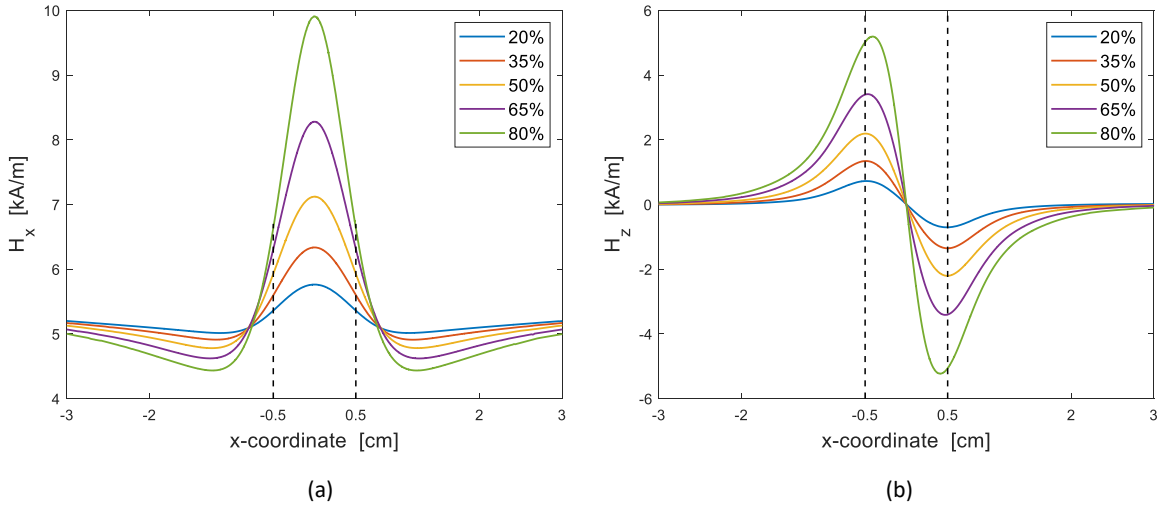

Figure 6.30: *Leaked field components of* ***outer defects*** *obtained by simulation. Defects of 10 mm in diameter and depths according to the legend in percentage of the plate thickness. Scanned lift-off at 3.5 mm and 2.1 mm respectively for: a) Axial component b) Radial component.*

H_x signals are presented including the shifting due to the off-set level. However, the off-set of H_z components is removed with the purpose to provide a clear feature comparison. Characteristics of the H_x and H_z off-sets are discussed in Section 6.4.1. In addition, a pair of examples are illustrated in Appendix E, considering signal treatment to eliminate the off-set levels for both components. Indeed, plotted results are taken from defects with different diameters, namely 5 mm and 15 mm to provide evidence from different defect sizes confirming that the behaviour is not a particularity of defects with 10 mm of diameter.

Results from 60 different simulation cases and 16 experiments are plotted as next in order to obtain a general overview of the H_x and H_z amplitudes relationship to the defect size. Figures 6.31 and 6.32 provide these simulation results fitted by a line and accompanied by the related regression coefficient. Variation in amplitude are considered related to changes in depths for three different defect diameters: 5 mm, 10 mm and 15 mm.

The signal amplitudes in Figures 6.31 and 6.32 are plotted after removing the off-set level generated due to the magnetisation, so that, only the amplitude of the leaked field is taking into account for the assessment. Based on these results, it can be affirmed that the amplitude of both signals, H_x as well as H_z increases as the defect diameter increases. Interestingly, this statement disagrees with results reported in Figure 6.26a where the amplitude of H_x decreases as the defect diameter increases, while the defect depth is kept constant. This difference in the behaviour of the H_x component arises from the fact that in the simulation model to obtain the results in Figure 6.26 is assumed with a lift-off of 1 mm, in contrast to that fact, the data in Figure 6.31 come from the simulation model, which considers the true lift-off, namely 3.5 mm for the axial component and 2.1 mm for the radial component. H_x and H_z dependencies on lift-off will be discussed below in Section 6.4.5.

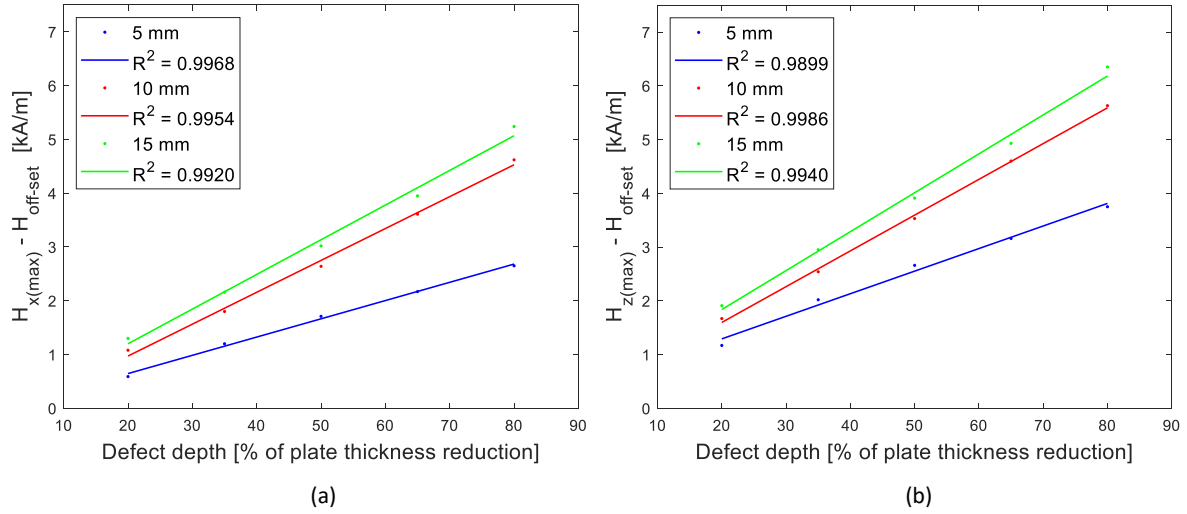

Figure 6.31: *Maximum amplitudes of H_x and H_z for* ***inner defects*** *with different depths. Defect diameters according to the legend.*

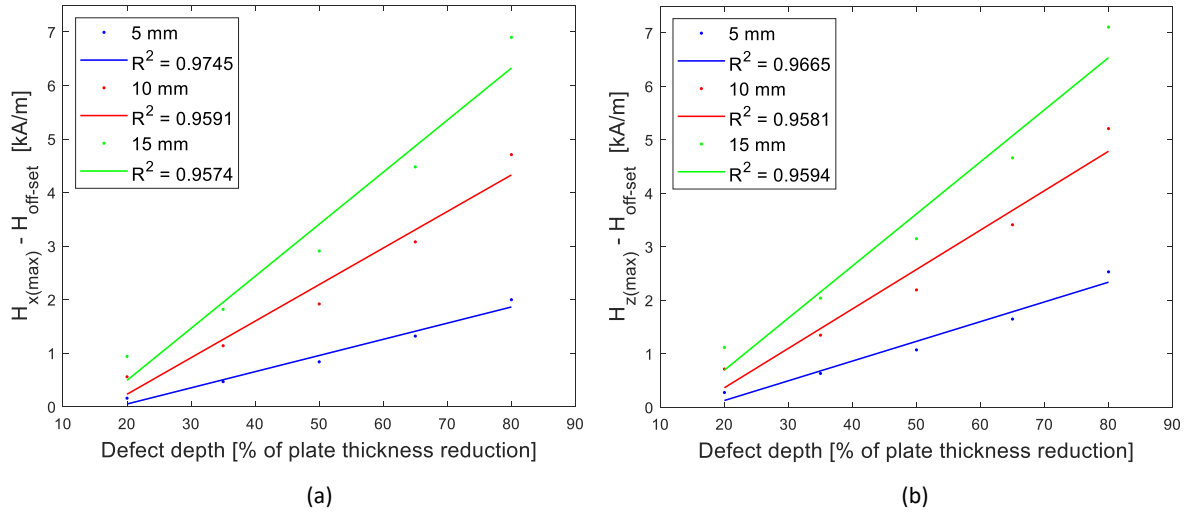

Figure 6.32: *Maximum amplitudes of H_x and H_z for* ***outer defects*** *with different depths. Defect diameters according to the legend.*

On the other hand, Figures 6.31 and 6.32 have confirmed that the signal amplitude of H_x and H_z components are larger for inner defects than for outer defects in most of the assessed defects. However, as the defect depth increases, this difference in the signal amplitude from inner and outer defects reduces and the amplitude of the outer defect becomes larger than the corresponding signal by inner defect. This behaviour is even more remarkable by defects with larger diameters. For example, the H_x and H_z amplitudes of a defect with a diameter of 15 mm and 35% wall thickness reduction are larger by inner defects than for outer defects, while the H_x and H_z amplitudes of the inner defect are smaller than the outer defect for a 15 mm in diameter defect with 80% of wall thickness reduction.

Figures 6.33 and 6.34 illustrate same simulation results from Figures 6.31 and 6.32

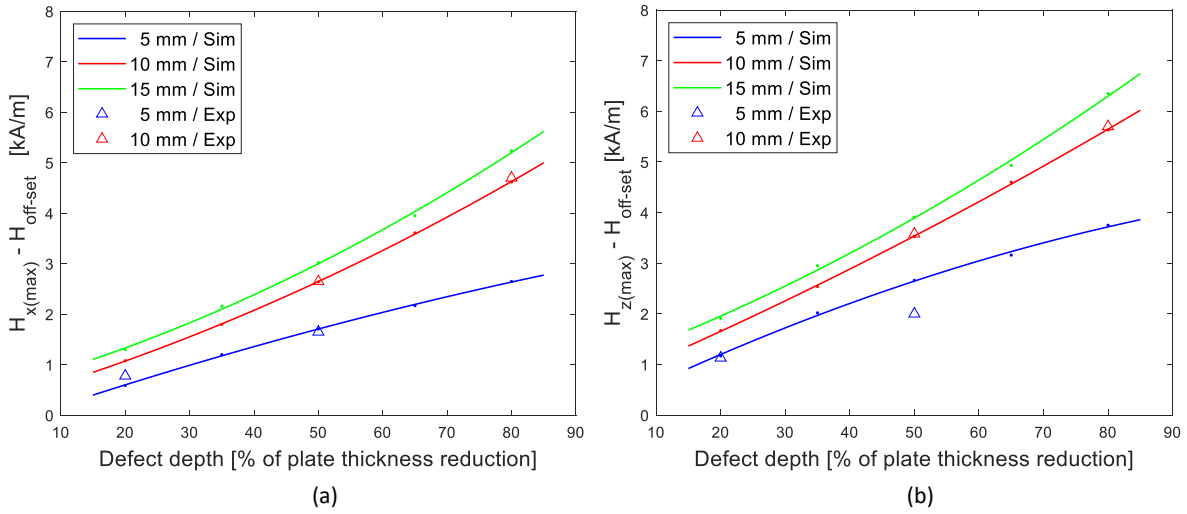

Figure 6.33: *Maximum amplitudes of H_x and H_z for* ***inner defects****. Simulation and experimental results. Defect diameters according to the legend.*

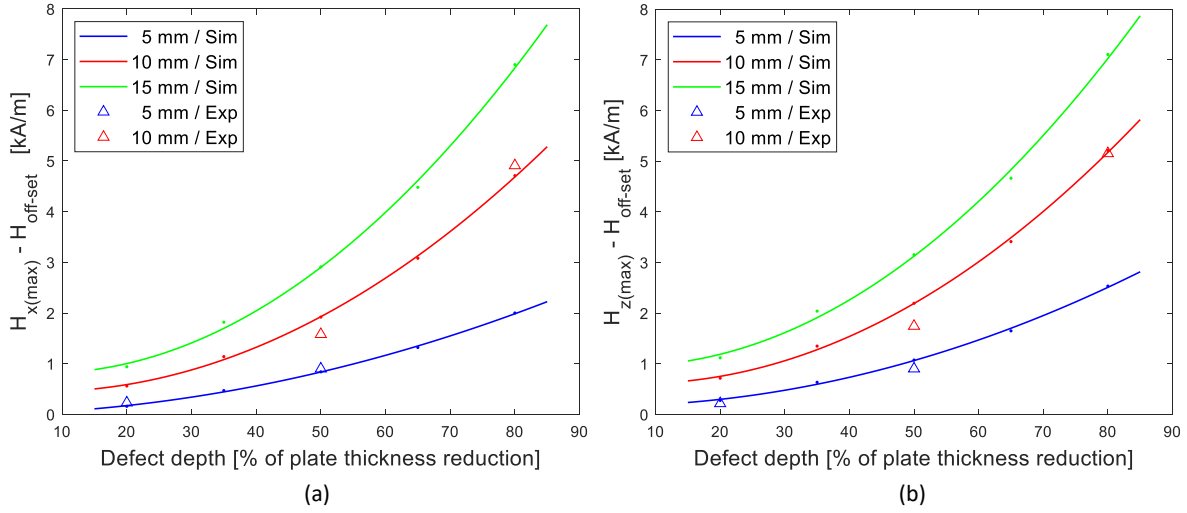

Figure 6.34: *Maximum amplitudes of H_x and H_z for* ***outer defects****. Simulation and experimental results. Defect diameters according to the legend.*

but now using a second order fitting. Experimental results of H_x and H_z amplitudes are also plotted for inner as well as for outer defect configurations. According to the results by inner defects in Figure 6.33, H_z amplitude is larger than the H_x amplitude for some hundreds A/m for all defect depths. While, by outer defects in Figure 6.34, the amplitudes by both components are very similar. In this context, should be emphasize that the H_x component is superposed to an off-set level equal to the applied field, which in this case corresponds to 5.2 kA/m and has been removed in Figures 6.33a and 6.34a for comparison purposes.

Hitherto, it has been discussed the amplitude of the leaked components. Now, the analysis is addressed to the signal length in relation with the defect diameter. In Figures 6.35 and 6.36 are reported H_x and H_z components for inner and outer location of 5

different defects. Each flaw has 10 mm of diameter and a specific depth according to the legend. Dashed lines are introduced in order to define a length equal to the defect length of 10 mm at $x = -0.5$ cm and $x = 0.5$ cm in order to identify the error obtained by applying the PWHM and PTPD criteria. Same dashed lines are drawn in Figures 6.27 to 6.30 for the results achieved by simulation and experiments to allow for comparison.

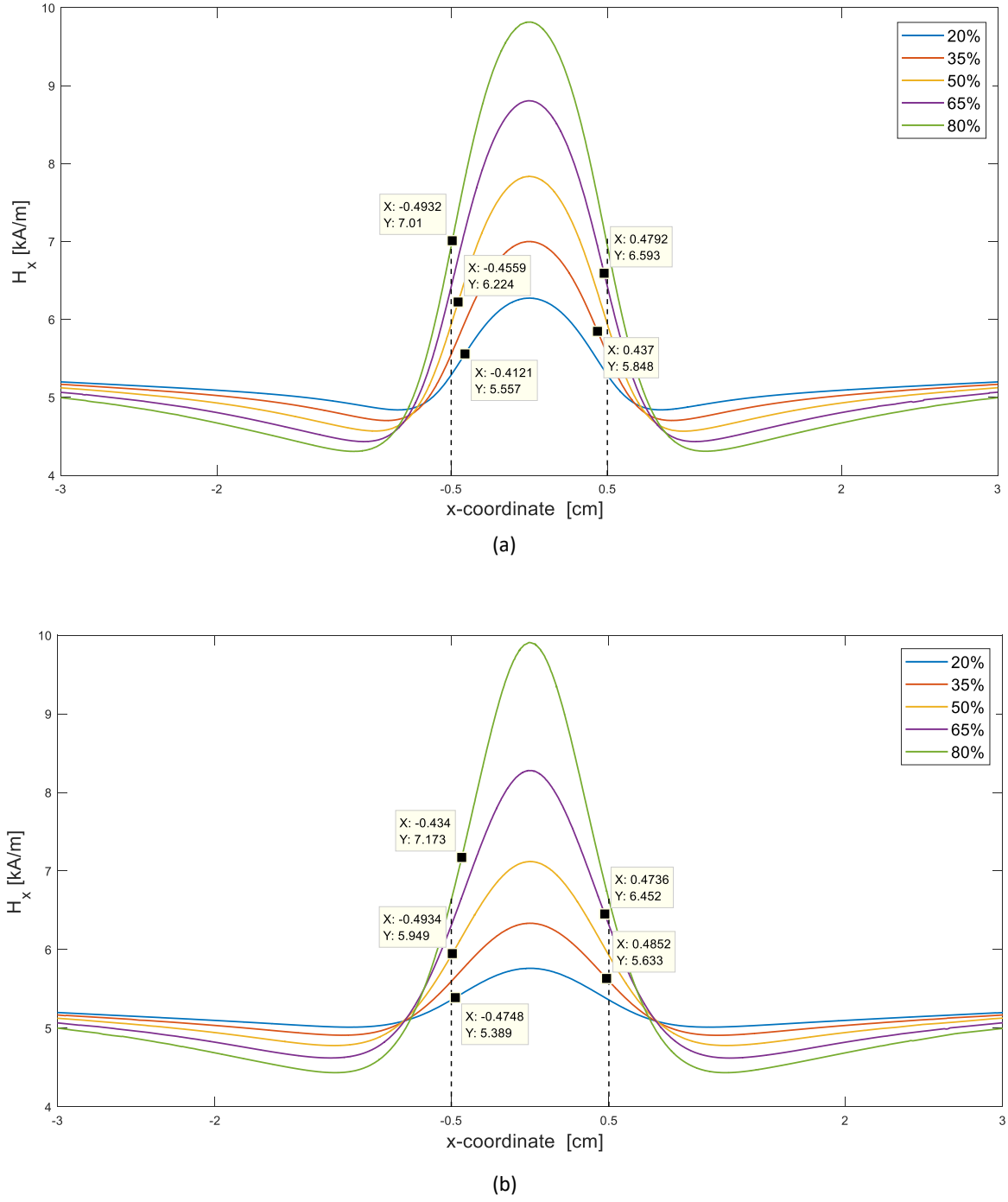

Figure 6.35: *Setting of the defect length based on the PWHM criterion for the axial component at 3.5 mm lift-off by means of simulation results of defects with 10 mm in diameter. a)* ***inner defects****. b)* ***outer defects****.*

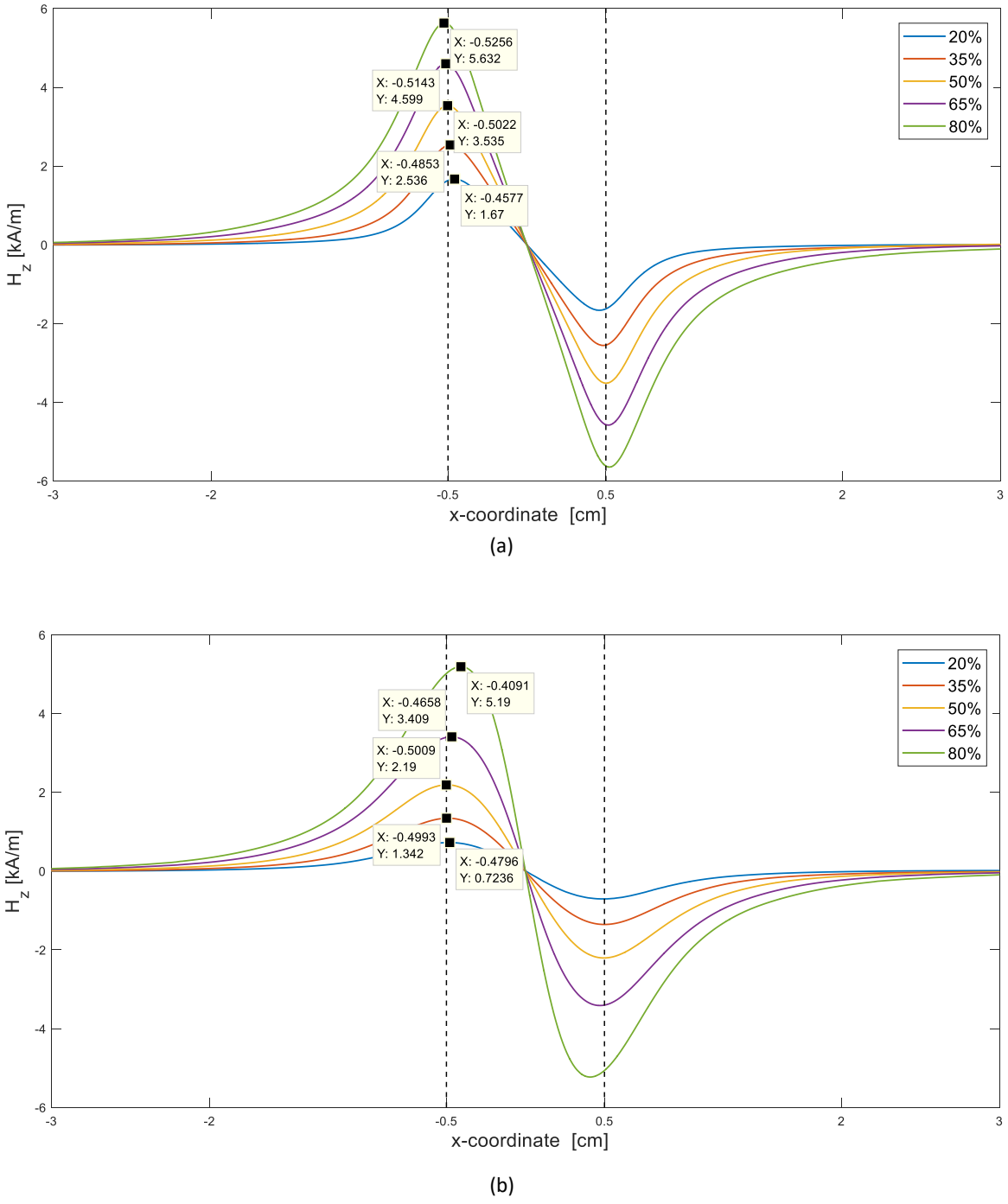

Figure 6.36: *Setting of the defect length based on the PTPD criterion for the radial component at 2.1 mm lift-off by means of simulation results of defects with 10 mm in diameter. a)* ***inner defects****. b)* ***outer defects****.*

The corresponding points obtained according to the PWHM and PTPD criteria are marked in Figures 6.35 and 6.36, respectively. Every figure considers separately the results for inner as well as for outer defects. These plots are an example of all studied cases which in fact demonstrate that the PWHM criterion for the axial component and

the PTPD criterion for the normal component will allow for estimation of the defect length. Auxiliary plots are presented in Section E.2 identifying the parameters to applied PWHM criterion. In addition, Appendix E reports experimental results applying PWHM and PTPD criteria, see Figure E.6.

Tables 6.1 to 6.4 summarise the calculated error on defect length estimation based on PWHM and PTPD for the cases plotted in Figures 6.29 and 6.30 to establish the accuracy of these criteria.

Depth [%]	20	35	50	65	80
Length [cm]	0.8242	0.874	0.9118	0.9584	0.9864
Error [%]	-17.58	-12.6	-8.82	-4.16	-1.36

Table 6.1: *Error by defect length estimation using the PWHM criteria on axial components of* ***inner defects*** *with a real diameter of 10 mm.*

Depth [%]	20	35	50	65	80
Length [cm]	0.9496	0.964	0.9868	0.9472	0.868
Error [%]	-5.04	-3.6	-1.32	-5.28	-13.2

Table 6.2: *Error by defect length estimation using the PWHM criteria on axial components of* ***outer defects*** *with a real diameter of 10 mm.*

Depth [%]	20	35	50	65	80
Length [cm]	0.9154	0.9706	1.0044	1.0286	1.0512
Error [%]	-8.46	-2.94	0.44	2.86	5.12

Table 6.3: *Error by defect length estimation using the PTPD criteria on radial components of* ***inner defects*** *with a real diameter of 10 mm.*

Depth [%]	20	35	50	65	80
Length [cm]	0.9592	0.9986	1.0018	0.9316	0.8182
Error [%]	-4.08	-0.14	0.18	-6.84	-18.18

Table 6.4: *Error by defect length estimation using the PTPD criteria on radial components of* ***outer defects*** *with a real diameter of 10 mm.*

In general, the error obtained by the defect length estimation is smaller than 20%. Particularly for inner defects, there is a clear tendency on the error using PWHM to decrease as the defect depth increases, see Figure 6.35a. In contrast, by outer defects is the error higher at the deepest defect as shown in Figure 6.35b. Regarding the PTPD criterion, the lowest error is achieved for defect depths around 50% of plate thickness

reduction in the case of inner defects as well as for outer defects, see plots in Figure 6.36. Interestingly, the biggest error by both criteria PWHM and PTPD in inner defects occurs for the slightest wall thickness reduction, while outer defects report the maximum error for the deepest defect. Moreover, the estimated defect length will be smaller than the real value by all cases using PWHM. All these statements are also accomplished by experimental results, as can be seen in Figure E.6 as an example.

6.4.5 Dependency on Lift-off

The assessment of the MFL signal behaviour depending on lift-off is addressed in this section to investigate two different signal parameters. First, the length of the axial and radial components to the defect length. And second, the maximum amplitude of axial and radial signal components regarding the defect depth. Simulation and experimental results are reported in this section.

Figures 6.37 and 6.38 present axial and radial components of the leaked field for inner and outer defect configurations, respectively. The selected flaw geometry remains the same, allowing comparison with previous results, that entails a calotte shape with a diameter of 10 mm and 50% of plate thickness reduction. The coordinates are kept constant by the plots of the inner and outer defect cases in order to emphasise differences. The corresponding lift-off of every signal states in the figure legend.

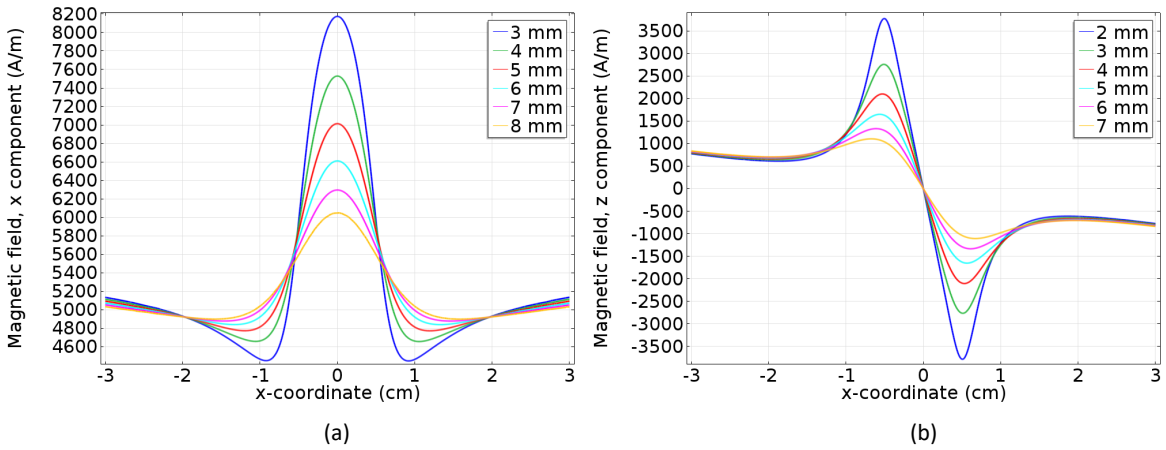

Figure 6.37: *Leaked field components obtained from a simulated defect of 10 mm in diameter and 50% plate thickness reduction.* ***Inner defect*** *configuration. Lift-off settings according to the legend. a)* H_x*. b)* H_z*.*

Additional simulated results are delivered in appendix E plotting the lift-off dependency for defects of 5 mm and 15 mm of diameter, each of them with a thickness reduction of 35%, see Section E.3.

The H_x signals in Figures 6.37a and 6.38a as well as (a) plots by Figures E.7 to E.10 report four points of intersection independently of the lift-off used to acquired each MFL signal. In particular, the two points of intersection in the main peak of H_x

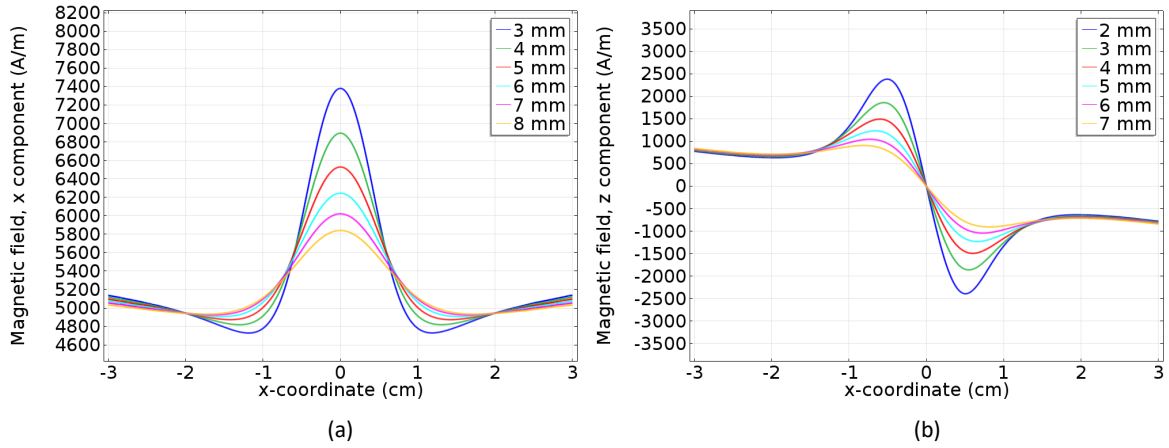

Figure 6.38: *Leaked field components obtained from a simulated defect of 10 mm in diameter and 50% plate thickness reduction.* ***Outer defect*** *configuration. Lift-off settings according to the legend. a) H_x. b) H_z.*

define the defect length. These two points can be used to delimit the defect length, particularly accurately as the defect length increases. In order to delve into this matter, the next section presents experimental results obtained at different lift-off as well as tables reporting the error by length interpretation. Afterwards, an additional section summarises the discussion about amplitude signal dependency on lift-off.

6.4.5.1 Length Dependency

A set of selected experimental results are reported in Figures 6.39 and 6.40. These scans are conducted under inner an outer defect configuration, respectively. In every case is plotted the axial and radial components obtained from samples with three different calotte defect dimensions: first, a defect with a diameter of 5 mm and 20% of plate thickness reduction, the second has also 5 mm in diameter while its depth reaches 50% of plate thickness. Finally, the third sample contains a defect with a diameter of 10 mm and 50% of plate thickness reduction. Related Lift-off was set according to the legend. Figures 6.39 and 6.40 are provided with marks in order to establish the defect length in each instance. On the H_x signals, the points of intersection between pair of signals at different lift-offs are identified, while on the H_z components are emphasised maximum and minimum amplitudes. In that regard, it should be noticed that both components are filtered suppressing the off-set levels, respectively. This process is carried out because it has been proved that removing the off-set reduces the error in the defect length determination. Table 6.5 summarises defect lengths deduced from the experimental results at different lift-offs.

It should be noted that the PWHM criterion is not used on H_x signals to stablish the defect diameter by Table 6.5, but rather the distance between the points of intersection from two H_x signals scanned at different lift-offs. This strategy counts as a valuable method since it is independent on the scanning lift-off. However, H_z signals at different lift-offs do not register any point of intersection allowing the stablisment of the defect

	T_r [%]	Inner defect Length [mm]					Outer defect Length [mm]				
H Comp.		H_x		H_z			H_x		H_z		
Lift-off [mm]		3.5/5.5	5.5/7.5	2.1	4.1	6.1	3.5/5.5	5.5/7.5	2.1	4.1	6.1
⊘ 5 mm	20	4.8	6.4	4.0	5.0	6.2	8.0	9.2	6.4	8.4	
	50	5.6	7.6	4.8	6.0	7.4	7.8	9.8	6.6	8.0	10.0
⊘ 10 mm	50	8.6	10.8	8.2	9.8	11.0	10.6	12.2	9.2	10.6	12.6
	80	9.2	11.4	8.4	10.2	11.8					

Table 6.5: *Experimental results for the calculation of the defect length through axial and radial components. Defect diameter (⊘) in mm and plate thickness reduction (T_r) in percentage.*

length, therefore the PTPD criterion is applied for the H_z component by Table 6.5. In this respect is worth to mention that establishing the maximum and minimum of H_z signal is harder as the lift-off increases because its amplitude reduces strongly and a clear peak tend to disappear. The error on defect length determination using these two strategies by the Table 6.5 is calculated as percentage and summarised in Table 6.6.

	T_r [%]	Inner defect Error [%]					Outer defect Error [%]				
H Comp.		H_x		H_z			H_x		H_z		
Lift-off [mm]		3.5/5.5	5.5/7.5	2.1	4.1	6.1	3.5/5.5	5.5/7.5	2.1	4.1	6.1
⊘ 5 mm	20	-4	28	-20	0	24	60	84	28	68	
	50	12	53	-4	20	48	56	96	32	60	100
⊘ 10 mm	50	-14	8	-18	-2	10	6	22	-8	6	26
	80	-8	14	-16	2	18					

Table 6.6: *Error on defect length determination by experimental results. Defect diameter (⊘) in mm and plate thickness reduction (T_r) in percentage.*

Based on the Table 6.6 can be stated that the accuracy in defect length determination decreases significantly as the lift-off increases. Other fact, is that the error in length determination is considerably high by defect diameters smaller than half of the plate thickness and tend to decrease as the defect diameter increases. This tendency occurs by inner as well as by outer defect configurations. Actually, the largest error in defect length determination for a 5 mm in diameter defect with 50% wall thickness reduction has reached 53% for inner defects and 100% for outer defects. In contrast, the related error for a 10 mm in diameter defect with 50% of wall thickness reduction has been reported at the most 18% for inner defects and 26% for outer defects. This behaviour has been further verified with simulations. Noticeable examples are plotted in Figures E.7 to E.10 for defects with different diameters. These plots show that the intersection point by H_x signals at different lift-offs are considerably sharper defined in the case of defects with a diameter of 15 mm than those with 5 mm in diameter. On the other

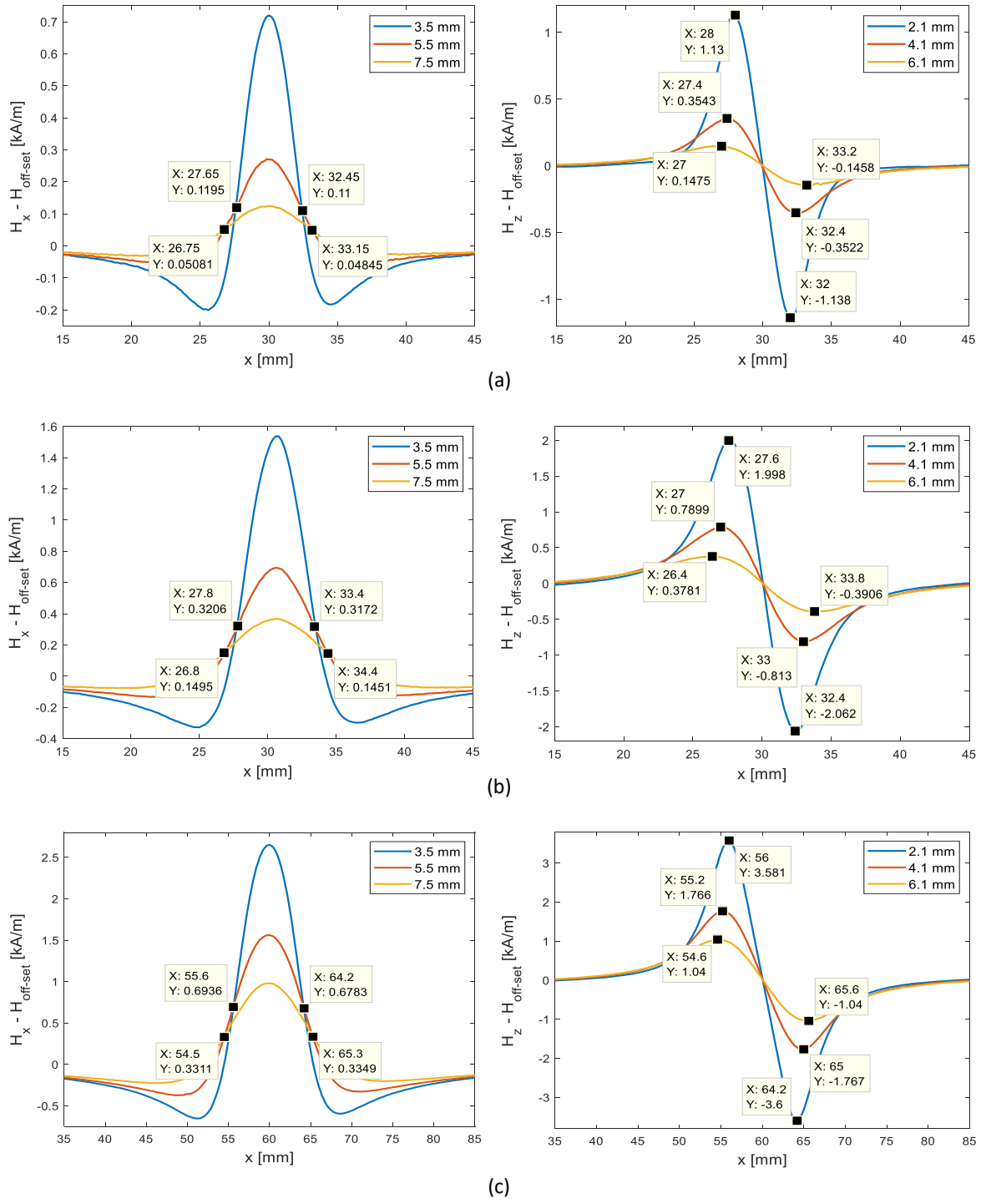

Figure 6.39: ***Inner defects*** *experiments. Lift-off according to the legend. Defect diameter/depth: a) 05mm/20%; b) 05mm/50% and c) 10mm/50%.*

hand, the shifting of the peak-to-peak distance by H_z signals as the lift-off increases is significantly smoother for the defects with larger diameter. Furthermore, from the Table 6.6 can be claimed that in general, the error is larger for outer defect configuration compared with inner defects. However, it should be stressed that most of the cases in Table 6.6 involve defects with 5 mm of diameter, means smaller than half of the plate

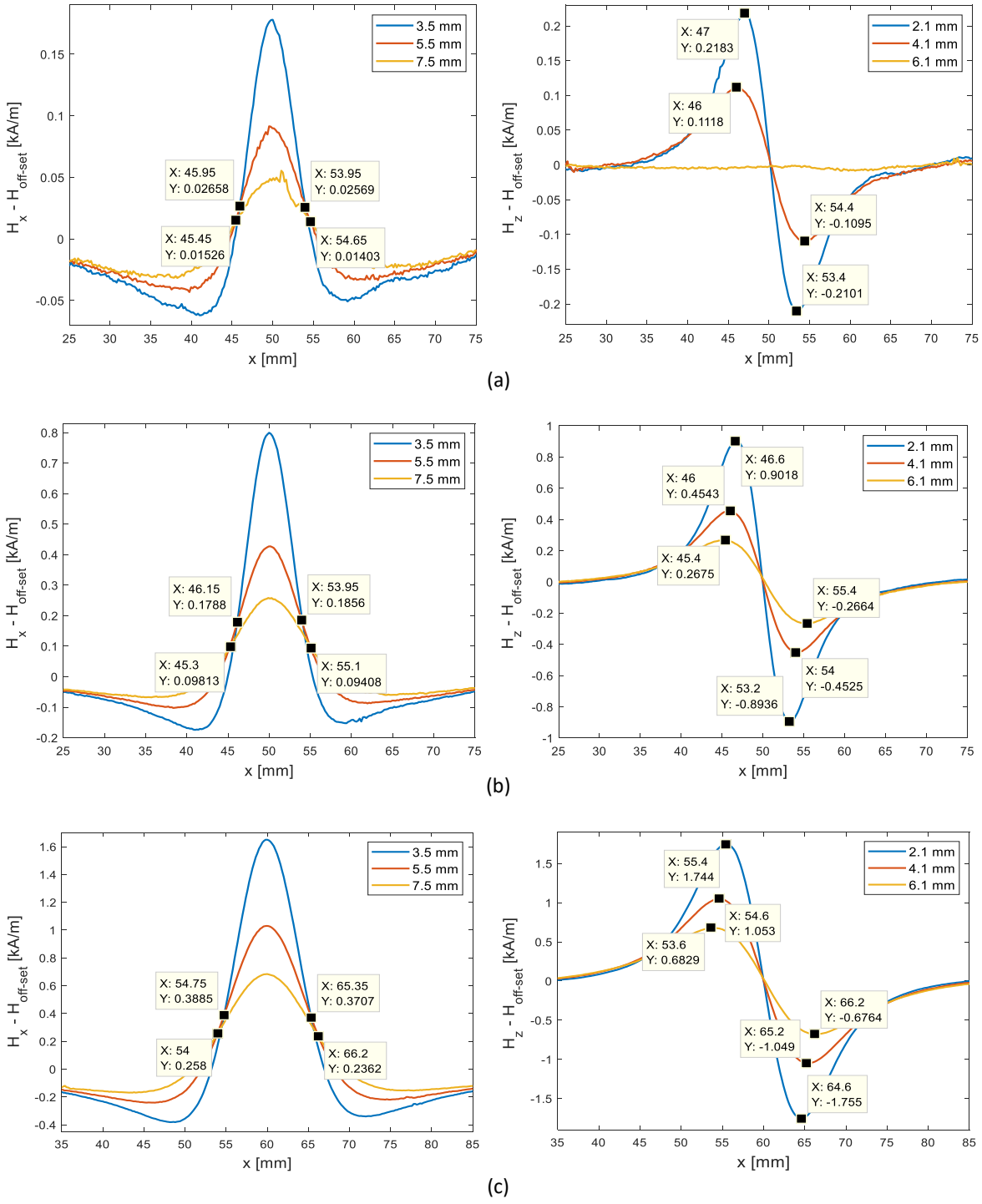

Figure 6.40: ***Outer defect*** *experiments. Lift-off according to the legend. Defect diameter/depth: a) 05mm/20%; b) 05mm/50% and c) 10mm/50%.*

thickness. In fact, for larger diameters, it is not the case as have been observed in Tables 6.1 to 6.4. Focusing on defects with a diameter larger than half of the plate thickness can be claimed that the error by defect length determination depends highly on the defect depth. Interestingly, the defect length defined based on the MFL signals is smaller than the real value in most of the cases, see Figures 6.35, 6.36 and E.6.

6.4.5.2 Maximum Amplitude Dependency

Seven different defects are considered to study the dependency of the leaked field on lift-off. In this regard, H_x and H_z components are assessed for both inner as well as for outer defects. Simulations are conducted for defects of three different diameters: 5 mm, 10 mm and 15 mm, while 20%, 50% and 80% are selected as plate thickness reduction. Initially, five different lift-offs are assumed, from 1 mm to 5 mm in steps of 1 mm. The relationship of the leaked signals is reported in Figures 6.41 and 6.42 for inner and outer defects, respectively.

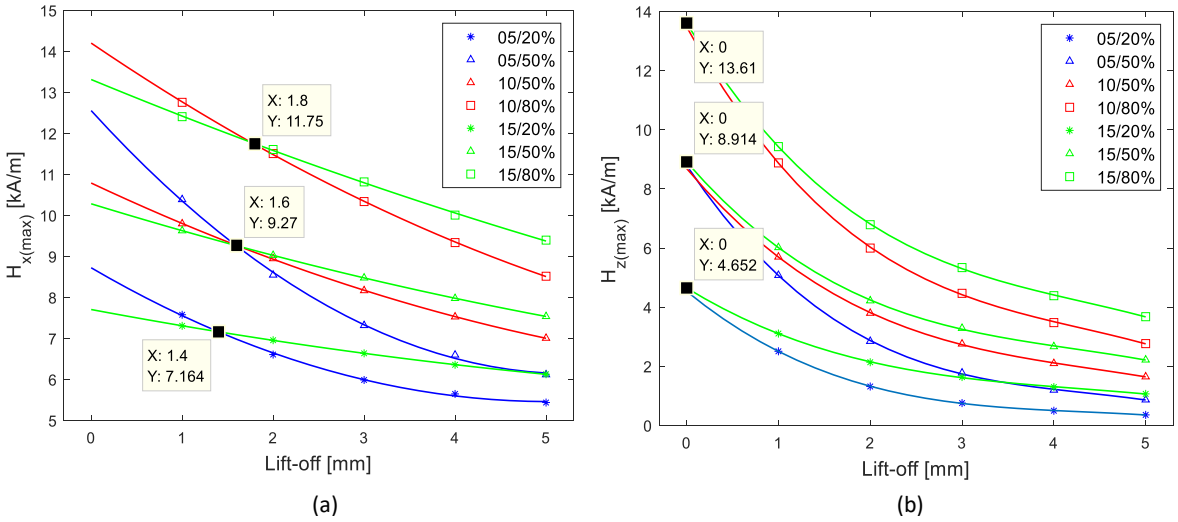

Figure 6.41: *Relationship between the maximum amplitude of leaked field and their related lift-off for* ***Inner defects****. On the legend: diameter in mm / percentage of plate thickness reduction. a)* H_x*. b)* H_z*.*

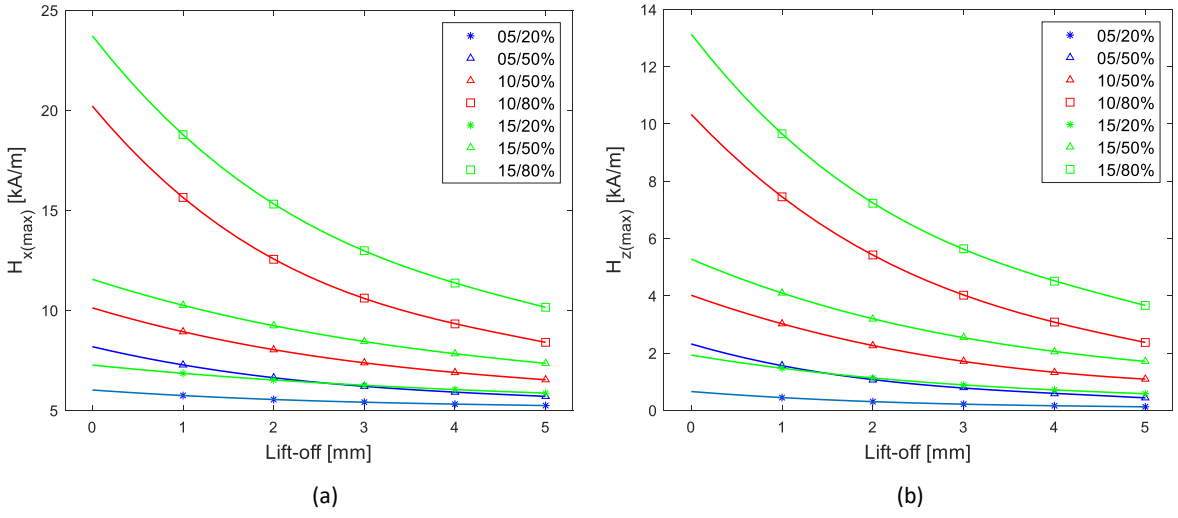

Figure 6.42: *Relationship between the maximum amplitude of leaked field and their related lift-off for* ***Outer defects****. On the legend: diameter in mm / percentage of plate thickness reduction. a)* H_x*. b)* H_z*.*

Interestingly, the defects with the same depth register a crossing point by the inner

defect configuration for both H_x and H_z components. For H_x signals, this joint point occurs in a specific lift-off value between 1 mm and 2 mm, see Figure 6.41a. As a consequence, the H_x signal reaches higher amplitudes for defects with smaller diameters as long as the assumed lift-off is lower than the respective point of intersection. While for higher lift-off values, the H_x signal amplitude increases as the defect diameter increases for defects with the same depth. This behaviour explains the results reported in Figure 6.26a and published in [102], where a lift-off of 1 mm was assumed. On the other hand, the amplitude of the H_z signals resulting from defects with same depth join each other at zero lift-off, as shown in Figure 6.41b.

Regarding the signals acquired from the model set-up as outer configuration, it can be observed in Figure 6.42 that the behaviour of H_x and H_z signals with respect to the lift-off are qualitatively very similar. Comparing them with the signals from inner defects, they differ significantly for small lift-off. However, signal amplitudes are comparable at larger lift-offs.

As pointed out before in Section 6.4.4 about Figures 6.31, 6.32, Figures 6.41 and 6.42 it can be claimed that: (i) The amplitude of the H_x and H_z components of the leaked field is significantly larger for inner defects than for outer defects as long as the plate thickness reduction is low. This is shown for the case of the defects with 20% of thickness reduction. (ii) On the contrary, the difference between inner and outer defects in the H_x and H_z amplitude decreases as the defect depth increases. However, the amplitudes can be larger for an outer defect than the corresponding inner defect. This is shown in the case of the defect with 15 mm in diameter which has 80% of thickness reduction as to be seen in Figures 6.41a and 6.42a. This magnetic behaviour in such a defect is understandably illustrated in Figure 5.15, which shows that most of the field leaks under the defect tip.

Indeed, the signal amplitudes for the leaked field obtained experimentally agree highly accurate with simulation results on all assessed instances during this research, as reported for defects of 10 mm in diameter as an example in Figures 6.13 and 6.14.

6.5 Saturation

Theoretically, magnetic saturation is obtained when the relative magnetic permeability reaches the value of $\mu = 1$. However, considering the permeability behaviour in Figure 6.3, it became obvious that for high values of $\mathbf{H}_0$, the permeability always decreases slower as the applied field increases suggesting as unfeasible to reach absolute saturation. Therefore, the assessed field range in this work is limited to the near saturation region, which can be considered as a valuable contribution in the practical field. The effect of increasing applied field on the MFL signals can be theoretically studied through the function $(\mu - 1)/(\mu + 1)$ which governs the saturation behaviour by the Equation 3.21. Figure 6.43 illustrates the behaviour of the function $(\mu - 1)/(\mu + 1)$ as the permeability decreases. In this figure, plotted data corresponds to S235JR steel used in this research and reported in Figure 6.3. Permeability range extends from the maximum until the

minimum values experimentally recorded, namely μ-values from 1876 to 22.25. Although the function shows a quasi-linear relationship with a very low gradient before $\mu = 150$, for smaller permeabilities presents a sharp drop which falls faster for μ-values $<$ than 10 [102].

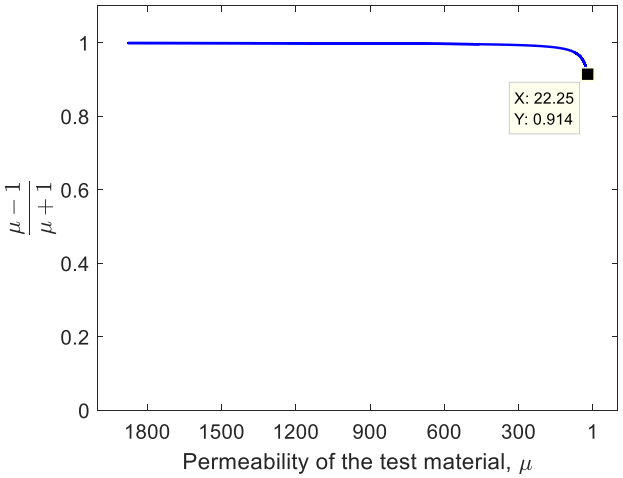

Figure 6.43: *Reliance of the term* $(\mu - 1)/(\mu + 1)$ *from Equation 3.21 respect to the permeability.*

Simulation and experiments are conducted in order to verify the effects of increasing applied field in the near saturation range, on the magnetic flux leakage behaviour. Section 5.6 introduces the methodology and related set-ups to obtain MFL signals as a response to the defect presence in a magnetised rod (refer to this section for the description of the set-up and sample features). Figure 6.44 shows the axial component of the generated field between electromagnet poles measured by a Hall-element scanning the location where the sample will be placed. Applied field magnitudes are defined at half distance between poles. Nine different levels are assumed from 9 kA/m until 81 kA/m in steps of 9 kA/m.

After recording the magnetic field which will be applied to the sample for each magnetisation strength, now the defected rod is placed in the experimental set-up in order to study the leaked field due to the presence of a flaw in the sample. The axial component of the leaked field is acquired an plotted in Figure 6.45. Same set-up is modelled in Comsol. Simulation results for the axial component are reported in Figure 6.46 using same coordinates for comparison purposes. Experimental and simulation results agree very well. Differences in signals approaching electromagnet pole-shoes emphasise as expected the effect of the method of magnetisation.

Related values are normalised to the minimum value to compare the amplitudes of the leaked signals, as illustrated in Figure 6.47. The figure reveals that the maximum amplitude is achieved with an applied field equal to 27 kA/m. Indeed, remaining signals guarantee smaller amplitudes even though the applied field increases.

Figure 6.48 outlines the behaviour of the leaked field amplitude from signals in Figures 6.45 and 6.46 as a function of the applied field. Experimental and simulation

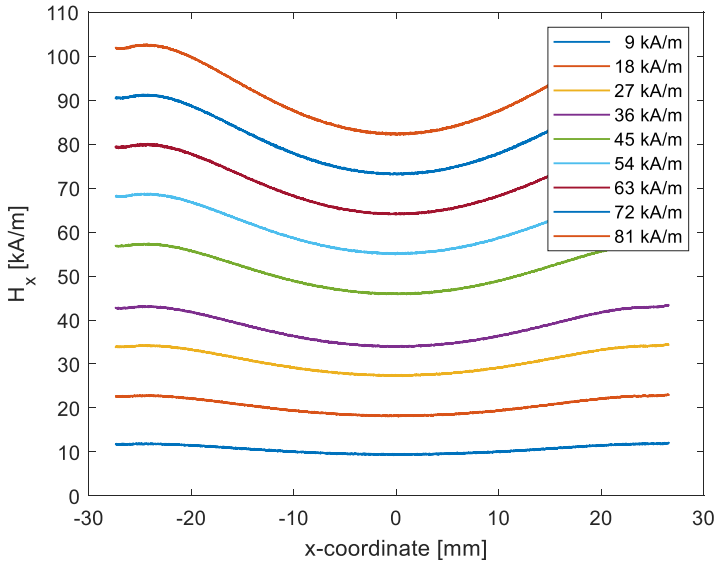

Figure 6.44: *Axial component of the applied field measured without sample between electromagnet poles at different excitation levels.*

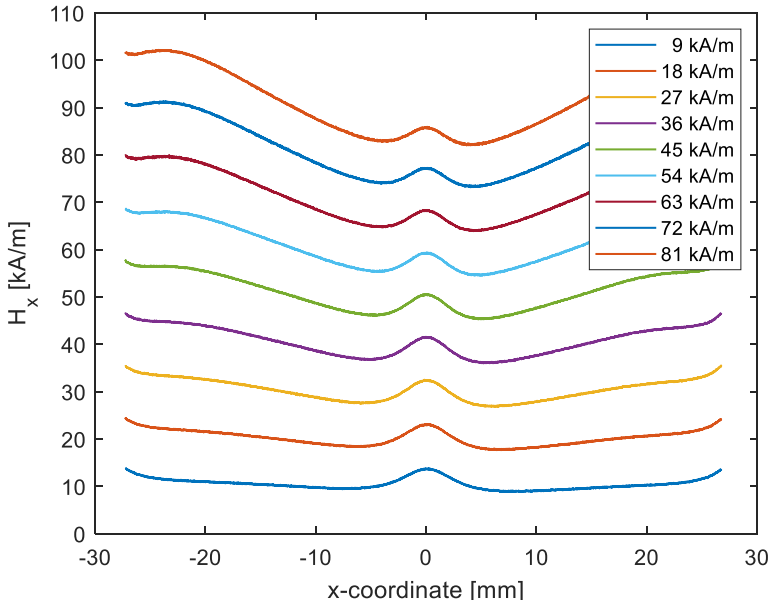

Figure 6.45: *Experimental results of the axial component at 3.5 mm lift-off.*

results are plotted for comparison.

The H_x amplitudes in Figure 6.48, in general, agree very well. However, the behaviour described by experimental data is, as expected, much smoother. Regarding the inaccuracies by numerical solutions, should be recalled that an approximation of the exact solution is achieved involving and error defined by Equation 3.29. Such inaccuracies on numerical solutions are associated, as discussed in Section 3.1.3.2, to: (i) the discretisation of the geometry and (ii) the discretisation of the solution. Certainly, the most complex geometries to reach convergence in a simulation model are those including domains which differ each other significantly in dimensions. This is the case of the bar

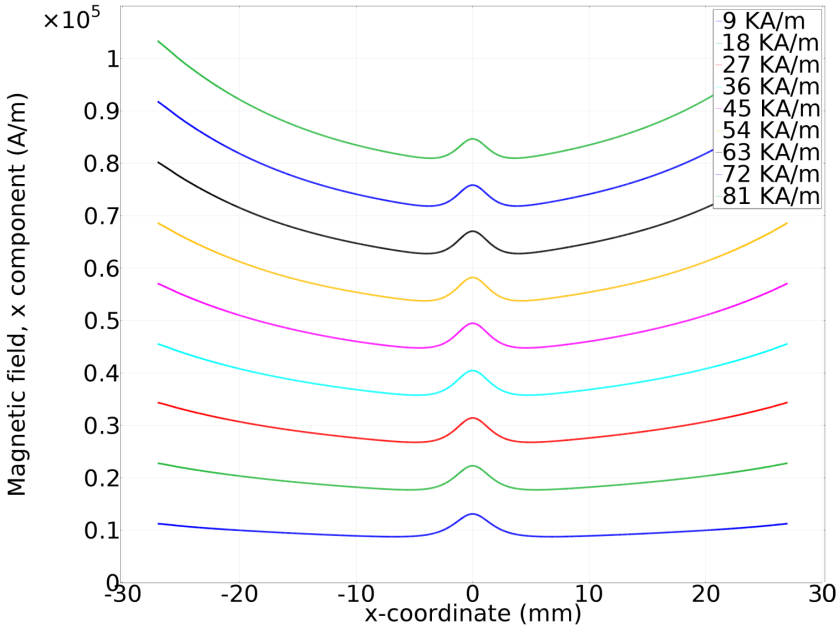

Figure 6.46: *Simulation results of the axial component at 3.5 mm lift-off.*

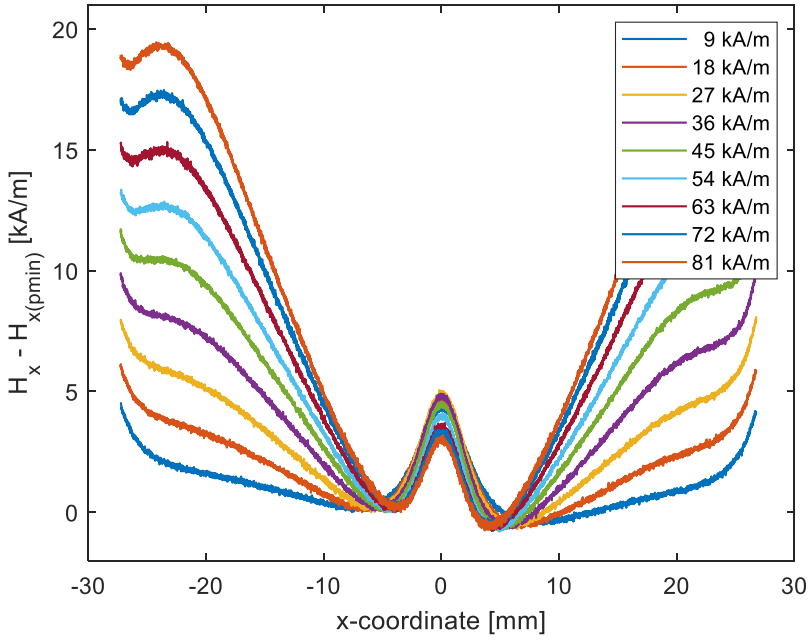

Figure 6.47: *Comparison of the leaked field amplitudes at different applied fields in the near saturation range.*

model used currently to study magnetic saturation shown in Figure 5.18: the width of the embedded flaw is 0.1 mm while the air domain containing the sample has an edge of 400 mm.

In order to define the related permeability and the resulting value of the function $(\mu - 1)/(\mu + 1)$ at the required field to reach maximum leaked amplitude, Figure 6.49 point out their values for an applied field of 27 kA/m.

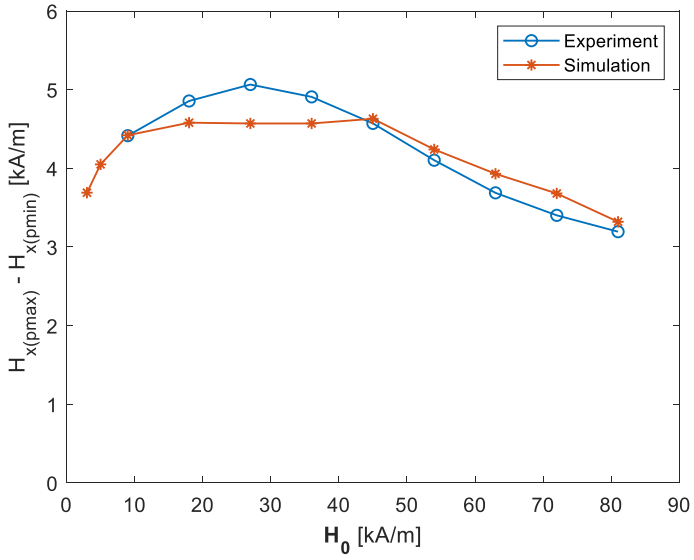

Figure 6.48: *Leaked field amplitudes as a function of the applied field in the near saturation range.*

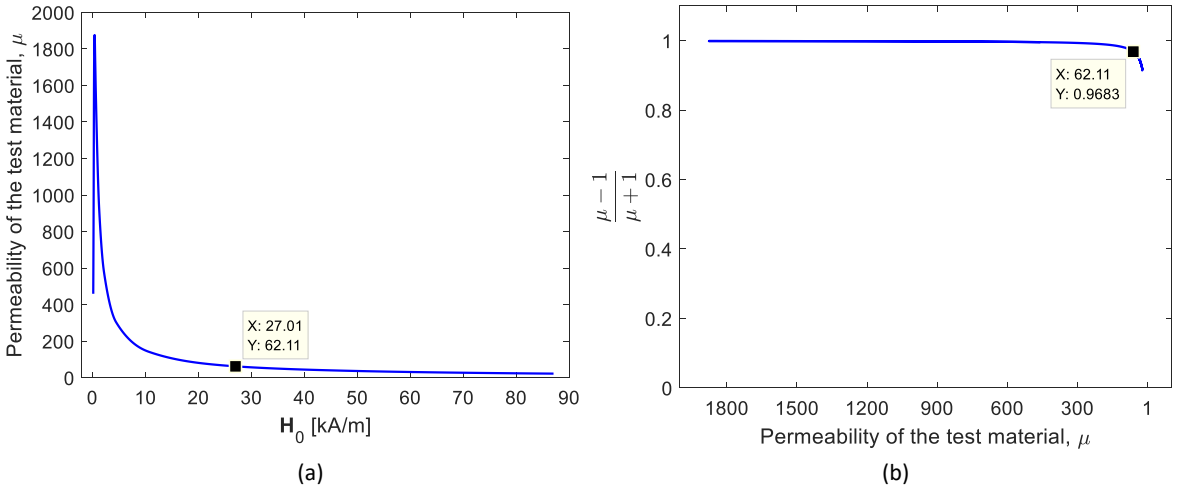

Figure 6.49: *a) Permeability. b) $(\mu-1)/(\mu+1)$ function. Corresponding values for an applied field equal to 27 kA/m are highlighted in every plot.*

Finally, a comparison of the MFL signal under three different circumstances is presented in Figure 6.50. H_x signal is acquired at 3.5 mm of lift-off from the defected rod applying 45 kA/m. Signals are acquired before and after thermal treatment is performed to the sample. Additionally, the axial component is obtained at the same position as the sample is removed.

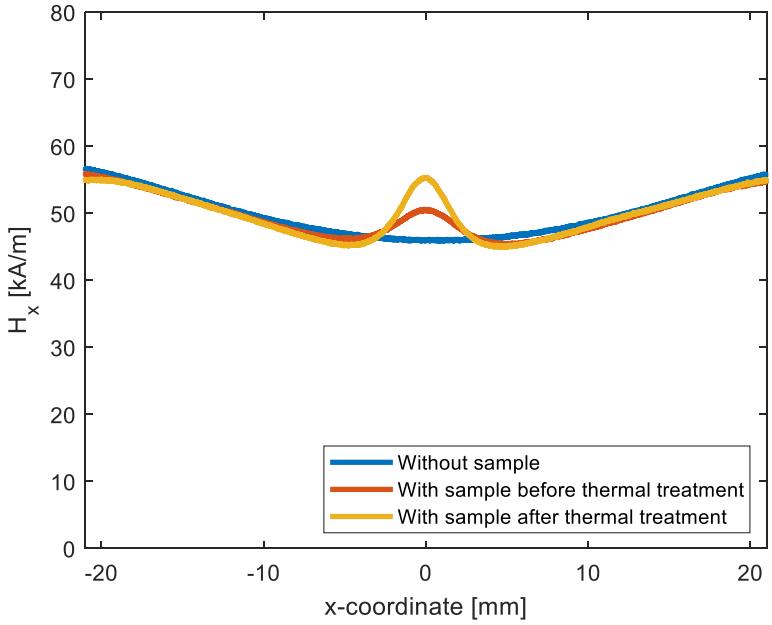

Figure 6.50: *Comparison of the leaked signal attained on the experimental set-up under three different conditions.*

7

Discussion

An overview of the data treatment process involved in the MFL technique is outlined schematically in Figure 4.1. The current study focuses on data interpretation demonstrating that a correlation exists between the dimensions of a part-wall defect and the resulting magnetic leaked signal. Results allow for the establishment of a robust model for defect reconstruction. The model delivers defect length and depth, which are key factors in determining strategies to guarantee pipeline integrity.

The introduction of this chapter clarifies the specifications, limitations and general features of the current research. Then, the first section discusses the methodology conducted to attain the objectives. The methodological strategy includes a closed-loop process to achieve a validated model. The second section presents the traits and particular applications of the research approaches, namely, theoretical, numerical and experimental. In particular, the factors which influence the MFL response are reported in the third section. All these factors have demonstrated a significant impact on data interpretation. The fourth section discusses the core of this study. Inner and outer defects are studied independently contrasting in detail current findings with previous publications.

This research establishes the relationship between wall-thickness reduction defects and the features of MFL signals. It is a valuable contribution since the dependency of MFL signal features on defect depth is still unexplained [12–17, 59, 101, 102]. The complexity to determine this relationship accurately owes particularly to the fact that the signal is strongly altered for a broad diversity of parameters. In order to enable the development of a 3D model, including a parameter assessment, this study is conducted under specific features taking into account the concerning reference framework as summarised in Table 7.1.

In addition to the issues mentioned in Table 7.1, there are other factors that can disturb MFL responses under specific conditions, such as: (i) wide detachment of the sensor system to the pipeline wall due to the presence of pronounced bends or elbows; (ii) vibration of the PIG body during the run; or (iii) exceeding maximum design speed for instance while descending steep hills. All of these factors require multidisciplinary research to develop specific plans to mitigate their influence on MFL signals during a

pipeline inspection. Indeed, the assessment of such factors is very important, however, they are beyond the scope of the current study.

	Reference Framework	Study Feature
1.	MFL has been the most-used technique for in-line inspection of pipelines transporting oil and gas in last decades [58, 59, 61, 99].	MFL signals as input.
2.	Corrosion, either internal or external, is the primary cause of pipeline failures (Section 1.1).	Corrosion type defects.
3.	MFL signals can be distorted by the curvature of the pipeline. However, the signals remain unaffected by pipelines with a diameter much larger than their wall thickness.	Steel plates are used as test samples since the influence of the curvature on target pipeline can be avoided.
4.	Characterisation of corrosion type defects as superposition of single defects (see Appendix D).	Calotte-shaped defects as a nearest representation of corrosion problematic.
5.	Acquired MFL signal behaviour differs depending on whether the same defect is located inside or outside of the pipeline wall (refer to Section 5.3).	Separate assessment for inner and outer defects.
6.	Non-linear dependency of the ferromagnetic materials on applied field (see Section 5.2.1).	Rigorous investigation regarding the influence of the magnetisation strength on MFL signals including the magnetic saturation definition.
7.	The dimensions of the sensor Hall body are comparable to the nominal lift-off of 1 mm (refer to Section 5.5).	Thorough study to establish the real lift-off by means of experimental results.
8.	High dependency of MFL signals on lift-off [13, 108, 111].	Painstaking assessment concerning lift-off on axial and radial components of the leaked field.
9.	Relationship between MFL signal features and defect length [12, 13, 58].	Error analysis by defect length estimation based on three different features of MFL signals.
10.	Relationship between MFL signal features and defect depth [12, 13, 58].	Establishment of calibration curves in order to determine defect depth depending on signal amplitude and defect length.

Table 7.1: *Reference framework and study features.*

7.1 MFL Signal Study Methodology

The main methodological goal of this thesis focuses on the development of a strategy which allows for a reliable study of the MFL phenomenon taking advantage of the theory, experiments and simulation since none of these approaches can independently solve the problem. Indeed, it is widely known that the theory is still not able to solve the MFL problem in 3D. Similarly, conducting this study merely experimentally would lead to excessive costs entailing a high demanding process. Simulation, however, offers an effective solution to avoid these disadvantages inasmuch as, firstly 3D models can be solved and secondly, required parameter variation can be performed without extra cost. Nevertheless, it is imperative that the simulation method comprises the concern for the agreement of the simulation outcome with the theory and experiments in order to validate the results. The diagram in Figure 7.1 summarises the research process employed during this work on a recurrent basis as a strategy to achieve reliable results. It is worth mentioning that limiting the simulation process to the model definition phase and consequently dismissing convergence analysis and results analysis stages could lead to meaningless results as output, especially if a feedback loop to validate the model is refused.

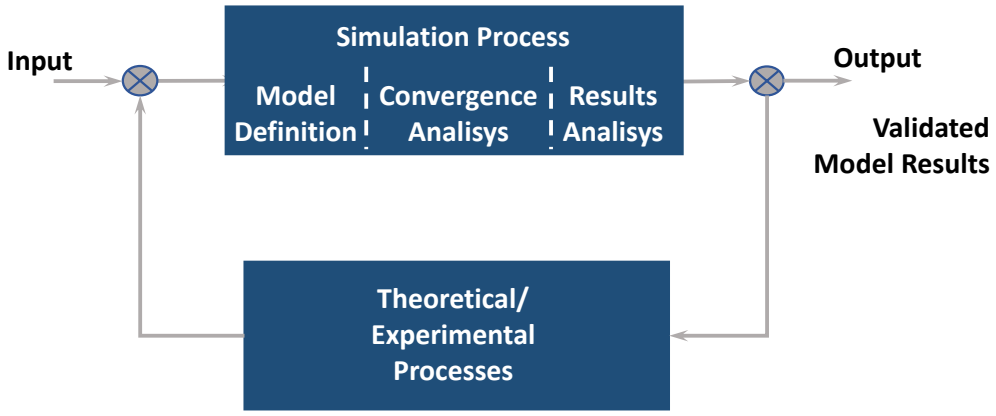

Figure 7.1: *Methodological strategy to take advantage of theoretical, numerical and experimental approaches.*

The MFL signal modelling procedure is outlined in Section 3.1 delving into theoretical, numerical and experimental approaches, emphasising their advantages and limitations. Specifically, the simulation process by COMSOL is described in Section 3.1.3.2 as an operational process, starting with the model definition and ending with the delivery of results after the finite element analysis is executed. Set-ups for simulation assessment in this research are modelled as stable and consistent posed problems providing proper boundary conditions (refer to Section 5.2). In accordance with Figure 7.1, convergence analysis has been carried out as a part of the simulation process (methodology described in Section 5.2.4). In particular, two factors have been studied in-depth. Firstly, the convergence of results as the dimensions of the air domain which contains the magnetised sample increase. In fact, the purpose of this convergence study is determining the proper

size for the related volume (Section 5.2.4.2). Secondly, the convergence of the MFL signal amplitude as a result of mesh refinement has been reported in Section 5.2.4.3. As a result, the size of the air domain can be properly limited, and the mesh size can be optimised provided that convergence of the results is attained in both cases.

The importance of implementing a results analysis phase continuously into the simulation process has become evident during this research (see the simulation process block in Figure 7.1). Specifically, three instances can be underlined as an example demonstrating the relevance of conducting a thorough analysis of the results. Following cases have been faced in different stages during this investigation, and they have required the validation of obtained data through theory and experiments:

- As illustrated in Figure 5.1, a fundamental decision was required in the first steps of this study in order to determine the research methodology. In general, 2D models are used to simplified 3D geometries without diminishing their integrity. However, their application can be limited because 2D models assumed a cross section of an infinite long geometry. Therefore, proving that the approximated results from the 2D model fulfil the objectives of the finite 3D model is fundamental for every simulation study. Indeed, 2D simulation will contribute in addition to geometry simplification, also to gain understanding of the model concept, the physics involved, the parameters' behaviour and to fine-tune the software settings like solvers. By the current work, the comparison of the results obtained from 2D and 3D simulations permitted to conclude that 3D simulation is needed to assess part-wall defects accurately (refer to Section 5.2.3). The need to implement a three-dimensional model for the simulation of the defect reconstruction process was a pivotal decision in obtaining reliable results. This resolution was only possible by means of analytical and experimental validation of the simulation models through a feedback loop, as shown in Figure 7.1. Particularly, the 2D numerical model was verified by the analytical study of the infinite cylinder in Section 5.2.3 and the validation of the 3D model through experiments.

- The establishment of a simulation strategy which provides a proper sample magnetisation has also required a detailed study by means of theory and experiments to achieve accurate correspondence between simulation and practice. Two recent publications can be cited concerning the simulation of the MFL phenomena. Huang and Zhao (2016) report in their book [13] pages 76-78, a piece of a pipeline as test sample being magnetised utilising a system consisting of a pair of permanent magnets, a pair of brushes and a yoke; unfortunately, the details of the simulation model are not provided. Pearson et al. [101] limit the possibilities of magnetising the sample either to a yoke-type design like Huang and Zhao did, or a homogeneous magnetic field, chosen the second for their research. However, during the current research was verified the problem of using any of these two approaches to magnetise the sample. First, modelling a yoke-type system adds several extra parameters to the simulation model, and consequently increases the potential for error and inaccuracies. Second, as a homogeneous field is applied to the sample, it generates poles in the sample ends, which are placed perpendicular to the applied field. The amplitude of these poles reaches a magnitude much higher than the ap-

plied field modifying the sample magnetisation and consequently the leaked field amplitude. This problem can be solved by increasing the length of the sample in order to accomplish a more homogeneous field at half-length where the defect is located; however, this change implies again a dramatical increase of the applied field shifting the operating point on the BH-curve of the material and again the MFL response will be modified. In this research, both approaches to magnetise the sample have been painstaking studied; nevertheless, they do not satisfy the requirements, and consequently, a third method is developed with reliable results. It consists of applying a magnetic potential to the sample ends (see Section 5.2.4.1); thus, it is not necessary to model a whole magnetic system introducing additional parameters, and the generation of poles is avoided. Results in plate magnetisation demonstrate very good agreement with the field behaviour around the sample in practice.

- And the last example concerns the nominal lift-off to emulate the position of the Hall sensor in the simulation model, which was initially assumed as 1 mm. However, after the correlation between simulations and experiments, it has been found that the real lift-off is considerably larger taking into account the active zone of the Hall sensors according to their specific position (see the introduction of Section 5.5). This is a critical issue since MFL signal features report a non-linear behaviour as a function of the lift-off and consequently, proper considerations are unfeasibly assuming an inaccurate lift-off.

Indeed, during the parameter analysis, it has been essential to validate the simulation results with a selection of experiments. Despite the fact that this study has considered a large amount of simulation and experimental instances (as discussed in Chapter 5), a defect that is 10 mm in diameter and 50% deep is selected to illustrate most of the results seeking clarity by data comparison. Moreover, additional results are reported using related features and addressed mainly to establish the calibration curves.

In summary, taking advantage of the theoretical, numerical and experimental approaches has been a profitable strategy for reaching the objectives of this thesis. Thus, this strategy is highly recommended for subsequent studies, primarily because MFL publications rarely comprise these three research methods in an individual work. Indeed, following this methodology has enabled a better understanding of the relationship between MFL signal features and defect dimensions. As a result, a robust and reliable model is developed for defect reconstruction.

7.2 MFL Signal Study Approaches

While the last section focusses on the relevancy of using the strengths of theoretical, numerical and experimental approaches conducting an MFL signal study employing a feedback process, this section discusses the traits of each approach providing practical advice.

7.2.1 Theoretical Analysis

The most relevant feature modelling MFL phenomenon with the theory lies in delivering an exact solution to the problem. Nevertheless, the complexity of related mathematics restrains their application only to simple defect geometries (see Section 3.1.2). The extensive work on the dipole model published by Zatsepin and Shcherbinin [49, 50] has been widely used. The authors fulfilled the objectives limiting the application of the dipole model to defects which can be approximated by a two-dimensional representation such slot type, namely defects with a high length to width ratio. In this respect, Zatsepin and Shcherbinin suggested two models, a linear magnetic dipole for flaws with a depth significantly smaller than the width, and a magnetic strip dipole if the defect depth is equal or greater than the defect width. In both configurations, defect boundaries are assumed straight and perpendicular to the surface. Although related results have reported good agreement with experiments, these 2D models and even 3D models based on the dipole model [112, 113] provide a solution only to highly limited flaw shapes and can under no circumstances be utilised for reconstruction of corrosion type defects.

A different theoretical approach consists of assuming a two-dimensional model in order to solve the related equations completely. For instance, the induced field of an infinite cylinder magnetised perpendicularly to the cylinder axis is reviewed in Section 5.1. The problem is solved taking advantage of the cylindrical coordinates. As a result, a homogeneous induced field is obtained inside the cylinder due to its circular cross-section. The magnitude of the field within the cylinder depends on the applied field and permeability. Moreover, the direction of the field is parallel to the applied field. Unlikely, the field outside the cylinder is inhomogeneous tending to the applied field as the distance from the observation point to the cylinder increases. On the other hand, the field distribution close to the cylinder surface is highly depending on the angle position respect to the direction of the applied field (see Figure 6.6). Unfortunately, applying this approach to three-dimensional geometries or even irregular shapes in two-dimensions is still not feasible.

Despite the fact that these analytical perspectives are unable to provide a full solution to the MFL problem, their study has been a valuable contribution to this research allowing a deep understanding of the physical behaviour of the MFL phenomenon and its related parameters. Furthermore, solving the cylinder case completely has allowed the validation of the 2D simulation model while enhancing the comprehension of the mechanism used by the simulation software.

7.2.2 Numerical Analysis

The numerical method has demonstrated to be a valuable tool for the MFL signal assessment. Agreement between simulation results and experiments can be clearly evidenced in Figures 6.16 to 6.21 for a calotte-shaped flaw that is 10 mm in diameter and has 50% of plate thickness reduction. The axial and radial components are plotted as C-scans as well as amplitude locus curves. Simulation and experimental results are compared

for both configurations, inner and outer defects. Four additional elements should be provided in a consistent posed simulation model in order to guarantee reliable results: specific material characteristics, proper sample magnetisation, precise defective sample geometry and exact lift-off.

Although the earlier publications on finite elements applied to MFL phenomenon [53, 63, 114] reported in detail their 2D model specifications and related methodology, recent works in 3D lack on information in this regard [13, 58, 101]. As in early studies, this thesis includes not only simulation results but also relevant details in the simulation process conducted through COMSOL multiphysics. COMSOL is selected as simulation software because it permits modelling in 3D and offers an optimised magnetic module where the magnetic characteristics of a specific material can be implemented. Moreover, it is based on the finite element method and offers a different kind of solvers for linear as well as non-linear systems being a robust tool, as reported in Section 3.1.3.2. In general, the finite element analysis is performed using a discretisation process which allows for numerical evaluation on computers. Although the solution delivered is an approximation of the exact solution, the related error will tend to zero only if the numerical model is defined as a stable and consistent system (see Section 3.1.3.1). Indeed, any numerical method requires a mathematical model which provides equations and conditions based on physical laws for the system of interest. Section 3.1.3 presents an overview of three different numerical approaches together with their respective analytical models as examples of solutions to the MFL problem. The high dependency of the solutions on the defect shape is demonstrated through these instances, which in fact apply in general to any MFL study. In Section 7.3, the defect shape as a factor altering the MFL signal will be discussed in detail.

There are two primary systems which have been simulated in this research: the cylinder model and the flawed plate model whose methodologies are reported in Sections 5.2.3 and 5.2.4 respectively. The study of the cylinder model allows for comparison between analytical and numerical outcome as plotted in Figure 6.7, the result from the 2D simulation model agrees very well with the theory reporting an error lower than 2%, while the result from 3D simulation converges to the theory as the cylinder length increases. For a cylinder shorter than 5 cm, however, the field obtained differs significantly as the cylinder length decreases. The cylinder model described in Section 5.2.3 can be compared to the case of a steel slab housing a hole with an identical cylindrical shape. Indeed, pole generation at the surface of a magnetised defective sample has been proposed in different studies as a tool to investigate its related leaked flux [95,96]. Certainly by definition, the free pole distribution on the surface of a magnetised specimen surrounded by air and this on the surface of a cavity located in a ferromagnetic piece are equal except on the sign provided two conditions: (i) the specimen and the cavity have the same shape, and (ii) the magnetisation of the specimen surface and the magnetisation of the material surrounding the cavity are the same. Since these two conditions can be fulfilled by a cylindrical specimen and a steel slab holding a cylindrical-shaped cavity, their pole distribution can be considered interchangeable. Considering that the steel slab sample selected for this investigation is 1.2 cm thick, then the depth of the corrosion-type defect will be limited to this thickness. According to the results reported in Figure 6.7 simulating a defect with a maximum depth of 1.2 cm through a

2D model will deliver a considerably high error compared with the 3D simulation (refer to Section 6.3). In consequence, the simulation set-up for MFL signal assessment in this investigation is modelled in three dimensions in all cases (refer to Section 5.2.4).

Primarily, two different mechanisms of magnetisation have been developed to implement the simulation model. Initially, the defective plate was magnetised by means of a homogeneous field applied to the boundaries of the air domain (see Section 5.5.2.1 for set-up details). However, after the validation of the model through a series of experiments, it became evident the necessity to improve the simulation model in order to attain a higher agreement with experimental results (refer to Section 5.5.2.2). Furthermore, applying a homogeneous field generates extremely strong leaked fields at the specimen edges perpendicular to the applied field, which affects the field homogeneity in the plate and around it. The advanced model instead utilises a potential difference for magnetisation (related traits can be found in Section 5.5.2.3).

One more observation related to the simulation concerns the meshing process. Such models, including domains on very different dimension scales, will require a careful selection of the mesh conditions. For instance, the flawed plate set-up comprises a broad air domain of some cubic meters containing a defective specimen whose flaw is only some millimetres deep. Hence, it is essential to define an extremely fine mesh for the flaw volume, its surrounding and the location where the signals will be acquired. Accordingly, the results will be accurate, and related signals will be smooth. On the contrary, a coarse mesh is required for the steel plate region away from the defect, and even coarser for the air domain. Consequently, the number of degrees of freedom reduces and thus facilitates the convergence of results. The features on mesh refinement and solving time for the plate model housing a single defect with different dimensions are summarised in Table 5.3. In disagreement with the claim published previously in [102] *"we cannot find a direct unique relationship to the changing complexity when the defect parameters are changed. It seems to be an individual COMSOL behaviour."*, after revision of the data and comparison with a broader range of simulation cases, what can be stated in general is that the number of degrees of freedom and correspondingly the solving time increases as the defect depth decreases. This behaviour occurs because the mesh in the defect domain needs to be refined by smaller depths. In this regard, the simulation of such a model is a highly demanding process for a parameter study since every change entails the modification of the mesh conditions. Despite the fact that COMSOL and similar software offer a parameter sweep tool in order to evaluate changes in parameters simultaneously, the results from such a model are inaccurate because the evaluation is executed under the same mesh conditions for the whole parameter range. Parameter sweep is very useful as a first approach, but for an accurate study, it is necessary to provide proper mesh features as the target parameter changes. This difficulty with mesh configuration will be even more extreme for very complex defect geometries defined by sharp angles. A primary advantage in the model proposed in this study is that calotte-shaped defects define closely corrosion defects permitting to configure an extremely fine mesh taking advantage of COMSOL settings (refer to Section 5.2.4.3).

In general, Layouni et al. [12] classified the literature concerning MFL signal assessment into three main categories. The first group includes the works using numerical

methods. While the second group comprises studies to detect and locate defects employing non-numerical methods. Finally, the third group is conformed for investigations in 2D based on non-numerical methods detecting, locating and determining the opening length of defects. The authors in [12] claimed to be pioneers using non-numerical methods in 3D models to detect, locate and determine defect length and depth (refer to Section 2.4.3.2 for a review of the methods). In particular, several studies have been published the assessment of MFL signals in the last decades using FEM as a numerical tool. FEM has been utilised in such works to generate MFL signals in order to validate the model developed [67] or to earn signals from known defect types which later will be used in the solution of the inverse problem [13, 56, 57, 59, 61, 111]. Pearson and coworkers in [58, 101], for instance, *"look to understand why [the relationships between the defect and the corresponding MFL signal] occur and attempt to minimise them by characterising the influence of two fundamental components of the defect geometry, namely the length and depth"*. The authors in [58, 101] provided a reference map based on a 2D finite element model considering a rectangular defect profile, which allows reducing the error in defect depth determination once the MFL signal amplitude and the defect length are known. By comparison, this research proposes a novel solution to the MFL inverse problem by delving into signal-defect relationships, taking advantage of the 3D simulation model and experiments. As a result, related calibration curves are delivered in order to establish an accurate process for defect sizing.

7.2.3 Experimental Analysis

In general, there is a lack of experimental works studying systematically the MFL phenomenon in relation to defect dimensions. This absence is understandable since the related experimental set-up is highly demanding and involves a vast number of parameters which can alter the signal. However, over the last years, experimental results have been fundamental in gaining confidence concerning the assessment of defects employing the MFL technique. For instance, experimental outcomes have demonstrated that the dipole model can be used reliably to estimate the size of crack type defects [112, 113]. Additionally, experiments have been used to study the parameters affecting the magnetic circuit as in [37,38]. And more recently, experimental studies have served to verify iterative models developed with the purpose of characterising slot and crack type defects [17] or to reconstruct surface-breaking flaws with geometrical shapes [61, 69, 103, 111] and even arbitrary-shape defects [59]. In particular, the experiments from Romero Ramírez et al. reported in [15], allow them to conclude that the discrimination of inner and outer defects utilising MFL signals is unlikely.

Furthermore, experimental assessment in this research has been a valuable contribution not only to validate the simulation models but also to study the spatial behaviour of MFL signals in relation to specific factors and parameters, as will be reported in next sections. Optimisation of the set-up traits was necessary as declared in Section 3.1.4 to achieve the final system shown in Figure 5.9. All features of the experimental arrangement and the set of experiments are presented in detail in Section 5.3. A total of 128 experiments acquiring simultaneously axial and radial components of the magnetic field

were conducted, modifying specific parameters. Repeatability of experimental set-up on results was proved by different defect dimensions located in different samples. Although the system is carefully tuned, some sources of error can be identified mainly related to the nominal lift-off of 1 mm. Indeed, the MFL response can be altered even by changes of a tenth of mm due to irregularities on sample thickness, set-up height or the active zone of the sensors according to their specific position. Therefore, a thorough study is conducted to establish the true lift-off based on the experimental results using different samples under different conditions, as discussed in the introduction of Section 5.5.

7.3 Factors Influencing the MFL Response

The characterisation of the inherent error by every inspection method is a relevant process because it allows the establishment of strategies to compensate for the error in the acquired data. Nevertheless, a risk of failure occurrence exists despite all efforts to guarantee the reliability of an inspection method. Section 2.3 presents two specific instances in order to underline the importance of ensuring the effectiveness of the inspection technique minimising the risk of failure. Timashev and Bushinskaya in [26] classify the sources of error by ILI assessment of pipelines in three groups: omission of severe defects, underestimation of the defect size and wrong defect-type identification.

The results in this thesis confirm that there are several factors which can alter the MFL response. These elements have been painstakingly studied seeking for improving the understanding of their relationships with MFL signals. Indeed, prior knowledge of these factors permits optimising the features of the inspection method. This section presents the factors which have been subject of discussion in a specific stage of the current research, precisely: Magnetisation strength (Section 6.2), saturation (Section 6.5), defect location concerning the sensing system (throughout Chapter 6), near field and far field (Section 6.4.2), and defect shape (throughout Chapter 6).

7.3.1 Magnetisation Strength

The comparison of MFL signals acquired under the same set-up at different magnetisation strengths in Figure 6.5 confirms that insufficient pipe wall magnetisation can lead with high probability to failure on defect report. This statement is completely in line with previous claims and for instance with the hypothesis from Jansen et al. in [34] claiming that *"the most serious error sources [concerning the reliability of pipeline inspection] are related to pipe wall magnetisation. A low-resolution MFL pig with good pipe wall magnetisation will give a better and more reliable inspection result than a high-resolution pig with poor pipe wall magnetisation"*. Distinctly, the response of the leaked field reported in Figure 6.5 demonstrates the influence of the initial mechanical state of the pipe material on the MFL response if relatively low magnetisation is applied. Furthermore, the BH curve and the permeability of the material are compared in the current research employing a sample under two different conditions. Namely, before

and after thermal treatment which allows for previous mechanical perturbations relief. The outcomes are plotted in Figure 6.4 to illustrate the dependence of the magnetic response on the mechanical conditions; mainly, as a magnetic field lower than 5 kA/m is applied. Indeed, this behaviour is implicit on the hysteresis loops of the material plotted in Figure 6.1, which reports a range of possible **B** values related to the same $\mathbf{H}_0$. This B range, however, becomes more restricted as the applied field increases becoming a single B value. Certainly, as Jansen and co-workers claimed *"hysteresis implies that B is not a single-valued function of applied field strength, H."* [34].

Pipelines, in particular, are exposed to several sources of mechanical disturbances. Material stresses and strains on pipelines can be caused, for instance, by transportation and installation. The execution of these two processes mostly entails challenging tasks, in order to fulfil the requirements of the topography where pipelines are going to be located. In general, the construction of a system demands to join pipelines together and their integration with other facilities and components for control and security. Even after installation, the system works under loads resulting from internal factors such as the pressure caused by the transported product, and also diverse external elements including, for instance, ground movements. However, it is well known that major stresses and strains in pipelines are caused by the UOE method used for pipeline manufacturing [115–117]. This alteration is a disadvantage of the method, which occurs since the weldable steel in plate-shaped is subjected to milling, crimping, U-forming, O-forming, longitudinal welding and circumferential expanding processes. According to Herynk et al. [116], *"Collapse experiments have demonstrated that these steps [milling, crimping, U-forming, O-forming, welding and expanding] especially the final expansion, degrade the mechanical properties of the pipe and result in a reduction in its collapse pressure upwards of 30%."*. Concerning the presence of mechanical deformations in pipeline wall, Crouch and co-workers [106] published experimental results using defective pipelines, where they identified that tensile and compressive stresses describe opposite slopes in relation to the increase in the magnetisation strength. Consequently, Crouch et al. have recommended applying a magnetic field higher than 16 kA/m to guarantee an MFL response independent on pipe-wall stress (refer to Section 5.2.1).

The effect of mechanical perturbations on the MFL response is verified in the current research utilising the specimen in Figure 5.18. The sample is magnetised by an electromagnet delivering an applied field of 45 kA/m. Figure 6.50 reports the axial component of the leaked field along with the sample at 3.5 mm of lift-off under three different conditions: removing the sample, placing the sample before its thermal treatment and placing the sample after its thermal treatment. Two different zones can be identified based on a comparison of the three plots: firstly, where the signals converge; and secondly, around the defect area and the slab ends where the signals significantly diverge. The convergence of the signals obtained with sample and without sample demonstrates that the material is magnetised achieving a relatively low permeability. According to Figure 6.49a, a permeability of 40 is attained by using 45 kA/m of applied field. These results do not fit with the claim of Crouch et al. [106] recommending an applied field of 16 kA/m to avoid the influence of stresses on the MFL response. However, based on the findings of Crouch and co-workers, a more plausible explanation is that the sample owns strong compressive stresses whose effect on the MFL response increases as the applied

field increases. These mechanical disturbances may have been induced in the sample as it was fixed tightened to embed the flaw. Indeed, the application of a very high strength was required in this process to conserve the sample shape and dimensions.

The MFL response also depends on the magnetic properties of the specific material used to manufacture the pipeline. This dependency is a crucial issue considering that a previous material characterisation is not viable in an in-line inspection. As Shur et al. claimed in [60]: *"the magnetic field depends on the properties of the ferromagnetic material"* based on a comparison of MFL signals acquired utilising defective samples from different steel grades. The results might suggest that the dependency on the properties of the ferromagnetic material occurs for any field magnitude. However, based on the findings of a robust investigation conducted by the International Institute of Welding [105] has been already established that applying a field beyond 3 kA/m avoids the individual behaviour of a specific material as reported in Figure 5.4. They showed that the permeability and BH curves from a representative collection of weldable steels converge as the magnetisation increases (see Section 5.2.1). In this perspective, the design of the magnetic circuit to perform MFL testing becomes an essential task. The magnetisation strength delivered to the test specimen should guarantee the independence of the MFL signal on (i) mechanical disturbances of the material, (ii) initial magnetic state and (iii) specific material properties. In addition, applying high magnetisation by MFL testing provides an advisable signal-to-noise ratio; this is a significant advantage taking into account that the noise by pipeline inspections can be considerably high. Nevertheless, increasing the magnetic field may involve some adverse impacts. Firstly, higher investment in structure and costs; secondly, extra space in the structure; and thirdly and most significant, does not necessarily enlarge the amplitude of the MFL response as will be argued in the saturation subsection below.

As already discussed, determining the proper magnitude of the applied field is fundamental in the MFL technique. Indeed, not only the magnitude but also the distribution trait of the applied field should be carefully defined since a highly inhomogeneous field supplied from the magnetic circuit to the sample, would distort the MFL signal. This distortion of the signal will be stronger as the magnetisation strength increases. Figure 5.12 presents the characteristic of the applied field experimentally provided to the plate set-up in the current study, where $\mathbf{H}_0$ is assumed as 5.2 kA/m. In addition, Figure 6.12 reports the related field attained in the simulation model.

As next, the discussion will be explicitly addressed to the magnetisation strength effect on the amplitude of the axial and radial components of the MFL signal. Dobmann and Höller reported in [36] experimental results of the radial component which leaks out from a crack-type flaw. The authors demonstrated that the radial component responds linearly as the applied field increases beyond 100 Oersted (approximately 8 kA/m). In contrast, results obtained experimentally in this research using cylindrical and calotte-shaped defects suggest that the amplitude of the axial and radial components of the MFL signal acquired at lift-offs of 3.5 mm and 2.1 mm respectively, behave linearly even for an applied field higher than 3 kA/m. Experiments were conducted using samples which house single defects with specific dimensions in every case. The experimental arrangement was set in each case as inner as well as outer defect configuration (refer

to Section 6.4.3. According to [36], the non-linear effects in the relation MFL signal to the applied field is due to the contribution of the volumetric sources and rotations in Equations 3.16 and 3.17, while the surface polarisation is responsible for its linear response (see Section 5.5.1).

7.3.2 Saturation

In almost all publications concerning MFL technique is recommended the magnetisation of the inspected sample to the saturation region. Although, the magnetisation strength is a crucial parameter as discussed in last subsection, the term *saturation* leads to an undefined magnetisation, since nowhere is documented the MFL behaviour related to a defect as the magnetisation reaches saturation. Section 3.2 presents an overview of the structural mechanisms that occurred as a material is magnetised. The micro-structural process in the saturation range, however, is still not well understood, and there is no consent from researchers.

Theoretically, magnetic saturation is obtained when the relative magnetic permeability reaches the value of $\mu = 1$. Analytical formulas exist only for the case of paramagnetic materials, as reported in Section 5.1 for the case of an infinite cylinder, and not to materials with hysteresis character. As can be observed, the function $(\mu - 1)/(\mu + 1)$ governs the Equations 5.6 as the applied field increases further in the saturation range. This function will very rapidly tend to zero only for μ-values $<$ than 10 [102]. The same can be assumed for a general case described by Equation 3.21. The function $(\mu - 1)/(\mu + 1)$ is plotted in Figure 6.24 for an applied field between 152 A/m and 87 kA/m, which covers the range utilised in the current research. Related permeability behaviour is plotted in Figure 6.43. Outcomes confirmed that the function reports a very low gradient before $\mu = 150$ and will rapidly approach to zero for μ-values $<$ than 10.

Experiments and simulations are carried out in order to verify the effect of saturation in the MFL response. A long and thin steel slab housing a crack-type defect is used as a test sample (refer to Section 5.6 for details on related set-ups). Results obtained through simulation and experiments agree very well, as reported in Section 6.5. As demonstrated in Figures 6.47 and 6.48, the largest amplitude of the MFL axial component is attained for an applied field of 27 kA/m. The results provide new insight into the relationship between magnetic saturation and MFL response, since increasing the applied field in the saturation range does not necessarily imply a larger amplitude of the MFL response. It is worth to mention that the determination of the applied field required to maximise the leaked signal should not be based only on simulations because it will probably lead in inaccuracies.

7.3.3 Defect Location in relation to the Sensing system

The results reported in Figures 6.8 to 6.11 indicate that the axial and radial signals do not provide evidence on the location of the defect in relation to the sensing system.

The signals originated from inner as well as outer defects configurations have similar features related to the defect dimensions. Romero Ramírez et al. have already published an investigation focused on the differentiation between top and bottom defects studying the MFL radial component [15]. They reported experimental results in tank floors, thus the use of the terms top and bottom instead of inner and outer, and concluded that the discrimination of the defects according to the location based on the MFL technique is not viable. Costain and co-workers confirmed in a more recent publication [118] which discusses, in general, the limitations and capabilities of modern tank floor scanning with MFL, that an extra system is required in order to discriminate top and bottom defects. However, the circumferential component describes clearly eight different peaks for the inner defect (Figure 6.8b), while for the outer defect, only four peaks are generated (Figure 6.9b). This feature of the circumferential component could be utilised for the identification of defects as inner or outer location; nevertheless, the severe disadvantage of basing the assessment in the circumferential component is its lower amplitude compared with the other two components as discussed in Section 6.4.

7.3.4 Near Field and Far Field

The outcomes in the current study build on existing evidence of the lift-off acting as a low-pass filter and consequently causing the loss of information related to the defect geometry [59]. The signal behaviour of the axial and radial components of the leaked field, H_x and H_z, report a noticeable difference by the inner defect configuration although both scans come from the same set-up, depending on the lift-off used to execute the scan. The shape of the axial component obtained at 1 mm lift-off in Figure 6.8a describes very closely the geometry of the defect opening, which appears limited in the y-coordinate for two maxima. These two maxima will be almost integrated if the signal is acquired at a lift-off of 3.5 mm as registered in Figure 6.15a. The same loss of information on the defect shape can be evidenced by the radial component at 1 mm lift-off in Figure 6.8c and the H_z plot in Figure 6.15a obtained at 2.1 mm. On the other hand, the signals acquired from the outer defect configuration in Figures 6.9 and 6.15b do not differ significantly in shape, of course, they do in magnitude since the scans are conducted at different lift-offs.

7.3.5 Defect Shape

It is well known that the opening of the defect can be defined based on the information provided by any of the components of the MFL signal. This occurs particularly accurate if the three components axial (H_x), circunferential (H_y) and radial (H_z) (refer to Sections 5.2.4 and 6.4 for detailed information), are analysed in conjunction [12, 13, 54]. Ravan et al. published in [59] satisfactory results on the reconstruction of opening contours of real metal-loss like defects whose MFL signals are gained employing simulation and experiments. The authors claimed that the maximum depth of the defect could be accurately established, although the sensing system affects the sharp variations of

the signal which hinders the defect reconstruction process. Although combining the information of the three MFL components and reducing the lift-off to zero will provide the best conditions for defect reconstruction. This is not easily feasible in practice by pipeline inspections due to the vast amount of data. In this regard, a different approach is necessary to guarantee defect sizing based on MFL signals.

Pearson and co-workers have published a series of papers focused on the understanding of the relationship between the MFL response and the related defect. In [58], the authors emphasised the claim from Saunderson concerning above ground storage tanks, which states that MFL signals are found to be *more closely related to the volume of the metal loss than to the depth of pitting* [119]. However, Pearson et al. reported later in [120] that *defects of the same volume but different shapes are unlikely to demonstrate a volumetric relationship with the MFL signal amplitude, but, defects of the same shape but different volume may give rise to a volumetric relationship*. The influence of the defect shape on the MFL response has been often studied for different authors [12, 13, 54, 120]. Thus, there is a consensus that the behaviour of the leaked field depends strongly on the defect shape. Indeed, the most significant limitation of the inverse method in most of the latest studies is the training characteristics since corrosion defects can have unlimited shapes. Therefore, in the current work is considered every corrosion defect as the superposition of single adjacent defects. Specifically, the calotte-shape is chosen as the best representation of corrosion like defects (see Section 5.2.4). Hence, an accurate assessment can be conducted for a specific geometry. In conclusion, the consideration of the corrosion defect as the conformation of single calotte-type defects is proposed in order to reduce the error by defect reconstruction for irregular defects.

In line with these hypotheses, this research takes advantage of the information provided independently by the MFL axial and radial components to determine the opening contour of the defect, namely its length. Concerning to the defect depth, the calotte-shape is assessed in order to establish calibration curves in relation to the signal amplitude since, as already discussed, the volumetric relationship is valid only comparing defects with the same shape. A model will be in future developed for defects with irregular opening contours, which allows the composition of any corrosion defect by single calotte-shape defects permitting the study using MFL signal superposition (see Appendix D).

7.4 Defect Reconstruction based on MFL Signals

This section focusses on the discussion of the main objective proposed for this thesis. It concerns the development of a reliable model for defect sizing based on MFL signals. As presented in Section 2.4, the magnetic flux leakage technique comprises four primary components: a magnetic circuit, a detection system, a data processing method and a strategy to present the results according to the standards. Every stage is carefully designed in order to determine the state of the inspected specimen. In the last decades, different models have been proposed to solve the so-called inverse problem, which allows for defect sizing. The most relevant proposals are summarised in Section 2.4.3.2. In par-

ticular, the modelling process of the MFL signal is classified under theoretical, numerical and experimental approaches through Section 3.1. Instances related to corrosion-type defects are included in every case. The current work takes advantage of these three modelling approaches, according to the methodology introduced in Chapter 5.

The relationship between the defect features and its related MFL signal has been studied in the earliest researches using 2D models of slot-shaped defects [49,50,52,53,108] and for instance, groove patterns as in [63]. More recently, rectangular flaw profiles have been chosen since the simulation software has been improved and currently allows for robust 2D and 3D modelling [58, 66, 101]. Although most of the works do not report results distinguishing inner and outer defects, in particular, [53] and [63] did under nearside and farside concepts. In this research, the independent assessment of inner and outer defects is considered fundamental for attaining accurate defect reconstruction.

7.4.1 Inner Defects

Simulation results of the MFL signal assessment assuming a virtual scanning of the plate surface by a magnetic point-probe, which scans at 1 mm lift-off from the surface, were reported in the Far East Forum on Nondestructive Evaluation/Testing in China and published in [102], indicating that:

- invariant relationships between the defect depth and two criteria: the peak-width at half-maximum (PWHM) and the peak-to-peak-distance (PTPD). Namely, each of these criteria is only a function of the defect width (refer to Section 6.4.4). And,
- a quasi-linear behaviour of the amplitude of the axial and radial components as the defect depth increases while the defect width remains constant (see Figure 6.26). Although the H_z amplitude is increasing with increasing defect width at a specific defect depth, the amplitude of H_x is decreasing. In any case this effect needs further exploration concerning the influence of the lift-off as explained below.

Subsequent experimental results compared with outcomes from an advanced simulation model permitted to determine the true lift-off achieved in practice. Indeed, the true lift-off could be established, taking into account the active zone of the Hall sensors (see Section 6.4.2). Due to the high dependency of the MFL signal amplitude on the lift-off, an additional study was conducted following the methodology reported in Section 5.5.3. H_x and H_z signals earned through simulation and experiments are plotted in Figures 6.37 and 6.39 for specific defect dimensions scanned at different lift-offs. Moreover, Figures E.7 and E.9 present the simulation outcome of different defect size seeking for comparison. Concerning the defect length, it can be observed that,

- The H_x signals acquired for a specific defect at different lift-offs report two points of intersection on the main peak (see Figure 6.37a). The distance between these two points defines the defect length, particularly accurate for defect lengths larger

than the wall thickness. Consequently, the determination of the defect length can be established based on two H_x signals scanned concurrently at different lift-offs. This feature can be used as a relevant strategy since the definition of the defect length can be attained without knowing each specific lift-off.

- The results plotted in Figures 6.37b, E.7b and E.9b suggest that the position distance between maximum and minimum (peak-to-peak-distance, PTPD) of the H_z signal can determine the exact defect length if the signal is propagated back to lift-off zero. However, according to the experiments summarised in Table 6.6, the PTPD criterion reports the smallest error at 4.1 mm lift-off. In general, it can be stated that the influence of the lift-off on the H_z signal is stronger as the defect length decreases.

While, about the defect depth, it can be concluded that,

- Based on Figure 6.41a, the H_x amplitude decreases in general as the lift-off increases. This relationship becomes linear as the defect width increases beyond the wall thickness. For lift-offs smaller than 1 mm, the H_x amplitude increases as the defect width decreases for a constant defect depth. Nevertheless, this behaviour becomes the opposite for lift-offs larger than 2 mm. For lift-offs between 1 mm and 2 mm, there is a specific crosspoint depending on the defect depth. The cross point by every set of defects with the same depth may have a relation with the wall thickness. This feature will explain the behaviour of H_x reported in Figure 6.26 and previously described as not fully understood, whose signals were acquired at 1 mm lift-off.
- The amplitude of the H_z signal in relation to the lift-off confirms the results published in [66]. Zuoying et al. reported results from three simulated rectangular defects with different dimensions and concluded that *the MFL amplitude has a noticeable decrease when lift-off value increases from 1 to 2 mm. When the lift-off value becomes larger, its influence to MFL amplitude decreases.* Specifically, the H_z signals in Figure 6.41b present a common amplitude at lift-off equal zero for defects with the same depth independently of their width. In general, it can be affirmed that the H_z amplitude increases as the defect width increases for defects with the same depth. The H_z signal behaviour reported in Figure 6.41b fit with the results published in [108] for crack-like artificial defects.

The study of the axial and radial components related to the MFL signal duration and amplitude are conducted at a fixed lift-off of 3.5 mm and 2.1 mm, respectively. It will be necessary an adjustment of the relationships for changes in the lift-off during the inspection. This fitting for H_x and H_z can be conducted utilising the curves in Figure 6.41.

The dependency of the MFL signal duration and amplitude on the defect size is assessed according to the methodology described in Section 5.5.2. A set of selected simulations and experiments are collected in Section 6.4.4. The outcomes permit to establish for inner defects that,

- The length of the defect can be determined independently of the defect depth by the peak-width at half-maximum (PWHM) criterion for the H_x signal and also by the PTPD criterion for the H_z signal as can be observed in Figures 6.35a and 6.36a. These results are in line with previous publications, indeed Huang and Zhao in [13] reinforce recently the dependency of the H_x and H_z signal duration only on defect length using rectangular defect assessment varying their dimensions. However, the claim in [13] is not entirely valid for calotte-shape defects, since the error in defect length determination employing PWHM criterion has reached 17% and using the PTPD criterion until 8%, for defects of 10 mm in diameter. It is noteworthy that most of the cases have reported error by default, as summarised in Tables 6.1 and 6.3. The resulting error in defect length determination by PWHM and PTPD criteria depends strongly on defect shape, defect dimensions and lift-off. Therefore, establishing a unique criterion to correct the error is not feasible as long as no defect geometry is selected.

- The defect depth can be determined through the calibration curves in Figure 6.33 once the defect length is defined. These plots show that after removing the related off-set, the H_x and H_z amplitudes are comparable, and their behaviour depending on defect length and depth are very similar. In this regard, it can be stated that there is not an advantage to use the axial component or the radial component preferably. Nevertheless, using the axial component is a profitable method to increase the signal to noise ratio, since the signal is shifted positively by an off-set level.

  The outcomes in Figure 6.33 can explain the following contradictions published previously. Lord and Hwang in [52] and later Atherton and Daly in [53] published the behaviour of the H_z amplitude related to the defect depth based on 2D simulations of rectangular defects. Lord and Huang reported an increase in the amplitude as the defect depth increases tending to saturation. While Atherton and Daly found ten years later that the amplitude rises very steeply for large penetrations, they explained the contradiction to previous findings by considering the differences in field excitation. Nevertheless, the results in Figure 6.33b suggest that the tendency towards saturation reported in [52] is the suitable behaviour for narrow defects, while the results in [53] concern the study of broader defects. Afterwards, Zuoying and co-workers [66] and later Huang and Zhao [13] published results from 3D simulations modelling rectangular cuboid flaws. The authors in [66] studied only the radial component and reported a *nearly linear* relationship between its amplitude and the defect depth, while in [13] stated a *monotonically increasing relationship* for H_x, H_y and H_z. These general results are confirmed for calotte-like defects with lengths approximate to the sample wall thickness and broader. More recently, Pearson et al. presented in [101] the characteristic of the H_z amplitude as the defect depth increases for a specific defect length. Unfortunately, the defect length utilised is not defined in the paper. Nevertheless, according to the magnitudes reported for the H_z amplitudes can be concluded that the related defect length is around 5 mm, which agree with the plot obtained for a narrow defect in Figure 6.33b.

7.4.2 Outer Defects

The assessment of MFL signals acquired from defects in outer configuration follows the same methodology as for inner defects (refer to Sections 5.5.2 and 5.5.3). Simulations and experiments are conducted to study the dependency of H_x and H_z signals on the lift-off. In particular, their relationship to the defect size is assessed at 3.5 mm and 2.1 mm, respectively. Figures 6.38, 6.40, E.8 and E.10 illustrate related H_x and H_z signals as a function of the lift-off for the case of outer defects. According to the results can be concluded concerning the defect length that,

- As in the case of inner defects, also in the case of the outer defects: the H_x signals acquired at different lift-offs present two intersection points on the primary peak. This crossing point is distorted as the defect length decreases below the wall thickness, as can be observed in Figure E.8a; nevertheless, it becomes very sharp as the defect length increases as in Figure E.10a. Obtaining two signals simultaneously at different lift-off is a valuable strategy to determine the defect length independently on the specific lift-off. However, the error can be higher than 50% as summarised in Table 6.6 for narrow defects.
- The PTPD criterion can also be applied to outer defects. The error in the length determination is strengthened as the defect length decreases, the lift-off increases or both of them occurred. Error for default may occur primarily for small lift-offs and broad defects; for instance, the case in Figure E.8b.

Figure 6.42 report the characteristic of the H_x and H_z signals amplitude as a function of the lift-off. According to these plots, it can be stated concerning the defect depth that the characteristic described for H_x and H_z are very similar to each other. The influence of the lift-off is much stronger for deeper defects. If the attention is focussed on the data scanned at the true lift-off and higher, it can be claimed that its behaviour becomes more linear as the lift-off increases. Error correction due to changes in lift-off by in-line inspections can be performed employing the curves in Figure 6.42.

The duration and amplitude of the H_x and H_z signals earned from outer defects depend not only on the lift-off but also on the defect size. Section 6.4.4 includes the results of concerning simulations and experiments. The assessment is conducted assuming a true lift-off of 3.5 mm for H_x and 2.1 mm for H_z. In this regard, the length and depth of outer defects can be determined by the MFL signal features using the same strategy as for the inner defects.

- Figures E.5 and E.6b illustrate the implementation of the PWHM and PTPD criteria on defects with the same diameter and different depths; these signals are achieved through simulations and experiments, respectively. Figures 6.35 and 6.36 show that the length of outer defects can be determined by the PWHM and PTPD criteria independently on the defect depth. However, as in the case of inner defects, an error for default is identified in almost all outer cases as can be observed in

Tables 6.2 and 6.4. The highest error is attained for the deepest defect under both criteria.

- Atherton and Daly used rectangular defects also to study the characteristics of the MFL signal amplitude obtained from the outer configuration. They concluded in [53] that the amplitude of the leaked field is *approximately linear for penetrations up to 60% and for larger penetrations, it rises very steeply.* Results gained in the current study demonstrate a similar behaviour for calotte-shape defects. Independently on the defect diameter, the amplitudes of the H_x and H_z signals increase nearly linear for defect depths below 50% and increase very fast for depths beyond. In agreement with the authors of [53], *the rate of increase of amplitude with depth is more rapid than linear for both farside [outer defects] and nearside [inner defects] signals, particularly for farside signals.* Nevertheless, the H_x and H_z amplitudes from calotte-shape defects deeper than 50% in the outer configuration are higher than those from inner defect configuration, which contradicts the claim in [53]. This behaviour suggests the dependency on the defect-shape. Charlton and Donne reported in [63] a study based on grooves. The authors found that the sensitivity of axial and radial components on defect depth from outer defects exceed the inner defects response for equivalent defects beyond 40% deep, which agrees qualitatively with the results in this research.

- After the establishment of the defect length, its depth in outer configuration can be accurately determined using the calibration curves in Figure 6.34. The characteristics of the H_x and H_z signals as a function of the lift-off in Figure 6.42 allow for error correction in case that modifications of lift-off occur during the inspection.

8

Conclusions and Perspectives

1. A novel solution to solve the MFL inverse problem is proposed taking advantage of the superposition of MFL signals generated by neighbouring defects. The signal-defect relationship is determined using a 3D simulation model, which is validated through theory and experiments. Experiments, in addition, allow the researcher to gain confidence in the assessment.

2. The results demonstrate a correlation between the features of the axial and radial components and the defect dimensions. This model allows for an accurate determination of the length and depth of a defect. The first step requires an establishment of the defect length, which can be performed either employing the PWHM criterion using the axial component or the PTPD criterion utilising the radial component. A third strategy is proposed if a parallel array of sensors located at two different lift-offs is feasible. These three methods can be applied for inner as well as for outer defects. After the defect length is set, the defect depth can be determined using the calibration curves in Figure 6.33 for inner defects and in Figure 6.34 for outer defects. As changes in lift-off during the inspection can cause estimation errors, a correction using the plots in Figure 6.42 is recommended.

3. Researchers have tried, for two decades, to apply simulation tools by the interpretation of MFL-inline inspection data. However, the proposed solutions from published studies have not achieve sufficient accuracy on the reconstruction of defects. This issue may be the result of considering solutions based on a finite number of simple geometries rejecting the irregular nature of corrosion defects, as well as the lack of the study of all critical parameters involved. This work demonstrates the significance of a thorough understanding of the relationship between MFL signal features and defect dimensions. Insisting on finding a solution to the inverse problem, but disregarding this relationship, prevents the improvement of the MFL technique.

4. The development of Hall-sensors with a reduced distance, from the sensor housing surface to the sensors' active zone, will significantly enhance the inspection efficiency. Also, the implementation of speed controllers will guarantee the correct

delivery of information contained in the signals. Finally, more useful data treatment will (i) reduce the noise superimposed on the Hall-sensors' signals, and (ii) manage double information obtained from sensors at two different lift-off positions.

5. Simulation can be used as a potential research tool in the assessment of defect reconstruction based on MFL signals. The leaked field can be accurately simulated using a finite element software. A feedback process is required in order to achieve a validated model. This process involves theoretical, numerical and experimental components.

6. Understanding the influence of factors such as magnetisation strength, saturation, defect location in relation to the sensing system, near field and far field and defect shape, on the features of the MFL signal is fundamental for its reliable assessment.

7. A future investigation is required in order to study the superposition of MFL signals from single adjacent defects. Both, the methodology followed in this research and the advice provided are highly recommended for further works.

Appendix A

AER Definitions

AER definitions are taking from the Report 2013-B: Pipeline Performance in Alberta, 1990-2012 [9].

Failure	An incident in which product is lost, either by a leak or a rupture.
Incident	Any incident must be reported to the AER and would include a pipeline leak, a pipeline rupture, or the striking of a pipeline (hit), even if that strike does not cause any loss of product. Note that pressure-test failures, though reportable as incidents, are reported separately in this report to allow a differentiation between operational incidents and qualification incidents.
Hit	A hit is an incident where a pipeline is struck but no product is lost.
Leak	A leak is defined as a pipeline failure where a pipeline is losing product but might continue to operate until the leak is detected.
Release	The loss of product from a pipeline. A pipeline incident or failure may result in more than one release, as gas, oil, and water are counted as separate product releases. This is why some charts indicate more releases than incidents.
Rupture	A pipeline failure where a pipeline cannot continue to operate.

Table A.1: *AER definitions for correct data comprehension.*

Pipelines failures are classified according to AER in 13 different groups depending on their cause. Definition of every cause appears in Table A.2.

Construction damage	Improperly applied or damaged coatings, inadequate support, faulty alignment, bending, improper backfilling.
Damage by others	Damage to the pipeline by other parties (third-party excavation or interference).
Earth movement	Watercourse change, slope movement, heaves, subsidence.
External corrosion	Corrosion to the external surface of pipe. Mechanical pipe damage (dents, scrapes, gouges leading to corrosion failure).
Internal corrosion	Corrosion to the internal surface of pipe. Corrosion to the internal surface of girth weld.
Joint failure	Mechanical joint failure (gasket or O-ring failure, internal joint coating failure, mechanical couplings failure). Miscellaneous joint failure (butt fusion, interference joints, fibreglass bonded or threaded joints, explosive welding).
Overpressure	Overpressure failure. Operating over the limits of the licence.
Pipe	Pipe failure (pipe body failure due to stress corrosion cracking [SCC], hydrogeninduced cracking [HIC], fatigue, laminations, mechanical damage).
Valve/fitting	Valve failure (seal blowouts, pig trap failures, packing leaks).
Weld	Girth weld failure (not by corrosion), sulphide stress cracking at the girth weld. Seam rupture (electrical resistance weld [ERW] or other seam weld failure). Other weld failure (weldolets, thermowells).
Miscellaneous	Installation failure (at compressor, pump, or meter station). Miscellaneous (erosion, vandalism, lightning, flooding, animals).
Operator error	Operator error (operating against closed valve or blind, etc.).
Unknown	Pipe cannot be exposed or examined.

Table A.2: *Classification of the cause of pipeline failure.*

Appendix B

POF Definitions

The Pipeline Operators Forum (POF) is constituted by members of pipeline inspection and pipeline integrity companies worldwide. The POF defines next terms as means of standardisation for intelligent pig inspection of pipelines [18].

Anomaly	An indication, generated by non-destructive examination of an irregularity or deviation from base pipe or sound weld material, which may or may not be an actual flaw.
Arc strike	Localised points of surface melting caused by an electrical arc (also referred to as hot spot).
Buckle	A partial collapse of the pipe due to excessive bending or compression associated with soil instability, land slides, washouts, frost heaves, earthquakes, etc.
Casing	A type of feature consisting of a large diameter pipe placed concentrically around the pipeline, usually in high stress areas such as road crossings.
Cluster	Two or more adjacent metal loss anomalies in the wall of a pipe or in a weld that may interact to weaken the pipeline more than either would individually.
Corrosion	An electrochemical reaction of the pipe wall with its environment causing a loss of metal.
Crack	A planar, two-dimensional feature with displacement of the fracture surfaces.
Debris	Extraneous material in a pipeline which may interfere with the ILI tool.
Dent	Distortion of the pipe wall resulting in a change of the internal diameter but not necessarily resulting in localised reduction of wall thickness.
Detection threshold	Minimum detectable feature dimension.

Feature	Indication, generated by non-destructive examination, of a pipeline.
Geometry tool	Configuration pig designed to record conditions, such as dents, wrinkles, ovalities, bend radius and angle, and occasionally indications of significant internal corrosion, by sensing the shape of the internal surface of the pipe.
Grinding	Reduction in wall thickness by removal of material by hand filing or power disk grinding.
Gouge	Mechanically induced metal-loss, which causes localised elongated grooves or cavities.
Heat affected zone	The area around a weld where the metallurgy of the metal is altered by the rise in temperature caused by the welding process, but this is distinct from the weld itself. For the purpose of this specification it is considered to be within 3A of the centre line of the weld, where A is the geometrical parameter related to the wall thickness.
In-Line Inspection (ILI)	Inspection of a pipeline from the interior of the pipe using an In-Line Inspection tool.
In-Line Inspection tool	Device or vehicle, also known as an intelligent or smart pig, that uses a non-destructive testing technique to inspect the pipeline.
Intelligent pig	Pig that can perform a non-destructive examination.
Joint	Single section of pipe that is welded to others to make up a pipeline.
Lamination	Imperfection or discontinuity with a layered separation, that may extend parallel or angular to the pipe wall surface.
Metal loss anomaly or feature	An area of pipe wall with a measurable reduction in thickness.
Mid wall feature	Any feature which does not run out to either the internal or external surface.
Measurement threshold	The minimum dimension(s) of a feature to make sizing possible.
Nominal wall thickness	The wall thickness required by the specification for the manufacture of the pipe.
Pig	Device that is driven through a pipeline for performing various internal activities (depending on the pig type) such as separating fluids, cleaning or inspecting the pipeline.
Pigging	Running of a pig or ILI tool in a pipeline.
Pig Trap	An ancillary item of pipeline equipment, with associated pipework and valves, for introducing a pig into a pipeline or removing a pig from a pipeline.

Pipeline	A system of pipes and other components used for the transportation of products between (but excluding) plants. A pipeline extends from pig trap to pig trap (including the pig traps), or, if no pig trap is fitted, to the first isolation valve within the plant boundaries or a more inward valve if so nominated.
Pipe mill anomaly	An anomaly that arises during manufacture of the pipe, as for instance a lap, sliver, lamination, non-metallic inclusion, roll mark and seam weld anomaly.
Pipeline component	A feature such as a valve, tee, bend, weld, casing, marker, wall thickness change, etc. that is a normal and intentionally fitted part of a pipeline.
Probability of Detection	The probability of a feature being detected by the intelligent pig.
Probability of Identification	The probability that an anomaly or a feature, once detected, will be correctly identified.
Reference wall thickness	The actual undiminished wall thickness surrounding a feature.
Reporting threshold	Parameter, which defines whether or not a feature will be reported.
Sizing accuracy	Sizing accuracy is given by the interval within which a fixed percentage of features will be sized. This fixed percentage is stated as the confidence level.
Spalling	Abrasion of the pipe surface resulting in shallow surface laps and possibly hardening of the material below.
Weld	The area where joining has been done by welding. This is distinct from the heat-affected zone, but is located within it.
Weld anomaly	Anomaly in the body or the heat affected zone of a weld.

Appendix C

Pipeline Integrity Management Approach

Threat	Assessment Tool	Typical Results
Time-dependent		
External Corrosion	MFL Inspection, DA or Pressure Test	Indications categorised as Immediate, Scheduled or Monitored
Internal Corrosion	MFL Inspection, DA or Pressure Test	Indications categorised as Immediate, Scheduled or Monitored
Stress Corrosion	MFL Inspection, DA or Pressure Test	Assessment planned if failure or leak experienced
Time-independent		
Operator Error	Audits	Process changes, training
Outside Force	Monitoring	Soil and other stresses not indicated
Excavation Damage	MFL Data and Data Integration or Caliper Inspection	Indications categorised as Immediate, One-year or Monitored
Stable		
Equipment	Inspection	No safety issues
Materials	Pressure Test	No test failures
Construction	Pressure Test	No test failures
Fatigue[1]	Analysis of Data	Cycles are insignificant

Table C.1: *Threat Matrix for Tool Selection*[2] *[79].*

[1]Fatigue is not a threat but the outcome of the interaction of changing internal hoop stress or external loads (either increasing or atypical) acting on one of the other threats enumerated in the table.

[2]The threat matrix for tool selection is provided as an example and not intended to imply that the tools for each threat are the only tools allowed or recommended.

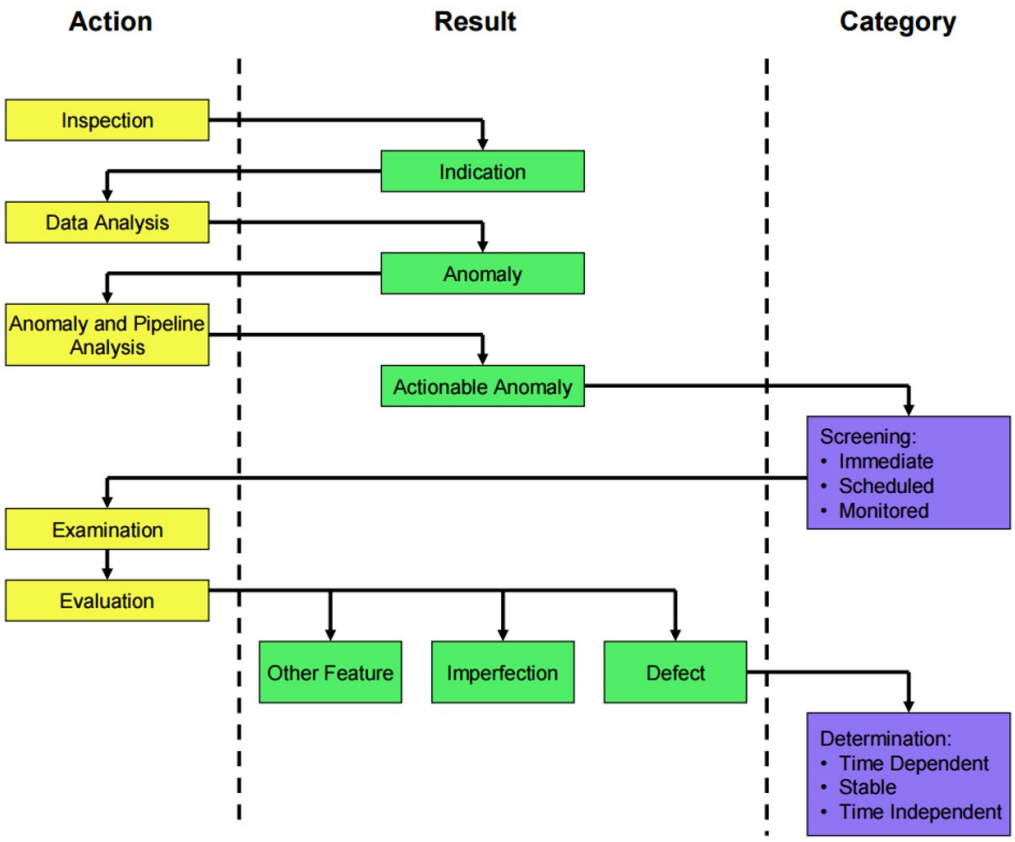

Figure C.1: *Hierarchy of Terminology for Integrity Assessment [79].*

Appendix D

MFL Signal Superposition

Simulation and experimental results are contrasted in order to explore superposition in MFL signals resulting from adjacent defects. A model to simulate nine different steel samples are prepared, assuming the features presented in Figure D.1 and Table D.1 based on the results of performed experiments by [1]. In every specimen are embedded three flaws with diameters of 10 mm, 15 mm and 30 mm, respectively and the same depth. Regarding the distance between defects, the centre of the smaller defects is separated 50 mm, while the centre of broader defects is 60 mm apart.

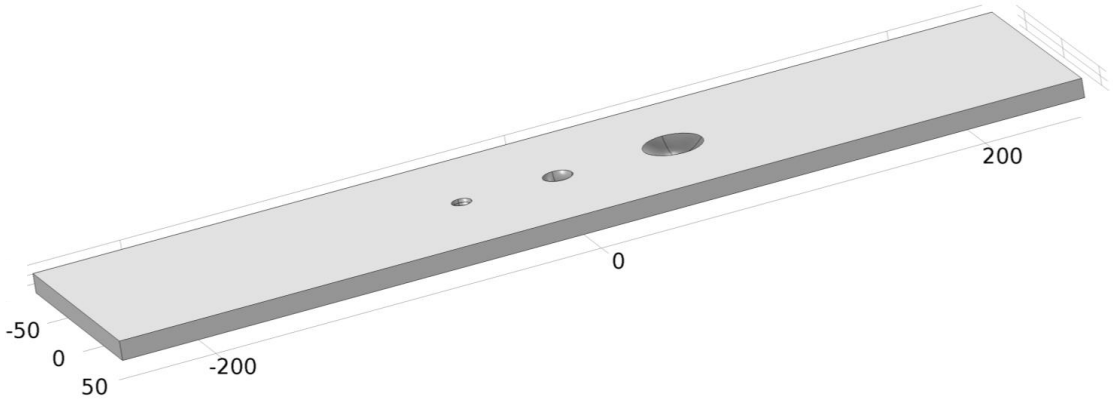

Figure D.1: *Sample features in mm to conduct signal superposition assessment.*

Non-linearities in ferromagnetic behaviour are neglected since the objective here is exploring signal superposition in leaked fields resulting from neighbouring flaws. As a consequence, a constant permeability and a homogeneous applied field are assumed for simulation. Agreement of simulated and experimental results on signal superposition can be observed, for instance, in Figure D.2 using the sample TK 10-70 referred in Table D.1.

Sample	Defect depth [%]	Plate thickness [mm]	Plate width [mm]	Plate length [mm]
TK 10-05	0.5	10	120	500
TK 10-30	30			
TK 10-70	70			
TK 15-05	0.5	15		
TK 15-30	30			
TK 15-70	70			
TK 20-05	0.5	20		
TK 20-30	30			
TK 20-70	70			

Table D.1: *Specimen set for MFL signal superposition study.*

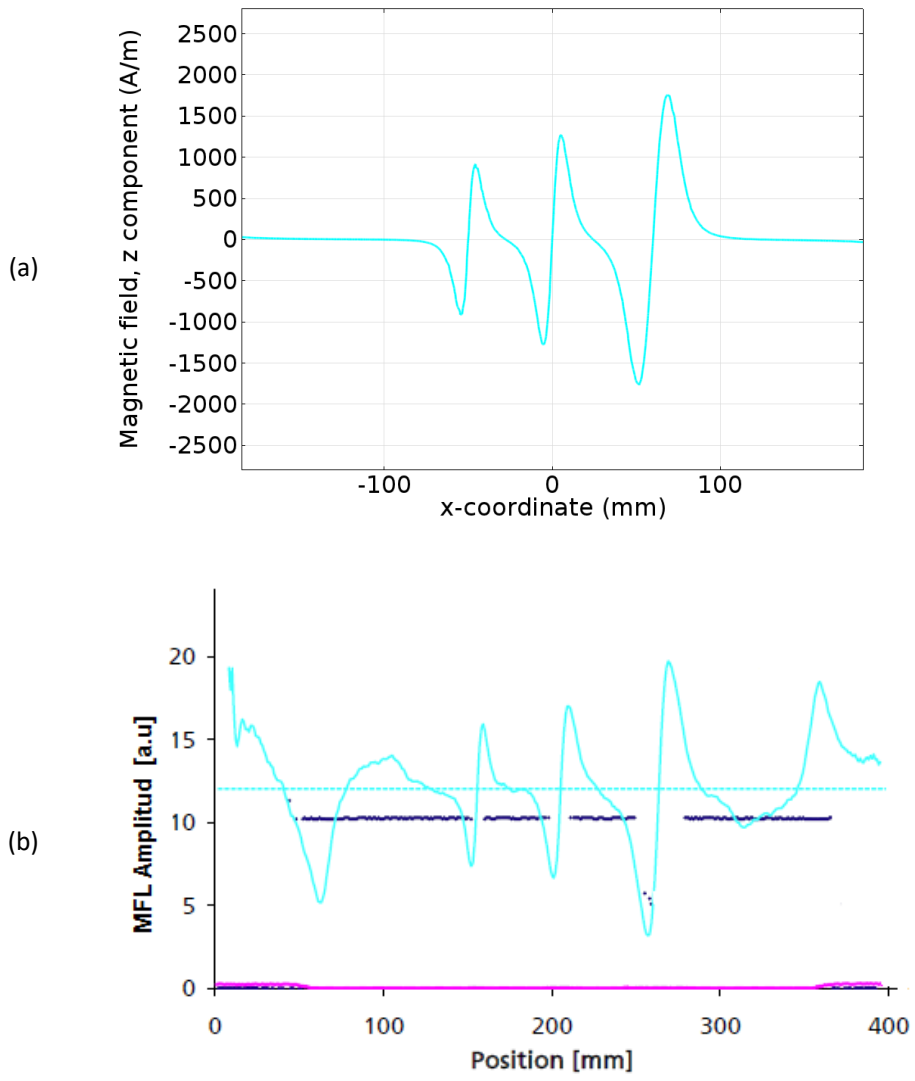

Figure D.2: *Comparison of superposed MFL signals resulting under: a) Simulation and b) Experiments [1].*

Alteration of the signals due to changes in the distance between defects is reported in Figure D.3. In this case, the defect in the centre remains in the same position, and the other two defects move away from the centre doubling the separation, namely 100 mm and 120 mm.

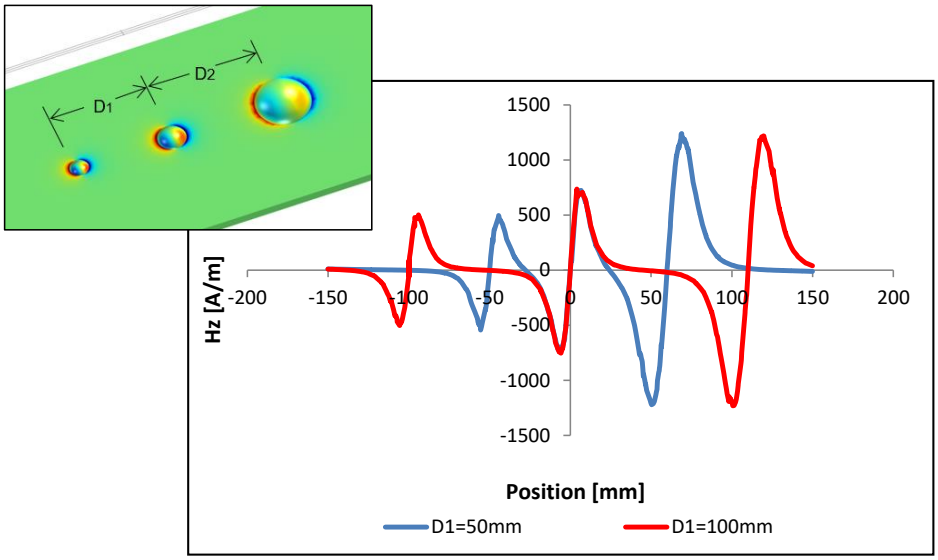

Figure D.3: *Comparison of the MFL signals obtained by simulation as the distance between adjacent defects increases.*

In contrast, superposition of MFL signals resulting from neighbouring defects is verified, decreasing the separation between flaws until they superimpose. Figures D.4 and D.5 report related results from 3D and 2D simulation models. The outcome from these simulations is meaningful and valuable since it validates the statement to consider real corrosion defects as the superposition of single defects mentioned in Chapter 4.

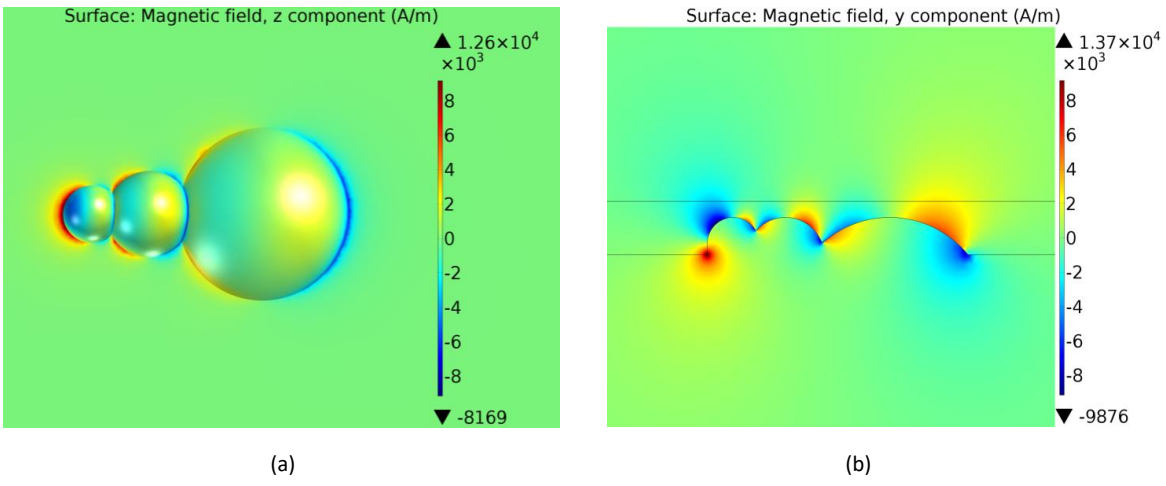

Figure D.4: *Radial component of the leaked field at the surface of simulated clustered defects. a) 3D. b) 2D.*

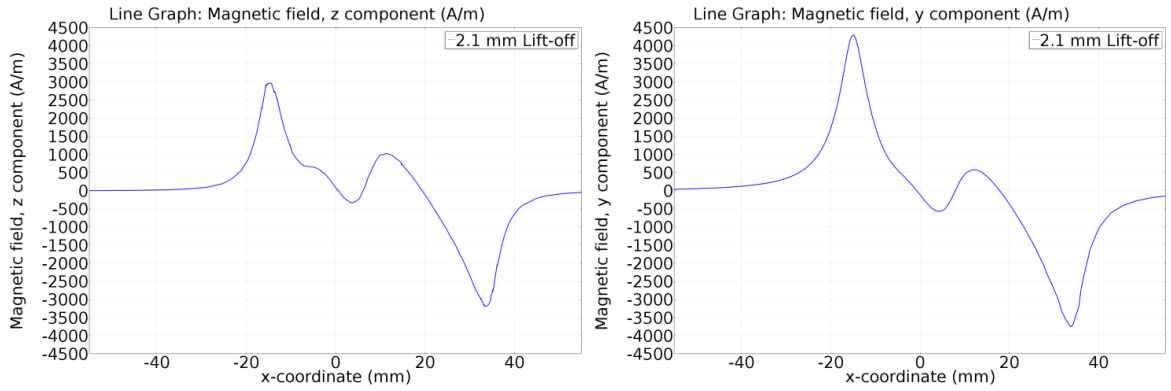

Figure D.5: *Amplitude locus curves of the leaked radial component at 2.1 mm lift-off of simulated clustered defects. a) 3D. b) 2D.*

Appendix E

MFL signal treatment instances

As discussed in Chapters 5 and 6, acquired signals in both, simulations as well as in experiments need some treatment to allow proper analysis. In this appendix are reported some results as examples of the requirements. Moreover, these plots provide the possibility to compare the results shown in previous chapters with results from different defects features. Due to the extension of the assessed cases, not all results are reported here, only a selection of them to give an overview.

E.1 Off-set level removal by H_x and H_z components

Figure E.1 presents the axial field component acquired at 3.5 mm of lift-off by inner defect configuration, before and after a filtered stage to eliminate the off-set level. Every defect has a diameter of 15 mm, and its specific depth is displayed in the plot legend.

The off-set level of the axial component has a constant behaviour, which is identified in this research as the applied field and by the results in Figure E.1 reaches 5.2 kA/m. Unlike, the off-set level of the radial component describes a negative field gradient, with a maximum in a plate-electromagnet boundary and a minimum in the opposite plate-electromagnet boundary. Figure E.2 illustrates the radial component leaked at 2.1 mm of lift-off generated due to 5 mm in diameter defects by different plate thickness reductions. Plots show the signals before and after a off-set filtered stage is applied.

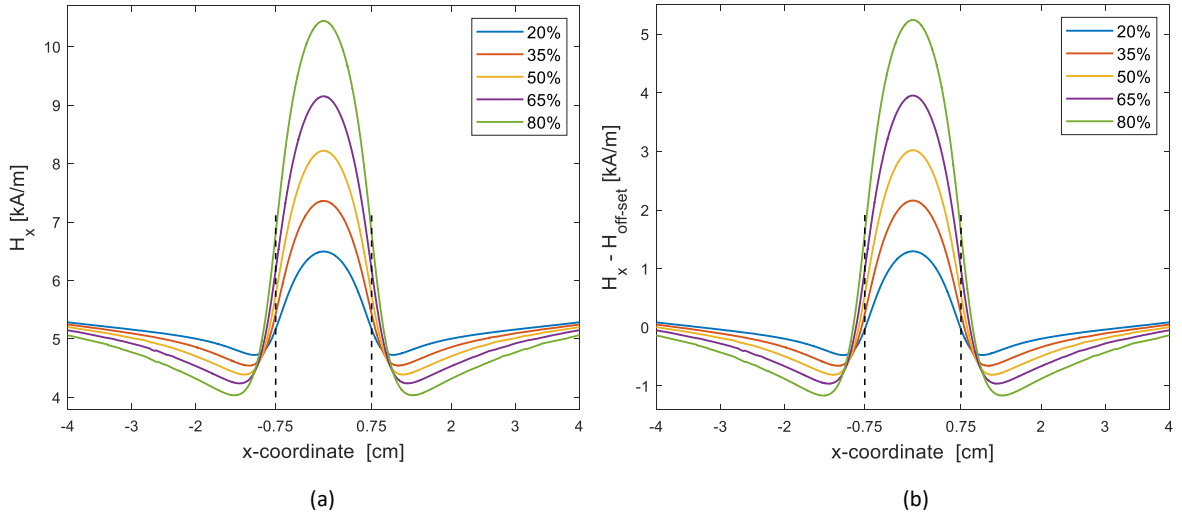

Figure E.1: *Axial field component by* ***inner defects*** *obtained by simulation at 3.5 mm of lift-off. Defects of 15 mm in diameter and depths according to the legend in percentage of the plate thickness. a) Measured signal. b) Off-set filtered signal.*

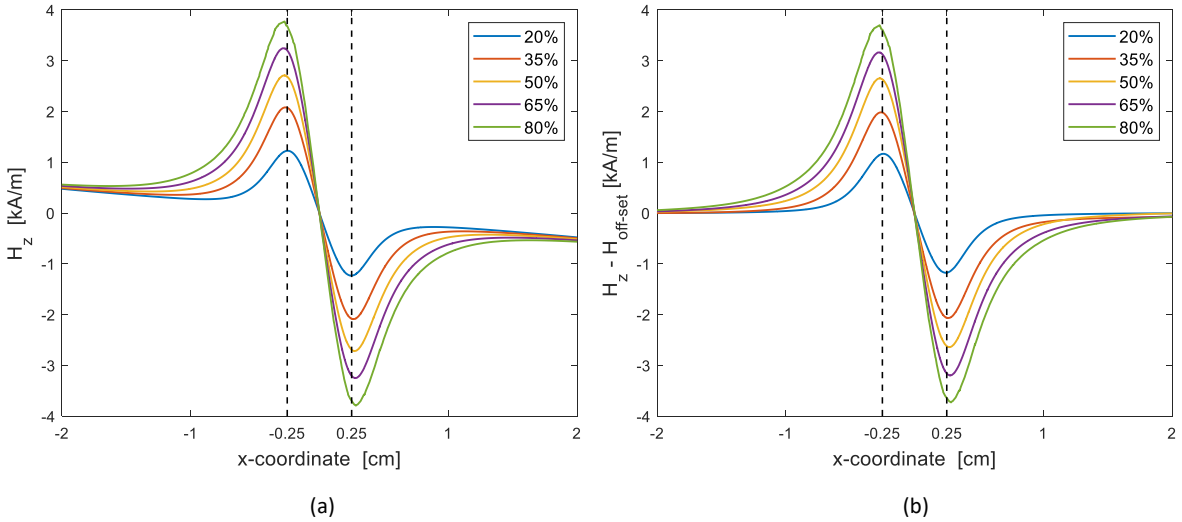

Figure E.2: *Radial field component of* ***inner defects*** *obtained by simulation at 3.5 mm of lift-off. Defects of 5 mm in diameter and depths according to the legend in percentage of the plate thickness. a) Measured signal. b) Off-set filtered signal.*

E.2 PWHM and PTPD criteria for defect length setting

The defect length is defined based on MFL signals according to the PWHM and PTPD criteria, as illustrated in Figure E.3. The PWHM criterion is understood in this research as the peak-width on the axial signal at the positions set by the fields equal to

$\left[(H_{x(max)} - H_{x(min)})/2\right] + H_{x(min)}$. While the PTPD criterion is the well-known peak to peak distance.

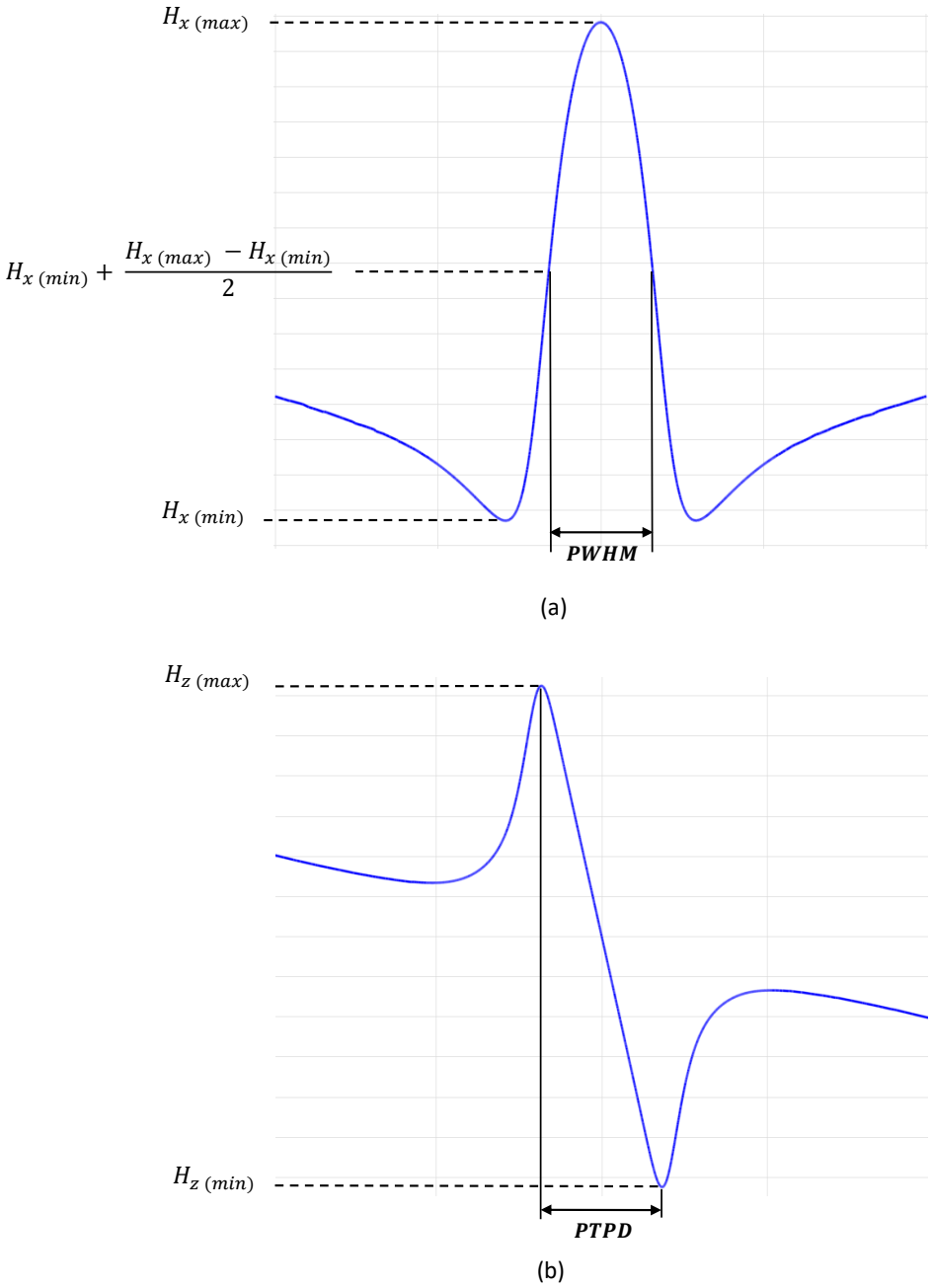

Figure E.3: *Criteria for the setting of defect length based on MFL signals. a) PWHM. b) PTPD.*

As next, some instances regarding PWHM criterion are introduced in order to identify the defect length. Figures E.4 and E.5 report maximum and minimum values of the axial component by inner and outer defect configurations, respectively. Furthermore, the point which defines the exact diameter is also identified in every plot. Analysis of the results based on the relation between MFL signal length and defect diameter is discussed in Section 6.4.4.

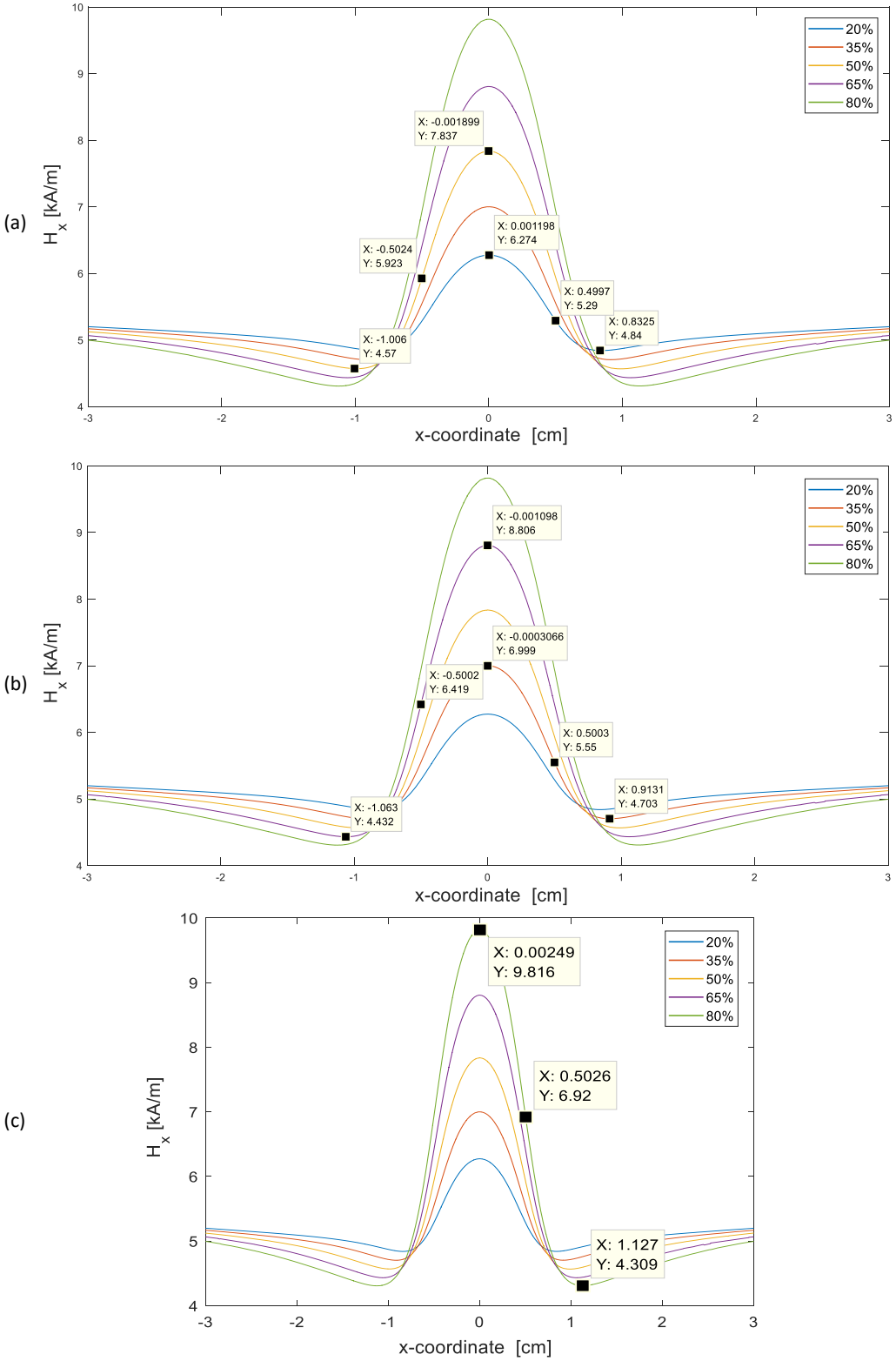

Figure E.4: *Maximum and minimum field of H_x used to determine the defect length based on the PWHM criterion for simulated* ***inner defects*** *with 10 mm in diameter and plate thickness reduction of: a) 20% and 50%; b) 35% and 65%; c) 80%. Additionally, the specific field value at a distance equal to the defect radius is also marked in every plot.*

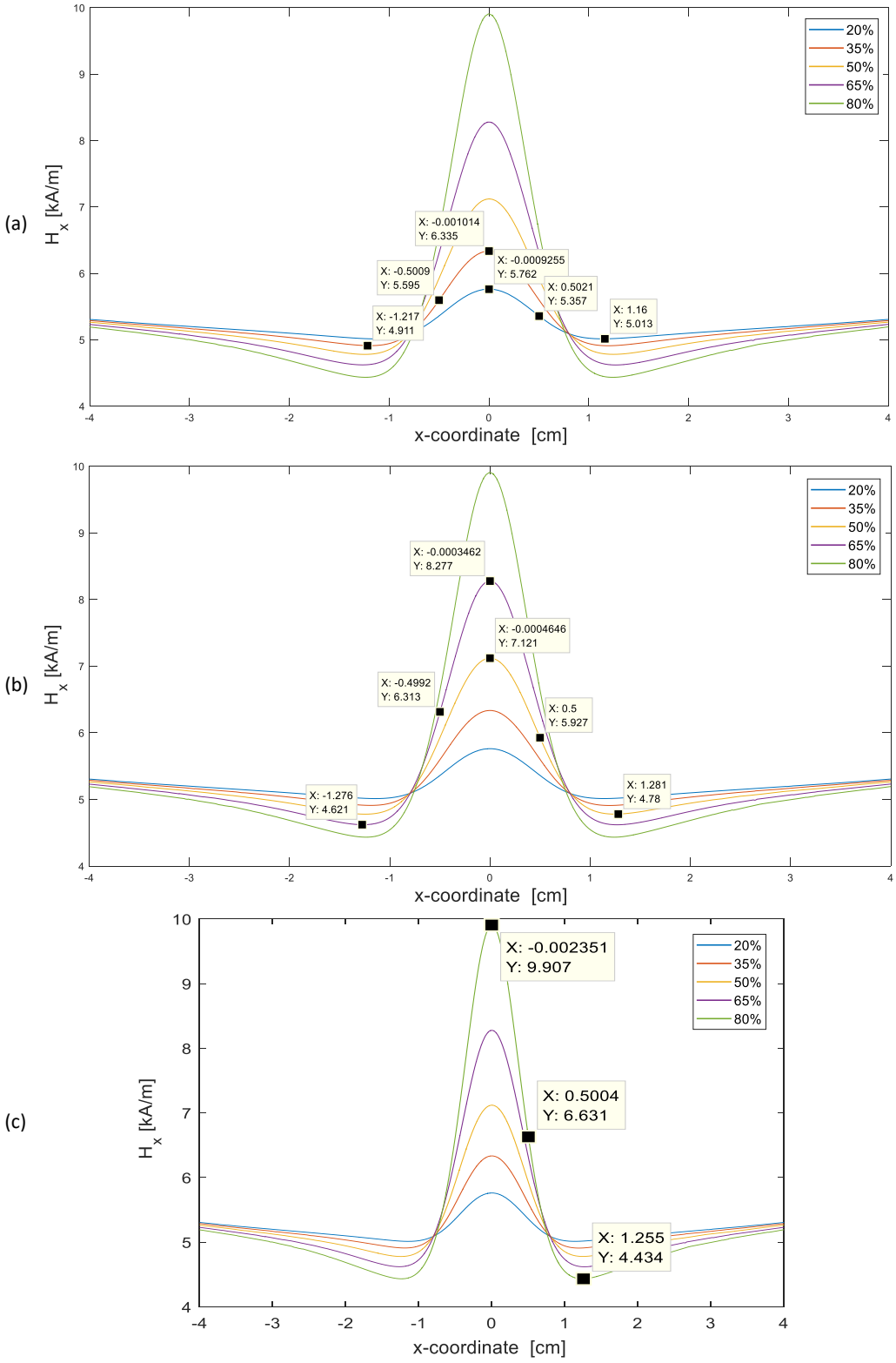

Figure E.5: *Maximum and minimum field of H_x used to determine the defect length based on the PWHM criterion for simulated* ***outer defects*** *with 10 mm in diameter and plate thickness reduction of: a) 20% and 35%; b) 50% and 65%; c) 80%. Additionally, the specific field value at a distance equal to the defect radius is also marked in every plot.*

Figure E.6 reports the PWHM and PTPD parameters for some selected instances from experimental results. Inspected defects have a diameter of 10 mm and depths of 50% and 80% of plate thickness reduction.

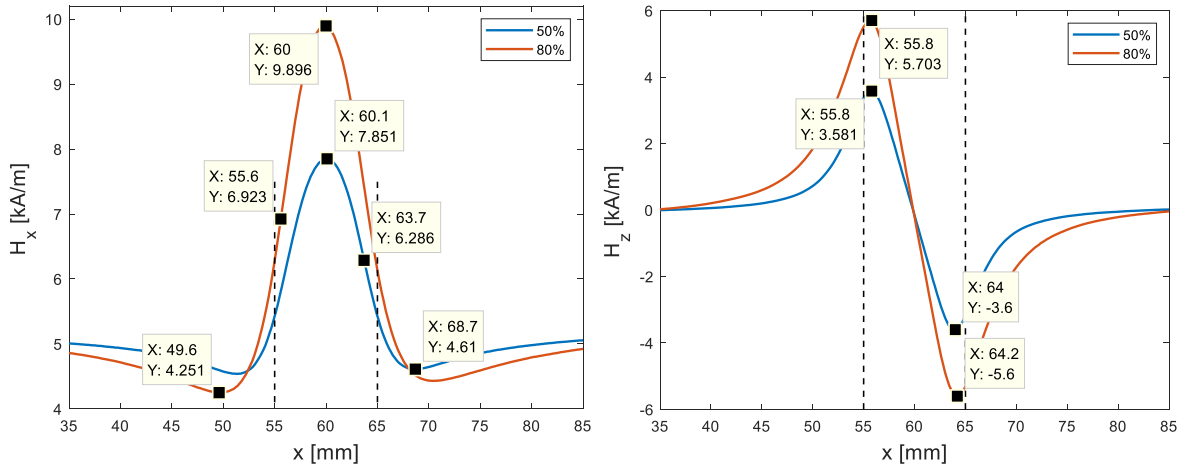

(a)

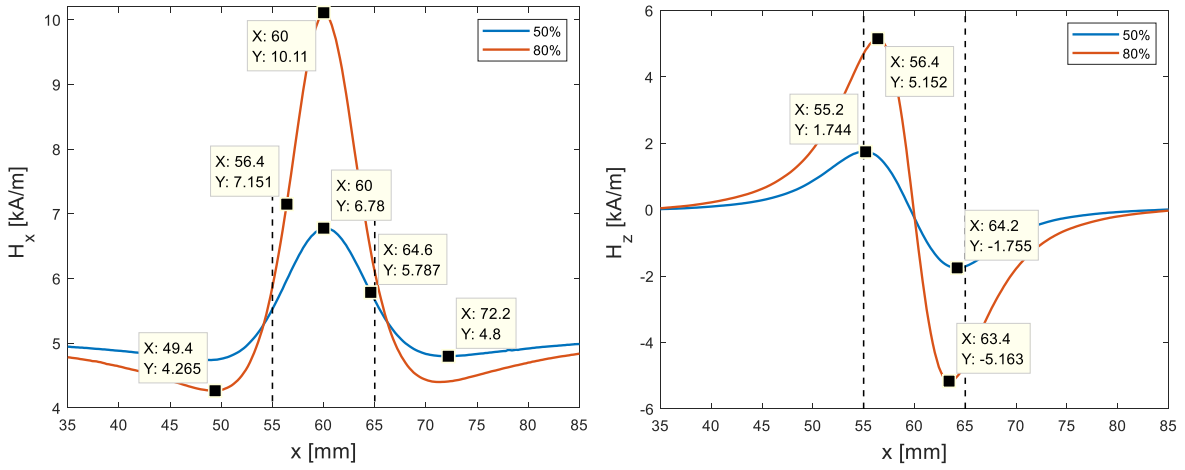

(b)

Figure E.6: *Maxima and minima fields to determine the defect length based on the PWHM and PTPD criteria for defects with 10 mm diameter and depths of 50% and 80% of plate thickness reduction. a)* ***inner defects****. b)* ***outer defects****.*

E.3 Lift-off dependency by H_x and H_z components

In the following results are exposed the lift-off dependency for two different flaws with calotte shape in both configurations, as inner and outer defects. The first has a diameter of 5 mm and 35% plate thickness reduction. The second has a diameter of 15 mm and likewise, plate thickness reduction of 35%. The coordinates are kept constant by inner and outer defect cases for each defect size in order to emphasise differences, see Figures E.7 to E.10.

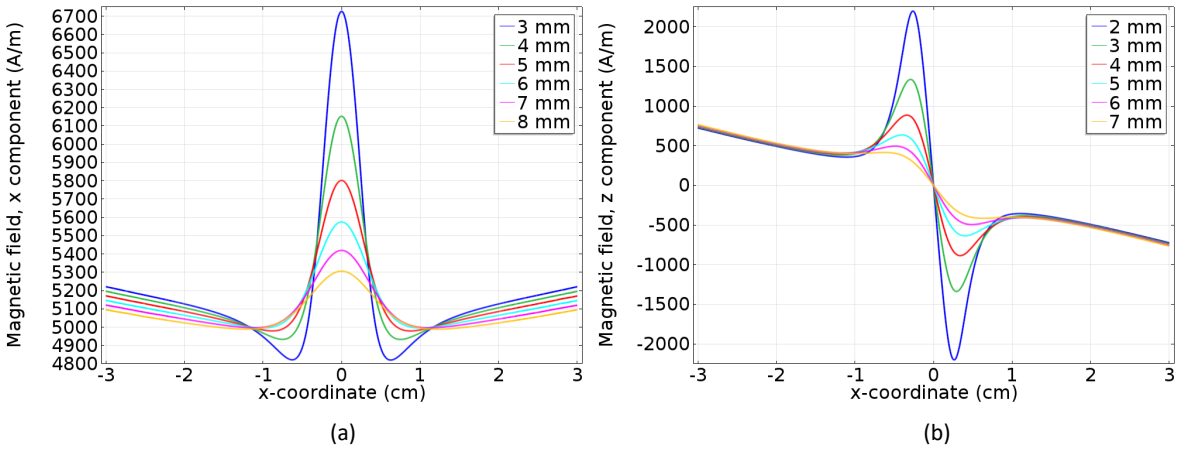

Figure E.7: *Leaked field components obtained from a simulated defect of 5 mm in diameter and 35% plate thickness reduction.* ***Inner defect*** *configuration. Lift-off settings according to the legend. a) H_x. b)H_z.*

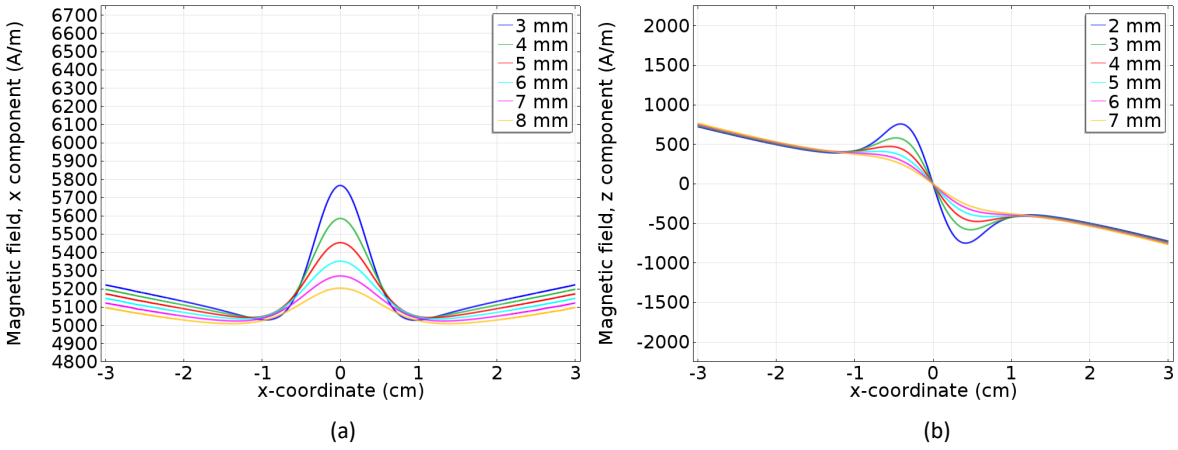

Figure E.8: *Leaked field components obtained from a simulated defect of 5 mm in diameter and 35% plate thickness reduction.* ***Outer defect*** *configuration. Lift-off settings according to the legend. a) H_x. b)H_z.*

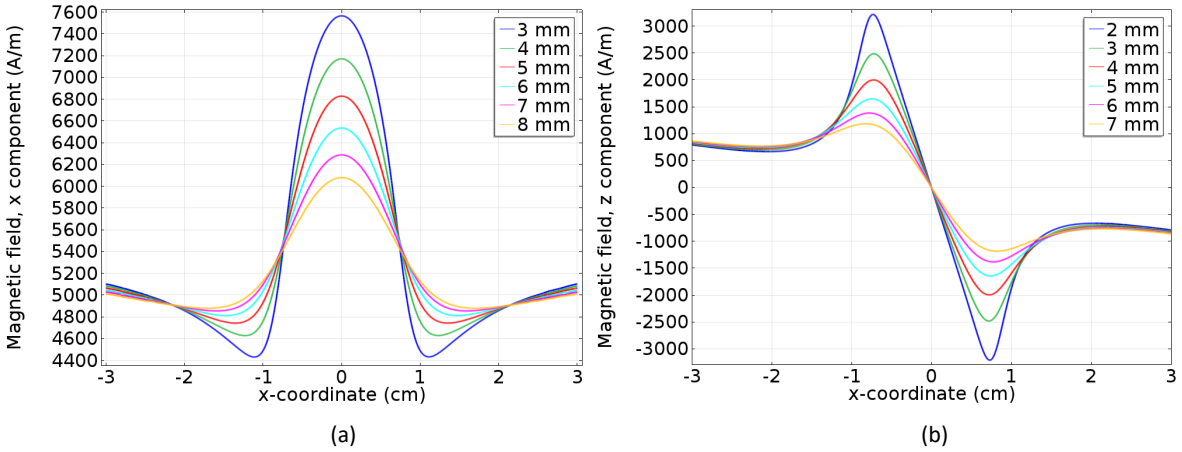

Figure E.9: *Leaked field components obtained from a simulated defect of 15 mm in diameter and 35% plate thickness reduction.* ***Inner defect*** *configuration. Lift-off settings according to the legend. a)* H_x*. b)*H_z*.*

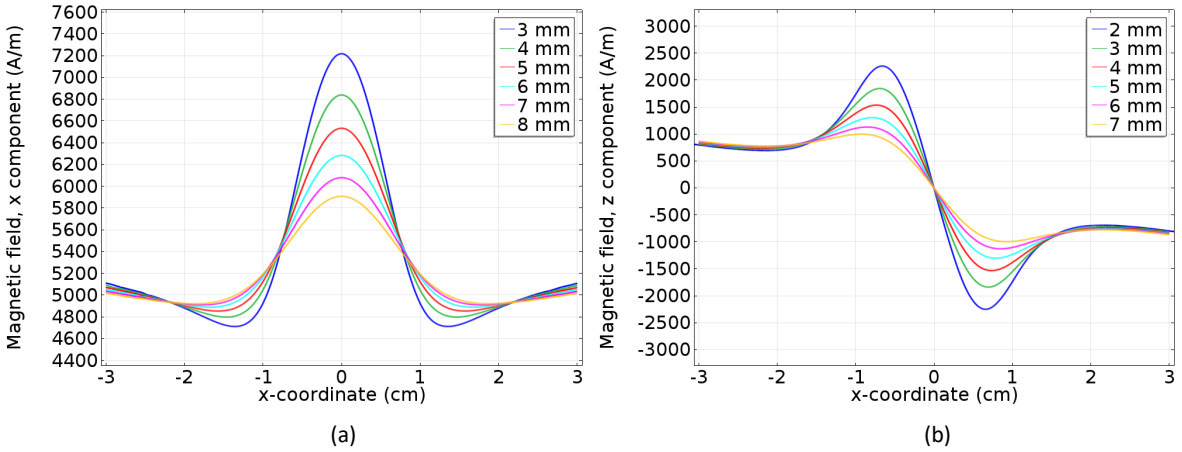

Figure E.10: *Leaked field components obtained from a simulated defect of 15 mm in diameter and 35% plate thickness reduction.* ***Outer defect*** *configuration. Lift-off settings according to the legend. a)* H_x*. b)*H_z*.*

Bibliography

[1] F. Niese. *EMUS-Wanddickensensor für die Pipelineinspektion mit integrierter Wirbelstrom- und Streuflussprüfung*. PhD thesis, Universität des Saarlandes, 2009.

[2] BP. BP Statistical Review of World Energy June 2015. 64th edition, London, UK, June 2015.

[3] S. Papavinasam. *Corrosion Control in the Oil and Gas Industry*. Elsevier, 2014.

[4] G. Dabholker. Pipeline Industry Growth Fueled By Increasing Global Energy Demand, Shale Gas Exploration. *Pipeline & Gas Journal*, 241(3), March 2014.

[5] R. Tubb. P & GJs 2014 Worldwide Construction Report. *Pipeline & Gas Journal*, 241(1), January 2014.

[6] R. Tubb. P&GJs 2016 Worldwide Construction Report. *Pipeline & Gas Journal*, 243(1), January 2016.

[7] Wikipedia. list of pipeline accidents, October 2014.

[8] National Energy Board. 2000-2013 Pipeline Incident Reporting, October 2014.

[9] Alberta Energy Regulator. Report 2013-B: Pipeline Performance in Alberta, 1990-2012. Technical report, Alberta Energy Regulator, 2013.

[10] R. Tubb. Pipeline & Gas Journals 2014 International Construction Report. *Pipeline & Gas Journal*, 241(8), August 2014.

[11] Corporación para la Investigación de la Corrosión (CIC) and Transportadora de Gas Internacional S.A. E.S.P (TGI). Desarrollo de Herramientas Inteligentes para Inspección y Diágnostico de Espesores de Líneas de Ttransporte de Hidrocarburos, ITION-E. Technical report, COLCIENCIAS, 2010.

[12] M. Layouni, M. S. Hamdi, and S. Tahar. Detection and sizing of metal–loss defects in oil and gas pipelines using pattern–adapted wavelets and machine learning. *Applied Soft Computing*, 52:247–261, 2017.

[13] S. Huang and W. Zhao. *Magnetic Flux Leakage. Theories and Imaging Technologies*, volume 1. Walter de Gruyter GmbH, Berlin/Boston, 2016.

[14] G. Kopp and H. Willems. Sizing Limits of Metal Loss Anomalies using Tri-axial MFL Measurements: A Model Study. *NDT & E International*, 55:75–81, April 2013.

[15] A. Romero-Ramírez, J. S. D. Mason, and N. Pearson. Experimental Study to Differentiate between top and bottom Defects for MFL Tank Floor Inspections. *NDT & E International*, 42(1):16–21, jan 2009.

[16] S. M. Dutta, F. H. Ghorbel, and R. K. Stanley. Simulation and Analysis of 3-D Magnetic Flux Leakage. *IEEE Transactions on Magnetics*, 45(4):1966–1972, April 2009.

[17] Y. Li, J. Wilson, and G. Y. Tian. Experiment and Simulation Study of 3D Magnetic Field Sensing for Magnetic Flux Leakage Defect Characterisation. *NDT & E International*, 40(2):179–184, mar 2007.

[18] Pipeline Operators Forum. Specifications and requirements for intelligent pig inspection of pipelines. *Pipeline Operator Forum*, pages 1–38, 2009.

[19] Rosen. *Technical Specifications of the ROCOMBO MFL–A/XT Tool*, 2013.

[20] W. H. Lewis, W. H. Sproat, B. D. Dodd, and J. M. Hanilton. Reliability of Nondestructive Inspections. Technical report, The Lockheed Georgia Company, 1978.

[21] G. A. Georgiou. Probability of Detection (POD) curves. Derivation, applications and limitations. Technical report, Health and Safety Executive 2006, 2006.

[22] Department of Defense Handbook. Nondestructive Evaluation System Reliability Assessment. Technical report, Department of Defense United States of America, 2009.

[23] A. P. Berens. NDT Reliability Data Analysis.

[24] G. A. Matzkanin and H. T. Yolken. A Technology Assessment of Probability of Detection (POD) for Nondestructive Evaluation (NDE). Technical report, Nondestructive Testing Information Analysis Center (NTIAC), 2001.

[25] W. D. Rummel and G. A. Matzkanin. *Nondestructive Evaluation (NDE). Capabilities Data Book.* Nondestructive Testing Information Analysis Center (NTIAC), third edition, 1997.

[26] S. Timashev and A. Bushinskaya. *Diagnostics and Reliability of Pipeline Systems*, volume 30. Springer International Publishing, 2016.

[27] L. Cartz. *Nondestructive Testing : Radiography, Ultrasonics, Liquid Penetrant, Magnetic Particle, Eddy Current.* ASM International, 1995.

[28] NDT Education Resource Center. Ndt course material.

[29] S. B. Costello, D. N. Chapman, C. D. F. Rogers, and N. Metje. Underground asset location and condition assessment technologies. *Tunnelling and Underground Space Technology*, 22(5-6):524–542, 2007.

[30] G. Desjardins. Optimized pipeline repair and inspection planning using inline inspection data. *Journal of Pipeline Integrity*, April 2002.

[31] F. Caleyo, L. Alfonso, J. M. Hallen, J. L. González, and E. Pérez-Baruch. Method proposed for calibrating MFL, UT ILI tools. *Oil & Gas Journal*, September 2004.

[32] S. Sadovnychiy, J. Lopez, V. Ponomaryov, and A. Sadovnychyy. Evaluation of distance measurements accuracy by odometer for pipelines pigs. *Journal of the Japan Petroleum Institute*, 49(1):38–42, 2006.

[33] American Society for Nondestructive Testing. Nondestructive testing handbook. In Robert C. McMaster, Paul McIntire, and Michael L. Mester, editors, *Electromagnetic Testing*, volume 4. American Society for Nondestructive Testing, 2 edition, 1986.

[34] H. J. M. Jansen, P. B. J. Van de Camp, and M. Geerdink. Magnetisation as a key parameter of magnetic flux leakage pigs for pipeline inspection. *Insight*, 36(9), September 1994.

[35] J. A. Parra-Raad and S. Roa-Prada. Multi-objective optimization of a magnetic circuit for magnetic flux leakage-type non-destructive testing. *Journal of Nondestructive Evaluation*, 35(14), January 2016.

[36] G. Dobmann and P. Höller. Physical analysis methods of magnetic flux leakage. In R. S. Sharpe, editor, *Research Techniques in Nondestructive Testing*, volume IV, chapter 2, pages 39–69. Academic Press, London, 1980.

[37] M. Katoh, K. Nishio, and T. Yamaguchi. FEM study on the influence of air gap and specimen thickness on the detectability of flaw in the yoke method. *NDT & E International*, 33:333–339, 2000.

[38] M. Katoh, N. Masumoto, K. Nishio, and Y. Tomiko. Modeling of the yoke-magnetization in MFL-testing by finite elements. *NDT & E International*, 36:479–486, 2003.

[39] S. Xiao-chun, H. Song-ling, and Z. Wei. Optimization of the magnetic circuit in the MFL inspection system for storage-tank floors. *Russian Journal of Nondestructive Testing*, 43(5):326–331, 2007.

[40] S. Yang, Y. Sun, L. Udpa, S. S. Udpa, and W. Lord. 3D simulation of velocity induced fields for nondestructive evaluation application. *IEEE Transactions on Magnetics*, 35(3):1754–1756, May 1999.

[41] Y. Li, G. Y. Tian, and S. Ward. Numerical simulation on magnetic flux leakage evaluation at high speed. *NDT & E International*, 39:367–373, 2006.

[42] P. Wang, Y. Gao, G. Tian, and H. Wang. Velocity effect analysis of dynamic magnetization in high speed magnetic flux leakage inspection. *NDT & E International*, 64:7–12, 2014.

[43] J. B. Nestleroth. Circumferential MFL in-line inspection for cracks in pipelines. Technical report, Battelle, June 2003.

[44] R. C. Ireland and C. R. Torres. Finite element modelling of a circumferential magnetiser. *Sensors and Actuators A*, 129:197–202, 2006.

[45] A. Kloster. *Aufbau einer Entwicklungsplattform für niederfrequente magnetische Prüfverfahren*. PhD thesis, Universität des Saarlandes, 2008.

[46] N. B. S. Gloria, M. C. L. Areiza, I. V. J. Miranda, and J. M. A. Rebello. Development of a magnetic sensor for detection and sizing of internal pipeline defects. *NDT & E International*, 42:669–677, 2009.

[47] J. Hwang, J. Lee, and S. Kwon. The application of a differential-type Hall sensors array to the nondestructive testing of express train wheels. *NDT & E International*, 42:34–41, 2009.

[48] M. Le, J. Lee, J. Jun, J. Kim, S. Moh, and K. Shin. Hall sensor array based validation of estimation of crack size in metals using magnetic dipole models. *NDT & E International*, 53:18–25, 2013.

[49] N. N. Zatsepin and V. E. Shcherbinin. Calculation of the magnetostatic field of surface defects. I. field topography of defect models. *Defektoskopiya*, 2(5):385–393, 1966.

[50] V. E. Shcherbinin and N. N. Zatsepin. Calculation of the magnetostatic field of surface defects. II. experimental verification of the principal theoretical relationships. *Defektoskopiya*, 2(5):394–399, 1966.

[51] V. E. Shcherbinin and A. I. Pashagin. Influence of the extension of a defect on the magnitude of its magnetic field. *Defektoskopiya*, 8(4):74–82, 1972.

[52] W. Lord and J. H. Hwang. Defect characterization from magnetic leakage fields. *British Journal of NDT*, 19:14–18, January 1977.

[53] D. L. Atherton and M. G. Daly. Finite element calculation of magnetic flux leakage detector signals. *NDT International*, 20(4):235–238, 1987.

[54] S. M. Dutta. *Magnetic Flux Leakage Sensing: The Forward and Inverse Problem*. PhD thesis, Rice University, 2008.

[55] R. K. Amineh, S. Koziel, N. K. Nikolova, J. W. Bandler, and J. P. Reilly. A space mapping methodology for defect characterization from magnetic flux leakage measurements. *IEEE Transactions on Magnetics*, 44(8):2058–2065, August 2008.

[56] X. Yuan, C. Wang, F. Ji, and X. Zuo. A magnetic flux leakage analysis model based on finite element neural network. *Insight*, 53(9):482–486, September 2011.

[57] C. Xu, C. Wang, F. Ji, and X. Yuan. Finite-element neural network-based solving 3-d differential equations in mfl. *IEEE Transactions on Magnetics*, 48(12):4747–4756, December 2012.

[58] N. R. Pearson, M. A. Boat, R. H. Priewald, M. J. Pate, and J. S. D. Mason. Practical capabilities of MFL in steel plate inspection. In *18th World Conference on Nondestructive Testing*, Durban, South Africa, April 2012.

[59] M. Ravan, R. K. Amineh, S. Koziel, N. K. Nikolova, and J. P. Reilly. Sizing of 3-D arbitrary defects using magnetic fliux leakage measurements. *IEEE Transactions on Magnetics*, 46(4):1024–1033, April 2010.

[60] M. L. Shur, A. P. Novoslugina, and Ya. G. Smorodinskii. On the inverse problem of magnetostatics. *Russian Journal of Nondestructive Testing*, 49(8):465–473, 2013.

[61] J. Chen, S. Huang, and W. Zhao. Three-dimensional defect reconstruction from magnetic flux leakage signals in pipeline inspection based on a dynamic taboo search procedure. *Insight*, 56(10):197–202, October 2014.

[62] F. Förster. On the way from the "know-how" to the "know-why" in the magnetic leakage field method of nondestructive testing (part one). *Materials Evaluation*, 43:1154–1162, 1985.

[63] P. C. Charlton and K. E. Donne. Computer modelling of magnetic flux leakage methods. *British Journal of NDT*, 36(3):128–133, 1994.

[64] S. Lukyanets, A. Snarskii, M. Shamonin, and V. Bakaev. Calculation of magnetic leakage field from a surface defect in a linear ferromagnetic material: an analytical approach. *NDT & E International*, 36:51–55, 2003.

[65] M. Katoh, K. Nishio, T. Yamaguchi, and V. Bakaev. The influence of modeled B-H curve on the density of the magnetic leakage flux due to a flaw using yoke-magnetization. *NDT & E International*, 37:603–609, 2004.

[66] Z. Huang, P. Que, and L. Chen. 3D fem analysis in magnetic flux leakage method. *NDT & E International*, 39:61–66, 2006.

[67] A. A. Snarskii, M. Zhenirovskyy, D. Meinert, and M. Schulte. An integral equations model for the magnetic flux leakage method. *NDT & E International*, 43:343–347, 2010.

[68] S. Mandayam, L. Udpa, S. S. Udpa, and W. Lord. Wavelet-based permeability compensation technique for characterization magnetic flux leakage images. *NDT & E International*, 30(5):297–303, 1997.

[69] R. Schifini and A. C. Bruno. Experimental verification of a finite element model used in a magnetic flux leakage inverse problem. *Journal of Physics D: Applied Physics*, 38:1875–1880, 2005.

[70] A. A. Carvalho, J. M. A. Rebello, L. V. S. Sagrilo, C. S. Camerini, and I. V. J. Miranda. MFL signals and artificial neural networks applied to detection and classification of pipe weld defects. *NDT & E International*, 39:661–667, 2006.

[71] Y. Zhang, Z. Ye, and C. Wang. A fast method for rectangular cracks sizes reconstruction in magnetic flux leakage testing. *NDT & E International*, 42:369–375, 2009.

[72] D. Mukherjee, S. Saha, and S. Mukhopadhyay. An adaptive channel equalization algorithm for MFL signal. *NDT & E International*, 45:111–119, 2012.

[73] S. Kathirmani, A. K. Tangirala, S. Saha, and S. Mukhoïadhyay. Online data compression of MFL signals for pipeline inspection. *NDT & E International*, 50:1–9, 2012.

[74] D. Mukherjee, S. Saha, and S. Mukhopadhyay. Inverse mapping of magnetic flux leakage signal for defect characterization. *NDT & E International*, 54:198–208, 2013.

[75] N. G. Thompson. Gas and liquid transmission pipelines. Dublin, Ohio.

[76] The American Society of Mechanical Engineers ASME. *B31.4 - 2009 Pipeline Transportation Systems for Liquid Hydrocarbons and Other Liquids*, 2009.

[77] The American Society of Mechanical Engineers ASME. *B31.8S - 2016 Managing System Integrity of Gas Pipelines*, 2016.

[78] G. Goodfellow and J. Haswell. A comparison of inherent risk levels in ASME B31.8 and UK gas pipeline design codes. *6th International Pipeline Conference*, September 2006.

[79] LLC Process Performance Improvement Consultants. Comparison of integrity management assessment techniques for natural gas transmission pipelines. Technical report, INGAA Foundation, Inc., September 2007.

[80] The American Petroleum Institute. *API Standard 1163. In-line Inspection Systems. Qualification Standard*, 2013.

[81] The National Association of Corrosion Engineers. *NACE Standard SP0102. In-line Inspection of Pipelines. Standard practice*, 2010.

[82] American Society for Nondestructive Testing. *ANSI/ASNT Standard ILI-PQ. In-line Inspection Personnel Qualification and Certification*, 2010.

[83] G. Dobmann and H. Münnich. Eine integralgleichungsnäherung zur berechnung von magnetostatischen streufeldern in umgebung von oberflächenrissen in ferromagnetischen materialien. *Deutsche Gesellschaft für Zerstörungsfreie Prüfung e.V.*, 71:627–635, 1978.

[84] S. M. Dutta, F. H. Ghorbel, and R. K. Stanley. Dipole Modeling of Magnetic Flux Leakage. *IEEE Transactions on Magnetics*, 45(4):1959–1965, April 2009.

[85] V. V. Dyakin and O. V. Umergalina. Calculation of the Field of a Flaw in Three-Dimensional Half-Space. *Russian Journal of Nondestructive Testing*, 39(4):297–309, 2003.

[86] V. V. Dyakin, O. V. Umergalina, and V. Ya. Raevskii. The Field of a Finite Defect in a 3D Semispace. *Russian Journal of Nondestructive Testing*, 41(8):502–513, 2005.

[87] V. V. Dyakin, V. Ya. Raevskii, and O. V. Umergalina. A Magnetostatic Problem for a Semispace with a Spherical Defect in an Inhomogeneous External Field. *Russian Journal of Nondestructive Testing*, 43(1):1–11, 2007.

[88] V. V. Dyakin, V. Ya. Rayevskiy, and O. V. Kudrjashova. The Field of a Finite Defect in a Plate. *Russian Journal of Nondestructive Testing*, 45(3):199–209, 2009.

[89] V. V. Dyakin, V. Ya. Raevskii, and O. V. Kudryashova. A Flaw in a Sphere. *Russian Journal of Nondestructive Testing*, 45(9):604–615, 2009.

[90] V. V. Dyakin and O. V. Kudryashova. A Flaw in a Sphere (Continuation). *Russian Journal of Nondestructive Testing*, 46(11):819828, 2010.

[91] V. V. Dyakin and O. V. Kudryashova. A Flaw in a Cylinder. *Russian Journal of Nondestructive Testing*, 48(4):226–237, 2012.

[92] V. V. Dyakin and O. V. Kudryashova. A Flaw in a Pipe. *Russian Journal of Nondestructive Testing*, 48(10):555–567, 2012.

[93] COMSOL. *COMSOL Multiphysics, Reference Guide*, 2012.

[94] COMSOL. *AC/DC Manual, User's Guide*, 2015.

[95] B. D. Cullity and C. D. Graham. *Introduction to magnetic Materials*. John Wiley & Sons, Inc.„ second edition, 2009.

[96] S. Chikazumi and C. D. Graham. *Physics of Ferromagnetism*. Oxford Science Publications, second edition, 1997.

[97] A. Cosham and P. Hopkins. The pipeline defect assessment manual. In *Proceedings of IPC 2002: International Pipeline Conference*, Calgary, Alberta, Canada, September - October 2002.

[98] A. Cosham, P. Hopkins, and K. A. Macdonald. Best practice for the assessment of defects in pipelines - corrosion. *Engineering Failure Analysis*, 14:1245–1265, 2007.

[99] H. R. Vanaei, A. Eslami, and A. Egbewande. A review on pipeline corrosion, in-line inspection (ILI), and corrosion growth rate models. *International Journal of Pressure Vessels and Piping*, 149:43–54, 2017.

[100] M. L. Shur, A. P. Novoslugina, and Ya. G. Smorodinskii. The Magnetic Field of an Arbitrary Shaped Defect in a Plane Parallel Plate. *Russian Journal of Nondestructive Testing*, 51(11):669–679, 2015.

[101] N. R. Pearson, M. A. Boat, R. H. Priewald, M. J. Pate, and J. S. D. Mason. A study of mfl signals from a spectrum of defect geometries. In *18th World Conference on Nondestructive Testing*, Durban, South Africa, April 2012.

[102] I. C. Perez-Blanco, J. H. Panqueva-Alvarez, and G. Dobmann. Simulation for magnetic flux leakage signal interpretation: A FE-approach to support in-line magnetic pipeline pigging. In *2014 IEEE Far East Forum on Nondestructive Evaluation/Testing*, Chengdu, China, June 2014.

[103] C. Mandache and L. Clapham. A model for magnetic flux leakage signal predictions. *Journal of Physics D: Applied Physics*, 36:2427–2431, 2003.

[104] S. Seely and A. D. Poularikas. *Electromagnetics. Classical and Modern Theory and Applications*. Marcel Dekker, INC., 1979.

[105] The International Institute of Welding. Handbook on the magnetic examination of welds. Technical report, The Welding Institute, Abington Hall, 1988.

[106] A. Crouch, T. Beuker, and B. Brown. Flux leakage signals from corrosion defects in pipelines subjected to bending loads. In John Tiratsoo, editor, *Pipeline Pigging and Integrity Technology*, chapter 3, pages 267–282. Scientific Surveys Ltd and Clarion Technical Publishers, 2003.

[107] G. Dobmann. Contribution about electromagnetic flux inspection techniques. Technical report, Fraunhofer Institut for Nondestructive Testing IZFP, 1983.

[108] G. Dobmann, G. Walle, and P. Höller. Magnetic leakage flux testing with probes: physical principles and restrictions for application. *NDT International*, 20(2):101–104, April 1987.

[109] W. Han and P. Que. A modified wavelet transform domain adaptive fir filtering algorithm for removing the spn in the mfl data. *Measurement*, 39:621–627, 2006.

[110] Y. Sun and Y. Kang. A new mfl principle and method based on near-zero background magnetic field. *NDT & E International*, 43:348–353, 2010.

[111] J. Feng, S. Lu, J. Liu, and F. Li. A sensor liftoff modification method of magnetic flux leakage signal for defect profile estimation. *IEEE Transactions on Magnetics*, 53(7), 2017.

[112] D. Minkov, J. Lee, and T. Shoji. Study of crack inversions utilizing dipole model of a crack and hall elements measurements. *Journal of Magnetism and Magnetic Materials*, 217:207–215, 2000.

[113] D. Minkov, Y. Takeda, T. Shoji, and J. Lee. Estimating the sizes of surface cracks based on hall element measurements of the leakage magnetic field and a dipole model of a crack. *Journal of Applied Physics A: Materials Science & Processing*, 74:169–176, 2002.

[114] J. Hwang and W. Lord. Finite element modelling of magnetic field/defect interactions. *ASTM Journal of Testing and Evaluation*, 3(1):21–25, 1975.

[115] S. Kyriakides, E. Corona, and F. J. Fischer. On the effect of the UOE manufacturing process on the collapse pressure of long tubes. In *Proceedings of the Annual Offshore Technology Conference*, pages 531–543, Houston, United States, May 1991.

[116] M. D. Herynk, S. Kyriakides, A. Onoufriou, and H. D. Yun. Effects of the UOE/UOC pipe manufacturing processes on pipe collapse pressure. *International Journal of Mechanical Sciences*, 49:533–553, 2007.

[117] G. Chatzopoulou, S. A. Karamanos, and G. E. Varelis. Finite element analysis of UOE manufacturing process and its effect on mechanical behavior of offshore pipes. *International Journal of Solids and Structures*, 83:13–27, 2016.

[118] J. Costain, N. R. Pearson, and M. A. Boat. Capability of modern tank floor scanning with magentic flux leakage. In *19th World Conference on Non-Destructive Testing 2016*, Munich, Germany, June 2016.

[119] D. H. Saunderson. The MFE tank floor scanner - a case history. In *IEE colloquium on non-destructive evaluation*, London, UK, January 1988.

[120] N. R. Pearson, M. A. Boat, and J. S. D. Mason. Bandwidth of MFL in steel plate inspection. In *19th World Conference on Nondestructive Testing*, Munich, Germany, June 2016.